JAGELLONIAN UNIVERSITY
THE FACULTY OF PHYSICS, ASTRONOMY
AND APPLIED COMPUTER SCIENCE
MARIAN SMOLUCHOWSKI INSTITUTE OF PHYSICS

ENERGY DEPENDENCE OF PROTON INDUCED FRAGMENTATION OF ATOMIC NUCLEI

Borys Piskor-Ignatowicz

PhD dissertation performed
in the Nuclear Physics Department
and in the Nuclear Physics Institute of the Research Center Jülich
Thesis supervisor: Prof. dr hab. Bogusław Kamys

Cracow 2009

Contents

Chapter 1

Introduction

In spite of the fact that reactions induced by protons of energies between hundred MeV and several GeV on atomic nuclei are subject of great interest since over a half of century, the mechanism of these reactions is still not understood satisfactorily. One of the most intriguing questions concerns the mechanism responsible for the specific energy dependence of the production cross sections observed for *"light charged particles" ("LCPs")*, i.e., the particles with Z $\leq$2, and *"intermediate mass fragments" ("IMFs")* ,i.e., particles with $2 <$ Z $< Z_{target}/3$. Investigation of this mechanism for proton induced reactions on Ni targets is the main subject of the present thesis.

It was observed in the studies published in the literature, that increasing of the proton beam energy from a value comparable with the Fermi motion energy of nucleons in nuclei to several GeV leads for all nuclei to a fast increase of the cross sections for the production of LCPs and IMFs – even by 2 - 3 orders of magnitude. It is important to note, that at these high energies the absorption cross section for the proton initiating the reaction is almost energy independent and, moreover, the sum of the production cross sections for all ejectiles becomes larger than the absorption cross section. This means, that the increasing of the cross sections is only due to the growing of multiplicity of the emitted particles. It is also worthy to emphasize, that the production cross sections for IMFs increase faster than those for LCPs. This agrees with the intuitive argument, that the energy transfer to the nuclei is larger at higher than at lower beam energies and, therefore, at higher energies the nuclei accumulate such amount of excitation energy that emission of complex particles may compete with emission of nucleons and LCPs. A fast increase of the multiplicity of produced IMFs observed for all target nuclei in the neighborhood of 1 GeV proton beam energy is interpreted in the literature as indication of the appearance of a reaction process called *"fragmentation"* (or *"multifragmentation"*), which occurs when several IMFs are produced in the reaction. At still higher beam energies – of the order of several GeV – the leveling of the cross sections was observed, what was explained by reasoning, that the deposit of the energy and thus excitation energy is limited by stability of the nucleus.

In spite of the fact, that a qualitative explanation presented above of the observed energy dependence of the production cross sections seems to be rather convincing, the satisfactorily, quantitative description of the data is still lacking. The theoretical approaches discussed in the literature, assuming various reaction mechanisms, are able to reproduce only a part of the observed facts. Even the total production cross sections and their energy variation can be at present predicted by the theory with moderate success only, i.e., deviations of the theoretical cross sections from data are frequently larger than factor two. Furthermore, the theoretical differential cross sections – angular and energy distributions – do not agree qualitatively with the data, what means that important properties of the reaction mechanism are not properly taken into account. This is a very significant drawback of the present situation, because besides the obvious need to understand the mechanism of proton induced reactions, there is also a broad range of applications which must rely on model predictions of the cross sections of such reactions. For example, the reliable data for the design and construction of spallation neutron sources and/or accelerator driven systems must be known for various proton beam energies on many targets and for different reaction products. The number of different reactions important for such applications is so large, that it is practically impossible to determine all these cross sections experimentally. On the contrary, the knowledge of reaction mechanism should allow for creation of realistic theoretical models, which are able to provide cross sections for all interesting reactions – even those which cannot be studied experimentally. It is, therefore, clear that studying of the mechanism of proton induced reactions is crucial both, for fundamental physical studies, and for the applications.

One of the most commonly used descriptions of proton induced reactions assumes that at GeV beam energies the reaction proceeds in two steps. In the first step a direct reaction emerges in which the incident proton knocks out several nucleons in a series of two-body collisions, leaving behind a single, heavy residuum of the target nucleus. Such a mechanism is called *"spallation"*. The residuum of spallation is usually excited and evaporates charged particles and neutrons forming finally target-like residual nucleus.

This approach to the reaction mechanism, describing usually the first step of the reaction by an intranuclear cascade or by Boltzmann-Uehling-Uhlenbeck model, has an obvious shortcoming, i.e., it allows only for emission of composite LCPs and IMFs with small energies, characteristic for the evaporation. The experimental spectra show, however, that the complex particles are in most cases emitted also with large energies - much higher than predicted by this approach.

A more sophisticated version of the above model allows for pre-equilibrium emission of complex particles which are formed by interaction of nucleons escaping from the nucleus in the first stage of the reaction, if the relative distance of these nucleons in the configurational and momentum space is small enough. This phenomenon is called *"coalescence"* and seems to be important mainly for the emission of composite LCPs because the probability to find a larger group of nucleons with appropriate spatial and momentum coordinates is strongly decreasing with the number of nucleons belonging to this group. Moreover, improving the description of composite LCPs by inclusion of a coalescence mechanism deteriorates the description of the nucleon spectra because the increasing of cross section for production of composite particles occurs on expense of the nucleon cross sections. In summary, the traditional two-step model is not able to reproduce quantitatively the energy distributions of IMFs and, to a large extent, of LCPs. This calls for searching for another reaction mechanism responsible for proton - nucleus collisions, especially for fragmentation.

Several scenarios of the mechanism of fragmentation have been proposed. They all assume that at proton beam energies around or/and above 1 GeV the deposited energy approaches a critical value at which the nucleus becomes unstable and starts to decompose into fragments. They differ, however, in postulating how this process proceeds; whether the excited nucleus emits sequentially composite particles or the nucleus disassembles simultaneously into several fragments. Furthermore, they differ in assuming whether the emission occurs from the equilibrated nucleus or before achieving thermal equilibrium. The presence of high energy particles in the spectra of LCPs and IMFs suggests that the disassembly of the nucleus does not appear from the equilibrium. A detailed study of differential cross sections is necessary to decide whether the ejectiles are emitted sequentially or simultaneously.

One of the vividly discussed hypotheses claims that the thermal expansion of the excited nucleus leads to decreasing of its density what, in turn, causes appearing of volume and surface instabilities leading to multifragment production. Such a transition from uniform nuclear matter consisted of nucleons into mixture of fragments and nucleons is frequently treated as analog of *"liquid-gas phase transition"*. The above described picture of proton induced multifragmentation should result in angular distributions consistent with emission of fragments from a single moving source.

Another possible mechanism of fragmentation is due to break-up of the target nucleus during the fast stage of proton - nucleus collision (*"fast break-up"*) resulting in the emission of 2 - 3 excited prefragments of the target nucleus, which in the following act as moving sources of emitted fragments. This mechanism could be, in principle, distinguished from the previous one by a number of moving sources of detected fragments. It should be, however, taken into consideration that the competition of both mechanisms is possible as well as the competition with the spallation reaction followed by sequential evaporation of fragments. Then, the presence of two sources of fragments may be due also to competition of mentioned mechanisms. To decide which effect occurs it is necessary to take into account the information on properties of moving sources of fragments , i.e., their dimensions, velocity and temperature. Such an information may be derived from the investigations of differential cross sections.

The ideal situation would correspond to exclusive experiments in which all products are identified and their momenta are known. Realization of such experiments would involve the application of sophisticated multidetector systems operating in coincidence and covering full solid angle of $\sim 4\pi$. Such investigations were performed by several groups (the ISiS collaboration [139], NESSI collaboration [89], and FASA collaboration [78]) for protons impinging on the gold target. Herbach et al. [66] studied also 1.2 GeV proton induced reactions on other nuclear targets but low statistics of coincidence experiments did not allow to extract double differential cross sections.

The common conclusion from these investigations is that the intensive IMFs production observed in p+Au collisions for proton beam energies between 1 and 14 GeV cannot be explained by a two-step process described by the intranuclear cascade and the statistical evaporation from excited residua of spallation reaction alone but involves additionally some other mechanism. Such a mechanism was treated as analog of the liquid-gas phase transition for proton energies higher than 8 - 10 GeV [78, 80], where leveling of the cross sections for IMFs production is observed. It should be, however, emphasized that an unambiguous explanation of the mechanism was not given in these investigations for lower proton energies, where production cross sections increase quickly with beam energy.

Recently p+Au system was studied by PISA collaboration [31, 33], which very well described a large amount of data consisted of double differential cross sections $\frac{d\sigma}{d\Omega dE}$, measured in inclusive experiment at three proton beam energies (1.2, 1.9, and 2.5 GeV), by introducing the competition of the mechanism described by traditional two-step model with the fast break-up of the target followed by the emission of particles from excited fragments of the target. It was found, that the high energy part of the energy spectra of all LCPs and IMFs is dominated by this mechanism, which was able to well reproduce the data assuming that the target nucleus decays into three groups of nucleons; small, fast and hot "fireball" emitting LCPs, and two larger, slower and colder prefragments emitting LCPs and IMFs. On the other hand, the spallation mechanism followed by evaporation of particles from an equilibrated residuum was responsible for the low energy parts of the spectra. Both mechanisms contribute almost equally to the total production cross section of IMFs and LCPs, whereas the coalescence process gives also significant contribution to cross sections for composite LCPs. Due to the analysis of energy and angular dependence of double differential cross sections $\frac{d\sigma}{d\Omega dE}$ it was possible to estimate properties of three types of emitting sources and to establish that they differ significantly in mass, temperature and velocity.

While above mentioned investigations resulted in receiving quite a lot of information on the mechanism of reactions in p+Au nuclear system it remains not clear whether the the here drawn conclusions are valid also for other nuclei.

The aim of the present thesis was to study whether the reaction mechanism of fragmentation proposed by the PISA collaboration for a Au target may be applied for other nuclei and to investigate its energy dependence for proton beam energies up to 2.5 GeV. To achieve this goal, a study was undertaken of proton induced reactions on nickel target, which is over three times lighter than gold, has different neutron to proton number ratio, and has larger binding energy per nucleon. Appearing of the same reaction mechanism for Ni, which has completely different properties, as for Au in the same beam energy range should suggest that such a phenomenon is common for all nuclei.

The measurements of double differential cross sections $\frac{d\sigma}{d\Omega dE}$ for isotopically identified H, He, Li, Be and B nuclei and elementally identified C and N nuclei have been done for the same three proton beam energies (1.2, 1.9, and 2.5 GeV) as those used for p+Au reactions in Refs. [31, 33]. This range of energy is significantly lower than energies where liquid-gas transition was quoted for p+Au system, but is broad enough to observe a possible variation of the mechanism responsible for the emission of IMFs. Thus, it may be expected that this study confirms (or excludes) the hypothesis of the fast break-up as a mechanism responsible for the fragmentation in the energy range where the strong increase of IMFs production sets in.

Moreover, the measurements were also performed for Ni targets at much lower energy, i.e. 0.175 GeV, to investigate whether the same mechanism is present also at this energy, where the energy transfer from the proton beam to the target nucleus is so small that the break-up of the target may be questionable. The analysis of these data allowed to get information on the energy dependence of the reactions in a broad range of proton energies.

An overview of present experimental knowledge on proton induced reactions is presented in Chapter 2 with emphasis on Ni target.

The models most frequently used to explain the phenomena observed in proton induced reactions are discussed in Chapter 3, whereas the selected models applied in the present work for the description of data are presented in Chapter 4.

The PISA collaboration experimental setup as well as the method of data normalization (cf. Section 5.4) is described in Chapter 5.

Experimental differential cross sections are presented in Chapter 6 together with results of the theoretical analysis performed in the frame of the two step spallation model. They are also compared in the same Chapter with available data published in the literature.

A description of the present data using the model, which takes into account the competition of the break-up process with two step mechanism is discussed in Chapter 7.

The energy dependence of all total production cross sections available in the literature for p+Ni reactions is presented in Chapter 8 and compared with predictions of the postulated reaction model.

A summary of results and their interpretation is given in Chapter 9 whereas details of experimental setup and data analysis are discussed in Appendices A, B, C, and D.

Chapter 2

Status of knowledge in experiments on proton induced nuclear reactions

In this chapter the status of knowledge on the energy dependence of proton induced reactions on atomic nuclei is presented as well as a comprehensive compilation of references found in literature on experiments performed for Nickel target and other nuclei with similar mass number. The section is organized as follows: (i) Dependence of the total (reaction and production) cross sections on proton beam energy and mass of products is presented, (ii) Overview of experimental results involving differential cross sections is given, (iii) Properties of total and differential cross sections, which indicate approaching to limiting fragmentation are discussed, (iv) Various interpretations of observed results are presented, and (v) The compilation of literature references on experiments dealing with proton induced reactions on Nickel as well as similar targets is given.

2.1 Total cross sections

It is well known that the total reaction cross sections for proton induced reactions vary smoothly with the beam energy showing a maximum for energies between 10 and 100 MeV and quickly approach (in the range of energies of several hundreds MeV to about 1 GeV) a constant value. The maximum is quite pronounced for light nuclei (factor two larger than the cross section value at very high energies) but almost disappears for heavy nuclei as it is seen on the figure 2.1.

The leveling of the ***reaction*** cross sections for higher energies - up to 20 GeV and more - at values in the neighborhood of the geometrical limit, i.e., πR^2, is observed experimentally and is well described by several phenomenological parameterizations (see, e.g., Wellisch and Axen [148], or Tripathi et al. [136] and references therein).

The ***production*** cross sections for the emission of light charged particles (LCPs), intermediate mass fragments (IMFs), fission products, and the spallation residua - obtained mainly in inclusive experiments - also indicate the leveling, but it appears at much higher energies than it is observed for reaction cross sections. *Therefore, the increase of the production cross sections observed at beam energy of several hundreds MeV up to several GeV must be attributed to* ***increasing of multiplicity*** *of emitted products. Moreover, this effect appears at different energies for different specific reactions what may suggest that different reaction mechanisms are responsible for energy dependence of various reaction products.*

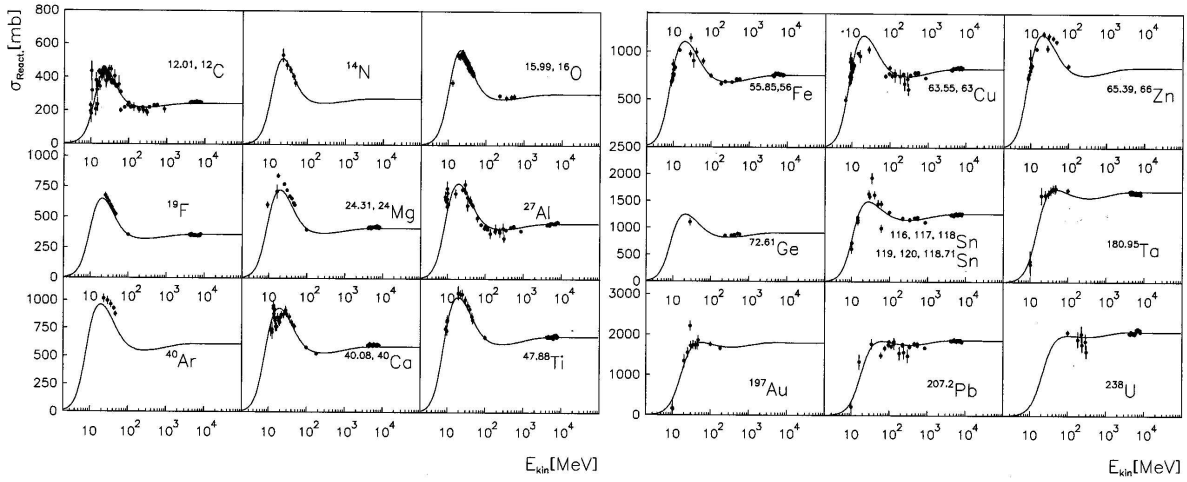

Figure 2.1: Energy dependence of the total reaction cross sections in proton induced reactions on targets ranging from ^{12}C to ^{238}U. The symbols present experimental data whereas the lines show results of the parameterization of Wellisch and Axen [148]. This figure was taken from ref. [148]

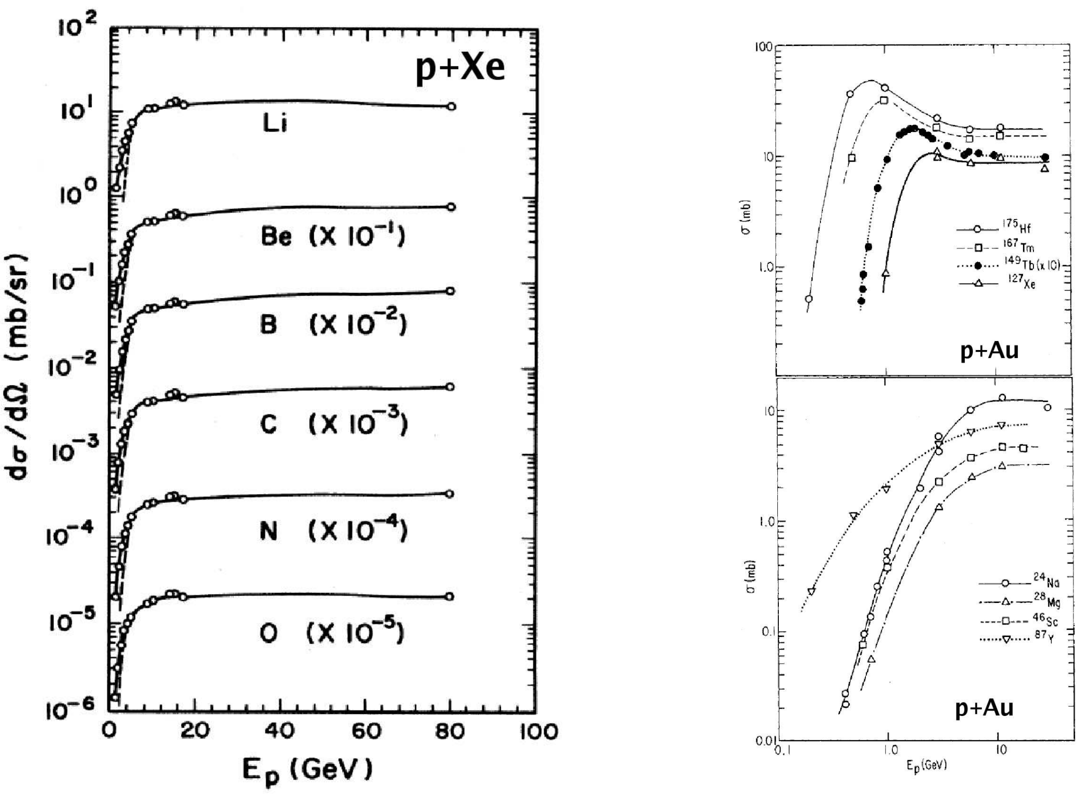

Figure 2.2: Energy dependence of the production cross section in function of impinging proton energy. On the left panel results obtained for IMFs by Porile et al. [111] in the reaction p + Xe. On the right panel results for heavier particles and residua of a reaction measured by Kaufmann et al. [79] in the reaction p+Au. The symbols represent experimental data whereas the lines are shown to guide the eye (with exception of dashed line for p+Xe below 6 GeV, which represents the estimate of contribution of the multifragmentation mechanism). Figures were taken from [111] and [79], respectively.

Typical energy dependence of production cross sections is presented in figure 2.2 for proton - Xe collisions - measured by Porile et al. [111], and for proton - Au collisions - investigated by Kaufman and Steinberg [79]. The left panel of figure 2.2 presents IMF production cross sections for a Xe target and the lower - right panel depicts these results for a Au target, whereas in the upper - right panel the cross sections for the production of heavy residua of the p+Au reaction are shown. It is worthy to point out that the IMFs production cross sections increase monotonically reaching the asymptotic value at very high energies but this is not the case for heavy reaction residua. Their production cross sections increase at proton energies below and in the neighborhood of 1 GeV, reach a maximum at energy which is the higher for the lighter residua, slightly decrease, and level at very high energies (higher than $\sim$ 10 GeV).

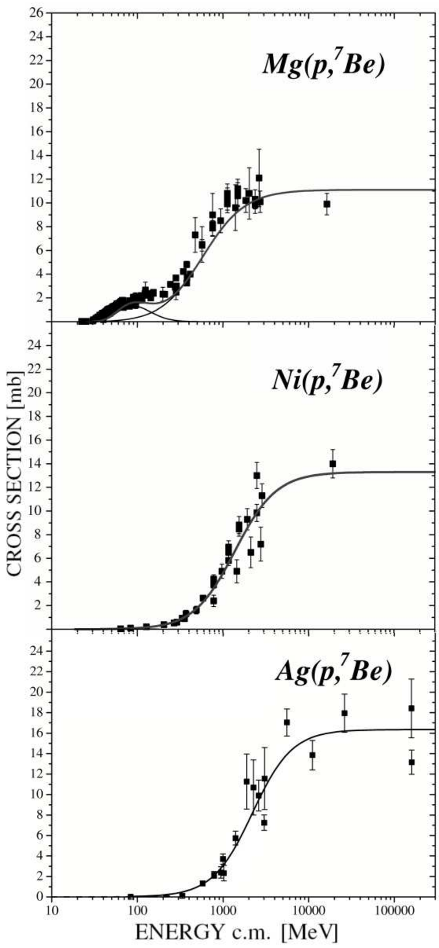

Figure 2.3: The energy dependence of the experimental (symbols) cross sections and results of parameterization (lines) for production cross sections of ^{7}Be in proton induced reactions on Mg (upper panel), Ni (medium panel) and Ag (lower panel), respectively. Figure was taken from Bubak et al. [32].

Heavy products of the reaction seem to be produced through the spallation mechanism, whereas the IMFs may appear also due to other mechanisms, as e.g., break-up of the nucleus. *It is, therefore, important to study IMFs production to understand the interaction mechanism of the protons with atomic nuclei.* As can be seen from fig. 2.2 the cross sections for IMFs have similar energy dependence for Xe and Au targets. It may be thus conjectured that this is typical behavior for all target nuclei. Indeed, this is proved by studying energy dependence of the production cross section of ^{7}Be particles, which were most frequently studied experimentally among all IMFs. This is due to the fact, that the total production cross sections of ^{7}Be were mainly measured by radiochemical methods which can be applied to specific reaction products only. The lifetime of ^{7}Be - 53 days - is long enough to allow for easy preparation of irradiated samples and short enough to assure large intensity of radiation and therefore collecting of good statistics in a reasonable time.

It was shown by Bubak et al. [32] that the energy dependence of the ^{7}Be production cross section is very regular. The cross sections for medium-heavy and heavy targets can be very well parameterized by the logistic function what is shown in fig. 2.3. The cross section increases smoothly starting from 100 - 200 MeV proton beam energy up to several GeV where the cross section levels at value which depends on the mass of the target, being larger for heavier target nuclei. *The increase of the cross sections is the fastest in the neighborhood of 1 - 2 GeV proton beam energy. This fact was the argument for selection of 1.2, 1.9, and 2.5 GeV proton beam anergies for investigation of the reaction mechanism in the present work.*

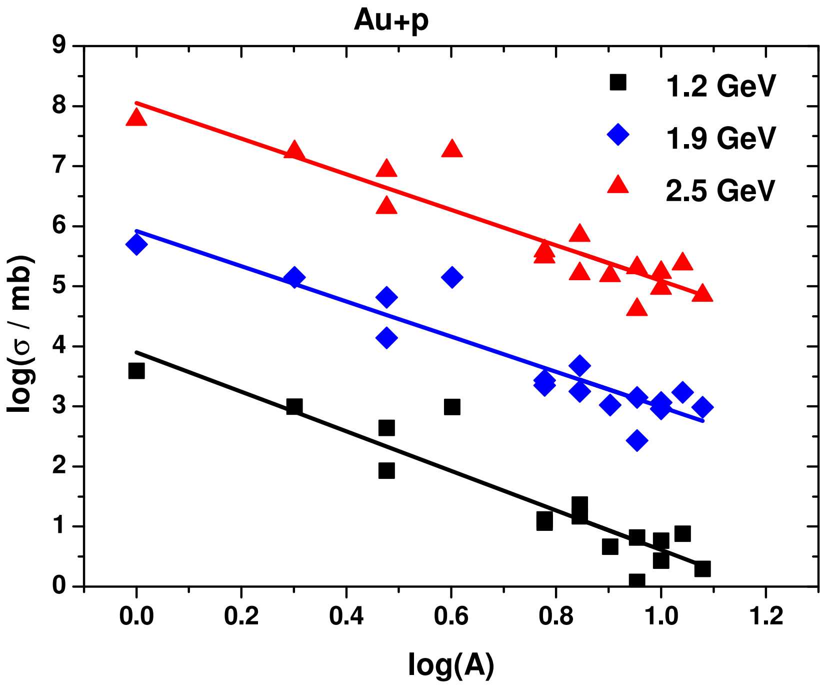

Figure 2.4: The ejectile mass dependence of the logarithm of production cross sections for Au+p reactions. The black squares present data for 1.2 GeV proton energy, the blue diamonds the data for 1.9 GeV (shifted up by 2), and the red triangles depict the data for 2.5 GeV (shifted up by 4). The data were taken from Bubak et al. [31] (for 2.5 GeV) and from Budzanowski et al. [33] (for 1.2 and 1.9 GeV). The lines show the fitted $A^{-\tau}$ dependence.

From inspection of figure 2.2 it is reasonable to conjecture, that the energy dependence of emission of other IMFs and LCPs should be similar to that of ^{7}Be. Another argument in favor of this assumption is the fact that the mass dependence of the IMFs and LCPs production cross sections was found in many investigations to be smooth. It follows a power law:

$$\sigma \propto A^{-\tau}$$

where the power exponent τ varies slowly with the beam energy. This is illustrated by fig. 2.4 where the logarithms of the production cross sections are presented for LCPs and light IMFs measured at three beam energies - 1.2, 1.9 [33], and 2.5 GeV [31] for p+Au system. To distinguish better the cross sections measured at different beam energies the logarithms of the data at higher energies were increased by 2 and 4 for 1.9 and 2.5 GeV beam energy, respectively. The ejectile mass dependence of the logarithms is indeed close to the straight line what should be fulfilled for the experimentally found power law relationship. Preserving the shape of functional dependence of the production cross sections on the mass of the products while varying the beam energy indicates that the cross sections for all LCPs and IMFs vary in the same systematic way with the energy.

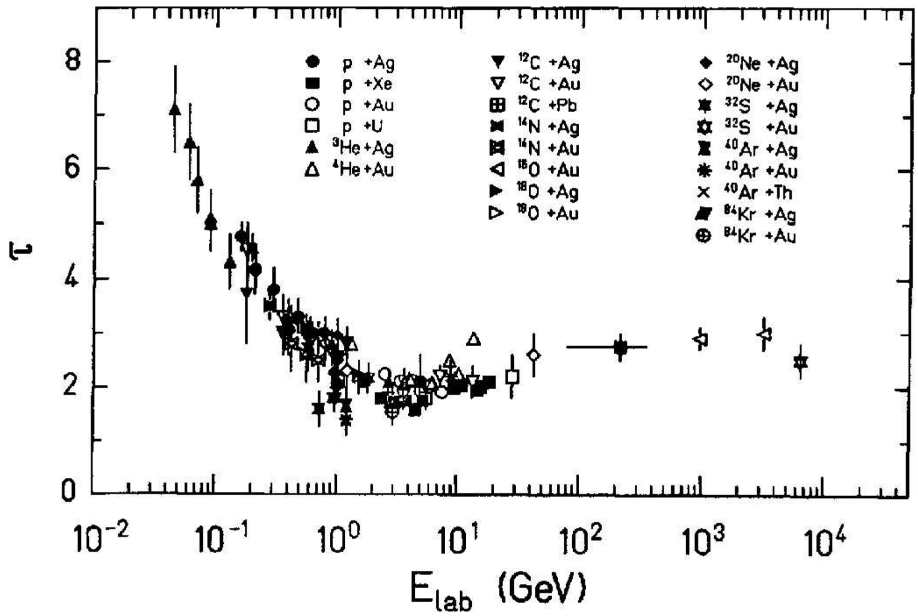

Figure 2.5: The beam energy dependence for various reactions of the power exponent τ for the power law $\sigma \propto Z^{-\tau}$. Picture was taken from [135].

The power law is fulfilled also when instead mass number of the ejectile, its atomic number is used: $\sigma \propto Z^{-\tau}$. The compilation of values of the power law exponent τ for different nuclear systems was made by Trautman et al. [135] and it is presented in fig. 2.5 as a smooth function of the beam energy. The τ value decreases with the beam energy for energies smaller than approx. 1 GeV, it has a minimum in the neighborhood of 1 GeV energy, then it slightly increases and levels for energies larger than 5 - 10 GeV. This leveling shows that the IMFs mass dependence of the production cross sections is "frozen" at higher energies, i.e. it starts to be energy independent at these energies.

It was mentioned while discussing the content of the fig. 2.2 that the cross sections for production of target residua vary with the energy in a different way than the cross sections for IMFs. In fig. 2.6 the mass dependence of the cross sections for target residua from the p+Fe reactions measured at several energies by Villagrasa-Canton et al. [138] are presented. The mass dependence

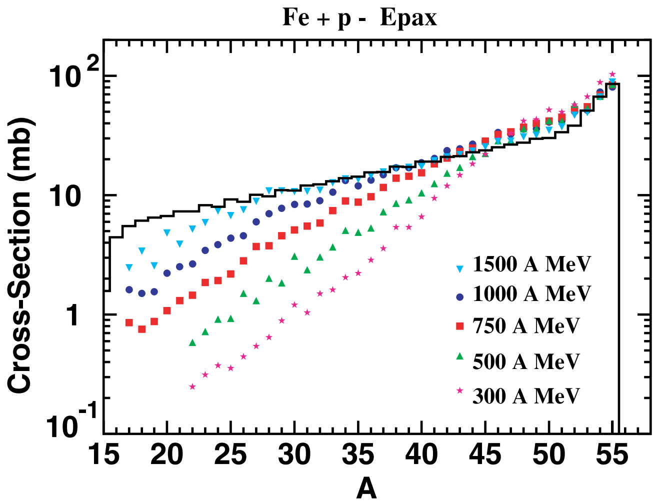

Figure 2.6: The product mass dependence of the production cross sections (symbols) for p+Fe reactions measured at several proton beam energies by Villagrasa-Canton et al. [138]. The histogram presents the "energy-frozen" mass dependence of the production cross sections evaluated according to the EPAX parameterization which is valid at high energies (larger than 5 - 10 GeV) [133]. Figure was taken from [138].

smoothly changes with the increasing energy. The cross sections for the production of residua with mass very close to the target mass are largest at lowest energy of 300 MeV and those for the lighter residua decrease quickly with the mass difference between the target and the residuum. The slope of this dependence is largest at lowest energy used in the experiments, i.e. at 300 MeV, and decreases quickly with beam energy. The shape of the experimental mass dependence of the cross sections measured at the highest studied beam energy, i.e. 1500 MeV, is very similar to the asymptotic distribution evaluated within the EPAX parametrization of Sümmerer and Blank [133]. This parametrization is valid for such high energies that the residue production cross sections do not depend anymore on the energy of the projectile. Thus it is clear that the cross sections for emission of heavy reaction residua also start to be energy independent at high beam energies as it was discussed above for light reaction products.

The experimental conditions did not allow the authors of the paper [138] to measure production cross sections for ejectiles with the mass number A smaller than 15 - 20 (with exception of the beam energy of 1 GeV where particles with smaller A - even as small as 6 were measured), thus to see the complete mass distribution of the cross sections it is necessary to use data from other experiments.

In fig. 2.7 the cross sections obtained at 300 GeV energy of the proton beam impinging on the Ag target [44, 112] are presented (mass of the products A>30) together with the cross sections measured at Xe target with the proton beam of energy varying in the range 80 - 350 GeV [67]. Both target nuclei have similar mass therefore the production cross sections are expected to be very similar for them. Furthermore, the energies of protons, used in these experiments are so high that the cross sections do not change anymore with the energy. The mass dependence of the production cross sections depicted in Fig. 2.7, which covers almost full range of product masses, can

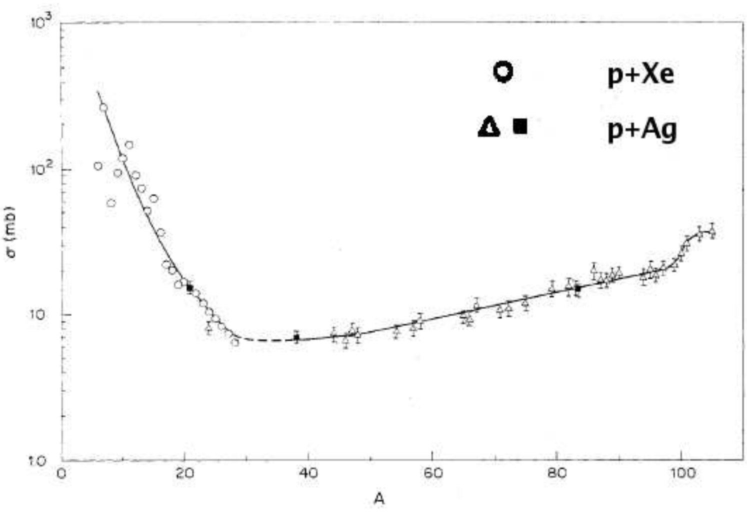

Figure 2.7: The production cross section dependence on the mass of the products for reactions of high energy protons on medium mass target nuclei: Ag at 300 GeV proton beam energy and Xe at 80 - 350 GeV. The IMF cross sections (open dots) correspond to experiments with Xe target and target residua cross sections (triangles) originate from experiments with Ag target. The lines are presented to guide the eye. Figure adapted from publication of Bujak et al. [34].

thus be treated as ***typical mass dependence of the production cross sections for medium mass target nuclei at high energies***.

In summary, the total production cross sections of proton induced reactions increase smoothly for LCPs and IMFs from low energies (of order of hundred MeV) to the asymptotic region of several GeV, where the cross section values do not depend anymore on the energy. The cross sections for target residua also increase with the energy and they level in the similar energy range as cross sections for lighter products. The production cross sections of target residua with masses very close to the target mass seem to vary with the energy in specific, different manner than other cross sections. ***It is very interesting to investigate proton induced reactions at proton beam energies in the neighbourhood of 1 - 2 GeV because in this energy range the rapid variation of all cross sections is observed.***

2.2 Differential cross sections

Data more exclusive than the total production cross sections should be able to provide some additional information concerning the mechanism of proton induced reactions. For example, the recent paper of Herbach et al. [66] presents a large amount of measurements of differential cross sections for reactions induced by 1.2 GeV protons on thirteen nuclear targets covering almost full range of mass numbers (from Al up to Th).

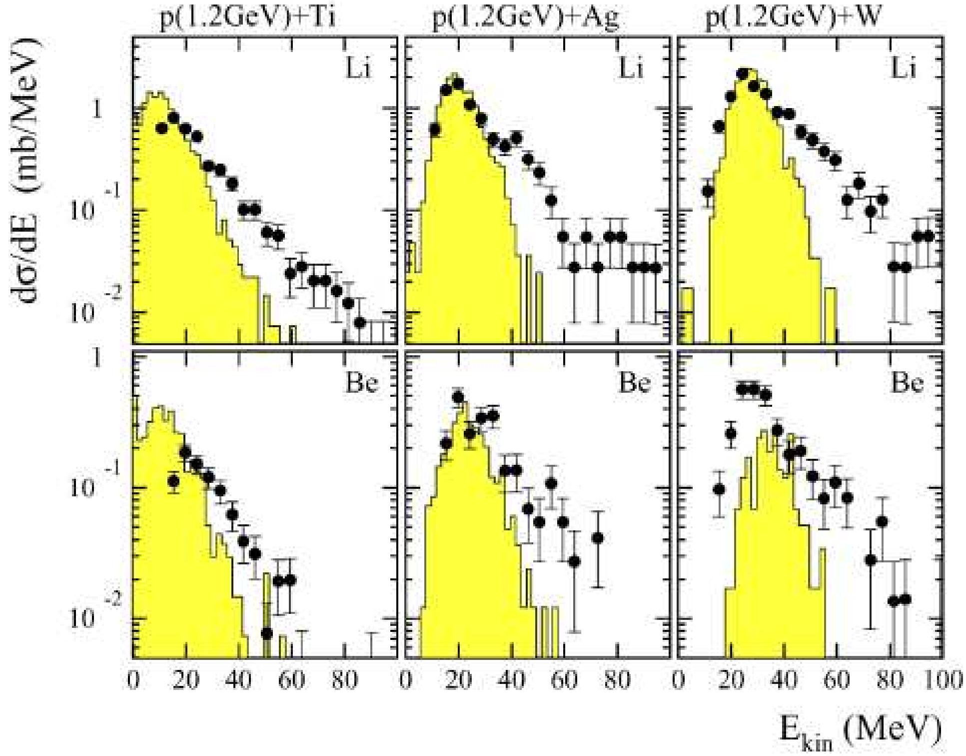

Figure 2.8: Differential cross sections $d\sigma/dE$ for emission of Li and Be particles from p+Ti, p+Ag, and p+W reactions - left, middle and right panels, respectively. The symbols represent experimental data, the yellow histograms show predictions of two-step model, i.e. intranuclear cascade plus evaporation. Figure taken from Herbah et al. [66].

The bullets in in fig. 2.8 present the experimental cross sections $d\sigma/dE$ whereas the shaded (yellow) histograms are obtained from INCL2 + GEMINI simulation calculations normalised to reaction cross sections from ref. [148]. It is obvious that the two-step model which takes into account the intranuclear cascade of nucleon-nucleon collisions and evaporation of particles is not able to describe high energy tail of the experimental energy spectra of Li and Be ejectiles. The disagreement of the theoretical histograms and the data for typical IMFs (Li and Be) indicates that another reaction mechanism has to be taken into consideration. The still more exclusive data, i.e. the double differential cross sections $\frac{d\sigma}{d\Omega dE}$ - obtained also by Herbach et al. - confirm this conjecture for LCPs as it is shown in the figure 2.9.

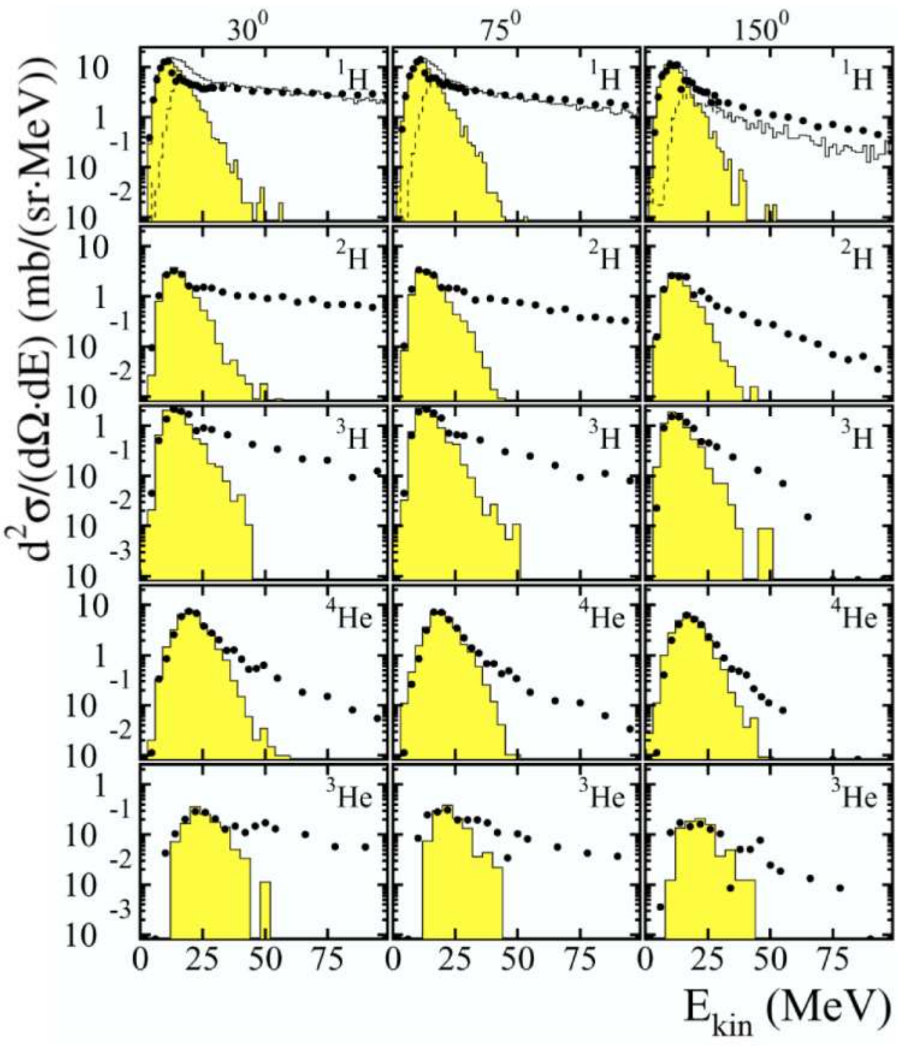

Figure 2.9: Double differential cross sections $\frac{d\sigma}{d\Omega dE}$ for emission of light charged particles from p(1.2 GeV) + Ta reaction at angles of 30° , 75° and 150° . The symbols represent experimental data, the dashed histograms show the predictions of intranuclear cascade, the shaded area the prediction of evaporation, and solid histogram is the sum of both contributions. Figure adapted from Herbah et al. [66].

It may be expected that the coincidence measurements for proton induced reactions should be even more sensitive to the reaction mechanism than the differential cross sections obtained in the inclusive measurements. Such investigations are rare, see e.g., papers of Wilkins et al. [152], Nakai [107], Viola et al. [139] because the coincidence experiments are much more complicated than inclusive measurements and obtaining a reasonable statistics in coincidence experiments is a difficult task. ***All such studies indicate also that the reaction mechanism is more complicated than that underlying the two-step model in which the cascade of nucleon-nucleon collisions describes the first stage of the reaction leading to equilibration of the nucleus and then the evaporation is responsible for de-excitation of the compound nucleus.***

2.3 Limiting fragmentation hypothesis

The observation that the total production cross sections do not vary for proton beam energies higher than approx. 10 GeV is a specific form of the so called "limiting fragmentation hypothesis" - originally proposed by Benecke et al. [15] - which claims that the differential cross sections $d\sigma/dp^3$ do not change at very high energies. The predicted behavior of the differential cross sections was observed, e.g., by Porile et. al [111] on xenon target or by Hsi et al. [70] in coincidence 4π experiment on Au target.

The spectra measured by Porile et al. [111] are presented on Fig. 2.10 for Be, C, and O ejectiles from proton induced reactions on the xenon target. The beam energies are depicted on individual panels. The smooth line corresponds to droplet model fit [111], which very well reproduces the spectra at energies larger than $\sim$ 9 GeV, but indicates contribution of another mechanism at lower energies. For higher beam energies 9$\leq$19 GeV the second contribution disappears completely and energy spectra become independent of the beam energy.

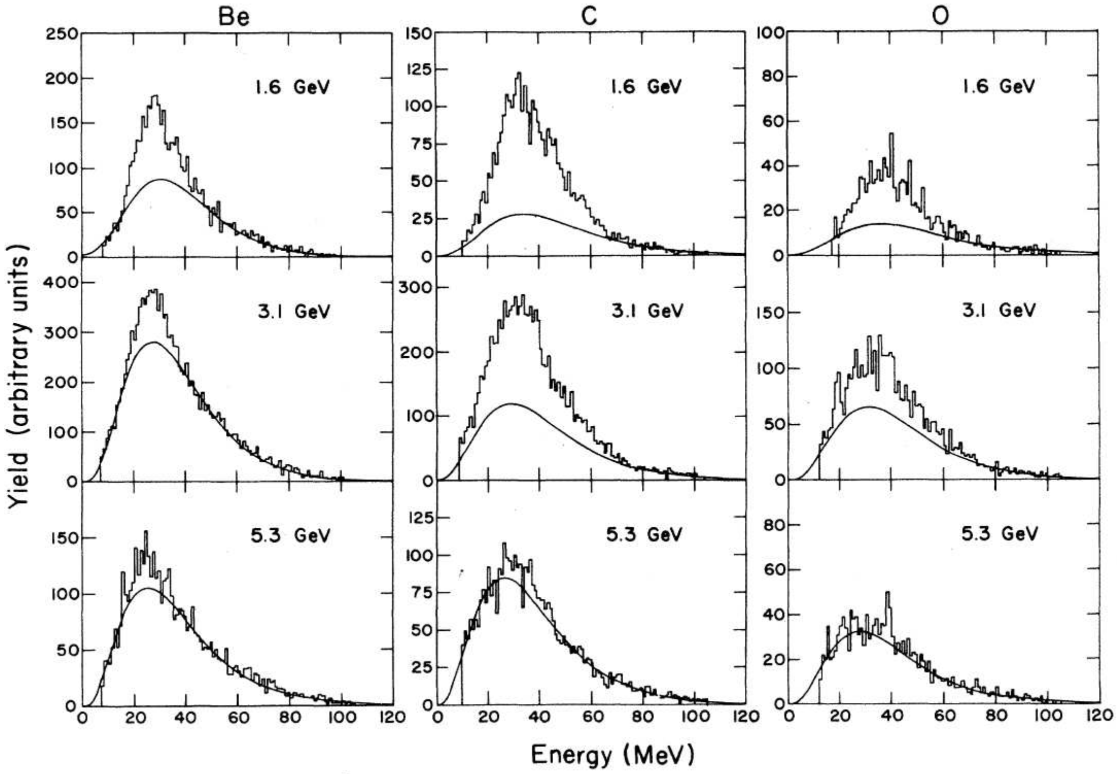

Figure 2.10: Energy spectra of Be, C, and O fragments emitted at 48.5° from proton induced reaction on xenon target. Value of the beam energy is depicted on separate pads. The curves represent the droplet model fit. The figure is taken from Porile et al. [111].

It is very interesting to investigate at which beam energy the limiting fragmentation hypothesis starts to apply. The recent studies of the PISA collaboration of the proton induced reactions on a Au nucleus show [33] that ***the shape*** of the spectra and angular distributions practically does not change for LCPs and IMFs when the beam energy is varied from 1.2 GeV to 2.5 GeV. It was, however, observed that ***the value*** of the cross sections increases systematically in this energy range.

The spectra of ^{4}He, ^{7}Li, ^{9}Be, and ^{11}B measured at 35° for three beam energies - 1.2 GeV (red circles), 1.9 GeV (blue squares), and 2.5 GeV (black triangles) are shown in Fig. 2.11 as typical examples for the data obtained in the studies of the PISA collaboration [31, 33]. It is obvious, that the limiting fragmentation hypothesis still does not work for p+Au system at these energies.

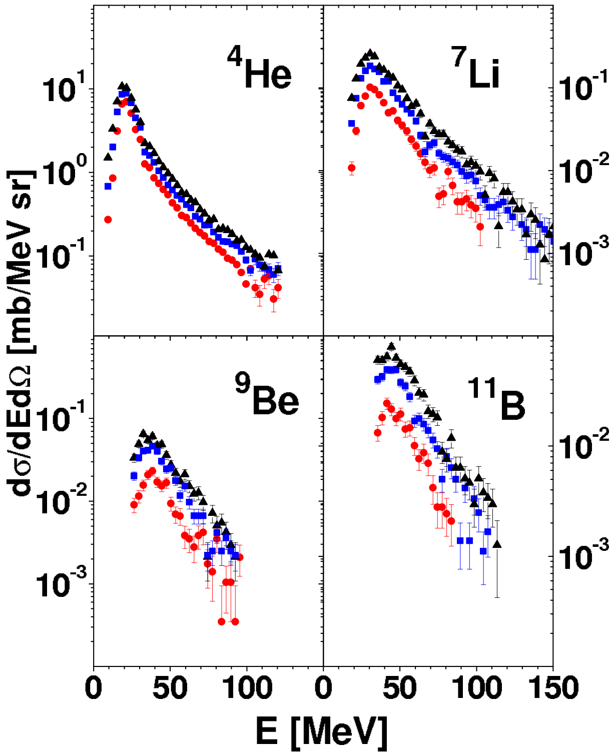

Figure 2.11: Energy dependence of the typical spectra of LCPs and IMFs measured at 35° by PISA collaboration [33] for p+Au reactions at three energies: 1.2 GeV (red circles), 1.9 GeV (blue squares), and 2.5 GeV (black triangles).

The analysis of the energy dependence of the total production cross sections for ^{7}Be particles (see Fig. 2.3) leads to the conclusion that the region of energies, where the leveling of the cross sections values appears, is placed at lower energies for lighter targets. Thus, studying the proton induced reactions at energies in the neighborhood of 1 - 2 GeV on targets with the mass number of about A=60 - significantly lower than that for Au (A=197) - might allow for the observation of the transition region where specific mechanisms can be responsible for starting the limiting fragmentation hypothesis to work.

The total production cross sections for p+Fe measured by Villagrasa-Canton et al. [138], shown in fig. 2.6 indicate that the data obtained at 1.5 GeV are quite close to the cross sections predicted by EPAX parametrization, which is valid in the energy region where the limiting fragmentation hypothesis should already work. Hence, it is reasonable to conjecture that the proton induced reactions on Fe or similar targets approach the limiting fragmentation region at energies of about 2 GeV.

The data obtained by Ammon et al. [4] for Ni target show similar properties as the data determined by Villagrasa-Canton et al. [138] for Fe target. This is illustrated on l.h.s. part of fig. 2.12 where the production cross section of noble gases are presented for broad range of energies

- almost from reaction threshold up to 2.6 GeV. For heavier isotopes produced on the Ni target, the tendency observed for iron is also reproduced. Data for the Ni target were measured in several experiments by the group of R. Michel et al. [42, 95–100, 126], and are presented on r.h.s part of the figure. In some of the latest experiments [95, 98], they also measured the emission of noble gases. Results of the above mentioned experiments are enriched by points from other experiments which extend the studied energy range.

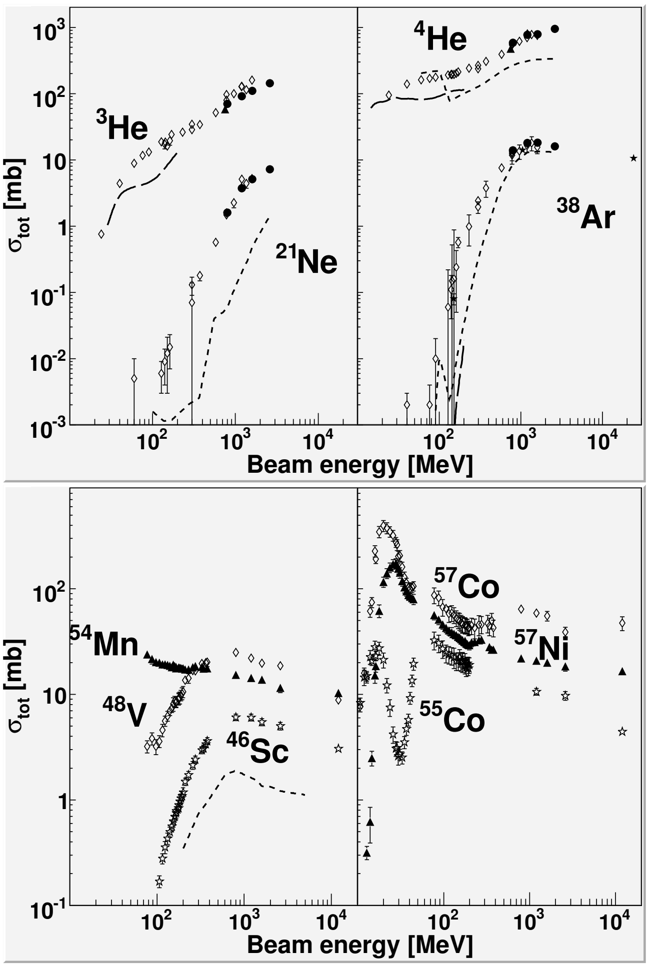

Figure 2.12: Excitation functions for several products of the proton induced reactions on Ni target. On the left hand side part of figure the cross sections for production of noble gases are presented. The open diamonds were determined in the study of Ammon et al. [4], full dots origin from the paper of Michel et al. [98], full triangles represent data measured by Green et al. [60], and full stars those from paper of Regnier [122]. Dashed and long dashed lines correspond to calculation performed by Ammon et al. [4] using INCL4 coupled with ABLA and TALYS computer programs, respectively. The right hand side panel of the figure presents data determined for heavy products in experiments performed by Michel et al. [96, 98–100, 126], with the exception of the data measured at 12 GeV, which were published by Asano et al. [7]. The long dashed line represents the calculation of a two-step model for ^{46}Sc presented in ref. [126].

For the heaviest residua strong fluctuations and deviations from the smooth trend are observed in the low energy range of proton beam (E $\leq$ 0.1 GeV). They are interpreted as produced by opening of some new reaction channels with increasing the beam energy. This energies are, of course, much lower than those at which validity of the limiting fragmentation hypothesis is expected.

The cross sections for noble gases increase with the beam energy up to about 1 GeV, however, at higher energies they seem to level. This is especially visible for the Ar target, for which the data are extended to the highest energies. The lines shown in the figure represent results of calculations performed in the frame of the two-step model. They reproduce the general energy trend of the experimental cross sections but are systematically lower by factor 2 - 5 than the data. It again indicates, that some other reaction mechanisms seem to participate in the interaction of protons with the Ni target.

2.4 Phenomena induced by large energy transfer to nuclei

It may be conjectured that the increase of the beam energy causes larger energy transfer to the target nucleus and therefore induces higher excitation of the nucleus. However, there are different scenarios of the behaviour of nuclei at increasing excitation energy (more detailed information can be found in review papers, as e.g., Hüfner [71], Lynch [90], Moretto and Wozniak [105], Richert and Wagner [123]). They can be divided in (at least) three groups of the models of possible reaction mechanisms:

1. The first one assumes that the increase of the energy of incident proton enables to dissipate more energy during its way through the nucleus. Then the residuum of the cascade of nucleon-nucleon collisions accumulates more energy before reaching the equilibrium, what leads to increasing multiplicity of the evaporated LCPs and IMFs. This mechanism originally were proposed by Serber [128] and is usually called the two-step approximation. The intranuclear cascade is most frequently used to calculate first step of the reaction, whereas the second step is described by sequential statistical evaporation from the equilibrated compound nucleus, eventually preceded by fissioning of the excited nucleus.

   Intranuclear cascade calculation are performed by various codes, as e.g., that of Metropolis et al. [94], Bertini [17], Boltzmann-Uehling-Uhlenbeck (BUU), e.g., [19, 56, 137] or Quantum Molecular Dynamics Model, e.g., Aichelin et al. [3], Niita et al. [110].

   The second step of reaction is calculated usually by evaporation codes like, e.g., ABLA [75] which is a "classical" de-excitation model which calculates only neutrons, protons and α emission; GEM code of Furihata [52–54], generalized model providing emission of 66 compound particles up to Mg; the statistical sequential emission modeled by GEMINI code of Charity [36]; or Statistical Multifragmentation Model SMM, developed by Botvina et al. [27], to name only a few.

   The typical quality of the description of differential cross sections by the above models is presented in figs. 2.8 and 2.9.

2. Another one postulates the expansion of the excited nucleus, while the transfer of the energy increases, and hence reaching by the nucleus the unstable, spinodal region what results in the phase transition from the nuclear liquid to the gaseous phase. Many calculations have predicted such a phase transition, e.g., Sauer et al. [125], or Curtin et. al [41]. The curves on

the fig. 2.13 represent the isotherms depicting nuclear equation of state relating the pressure to the density. The mixed phase region is marked by hatched area.

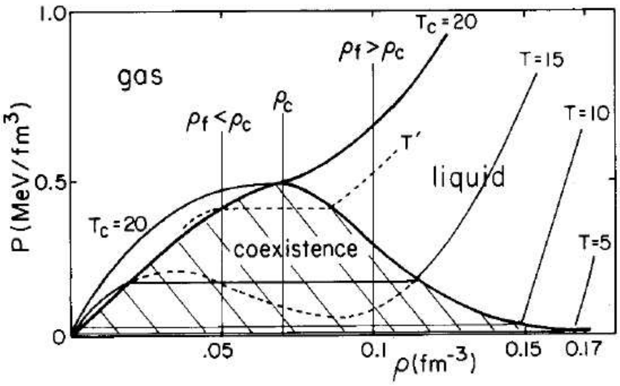

Figure 2.13: Nuclear matter phase boundaries presented as a function of density and pressure. Liquid and gas phase region are indicated as well as coexistence phase of the both denoted as a hatched area is shown. Figure is taken from [41].

The concept of phase transition at high proton beam energies was fruitfully used by Hirsch et al. [67] for prediction of the power law dependence of the fragment mass yields $\sigma(A) \propto A^{-\tau}$ as well as isotopic yields in p+Kr and p+Xe reactions in the broad range of proton energies (from 80 GeV to 350 GeV)- see figures 2.14 and 2.15.

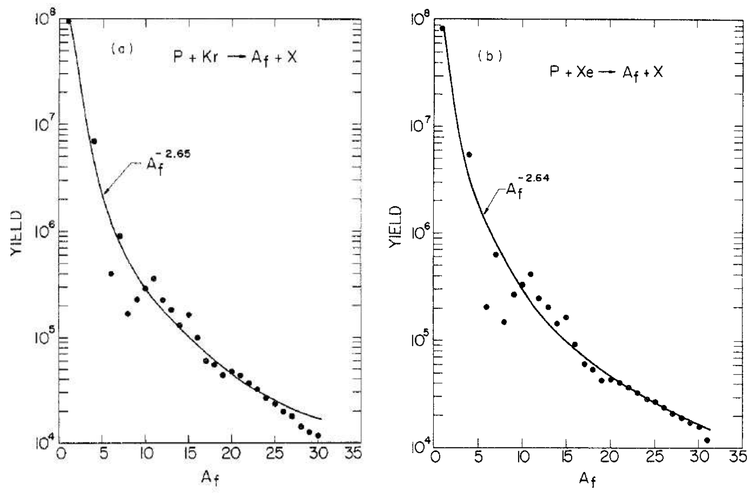

Figure 2.14: Fragment mass yield in function of A_f produced in proton induced reaction on Kr nuclei (l.h.s. panel) and on Xe nuclei (r.h.s.panel) in the proton energy range from 80 GeV to 350 GeV, where these distributions do not change. The figures were taken from Hirsch et al. [67].

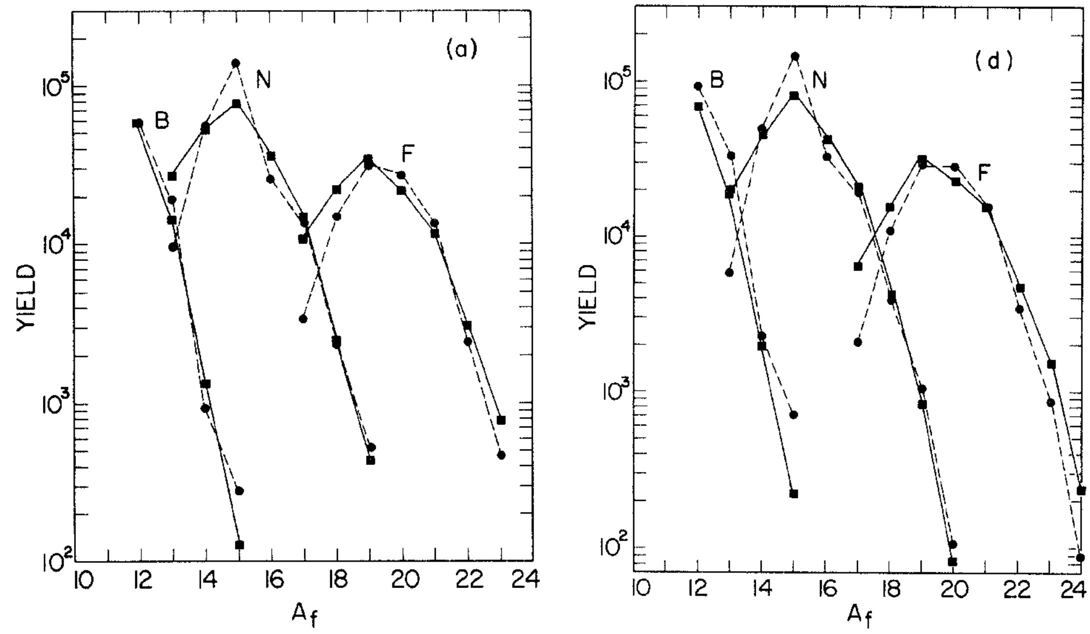

Figure 2.15: Examples of the isotopic yields from p+Kr (left panel) and p+Xe (right panel) measured in the proton energy range from 80 GeV to 350 GeV, where these distributions do not change as a function of incident energy. The circles represent the experimental data and squares depict the theoretical predictions based on the droplet model of the phase transition. The lines are shown to guide the eye. The figures were taken from Hirsch et al. [67].

The recent experiments, of the ISiS project, reported e.g., by Kleine Berkenbusch et al. [80] and summarized in review paper of Viola et al. [139], were interpreted as a strong evidence for a continuous phase transition for p+Au and ^{3}He + ^{nat}Ag reactions in the energy range from 5 to 15 GeV.

Other authors, e.g., Avdeyev et al. [11] and Karnaukhov et al. [78] also applied the phase transition interpretation of the p+Au reactions at 8.5 GeV, however, they extracted different values of the critical temperature.

More information concerning liquid-gas phase transition interpretation of the reaction mechanism can be found, e.g., in review paper of Das Gupta et al. [63].

3. The third scenario of the strong increase of the IMF yields assumes that the energetic proton can induce in the first stage of the reaction a fast break-up of the target nucleus into several excited prefragments. The excitation energy of the prefragments may increase also with the beam energy. Then, they emit in turn more abundant LCPs and IMFs.

   Assuming that high energy proton drills a hole on its path through the nucleus it is possible that distortion caused by this hole will lead to cleavage of the nucleus. The original idea of such an effect was proposed by Wilkins et al. [152] on the basis of coincidence measurements of heavy products from 11.5 GeV proton induced reaction on ^{238}U. They observed break-up with the characteristics of a two body process, however, they found that the sum of kinetic energies of both heaviest fragments is bigger than that expected from fission reactions. On Fig. 2.16 the correlation between masses of two heavy products are depicted on the l.h.s

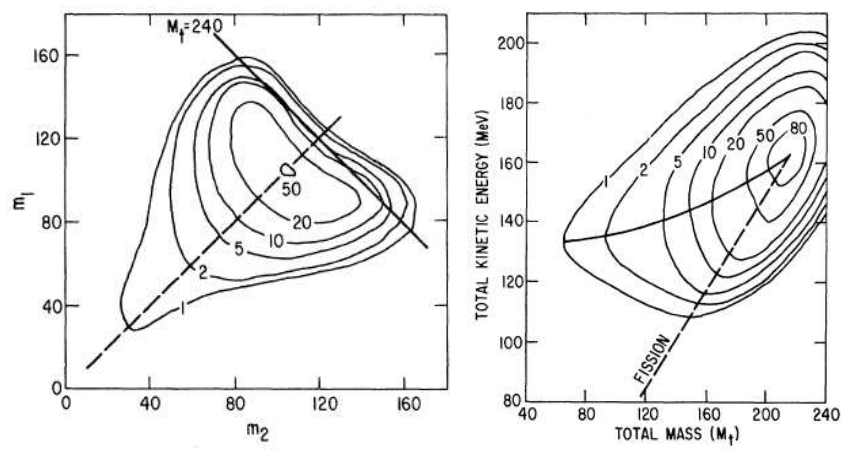

Figure 2.16: On the l.h.s correlation between fragment masses m_1 and m_2 is presented as a contour plot, on the r.h.s same presentation of correlation between total kinetic energy and total mass of the 2 binary fragment masses. The figures were taken from [152].

part of the figure, whereas on the r.h.s of the picture the total kinetic energy of the fragments is depicted as a function of sum of masses of registered particles and is compared with predictions valid for fission mechanism.

Cumming et al. [40] have observed even earlier an exceptional sideway peaking for Na isotopes emitted from a Bi target bombarded by a 2.9 GeV proton beam. This result was not understood and provoked to searching for such a behavior of emitted fragments from different targets in a wide range of beam energies. For example, Beg and Porile [14] performed a measurement for a ^{238}U target in the wide range of proton beam energy 0.45-11.5 GeV. They found at beam energy close to 1 GeV that a strong contribution of binary fission was replaced by another process identified by the authors as *fragmentation*, with the characteristic property that "*this process involves the emission of light fragments on the scale comparable to that of the intranuclear cascade*." Furthermore, Porile et. al [113] have found not only the sideway picking but even undeniable backward enhancement in the angular distribution of some products from 400 GeV proton induced reaction on ^{238}U. The clear evidence for a strong modification of the shape of the product spectra with the proton beam energy was also found by Fortney and Porile [49] for reactions induced on this target.

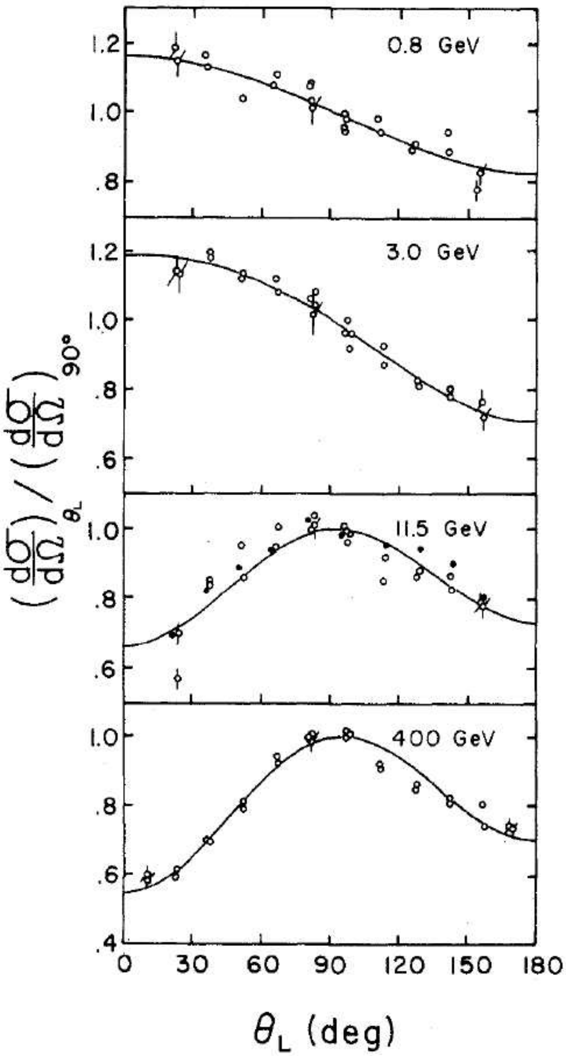

Figure 2.17: Angular distribution of ^{47}Sc products from the interaction of protons of different energies (shown in individual panels) with the ^{238}U target. The figure was taken from Fortney and Porile [49].

The results described above were interpreted by Bohrmann, Hüfner and Nemes [24] as an effect of fast cleavage of the nucleus into at least two fragments which is able , as shown by Hüfner and Sommermann [72], to explain in a natural way the sideway or backward enhancement of the angular distributions .

The coexistence of these different reaction mechanisms is not excluded and can be mediated besides the beam energy by other physical quantities, as e.g., values of the impact parameter. To decide which of the scenarios is correct a systematic study of the energy dependence of various physical observables is desirable and therefore the aim of the present PhD-thesis..

The range of the proton beam energies for which a rapid variation of the observables is observed seems to be the most suitable for studying the interplay of different reaction mechanisms. It was found, in recent investigations of the energy dependence of proton induced reactions on gold targets, performed by Budzanowski et al. [33], that various reaction mechanisms contribute for beam energies between 1.2 and 2.5 GeV. The two step mechanism described by a combination of the intranuclear cascade model and the evaporation model is responsible for approximately half of the observed yield of the LCPs and IMFs. The second half for LCPs production is due to a contribution of the emission from a hot, fast-moving source - "the fireball", competing with the coalescence of the nucleons leading to production of light complex ejectiles. The fireball could not contribute to the emission of IMFs because of its too small mass - smaller than the mass of most IMFs. On the other hand, the strong contribution from one or two moving sources (besides the yield originating from the two step mechanism) is necessary for IMFs to properly describe the angular and energy dependence of $\frac{d\sigma}{d\Omega dE}$.

It is reasonable to expect that the competition of various mechanisms is present also for other nuclear targets in the same proton energy range. Information on this phenomenon may be very important for establishing the appropriate microscopic description of the reaction mechanism. In the present thesis the reactions induced by protons on Ni targets were studied in a broad proton beam energy range; from 0.175 GeV up to 2.5 GeV. This nucleus is interesting not only because of its physical properties, but especially because it is widely used as the construction material, e.g., as one of ingredients of the stainless steel which is necessary in constructing spallation sources and Accelerator Driven Systems.

2.5 Compilation of experiments on p+Ni and p + similar targets

The results available in scientific literature experimental on proton induced reactions on nickel target are presented in table 2.1. As can be seen, in spite of rather large number of publications dealing with the reactions under consideration, the data are not abundant enough to form a basis for systematic study of the energy dependence of the reaction mechanism. This is because the total production cross sections, which are not very sensitive to the details of the reaction mechanism were mainly measured. The differential cross sections, which enable to put more stringent constraints to the possible physical models of the reaction mechanism are rather scarce, especially for energies in the neighborhood of 1-2 GeV proton energies. Moreover, the existing measurements do not supply the consistent set of data which could be analyzed theoretically with the aim to find the details of the reaction mechanism.

Table 2.1: Experimental studies on proton induced reaction on Ni targets

Beam Energy GeV/A	Projectile	Target	Measured Particles	Measured Observables	Comments	Ref.
up to ≈20	p	C, N, O, F, Na, Mg, Al, Si, Ti, V, Mn, **Fe, Co, Ni, Cu**, Y, Zr, Nb, Ag, Ta, Au, Pb, U	^{7}Be	production cross section	parametrisation of production cross section of ^{7}Be in whole range of target mass, comparison with Silberberg Tsao [131] param.	[32]
0.008–0.016	p	Ti, Cr, Mn, **Fe, Ni**	radionuclides ^{48}V–^{57}Ni	formation cross section	radiochemical detection method	[96]
0.012–0.045	p	**Ni**	radionuclides ^{52}Mn–^{61}Cu	formation cross section	radiochemical detection method	[100]
0.014–0.09	n, p, d, ^{3}He, α	Al, Si, Cr, **Fe, Ni, Co, Cu**, Y, Zr, Rh, Nb, Ag, In, Sn, Au, Pb, Bi, Th, U	n, p, d, t, ^{3}He, α	$\frac{d\sigma}{d\Omega dE}$	theoretical paper data mostly from [18, 77, 153] clusterisation, pickup	[76]
0.02–1.6	p	**Fe, Ni**	^{3,4}He ^{21,22}Ne,^{36,38}Ar	production cross section	excitation function compaired with calc data also presented, e.g., from [20, 57, 60]	[4]
0.065,0.085	p	O, Al, Ti, V, **Fe, Co, Ni, Cu**, Ag, Au, U	^{7}Be	formation cross section	radiochemical method	[86]
0.08–0.2	p	Ti, **Fe, Ni**	radionuclides ^{42}K–^{57}Ni	production cross section	excitation energy	[99]
0.08–24	p	Sc, Ti, **Fe, Co, Ni, Cu**	^{36,38,39,42}Ar	production cross section	excitation function charge dispersion	[122]
0.09 0.1	p	^{27}Al, ^{58}**Ni**, ^{90}Zr, ^{209}Bi	p, d, t, ^{3}He, α	$\frac{d\sigma}{d\Omega dE}$ $15^\circ \leq \theta \leq 155^\circ$	strong anisotropy observed	[153]
0.09	p	^{27}Al, ^{58}**Ni**, ^{90}Zr, ^{209}Bi	n	$\frac{d\sigma}{d\Omega dE}$ $20^\circ \leq \theta \leq 135^\circ$	energy spectra similar to p from [153] but 2-3 times smaller magnitude	[77]
0.14/4	α					

Table 2.1: Continuation

Beam Energy GeV/A	Projectile	Target	Measured Particles	Measured Observables	Comments	Ref.
0.07–2.6	p	C, N, O, Mg, Al, Si, Ca, Ti, V, Mn, **Fe, Co, Ni, Cu**, Sr, Y, Zr, Nb, Ba, Au	radionuclides ^{3}He–^{197}Hg	total cross section	γ and mass (gas) spectroscopy consistent set of excitation functions data analyses include, e.g., [98, 126] data for Al, Fe and Z≥38 target	[95]
0.09–0.2	p	^{27}Al, ^{58}**Ni**, ^{90}Zr	n, p	$\frac{d\sigma}{d\Omega dE}$	QMD and FKK model calculation data mostly from [50, 153]	[38]
0.100 0.164	p	^{27}Al, ^{58}**Ni**, ^{62}Ni, ^{208}Pb	p, d, t ^{3}He, α	$\frac{d\sigma}{d\Omega dE}$ $25^\circ \leq \theta \leq 150^\circ$		[127]
0.1–0.2	p	^{58}**Ni**	p	$\frac{d\sigma}{d\Omega dE}$ $15^\circ \leq \theta \leq 120^\circ$	data used for normalisation Pisa data for E_p=175 MeV	[50]
0.1–2.6	p	O, Mg, Al, Si, Mn, **Fe, Ni**	^{10}Be, ^{26}Al	production cross section		[42]
0.13–0.4	p	C, O, Mg, Si, **Fe, Ni**	radionuclides ^{7}Be,^{22}Na–^{56}Co	formation cross section	results inconsistent with later papers [32, 118]	[120]
0.175, 1.2, 1.9 2.5	p	C, Al, **Ni** Ag, Au	^{1,2,3}H, ^{3,4,6}He $^{6-9}$Li, $^{7-11}$Be, $^{10-13}$B, C - Al	$\frac{d\sigma}{d\Omega dE}$ $15^\circ \leq \theta \leq 120^\circ$	PISA collaboration **PRESENT THESIS**	[31] [33]
0.2–0.4	p	C, N, O, Mg, Al, Si, Ca, Ti, Mn, **Fe, Co, Ni, Cu**,	radionuclides ^{7}Be–^{65}Zn	total cross section	γ spectroscopy excitation functions data from different papers collected	[126]
0.4–0.65	^{9}Be, ^{11}B, ^{12}C, ^{14}N, ^{15}N, ^{16}O, ^{20}Ne, ^{22}Ne, ^{56}**Fe,** ^{58}**Ni**	LH2 liquid hydrogen	Li-Co	elemental production cross section charge changing	inverse kinematics	[143]
0.4–0.65	^{9}Be, ^{11}B, ^{12}C, ^{14}N, ^{15}N, ^{16}O, ^{20}Ne, ^{22}Ne, ^{56}**Fe,** ^{58}**Ni**	LH2 liquid hydrogen	^{7}Be–^{57}Co	isotopic production cross section	inverse kinematics very small energy dependence of the mass fractions	[144]
0.4–0.9	^{4}He, ^{22}Ne, ^{26}Mg, ^{32}S, ^{36}Ar, ^{40}Ar, ^{40}Ca, ^{52}Cr, ^{58}**Ni**	LH2 liquid hydrogen		charge changing summed over ΔZ≥1	inverse kinematics	[37]

Table 2.1: Continuation

Beam Energy GeV/A	Projectile	Target	Measured Particles	Measured Observables	Comments	Ref.
0.4–0.9	^{4}He, ^{22}Ne, ^{26}Mg, ^{32}S, ^{36}Ar, ^{40}Ar, ^{40}Ca, ^{52}Cr, ^{58}**Ni**	LH2 liquid hydrogen	B–Co	elemental production cross section	inverse kinematics, comp. with prediction of Webber [145], and Silberberg Tsao [131]	[81]
0.5	p	^{4}He, **Ni**, Ta	p	$\frac{d\sigma}{d\Omega dE}$ $65° \leq \theta \leq 160°$	knockout model calculation	[124]
0.5	p	Ti **Fe, Co, Ni, Cu** Zn	radionuclides ^{7}Be,^{22}Na–^{66}Ga	total cross section	γ spectroscopy charge dispersion discussed with [7]	[8]
0.5–2.9	p	C, O, Mg, Si, **Fe, Ni**	radionuclides ^{7}Be,^{24}Na–^{56}Co	production cross section	results inconsistent with later papers [32, 118]	[121]
0.6	p	O, Mg, Al, Si, Ti, V, Cr, Mn, **Fe, Co, Ni, Cu**, Y, Zr, Rh, Ba, Lu, Au	radionuclides 73Be–^{196}Au	total cross section	γ spectroscopy excitation functions	[97]
0.8–2.6	p	O, Mg, Al, Si, Ca, Ti, V, Mn, **Fe, Co, Ni, Cu**,	radionuclides ^{3}He–^{65}Zn	totalcross section	γ and mass (gas) spectroscopy consistent set of excitation functions	[98]
1	p	Ti ^{58,64}**Ni** ^{112,124}Sn	^{3,4,6}He, $^{6-9}$Li, $^{7,9-11}$Be, $^{10-13}$B, ^{12}C	$\frac{d\sigma}{d\Omega dE}$ θ=60°	data also from different papers collected	[140]
1	p	Al, ^{58}**Ni** Ag, Au	elements He–K	$\frac{d\sigma}{d\Omega dE}$ θ=30° , 126°	One moving source fit performed as [150]	[82]
1	p	^{6,7}Li, Be, C, Al ^{58}**Ni** Ag, Au, Pb, ^{238}U	LCP or IMF	apparent temperature	previous data analyses for Ni data from [140]	[6]
1	p	^{54}**Fe, Fe** ^{58,60,62,64}**Ni** ^{70,76}Ge, Rb, Ag, Cs	radionuclides ^{20}F–^{65}Zn	total cross-sections	γ spectroscopy isoscaling, e.g., [154]	[5]

Table 2.1: Continuation

Beam Energy GeV/A	Projectile	Target	Measured Particles	Measured Observables	Comments	Ref.
1, 2, 3, 23	p	Si, Mg, Fe, **Ni**	radionuclides ^{7}Be,^{22}Na	production cross section	γ spectroscopy comparison with prediction of Silberberg Tsao [131]	[118]
1.2	p	Al, Ti, **Fe, Ni, Cu**, Zr, Ag, Ho, Ta, W, Au, Pb, Th	^{1,2,3}H, ^{3,46}He, ^{6,7,8,9}Li, ^{7,9,10}Be	$\frac{d\sigma}{d\Omega dE}$ $30^\circ \leq \theta \leq 150^\circ$	$\frac{d\sigma}{d\Omega dE}$ compared with programs INCL2.0 coupled with GEMINI	[66]
3	p	**Ni**	^{6,7}Li, ^{7,9,10}Be, ^{10,11}B	$\frac{d\sigma}{d\Omega dE}$ $30^\circ \leq \theta \leq 150^\circ$	good agreement with our results discussion of astrophysics aspects	[117]
12	p	Al, **Fe, Co, Ni, Cu**, Zn, Ag, Au	^{10}Be, ^{26}Al	production cross section	Discussion with ^{7}Be, ^{22,24}Na production cross section	[129]
12	p	Ti **Fe, Co, Ni, Cu**, Zn	radionuclides ^{7}Be,^{22}Na–^{65}Zn	total cross section	γ spectroscopy charge dispersion	[7]

Chapter 3

Overview of theoretical models on proton induced reactions

In this chapter theoretical models of possible reaction mechanisms will be discussed, with emphasis on the models which - according to qualitative properties of the data determined in this thesis - seem to be prevailing in the interaction of protons with Ni nuclei in the studied energy range.

Reactions induced by GeV protons are most frequently described by two-step models. The standard two-step model of reaction mechanism was proposed over sixty years ago by Serber [128]. The model assumes that the impinging proton interacts only with few nucleons in the nucleus. Some of the fast nucleons can escape from nucleus and the rest of them may collide with other nuclear particles. Thus, the energy will be distributed over the whole excited nucleus leading finally to its equilibration. The subsequent events can be described in terms of the statistical model emission.

3.1 Fast stage of the reaction

Due to the short de Broglie wave length of the fast protons bombarding the nuclei it is believed that the first stage of the reaction consists in an **intranuclear cascade** of nucleon-nucleon collisions which results in the emission of nucleons and pions. It is also possible, that **a nucleon leaving the nucleus coalesces** with neighboring nucleons and forms a composite ejectile emitted from this stage of the reaction. This phenomenon as well as other mentioned here will be described in more detail in the following.

The knock-out of the pre-formed cluster of the target nucleons by the impinging proton may compete with the above coalescence mechanism.

The straight track motion of the projectile in a high-energy proton-nucleus collision defines an overlap volume of projectile and the target nucleons. The nucleons placed in the overlap zone can be simultaneously removed from the target **forming a highly excited "fireball"**. This mechanism is different from knock-out of clusters because correlation of nucleons into "fireball" has only spatial origin in contrast to the dynamical formation of clusters.

Each of these mechanisms will be quantitatively described by theoretical models discussed below.

3.1.1 Sequential N-N collisions

In the first step of the reaction – called the intranuclear cascade – the impinging nucleon can scatter in the field produced by target nucleons or collide with individual nucleons. These collisions may lead to elastic scattering or to inelastic processes, as e.g., to creation of nucleon resonances, production of mesons and their scattering or reabsorption by the nucleons. There exist several models which quantitatively describe this stage of the reaction. All the models are realized by computer programs using computational algorithms based on Monte Carlo methods.

All these microscopic models at first generate space and momentum nucleon distributions of the target nucleus taking into account its known properties. The stability of a generated virtual nucleus is required i.e. the generated group of nucleons should preserve the desired properties during the time period longer than the typical time of the proton - nucleus collision. Different models assume practically the same mechanism and the cross sections of elementary nucleon-nucleon collisions, however, they treat differently the propagation of the nucleons in the field of other nucleons. They assume that the motion is determined by classical equations with the quantum character of the problem taken into account by Pauli blocking of the occupied phase-space for interacting nucleons. Three such models will be discussed in the following.

Intranuclear Cascade – static potential well

The first approach to model of the fast stage of the reaction, dubbed Intranuclear Cascade Models, describe the propagation of the nucleons between nucleon-nucleon collisions as the motion in the static (time independent) potential. Examples of the computer programs which realize this model are the codes of Metropolis et al. [94], Bertini [17], and Cugnon et al. [39]. In more involved versions of the Intranuclear Cascade Model the static potential may be momentum dependent what implies diffuse nuclear surface as it was implemented into the INCL computer program of Cugnon et al. by Boudard et al. [28]. In such models the simplification, consisting in the assumption that the nucleons move along the straight lines, can be introduced. It is then enough to evaluate positions and momenta of the nucleons at collisions of any two of them instead of following their positions and momenta in the constant time intervals. This can significantly speed up the calculations in comparison to more sophisticated models of the reaction as, e.g., quantum molecular dynamics model (QMD) discussed below.

It is worthy to emphasize that these simple models give quite similar results to those obtained by the time consuming calculations performed within the more sophisticated models.

The Boltzmann-Uehling-Uhlenbeck (BUU) equation – time dependent mean field

The cascade model described above is limited to nucleon-nucleon and meson-nucleon collisions ignoring deflection of the particle trajectories by the field of target nucleons and other mean-field effects. A transport equation which contains both the time dependent mean field and hard collisions is called the Boltzmann-Uehling-Uhlenbeck (BUU) equation [19, 137] or sometimes the Vlasov-Uehling-Uhlenbeck equation [85].

Computational realization of BUU model was first developed at Michigan State University by Bertsch, Kruse, Stöcker et al. [19, 84, 85, 102, 103]. The model was used originally for description of colliding nuclei at energies of several tens of MeV per nucleon but was found to work well in the broad range of energies, being adapted by Geiss, Cassing and Greiner [56] even to reactions proceeding at such high energies that the quark degrees of freedom become important.

In BUU model each nucleon is represented by many (typically $\approx$100) test particles. Averaging over the positions and momenta of all test particles allows to estimate the nucleon density distribution in the nucleus at each moment of the time of the cascade evolution. Taking into consideration the short range of nuclear interaction it is natural to conjecture that the shape of the mean field should resemble the density distribution of the nucleons. A typical parametrization of the mean field – often called the Skyrme parametrization – is

$$U(\varrho) = A\left(\frac{\varrho}{\varrho_0}\right) + B\left(\frac{\varrho}{\varrho_0}\right)^{\sigma}$$

where $\sigma > 1$, A and B are parameters describing attractive and repulsive forces, respectively.

The advantage of the BUU model is the presence of the dynamically changing, self consistent mean field of the nucleons, resulting in the possibility to describe collective effects like, e.g., giant monopol resonances. However, the method of the estimation of the nucleon density distribution by averaging over many test particles causes that the fluctuations of the nuclear matter are to small to reproduce possible dynamical clusterization of the nucleus.

Quantum Molecular Dynamics model – nucleon correlation

One of the most advanced approaches to describe the fast stage of the reaction, based on Quantum Molecular Dynamics formalism, is realized by the QMD model originally proposed by Aichelin et al. [3] and elaborated further by other authors, e.g., Niita et al. [110]. In this model the nucleons are represented by Gaussian wave packets which interact by mutual two and three body forces. Therefore the ensemble averaging, which in the BUU model smears out fluctuations is avoided in QMD, what is essential for the formation of the many clusters observed in a nucleus-nucleus collisions. On the other hand the fluctuations present in the initial n-body momentum and spatial distributions of nucleons in the target nucleus must be compatible with the experimentally measured observables, e.g., a one-body density distribution should coincide with observed density profiles.

The QMD model implements the same important quantum features, which are present in modern INC and BUU realizations, namely:

- the Pauli principle which prohibits the nucleons from nucleon-nucleon collisions to scatter into occupied parts of the phase-space,
- stochastic scattering in which the momentum transfer in nucleon-nucleon collisions is not unambiguously determined by the initial conditions, and
- secondary particle production.

The time evolution of position and momentum of nucleons is described by a Newtonian equation of motion and by a stochastic two-body collision term. The biggest advantage of the QMD model is the possibility to calculate nucleon correlations leading to density distortion, nucleus shape changing, and composite particle emission. For higher beam energies some additional changes were implemented in the model to calculate particle production on the quark level, e.g., RQMD [132] and UrQMD [13].

In spite of many advantages, very time consuming calculations needed to obtain the satisfactorily accurate theoretical results for comparison with experimental data, limit practical applicability of this model in particular for heavy nuclei, i.e., many nucleon systems.

It turned out that results of the calculations performed in the framework of QMD as well as by means of simpler models, i.e. Intranuclear Cascade or BUU, cannot be compared in straightforward way with the experimental data because the de-excitation of the reaction products can significantly modify the observables. Thus the process of de-excitation of the products of the fast stage of the reaction must be taken additionally into consideration, e.g., by statistical emission of the particles. The theoretical production cross sections obtained in such a way are quite similar for all applied models , in spite of the fact that they differ significantly in the complexity of physical assumptions and computational effort which is much larger for BUU and QMD than that for the INC model [45, 83].

3.1.2 Nucleon interaction with a part of the nucleus

It is possible that the nucleon moving inside the nucleus interacts with a group of nucleons instead of colliding with a single nucleon. This group may be formed dynamically as a cluster existing in the nucleus or may be determined as a group of nucleons lying on the trajectory of a moving nucleon. If the nucleons of this group have small relative momenta they may leave the nucleus as a complex, excited ejectile.

3.1.2.1 Coalescence of nucleons into clusters

The emission of high energy composite particles has not been understood since many years. One of the possibilities to explain the origin of this phenomenon is the creation of composite particles by coalescence of nucleons escaping from the nucleus. In this model, composite fragments are formed only when nucleons are emitted close together in the momentum space. Already in the sixties Butler and Pearson proposed [35] the coalescence model of proton and neutron to explain the origin of high energy deuterons emitted in proton induced reactions. It was assumed that the formation of deuterons arose only from pairs of particles with small relative momenta, interacting by the ordinary deuteron potential.

Gutbrot et al. [64] adapted the coalescence model for the description of all hydrogen and helium isotopes. Their reasoning was based on pure statistical arguments that the complex particle density in the momentum space is proportional to the product of nucleon densities for all nucleons forming the complex particle. This assumption allows to determine the probability to find them in the small sphere of radius p_0 (parameter of the model) around the momentum of the escaping nucleon and thus the probability to create a complex particle. Later on these authors tried with moderate success to describe also the experimental spectra of IMFs by the coalescence of nucleons [58].

Jacak et al. [74] have found that "not only can the production of light nuclei from high energy nucleus-nucleus collisions be described by the coalescence model, but that intermediate rapidity complex fragments up to A = 14 can be described as well".

Recently the coalescence model was implemented to microscopic model calculations, e.g., to Intranuclear Cascade Model by Boudard et al. [29], and QMD model by Watanabe and Kadrev

[142]. A more detailed description of the realization of this model is presented in section 4.2 for the coalescence of nucleons in the frame of the Intranuclear Cascade Model.

3.1.2.2 Knock-out of clusters

A nuclear cluster according to Ikeda [73] may be defined as a spatially located subsystem of strongly correlated nucleons. If such a subsystem is characterized by intrinsic binding stronger than its external binding, then it can be considered as a single unit, without necessity of reference to its internal structure. More detailed information on this subject can be found, e.g., in review by Hodgson and Běták [68]. An impinging nucleon can knock out a preformed cluster from the target nucleus, and hence allow to observe it as the reaction product. Such a mechanism is most probable for low energy beam, because then the de Broglie wave length associated with beam particle is of the same order of magnitude as the cluster dimensions. As was discussed, e.g., by Kalbach [76] knockout of clusters is important in the reproduction of experimental data for beam energies smaller than 100 MeV. Boal and Woloshyn [23] proposed a direct knockout model for (p,α) reactions in the proton energy range up to 500 MeV, assuming the single scattering of a proton from a transient α-cluster in the nucleus. The authors achieved good quality of the description of experimental energy spectra even at backward scattering angles for reactions performed on ^{9}Be, ^{27}Al and Ag. The authors pointed out that the model assumes far reaching properties of the knocked out clusters, as e.g., high probability of cluster formation as well as high probability that the cluster is emitted with sufficiently small excitation energy that it will not break-up after leaving the nucleus. While this may be true for the α-particles because of their strong binding and a large gap between the ground and excited states, it is disputable for other clusters, especially for those of higher mass.

3.1.2.3 Fast break-up of the nucleus

It may happen at sufficiently high incident energy that the impinging proton removes from the nucleus that group of nucleons which are lying on its straight track through the nucleus. Different models have been used to describe quantitatively this mechanism of the reaction. For example, the energy flux model invented by Gottfried [59], the collective tube model proposed by Berlad, Dar and Eilam [16], or the effective target model described by Ta-chung [134] used this picture of the reaction mechanism as the basis. Such a phenomenon causes a strong distortion of the target nucleus what can lead to its break-up into several parts which can appear as excited sources of the particles.

Many authors reported the importance of the emission from two moving sources for understanding the qualitative behavior of the angular and energy dependence of the data in proton induced reactions. For example, Westfall et al. [150] used the emission from two moving sources for the description of experimental spectra of products measured in inclusive reactions on several targets. Biswas and Porile [22] proposed the break-up of the target nucleus into two or more bigger parts as an origin of the moving sources. They argued that the sideward peaked angular distributions and low forward-backward asymmetry, observed in high energy proton-nucleus reactions, may be due to Coulombic repulsion of appearing fragments of the nucleus. Hüfner and Somermann [71] performed formalization of the above mentioned mechanism in case of fast break-up into two heavier fragments. They assumed that the fast proton creates a trumpet-shaped channel in the nucleus, what allows to explain the strong sideward emission of Sc ejectiles as well as small backward enhancement of angular distributions observed in p-U collisions at high energies (see chapter 2). Aichelin, Hüfner and Ibarra [2] proposed a model of fragmentation which is similar to the shattering of glass. In the first step an impinging particle traverses a nucleus along a straight line forming a fireball around its path, whereas the spectator matter remains cold. In the second step, some fireball nucleons can enter the cold spectator matter and deposit energy and momentum. This leads to a global destabilization of the spectator matter and finally to fragmentation. The mass and charge distributions are assumed to be purely statistical as Aichelin and Hüfner proposed earlier [1]. Emitted prefragments are usually excited and may evaporate some particles.

The mentioned models take into account either the emission from heavy products of the nucleus break-up or from the fireball, omitting the possibility of emission from all excited prefragments.

3.2 De-excitation of equilibrated residua after the fast stage of the reaction

It is commonly accepted that after the fast stage of the reaction the excited residuum of the nucleus reaches a state of thermal equilibrium. Therefore the second stage of the reaction is usually described by statistical models. At low excitation energies of the residua the sequential processes dominate. They can manifest themselves as evaporation of neutrons, light charge particles (LCPs) and/or intermediate mass fragments (IMFs), binary decays with emission of IMFs as well as fission – in the case of heavy residua.

At sufficiently high excitation energy the multiplicity of emitted particles increases quickly, what is interpreted as simultaneous disassembly of the target nucleus into fragments, called multifragmentation. It may be, however, conjecture that this copious production of particles is due to sequential emission of fragments. Thus the term multifragmentation is sometimes used in more general sense to refer to these both mechanisms. Here, the multifragmentation is used as the name of simultaneous emission process.

3.2.1 Sequential emission

There exist many different theoretical models of the de-excitation of equilibrated residual nucleus. They can be divided in two main groups: First of them treats evaporation of particles as the main mechanism whereas the second group assumes that the emission of particles is due to binary decays proceeding, similarly to fission, via dynamically developing decay barriers.

Statistical evaporation

Statistical evaporation models base on the classical approach proposed by Weisskopf and Ewing [146, 147] or on the Hauser-Feshbach formalism [65]. The main assumption of both models is that the emitting nucleus achieved the thermodynamic equilibrium. Then the probability to populate individual exit channels may be estimated on the basis of statistical considerations.

In the first approach the probability of the particle emission is proportional to the ratio of level densities of daughter and parent nuclei. It is possible to express the proportionality coefficient by the cross section corresponding to the reverse process: i.e., by the cross section for the collision of a given particle with the daughter nucleus to create the compound nucleus. The level densities are usually taken from the Fermi gas model whereas the cross sections for the reverse processes are determined from the experiments.

Examples of this approach realizations are the ABLA computer program of Gaimard and Schmidt [55] and reviewed by Junghans et al. [75], as well as GEM (Generalized Evaporation Model) computer program of S. Furihata [52–54]. The first of these two programs is limited to evaporation of nucleons and α-particles whereas the second one allows for emission of 66 stable (or long lived) light particles and IMFs up to Mg.

The cross section for the emission of particles from a compound nucleus reactions in the Hauser-Feshbach formalism is equal to the product of probability to form the compound nucleus and probability to emit the desired particle from the compound nucleus. Both probabilities are expressed by appropriate transmission coefficients. The incoherent sum of contributions due to different orbital angular momenta in the entrance channel is performed. The spins of all particles are explicitly taken into consideration and their couplings are calculated by means of Clebsch-Gordan coefficients. The cross sections in this formalism should be averaged over many states of the compound nucleus as well as over states of the daughter nuclei when the excitation energy of them corresponds to a continuum of the excited states. Then the densities of states of these nuclei enter to the formula, moreover, they must be spin dependent because the spins of particles are explicitly treated.

This formalism was implemented, e.g., in the GEMINI computer program by Charity et al. [36] for evaporation of LCPs.

Sequential binary decays

Both mentioned formalisms of evaporation process, i.e. Weisskopf and Ewing model [146, 147] and Hauser-Feshbach model [65], assume that the complex emitted particles are preformed inside the nucleus and they pass the static potential barrier which determines the lifetime of the nucleus for their emission. The fission, which proceeds via very large deformation of the nucleus, may be treated as a process which appears due to traversing the dynamically created fission barrier. Therefore, a formalism different from the evaporation has to be applied for the fission process, as e.g., the Bohr-Wheeler formalism [151], which takes advantage of the saddle point in the nuclear potential energy as a function of deformation.

Another approach has been proposed by Moretto [104] which claims that the apparent distinction between evaporation and fission should be treated as rather artificial because it is possible to formulate a model which describes both these processes on the equal footing. In analogy with the fission saddle point, a ridge line in the potential energy surface is defined which controls the decay width of the system into any two given fragments. For details see paper of Moretto [104].

the formalism of Moretto was implemented by Charity et al. [36] in the GEMINI computer program. Originally this program was created to describe low energy heavy ion collisions. It was later successfully used to describe the slow stage of nuclear reactions in high energy reactions induced by various beams. This model assumes that two competing processes exist; evaporation of particles with $Z \leq 2$, or decay of the residuum into any two given fragments. Each of the product nuclei can also decay or evaporate LCPs. In the case of $Z \leq 2$ the probability of emission of individual particles is characterized by the decay width, predicted by Hauser-Feshbach formalism [65], whereas for heavier ejectiles it is calculated using the transition state formalism of Moretto [104]. In both cases information on the compound nucleus rotation and deformation energy was taken from rotating finite-range model (RFRM) calculations of Sierk [130].

As was shown by Villagrasa-Canton et al. [138] hybrid of this program with intranuclear cascade INCL program, gives quite reasonable reproduction of experimental total cross sections of p+Fe reactions in a broad range of energies. On the other hand, Herbach et al. [66] (see fig. 2.8 and 2.9) claim that this hybrid model fails in describing the high energy tails of energy spectra $\frac{d\sigma}{d\Omega dE}$ of LCPs and IMFs.

3.2.2 Multifragmentation

It is assumed that a piece of excited nuclear matter is formed as a result of the fast stage of the reaction. Internal pressure caused by the high excitation energy and possible compression of the system leads to expansion of nuclear matter and cooling it down. The initial fluctuations of the nucleon density grow up in the course of the expansion, what can cause a break-up of the nucleus into several fragments and nucleons. This phenomenon is called multifragmentation.

The multifragmentation is usually described by statistical methods under the assumption that the thermodynamical equilibrium is reached. There exist several realizations of the statistical multifragmentation model like, e.g., Statistical Multifragmentation Model (SMM) by Bondorf et al. [25], Microcanonical Metropolis Monte-Carlo model (MMMC) of Gross et al. [61] and Randrup and Koonin [119], or MMM by Al.H. Raduta and Ad.R. Raduta [116]. According to Botvina and Mishustin [26] the predictions of models which concern mass and excitation energy distributions of the reaction products differ generally by not more than 10%. The larger differences appear only for some more sophisticated observables, as e.g., isotope properties of the reaction products.

The typical assumptions and simplifications used in multifragmentation models will be discussed below on the example of the most popular SMM model. The model is based on the assumption of the simultaneous break-up of a thermalized nuclear system. This could be, in principle, treated as an analog of the phase transition from liquid to gaseous phase of nuclear matter. However, the real nuclear systems contain no more than a few hundred nucleons and this introduces significant distortions into the phase transition picture. Furthermore the surface tension and Coulomb interaction affect significantly the matter distribution at low densities.

It is expected that the compound nucleus excited in the first stage of the collision can expand to achieve the density ϱ smaller than equilibrium nuclear density ϱ_o of the nuclei in the ground state. Then, at $\varrho_o/2 < \varrho < \varrho_o$ the "bubble phase" (with nucleon gas inside) is created, while at $\varrho < \varrho_o/2$ the phase of droplets surrounded by nucleons is realized. If the internal pressure is not sufficiently high the system does not reach the "cracking point" and after some expansion it reverses to higher density. Several damped oscillations of this sort may occur before the system looses excitation by the evaporation and/or fission.

The break-up occurs when the surfaces of nuclear matter drops become well separated from each other to prevent action of attractive nuclear forces, i.e., distances between them are of order of 2-3 fm. This freeze-out configuration is expected to appear at density in the range $(1/2 - 1/10)\ \varrho_\mathrm{o}$. After freeze-out prefragments propagate under the influence of the long-range Coulomb force and loose their excitation by particle emission or a secondary break-up. Only final cold reaction products are observed experimentally.

In the SMM the sum (or integration) is performed over coordinates, momenta and excitation energies of the fragments, thus the break-up channels are characterized only by a set of fragment multiplicities defining the partitions of nucleons. The free energy of individual partitions has been estimated on the basis of the liquid drop picture of the nucleus and the fragments. It was parameterized for each fragment as a sum of the bulk, surface, symmetry and Coulomb contributions. The sum over all fragments of these contributions together with the translational free energy and the Coulomb energy of the system was used as an estimate of the free energy of the individual partition. The free energy depends on the volume of the interacting system determining the dependence of shape and height of the fragmentation barrier on the radius of the nuclear system. At a given excitation energy of the system the probability of a particular fragmentation channel is proportional to the number of states in the energy gap above the barrier.

The fragmentation barrier is an analog of the fission barrier. Moreover, among the fragmentation channels there exists a prompt fission (with multiplicity of emitted products M = 2). It is a dominant decay mode in heavy composite systems at low excitation energies. With increasing excitation energy the channels with M = 2,3,4,... are gradually opened and the break-up process acquires the character of statistical multifragmentation.

The fragments which pass the fragmentation barrier fly away from each other under the influence of the mutual Coulomb field. They simultaneously are de-exciting by evaporation or by fission (the latter possible only in case of a heavy fragment). These two processes lead to the enrichment of light clusters component and to the redistribution of fragment energies.

More detailed information on the SMM realization is presented by Bondorf et al. [25]

Chapter 4

The models used for theoretical analysis of the present thesis data

It can be concluded from the review of the experimental investigations on proton induced reactions – presented in chapter 2 – and from inspection of the models used to describe the data – presented in chapter 3, that the presence of specific mechanisms manifests itself in all the reactions studied. Therefore these mechanisms must be taken into consideration in the analysis of the present thesis data.

It is evident from the observation of high energy tails of the nucleon spectra, that the cascade of nucleon-nucleon collisions has to be taken into account in the description of the fast step of proton-nucleus collisions. Furthermore, the coalescence mechanism seems to be dominant for high-energy, complex light charge particles (LCPs) emission as it was emphasized, e.g., by Letourneau [88, 89]. In the case of high energy intermediate mass fragments (IMFs) the presence of strongly anisotropic emission can be modeled by the emission from moving sources [150] originating presumably from the break-up [2] of the target nucleus in the first stage of the reaction.
A large contribution of isotropic, low energy emission of particles is present in all the experimental spectra pointing out the importance of statistical emission from the equilibrated nuclear systems created in the first, fast stage of the reaction.

The following computer realizations of these reaction models have been selected to perform theoretical analysis of the data:

- INCL4.3 (IntraNuclear Cascade - the Liége version) - the computer program of the intranuclear cascade model for the first stage of the reaction.
- Coalescence model of nucleons to form LCPs - implemented in the INCL4.3 computer program.
- GEM2.0 (Generalized Evaporation Model) - the computer program which enables one to calculate evaporation of particles (up to Mg) from the excited and equilibrated residuum of intranuclear cascade.
- Analytical formulae of a phenomenological model of emission of particles from moving sources [31] to describe the process of de-excitation of residua of the fast break-up of the target nucleus with fireball emission.

4.1 Intranuclear cascade - Liège version (INCL)

The INCL code describes a fast stage of nuclear reactions as cascade of nucleon-nucleon and pion-nucleon collisions proceeding during motion of these particles through the target nucleus. The particles are assumed to move between collisions in a static, i.e., time-independent, mean field. The program contains physical information (as e.g., the nucleon-nucleon cross sections) which allows to use it for reactions induced by light particles (up to ^{4}He) of energies in the range from ~ 0.1 to $\sim$ 3A GeV. In the present thesis the INCL4.3 version of this program [29] was applied for the description of the intranuclear cascade and for the emission of complex LCPs created due to surface coalescence of nucleons. This program is a generalized version of the INCL4.2 program [28], in which the calculation of the surface coalescence of the nucleons was not yet implemented.

The code treats the target nucleus as a set of nucleons with randomly generated positions and momenta. Positions of nucleons are sampled with a Saxon-Woods density distribution:

$$\varrho(r) = \begin{cases} \dfrac{\varrho_0}{1+\exp\left(\frac{r-R_0}{a}\right)} & \text{for} \quad r < R_{\max} \\ 0 & \text{for} \quad r > R_{\max}, \end{cases}$$

with A_T beeing the target mass number, $R_0 = (2.745 \times 10^{-4} A_T + 1.063) A_T^{1/3}$ fm, $a = 0.510 + 1.63 \times 10^{-4} A_T$ fm, and $R_{max} = R_0 + 8a$. Initial momenta are generated stochastically in a Fermi sphere, without distinction of protons and neutrons. It is assumed, that nucleons move in spherical potential well of constant depth $V_0 \approx 45$ MeV and of radius $R(p)$, dependent on nucleon momentum. This momentum dependence is determined by local density distribution of nucleons in the nucleus [28]. Nucleons move along straight-line trajectories until two of them reach their minimal relative distance or until one of them reaches surface of the nucleus. In the former case collision of two nucleons appears and in the latter the nucleon can leave the nucleus or can be reflected by the potential gradient.

Collisions of nucleons are described quantitatively using experimental nucleon-nucleon cross sections for elastic and inelastic scattering with Δ production according to the parametrization published in Ref. [39]. Pions are produced and/or absorbed by inelastic collisions in the following reactions: $NN \rightleftharpoons N\Delta$, $\Delta \rightleftharpoons N\pi$. Relativistic kinematics is used in description of all collisions. Modification of free nucleon-nucleon collisions by the presence of the nucleus matter is taken into account by implementing Pauli blocking which prevents two fermions to appear with the same quantum numbers.

For a nucleon approaching the nucleus surface a probability is calculated to decide whether the nucleon can be transmitted through or reflected from the surface. The emission probability depends on the nucleon isospin, its kinetic energy, and angle between particle trajectory and surface of the nucleus. Conservation laws are mostly handled by the INCL model with exception of the momentum conservation law, which is broken by interaction of nucleon with the infinitely heavy surface of the nucleus.

As can be seen from the above comments the computer program gives the possibility to extract almost parameter free predictions of the production cross sections for the emission of nucleons and pions, and provides information on the properties of the heavy nuclear remnant of the reaction. There are, however, two parameters which cannot be *á priori* fixed unambiguously; the depth of the potential well and the stopping time, i.e., the time at which the cascade is stopped to leave the residual nucleus in the thermodynamical equilibrium.

It was found by the authors of the INCL program in the analysis of neutron and proton spectra, emitted from proton induced reactions on Al, Fe, Zr, Pb, and Th for a broad range of energies (from 0.113 GeV to 1.6 GeV), that the depth of the potential well should be equal to $\approx$ 45 MeV [28]. This choice of potential depth reproduced also the mass and charge distributions of heavy residua of the reactions.

The second parameter, i.e., the stopping time, can be determined as the time at which the excitation energy of the residual nuclei stabilizes. It was found that other observables, e.g., average kinetic energy of emitted nucleons and pions or momentum asymmetry of nucleons participating in collisions also do not vary significantly at time longer than the stopping time extracted from time variation of the excitation energy. It is recommended to use the following, default value of the stopping time:

$$t_{stop} = f_{stop}\, t_0 \left(\frac{A_T}{208}\right)^{0.16},$$

where t_0=70 fm/c, f_{stop} = 1, and A_T is the mass number of the target [28].

4.2 The Coalescence Model - implementation in the INCL code

In the current section a method of implementation of a coalescence mechanism (cf. subsection 3.1.2.1) into the INCL program is presented. A more detailed description of this specific version of INCL program (version INCL.4.3) can be found in ref. [29].

In the standard intranuclear cascade model nucleons travel along the straight-lines trajectories up to the moment of collision with other nucleons or when they reach the nucleus surface. In the latter case they can be reflected from the surface or they are allowed to escape from the nucleus. If the escaping nucleon is able to capture the nucleons placed on its way in the nucleus then this group of nucleons might be observed as a composite particle. The necessary condition for such a phenomenon (called coalescence) is the proximity of momenta of all nucleons forming the group of nucleons escaping from the nucleus. This condition is formulated in the INCL.4.3 program by the relation:

$$r_{i,[i-1]}\; p_{i,[i-1]} \leq h_0$$

where h_0 is a parameter of the model, $r_{i,[i-1]}$ and $p_{i,[i-1]}$ are the Jacobian coordinates of the *i*th nucleon, i.e., the relative spatial and momentum coordinates of *i*th nucleon with respect to the subgroup constituted of the first $[i-1]$ nucleons. The following composite particles: ^{4}He, ^{3}He, t, d are taken into account as candidates for group of nucleons formed in the coalescence mechanism. When the above inequality is fulfilled, the program examines whether the composite particle can be transmitted through the appropriate potential barrier. The procedure is realized starting from the heaviest cluster, because the imposed conditions are fulfilled for lighter particles when they are fulfilled for the heavier one.

The possibility of forming the clusters by coalescence is checked only for nucleons which reach the surface of the nucleus and might escape outside. However, it is obvious that the coalescence may appear with higher probability inside the nucleus because there the density of nucleons is much higher than at the surface. Thus the program checks all conditions for forming and emission of clusters not at the surface, i.e., not at $r = R_{max} \equiv R_0 + 8a$ but in more favorable place, i.e., at distance D along the nucleon's trajectory, outside the sphere of radius R_0. D is the parameter of the coalescence model and R_0 and a are the radius and diffuseness parameters of the Saxon-Woods density distribution of nucleons (cf. section 4.1).

4.3 The Generalized Evaporation Model GEM 2.0 of Furihata

The Generalized Evaporation Model GEM 2.0 by Furihata [52–54] is based on the classical approach proposed by Weisskopf and Ewing [146], [147]. In the program 66 nuclides (listed in the table 4.1) are considered as possible evaporation ejectiles. The fission is also taken into account using formalism of Rutherford Appleton Laboratory (RAL) model [9, 10].

Table 4.1: The ejectiles taken into consideration in the GEM model.

Z_j	Ejectiles						
0	n						
1	p	d	t				
2	^{3}He	^{4}He	^{6}He	^{8}He			
3	^{6}Li	^{7}Li	^{8}Li	^{9}Li			
4	^{7}Be	^{9}Be	^{10}Be	^{11}Be	^{12}Be		
5	^{8}B	^{10}B	^{11}B	^{12}B	^{13}B		
6	^{10}C	^{11}C	^{12}C	^{13}C	^{14}C	^{15}C	^{16}C
7	^{12}N	^{13}N	^{14}N	^{15}N	^{16}N	^{17}N	
8	^{14}O	^{15}O	^{16}O	^{17}O	^{18}O	^{19}O	^{20}O
9	^{17}F	^{18}F	^{19}F	^{20}F	^{21}F		
10	^{18}Ne	^{19}Ne	^{20}Ne	^{21}Ne	^{22}Ne	^{23}Ne	^{24}Ne
11	^{21}Na	^{22}Na	^{23}Na	^{24}Na	^{25}Na		
12	^{22}Mg	^{23}Mg	^{24}Mg	^{25}Mg	^{26}Mg	^{27}Mg	^{28}Mg

According to the Weisskopf approach [146] evaporation of the particle j (with the mass and atomic numbers A_j, Z_j), emitted in its ground state from the parent compound nucleus i (with mass A_i and charge Z_i, excited to the energy E^*) proceeds with the probability $P_j(E)$ dependent on its kinetic energy E:

$$P_j(E)dE = g_j\sigma_{inv}(E)\frac{\rho_d(E^* - Q - E)}{\rho_i(E^*)}EdE. \tag{4.1}$$

Q denotes the Q – value of the reaction in which particle j is emitted leaving the daughter nucleus d. Level densities of the emitted particle and the daughter nucleus are depicted as ρ_i, ρ_d (MeV^{-1}), respectively. The cross section σ_{inv} for the inverse reaction is parameterized according to formulae given by Furihata in ref. [54] whereas the statistical and normalization factor g_j is defined as follows

$$g_j = \frac{(2S_j + 1)m_j}{\pi^2\hbar^2}, \tag{4.2}$$

where S_j and m_j are the spin and the mass of the emitted particle j, respectively. In the GEM2.0 computer program two versions of evaluation of the inverse cross sections for LCPs are provided.

One of them follows prescription given by Dostrovsky et al. [43] whereas the other one uses formulae proposed by Furihata [54]. The latter one is applied in the present thesis.

In the Generalized Evaporation Model the particle evaporated from the parent nucleus can be excited. Such a generalization significantly improves model predictions for IMFs.

The total decay width of particle emission is calculated by integration equation 4.1. Level densities are evaluated according to the Fermi gas model with two versions of the density parameter a. This parameter is used either in the simplest form, e.g., $a = A/8$ or with the Gilbert-Cameron-Cook-Ignatyuk (GCCI) level density parameter [114, 115]. The latter possibility was used for calculations performed in the present studies.

4.4 Nucleus break-up with "fireball" formation – phenomenological model of particle emission from moving sources

It was found in the recent investigations of PISA collaboration [31, 33], and as an outcome of the present analysis in this work that besides the contributions originating from the intranuclear cascade with the possibility of coalescence of nucleons into composite particles, and evaporation of particles, another mechanism of the reaction was present. This competitive mechanism was described and interpreted as emission of particles from moving sources.

Three different sources of particles have been identified. The fast, hot source - called "fireball" - was responsible for large part of the cross section of LCPs emission. Two slower sources, characterized by lower temperatures than the fireball, participated significantly in the IMF production whereas their contribution to the LCP emission was much smaller.

The origin of these three sources was explained by the following reasoning; The fast proton impinging onto the target nucleus can drill the cylindrical hole in the nucleus what in turn can lead to break-up of the "injured" nucleus. The part of the nucleus consisted of the nucleons lying on the way of the impinging proton through the nucleus form the small, fast source - the fireball, whereas the residual nucleus and/or the products of its break-up manifest themselves as two slower sources.

Originally the fireball model was proposed by Westfall et al. [149] and by Gosset et al. [58] to describe proton inclusive spectra from heavy ion collisions. It was assumed that the target and projectile are spheres and make clean cylindrical cuts through each other, leaving a spectator piece of target and projectile if dimensions and impact parameters allow for it geometrically. It was assumed that nucleons swept out from both the projectile and target were heat up by the available energy forming quasiequilibrated nuclear "fireball". The fireball was treated relativistically as an ideal gas, i.e., only nucleons can be emitted without possibility to form composite particles because this can be achieved only by interaction of nucleons. Parameters describing properties of the fireball, i.e., its velocity - β, and its temperature - τ, were calculated as a function of number of nucleons in the fireball, which in turn was determined by the impact parameter. The laboratory angular distributions and spectra of emitted protons were calculated assuming isotropic decay and the Maxwell-Boltzmann shape of the spectra in the rest frame of the fireball for each impact parameter. The final calculations involved summing over all impact parameter values.

Many variations of the original fireball idea have been proposed, with the same thermodynamical content, only with the different kinematics. Myers [106] proposed a firestreak model where the collision region is broken up into tubes. A tube from the projectile fuses with the corresponding tube in a target nucleus forming a "firestreak". The velocity of a firestreak in the laboratory system as well as all intensive thermodynamic properties like temperature, chemical potential, depend only on the number of particles in the firestreak, and characterize the distribution of emitted protons. Das Gupta [62] proposed two-fireball model, assuming that the nucleons - participants from the target move with lower velocity than those from projectile what can be explained by introducing a transparency factor.

All these considerations of fireball formation can be valid for proton induced reactions as well assuming that the impinging proton interacts collectively with nucleons on its path while traversing the nucleus. Models presenting the formalism of such a phenomenon were mentioned in the previous chapter.

In the present thesis the picture of the fireball, proposed by Westfall et al. [149], is coupled with the two moving sources model by Westfall et al. [150] and is adopted with some modifications. The following assumptions were concluded:

1. The proton impinging onto the target can create the fireball as it was observed in heavy ion induced reactions. This is because of experimental observations of collective interaction of the proton with the group of nucleons ("effective target") discussed in the chapter 2.

2. The supposition that the nucleons of the fireball form an ideal gas is postponed, i.e. , the interaction between nucleons is taken into consideration. Therefore it is natural to expect that the composite particles like d, t, ^{3}He can be emitted besides the nucleons from the fireball. However, the Maxwell energy distribution of the ejectiles is still accepted as a reasonable approximation.

3. The spectator part of the target nucleus appears as the single moving source or as two moving sources - in the case of its break-up. It is assumed in the model, that all the sources move in direction parallel to the beam, what is in apparent contradistinction to the physical intuition, according to which various directions for different sources could be expected. However, in the inclusive experiment the observables are averaged over the azimuthal angle (in the case of the lack of polarization) and hence they appear as originating from the source moving effectively in the direction parallel to the beam.

4. The composite ejectiles should be emitted besides the nucleons from all the moving sources. The supposition of the isotropic emission of all ejectiles is supported in the present model.

5. The velocities and temperatures of the sources are treated as free parameters. This is also true for total production cross sections of the ejectiles as well as the heights of the barriers which prevent low energy ejectiles to be emitted from the sources.

A detailed formulation of the moving source model was presented by Westfall et al. [150] whereas its modifications utilized in the present thesis can be found in the paper of Bubak et al. [31] and are placed in Appendix A for convenience of the reader.

Chapter 5

PISA experimental setup and method

The aim of the present thesis is to study the energy dependence of the reaction mechanism of proton induced reactions on the Ni target. For this purpose the double differential cross-sections $\frac{d\sigma}{d\Omega dE}$ (θ, E) for emission of light charged particles (LCPs), i.e., ^{1,2,3}H and ^{3,4}He, and intermediate mass fragments (IMFs), i.e., the particles heavier than ^{4}He and lighter than possible fission fragments, were measured with the mass and charge identification at four energies of the proton beam: 0.175, 1.2, 1.9, and 2.5 GeV.

The identification of (A, Z) was achieved by applying telescopes consisted of semiconductor silicon detectors and/or telescopes built of silicon and scintillator CsI detectors. Properties of the different detectors are described in subsections, 5.2.1, and 5.2.2 for silicon telescopes and CsI detectors, respectively.

It was expected, according to the present knowledge of proton induced reactions, that the angular dependence of the cross sections is smooth. Thus, to study this dependence it was enough to measure the $\frac{d\sigma}{d\Omega dE}$ at several selected scattering angles.
The shape of the spectra was expected to be similar to the Maxwellian distribution with the maximum in vicinity of the height of Coulomb barrier between the emitting nucleus and the ejectile. The knowledge of the exact shape of the spectra is crucial in judging about the mechanism of the studied reactions. Thus the detecting system should be able to measure the spectra in a broad range of energies. The high upper level of detected energies was achieved by using the telescopes consisted of semiconductor detectors accompanied by thick scintillating detectors built of dense material (CsI). The low energy threshold was obtained by using thin silicon detectors (50 μm) as the ΔE detectors in the telescopes. Thin, selfsupporting targets of thickness of (200 - 300 μg/cm^2) were used to avoid deformation of spectra of emitted particles by their rescattering in the target. Low luminosity caused by application of such thin targets were compensated by the fact that the targets were placed on the internal beam of COSY (COoler SYnchrotron) in Forschungszentrum Jülich (see Section 5.1), what led to the multiple passing of the beam protons (e.g., $\sim 10^4$ times) through the target during one cycle of acceleration of the protons and irradiation of the target. A detailed description will follow.

To assure identical conditions (the target thickness, the counting rate, the electronics adjustment, etc.) for measurements of the cross sections for all studied beam energies, the irradiation of the same target was performed alternating the beam energy in subsequent cycles of proton injection to the COSY ring. This is so called "supercycle" mode of operation of COSY (see Subsection 5.1.1).

5.1 COSY - COoler SYnchrotron facility

"COSY" is a cooler synchrotron and storage ring operated at the Institute of Nuclear Physics (IKP) of Forschunszentrum Jülich.

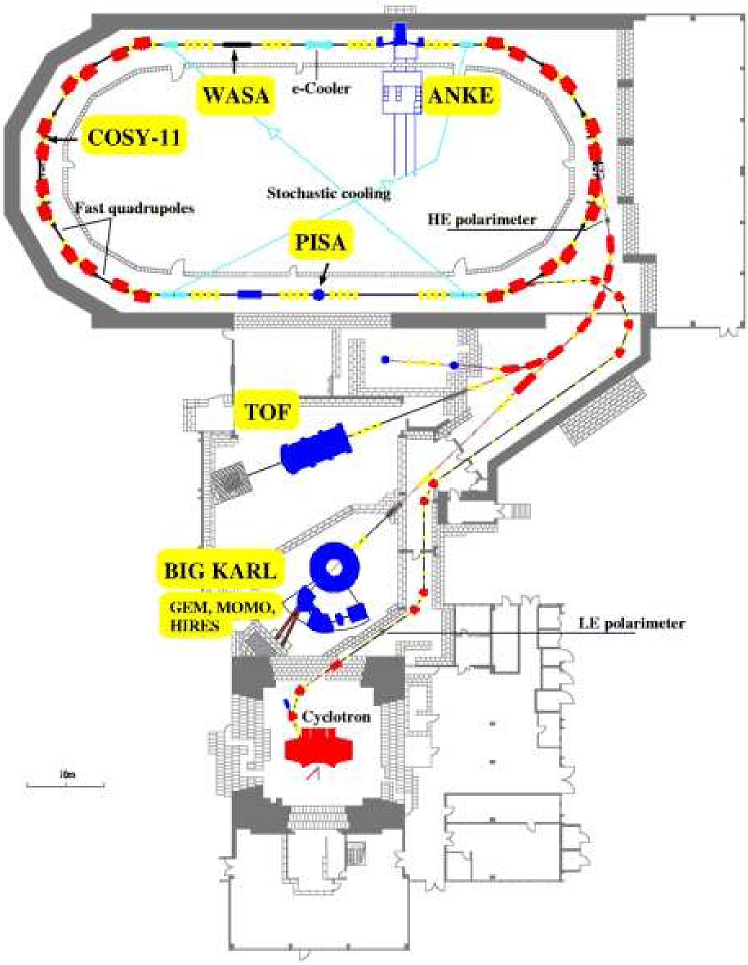

Figure 5.1: Floorplan of the accelerator complex in Forschunszentrum Jülich. On bottom JULIC-cyclotron, on top COSY ring with internal experiment: PISA, COSY-11, WASA, ANKE, in the middle external experiment: BIG KARL and TOF.

The accelerator complex (see Fig. 5.1)comprises an isochronous cyclotron (JULIC), used as an injector, a race track shaped cooler synchrotron with a circumference of 184 m, and internal and external target stations [93]. COSY delivers beams of polarized and unpolarized protons and deuterons in the momentum range between 0.3 GeV/c and 3.7 GeV/c. The ring can be filled with up to 10^{11} particles leading to typical luminosities of 10^{31} cm^{-2}s^{-1} when using an internal cluster or pellet target. Beams can be phase-space cooled by means of electron cooling at injection energy as well as stochastic cooling at high energies. Typical beam preparation times, including injection, accumulation and acceleration, are of the order of a few seconds. After acceleration the beam can be cooled down. The accelerated particles can be extracted to one of the external experiments and than the total beam has to be used in one act of the target irradiation, or the beam can be applied in an internal experiment and then it circulates inside the synchrotron ring being continuously used up by slow ramping on to the internal target. During realization of the present experiment the four internal target stations (ANKE, COSY-11, PISA, and WASA) and two external detector systems (BIG KARL, TOF) were operated by large international collaborations. On the average COSY was running for more than 7000 hours per year.

5.1.1 Advantages and drawbacks of internal beam experiments

PISA is one of the internal beam experiments of COSY. The great advantage of measuring on the internal beam is a possibility to use very thin targets, which assure negligibly small rescattering of the reaction products without loosing high luminosity. Moreover, it is possible to set the luminosity at the stable, controlled level what allows to collect the data with the optimal counting rate. This may be achieved due to the fact that the particles injected to the synchrotron ring are circulating along to computer controlled trajectories, which are adjusted by electromagnetic fields to be placed during the acceleration well apart of the target position. After acceleration the beam is slowly ramped on to the target position and the speed of the ramping may be adjusted by feedback loop with one of signals obtained from the detecting system (e.g., counting rate of some selected detector). Therefore it is possible to set up the luminosity on (approximately) constant level, which is most efficient for the detection and the data acquisition systems.

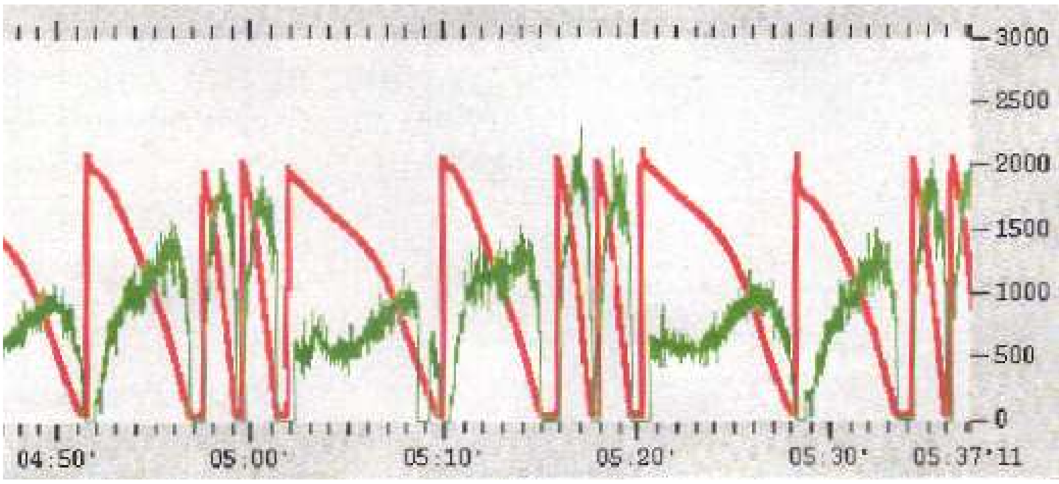

Figure 5.2: Example of the energy supercycle; red line corresponds to beam intensity, green one to the counting rate of PISA detectors.

Furthermore, due to the fact, that injection of particles from the cyclotron, their acceleration and irradiation of the target is realized as one separate cycle for a given final energy, it is possible to perform the alternating cycles leading to different final energies of the accelerated particles. It is very important because experimental conditions may change during experiment which lasts several days or weeks. To avoid modification of experimental conditions for the measurements performed at different energies it is thus reasonable to arrange the subsequent acceleration cycles in the "supercycles", i.e., sets of cycles with different energies of accelerated particles. This assures achieving the same experimental conditions like, e.g., target thickness and its position, setup, electronics, etc., for all studied energies.

Figure 5.2 presents an example of the experiment in which three proton beam energies were used: 1.2, 1.9, and 2.5 GeV. The supercycle consisted then of two short cycles of measurements at 1.2 GeV, one long cycle at 1.9 GeV and one cycle of the intermediate length at 2.5 GeV energy of accelerated protons. It is well visible that two goals have been achieved: (1) The speed of beam ramping on to the target was adjusted to obtain approximately constant rate (constant luminosity) in spite of strong variation of the beam intensity, and (2) the number of events collected during one supercycle is approximately the same for each energy, thus the accuracy of measurements determined by statistics of events is comparable for all energies.

The internal beam experiments have a lot of drawbacks besides the advantages listed above. The drawbacks are caused by the fact that in such experiments the scattering chamber is a part of the synchrotron ring. Therefore, the following conditions have to be fulfilled :

- The vacuum in the scattering chamber has to be very good, i.e., the pressure inside the scattering chamber must be lower than approx. 10^{-8} mbar. To fulfill this condition each piece of the experimental apparatus installed inside or connected straightforward to the chamber has to be made from specific materials and must be very well cleaned. Of course it has to pass very restrictive vacuum tests before installation.
- Installation of the detectors and other parts of the apparatus, as e.g., target holder, in the scattering chamber as well as dismounting them can be done only when the synchrotron does not work and when the scattering chamber is separated from the rest of the synchrotron ring by special vacuum valves. Thus, such an activity is possible only during the maintenance time of the synchrotron ring or it must be done on account of restricted beam time assigned to the given experiment. Furthermore, each break in the measurements which needs opening of the scattering chamber lasts rather long because the valves separating the scattering chamber from the rest of the synchrotron ring may be opened only after achieving very good vacuum in the scattering chamber.
- The access to the apparatus which is placed in the neighborhood of the scattering chamber is restricted to the time when the synchrotron ring is switched off because of the safety reasons. This condition does not allow to add, remove or exchange the parts of the apparatus, which are positioned closely to the scattering chamber.
- Normalization on incident number of protons as well as controlling the beam position and its quality (e.g. possible beam halo) is much more complicated than at external beam location.

5.2 Detector setup of PISA experiment

The scattering chamber of PISA experiment is installed on the ion-guide of the COSY ring. Schematic view of the scattering chamber and detecting system is presented in Fig. 5.3.

The circle with the description "TARGET" represents the flange positioned on the top of the scattering chamber at which the target manipulator is mounted. The vertical manipulator operated from outside of the chamber, allows without opening the chamber, to take the target from the target magazine - placed at the bottom of the scattering chamber - and to shift it vertically to the requested position. The target - strip of foil $\approx 150\ \mu g/cm^2$ thick, 6 cm long and 0.2 cm wide - was mounted on the fork-like target frame shown in Fig. 5.4. The target magazine, which contains 4 - 6 targets mounted on the target frames, can be reloaded without opening of the scattering chamber. As can be seen in Fig. 5.3 the target position is shifted upstream to the beam with respect to the geometrical center of the scattering chamber. Such a position increases distance of the target from the detectors placed at forward scattering angles and decreases the distance to the detectors placed at backward angles. Consequently the solid angles of forward detectors are smaller in comparison to solid angles of detectors of the same dimensions but placed at backward scattering angles. This helps to diminish the difference between counting rate for forward and backward detectors.

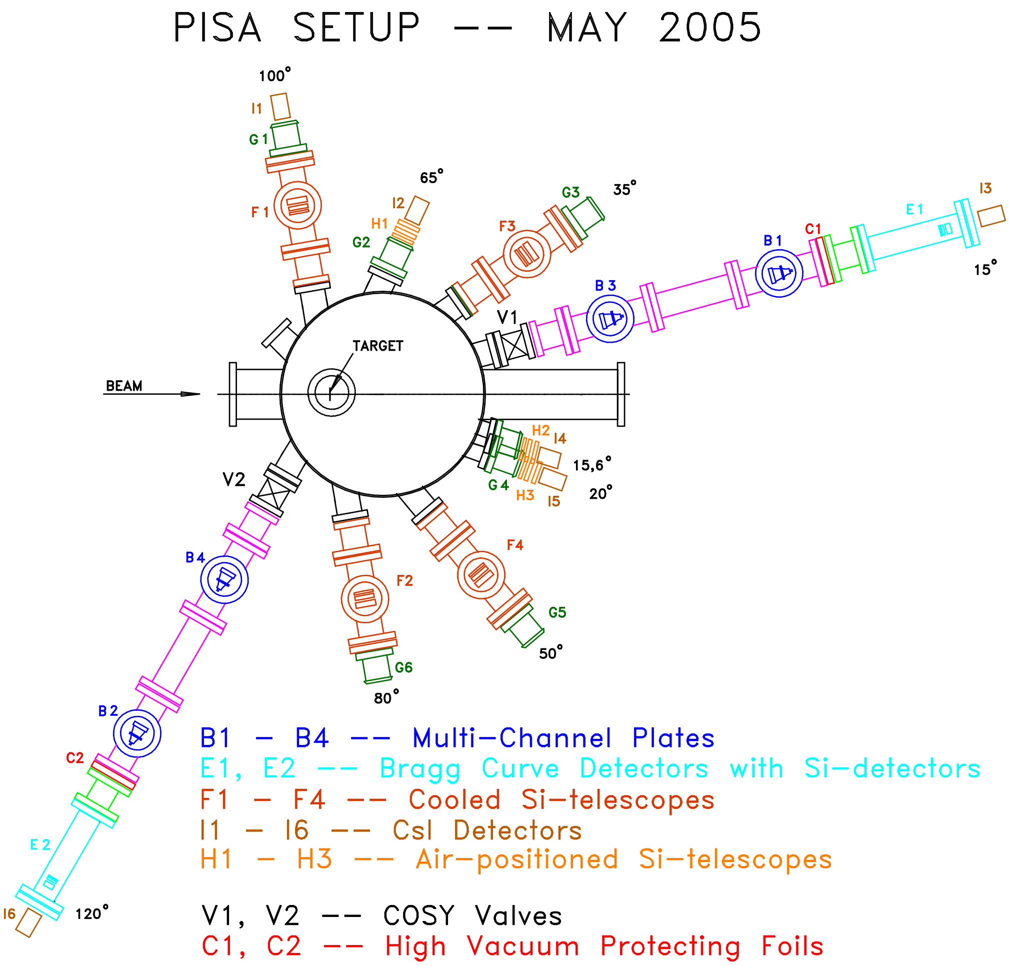

Figure 5.3: Experimental setup of PISA experiment mounted on internal beam of COSY in Jülich

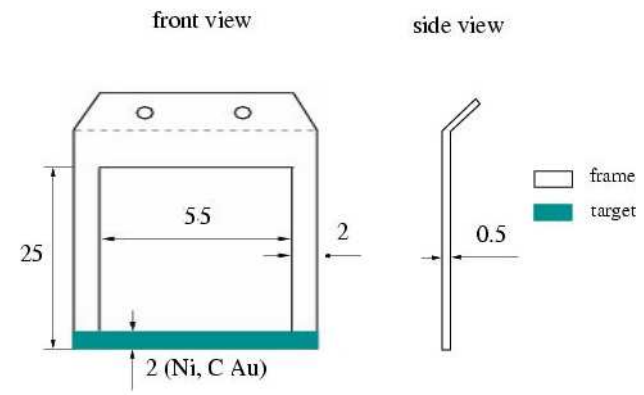

Figure 5.4: Target frame - dimensions in mm.

The detectors are installed at 9 selected angles inside the vacuum channels called "arms". There are three types of the detection arms:

- The detection system at 15° and 120° which consists of four types of the detectors:

  1. Bragg Curve Detector (BCD) to measure energy and charge of intermediate mass fragments up to Si. Advantage of this detector is the low energy treshold ≈0.5 MeV/nucleon.
  2. Time of flight detector, composed of two telescopes with MicroChannel Plates (MCP), positioned in front of BCD, i.e., between the target and the BCD. The time-of-flight information gained from this detector, combined with information from BCD detector enable mass and charge identification of intermediate mass fragments [12].
  3. Two Silicon detectors installed behind the BCD to measure particles with energies that punch through the BCD detector.
  4. Cesium Iodide (CsI)- scintillator to measure energy of the light charged particles, (p, d, t, ^{3}He, ^{4}He) which go through BCD detector and the silicon detectors.

  In the present thesis the data obtained by means of these two detector arms were not taken into consideration.

- The detection system at 35° , 50° , 80° , 100° consists of silicon detector telescopes installed in the vacuum of the scattering chamber:

  1. The telescopes are built of three or four silicon detectors cooled to -10° C to improve their energy resolution. This resolution allows to distinguish isotopes of light nuclei up to boron.
  2. At 100° a 50μm stainless steel foil is placed behind the silicon telescope to close the vacuum of the scattering chamber, and the CsI scintillator detector is installed in the air, behind the foil.

  Detailed information concerning silicon detectors is presented in the table B.1.

- For 15.6° , 20° , 65° there are telescopes of four silicon detectors and CsI detector all installed in air (behind 50μm stainless steel foil closing the vacuum of the scattering chamber).

In the present work the data obtained by means of seven above detector arms were analyzed.

Details of the used detectors as their geometrical dimensions, distance from the target, the solid angle, etc., are collected in the Table 5.2.

In the following, only properties and the method of application of the silicon and scintillator detectors will be discussed because in the present thesis the information from the detector arms positioned at 15° and 120° , which contain BCD and MCP detectors, has not been used.

5.2.1 Silicon telescopes

Silicon telescope consists of at least two silicon detectors positioned one behind another with the active surface placed perpendicularly to the direction of the registered particles. All detectors of the telescope, with possible exception of the last one, have to be transmission detectors.

It means that their whole volume should be active and homogenous. Furthermore, the front and end surfaces of the detectors should be exactly parallel, i.e., the thickness of the detector should be the same in each point of the active area. Extensive description of semiconductor detectors can be found, e.g., in Ref. [87] p. 207. Undeniable advantage of silicon detectors is high unfailing, relatively low price and easy calibration method because of linear dependence between amplitude of the impuls and amount of the energy lost by particle in the detector. On the other hand these detectors are much more sensitive to radiation damages than, e.g., gaseous detectors. This should be taken into consideration while performing the internal beam experiment, because then the radiation is on the high level all the time during work of the accelerator. This implies necessity of mounting the silicon detectors only for the beam time of the experiment and dismounting them just after the experiment.

In the contrast to the germanium detectors it is possible to use silicon detector without cooling, but cooling down improves properties of the detector work because it decreases detector noises, e.g., cooling down to $-10°$ C from the room temperature decreases the noises by factor of about two.

In four of the detection arms in PISA experiment, i.e., at 35° , 50° , 80° , and 100° the silicon detectors were cooled to the temperature $-10°$ C. For the rest of the arms it was not possible because the detectors worked in a gas environment (air, or isobutane in the BCD). It was also not possible to cool down the thinnest detectors of the cooled telescopes because their construction did not allow for this.

Detailed information concerning thickness, producer, type and window of silicon detectors is given in the Table B.1. Detector diameter, distance from the target and solid angle are listed in the Table 5.2.

The telescope consisted of two or more detectors allows to identify charge and mass of the detected particles using the ΔE-E method. This method is based on the observation that the energy deposit in the detector depends on the charge and mass of the particle as well on its energy. In the first approximation this dependence may be approximated by the following formula

$$\frac{dE}{dx}(E) \sim \frac{\mathbf{Z^2 A}}{E} \tag{5.1}$$

Table 5.1: Information concerning all detection arms including thickness, distance from the target, active ares, solid angle of each detector, and material between detectors. For arms equipped with MCP detectors also thickness of MCP foils is given, and effective grid transparency taking into account transparency of the previous grids. The estimation of the effective solid angles takes into consideration the fact, that the part of these detectors is shadowed by grids. Silicon detectors with the symbol Si4 taken in the brackets were not used for trigger definition.

Arm 15°	detector	MCPSt	MCPSp	BCD	Si1	Si2	steel layer	CsI
	thickness	90 μg/cm^2	90 μg/cm^2	22 cm	150 μm	500 μm	50 μm	7 cm
	surface	250 mm^2	250 mm^2	300 mm^2	900 mm^2	900 mm^2		1250 mm^2
	grid transp.	88,25%	77,94%	74,6%	74,6%	74,6%		
	dist fr trg	870 mm	1410 mm	1715 mm	1990 mm	2001,5 mm	2094 mm	2101,7 mm
	solid angle	330 μsr	126 μsr	102 μsr	227 μsr	225 μsr		1345 μsr
	active s.a.	291 μsr	98,2 μsr	76,1μsr				
Arm 15,6°	detector	steel layer	Si1	Si2	Si3	(Si4)	CsI	
	thickness	50 μm	89 μm	1016 μm	1016 μm	89 μm	7 cm	
	surface		300 mm^2	300 mm^2	300 mm^2	300 mm^2	1250 mm^2	
	dist fr trg	714 mm	731,5 mm	732 mm	748 mm	749,5 mm	754 mm	
	solid angle		561 μsr	560 μsr	536μsr	534μsr	2199μsr	
Arm 20°	detector	steel layer	Si1	Si2	Si3	(Si4)	CsI	
	thickness	50 μm	89 μm	1016 μm	1016 μm	89 μm	7 cm	
	surface		300 mm^2	300 mm^2	300 mm^2	300 mm^2	1250 mm^2	
	dist fr trg	670 mm	687,5 mm	688 mm	704 mm	705,5 mm	710 mm	
	solid angle		635 μsr	634 μsr	605 μsr	603 μsr	2480 μsr	
Arm 35°	detector	Si1	Si2	Si3	steel layer	S-0L(mon)		
	thickness	47.8 μm	426 μm	6000 μm	50 μm			
	surface	150 mm^2	150 mm^2	200 mm^2				
	dist fr trg	688 mm	707 mm	723 mm	952 mm			
	solid angle	316 μsr	300 μsr	383 μsr				
Arm 50°	detector	Si1	Si2	Si3				
	thickness	40.5 μm	398 μm	6000 μm				
	surface	150 mm^2	150 mm^2	200 mm^2				
	dist fr trg	652 mm	671 mm	687 mm				
	solid angle	353 μsr	333 μsr	424 μsr				
Arm 65°	detector	steel layer	Si1	Si2	Si3	(Si4)	CsI	
	thickness	50 μm	84 μm	1016 μm	1016 μm	89 μm	7 cm	
	surface		300 mm^2	300 mm^2	300 mm^2	300 mm^2	1250 mm^2	
	dist fr trg	556,5 mm	574 mm	574,5 mm	589,5 mm	590 mm	594,5 mm	
	solid angle		910,5 μsr	909 μsr	863,3 μsr	861,8 μsr	3537 μsr	
Arm 80°	detector	Si1	Si2	Si3-destroyed				
	thickness	56.3 μm	420 μm	5000 μm				
	surface	150 mm^2	150 mm^2	200 mm^2				
	dist fr trg	551 mm	567 mm	586 mm				
	solid angle	494 μsr	466 μsr	582 μsr				
Arm 100°	detector	Si1	Si2	Si3	Si4	steel layer	CsI	
	thickness	51.7 μm	401 μm	1000 μm	2012 μm	50 μm	7 cm	
	surface	150 mm^2	150 mm^2	150 mm^2	150 mm^2		1250 mm^2	
	dist fr trg	508 mm	523 mm	546 mm	557 mm	770 mm	782,5 mm	
	solid angle	581 μsr	548 μsr	503 μsr	483 μsr		2041 μsr	
Arm 120°	detector	MCPSt	MCPSp	BCD	Si1	Si2	steel layer	CsI
	thickness	90 μg/cm^2	90 μg/cm^2	22 cm	150 μm	500 μm	50 μm	7 cm
	surface	250 mm^2	250 mm^2	320 mm^2	900 mm^2	900 mm^2		1250 mm^2
	grid transp.	88,25%	77,94%	74,6%	74,6%	74,6%		
	dist fr trg	615 mm	1155 mm	1460 mm	1736 mm	1747,5 mm	1843 mm	1850,7 mm
	solid angle	661 μsr	187 μsr	150 μsr	299 μsr	295 μsr		365 μsr
	active s.a.	583 μsr	146 μsr	117 μsr				

where Z, A, and E are the atomic number, the mass number, and the energy of the particle, respectively.

Let us consider the telescope built of two silicon detectors of such a thickness that the registered, charged particle of energy E is able to punch through the first detector - depositing the energy ΔE_1, and is stopped in the second detector, thus depositing energy $\Delta E_2 \equiv E - \Delta E_1$. Presentation of all detected particles on two-dimensional diagram; ΔE_1 versus $\Delta E_1 + \Delta E_2 \equiv E$, allows to select the particles with given (A, Z) values because the points representing such particles should be concentrated along the hyperbola $const(A, Z)/E$. Furthermore, the hyperbolas corresponding to different values of the atomic number Z for a given mass number A should be separated by larger distances in the picture than the hyperbolas which represent particles with the same Z number but different mass numbers A. This fact, which is due to the relation $const(A, Z) \sim AZ^2$, is well visible in Fig. 5.5. The groups of curves corresponding to different elements: H, He, Li, etc., i.e., different Z numbers: 1, 2, 3 ... are well separated, whereas the distance between the curves inside the same group (corresponding to isotopes of the same element, thus differing only by the mass number A) is much smaller.

What happens, when the energy of the detected particle is large enough to punch through both detectors of the telescope ? In this case deposit of the energy of the particle in the second detector ΔE_2 is smaller than $(E - \Delta E_1)$ what means that the sum $\Delta E_1 + \Delta E_2$ is smaller than total energy of the particle E.

Hence the vertical position of the point representing the particle on the two-dimensional plot is not disturbed but the horizontal position is false - smaller than that corresponding to the total particle energy E. Thus, starting from the threshold energy of the particle E_{thr}, which is equal to its minimal energy allowing to punch through the both telescope detectors, the hyperbola is no longer good approximation to the observed $\Delta E_1 - (\Delta E_1 + \Delta E_2)$ dependence. This effect is also well visible in the lower part of Fig. 5.5. The curves which correspond to energies higher than the threshold energy mentioned above are usually strongly overlapping for various (A, Z) values and, therefore, it is quite difficult to identify the particles using this region of two-dimensional plot ΔE-E.

The (Z, A) identification of the particles can be done using the above discussed method even in the case when the height of signals from the detectors is given in arbitrary units. However, it is necessary to calibrate the height of signals in energy units if the data are to be presented in the form of energy spectra. A crude calibration of the signals can be done from knowledge of "punch-through energy" for each kind of particles, i.e., the threshold energy discussed above at which the particle punches through both detectors of the telescope, and from knowledge of energy ΔE lost by the particles in the first detector. This information can be obtained from known thickness of the silicon detectors and the energy dependence of the differential energy losses of given particles dE/dx in the silicon. Such a method of calibration relies on known energies of several specific points in the two-dimensional identification plot.

In the present study another method has been applied for energy calibration of the signals. Namely, the simultaneous fit of theoretically evaluated curves ΔE_1-ΔE_2 to all the experimental ones was done varying coefficients of the linear dependence between number of the channel representing the signal height and its energy. Such a fit could not be done automatically by standard method of searching for minimal chi-square value or by maximum likelihood method because of difficulty to assign proper weights to individual channels. This is, for example, caused by the fact, that the knowledge of $dE/dx(E)$ values is significantly poorer for some isotopes, as e.g. ^{9}Be, than

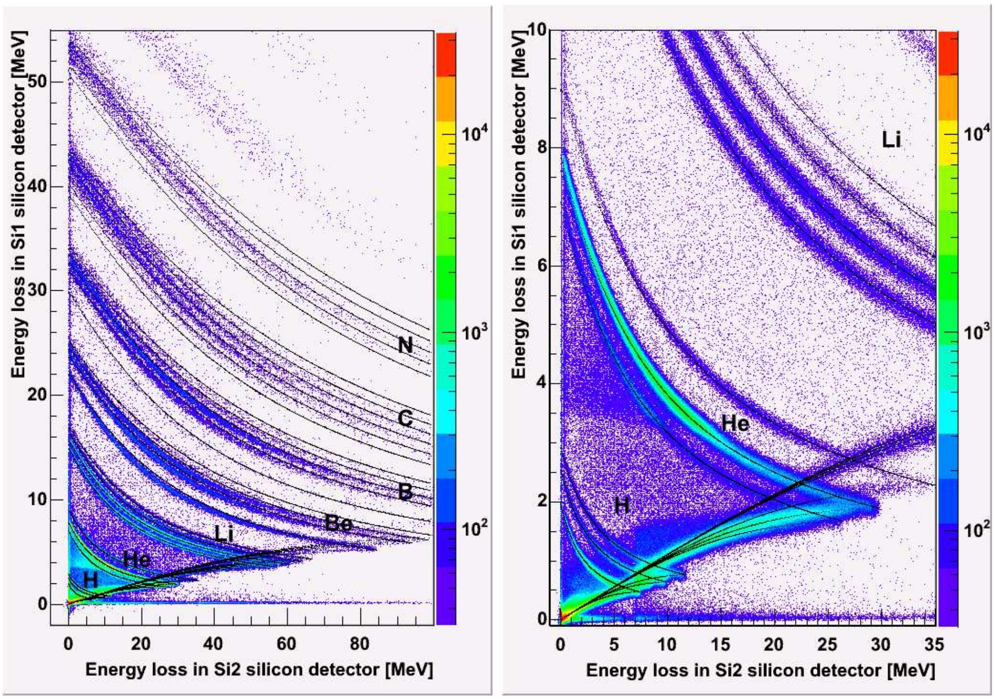

Figure 5.5: Example of identification plot ΔE_1-ΔE_2 for the first pair of silicon detectors placed at the scattering angle 35° in respect to the beam direction. Different colors are attributed to different ranges of number of counts stored in channels (ΔE_1, ΔE_2). Left picture corresponds to small and the right to large amplification of the detector signal.

for other particles (see appendix B.1.1). Therefore the quality of the agreement between theoretical and experimental curves was judged using subjective opinion which treated all the points on the approximately equal footing.

5.2.2 Silicon+CsI telescopes

The detector telescopes built of the silicon detector and the scintillator - cesium iodide detector activated with thallium CsI(Tl) - operates according to very similar principle as the telescope consisted of silicon detectors. The main advantage of using scintillator detector instead the silicon one is possibility to built very thick scintillator detectors what allows to stop energetic particles. The thinner, transmission silicon detector is placed in front of the scintillator in the telescope.

The cesium iodide is an inorganic scintillator with undeniable advantage of high density ≈4.53 g/cm^3 (therefore it has a high stopping power) and high unfailing. Drawback of using it is nonlinear light response for energy deposited in the CsI crystal.

The quenching of light output from charged particles in the scintillator has been associated with specific dependence of light production dL/dx on the charged particle energy loss dE/dx.

For example, Birks [21] proposed the following form of this dependence:

$$\frac{dL}{dx} = \frac{S(dE/dx)}{1 + [kB(dE/dx)]},$$

where S is the scintillation efficiency and kB the quenching factor. According to Horn et al. [69] the foregoing dependence can be integrated providing in good approximation the following equation for the light output L as a function of the energy of detected particles E :

$$L = a_0 + a_1 \left\{ E - a_2 A Z^2 \ln \left| \frac{E + a_2 A Z^2}{a_2 A Z^2} \right| \right\},$$

where a_0 represents the zero offset of the electronics, a_1 is product of the scintillator efficiency and the gain factor from the electronics, and a_2 corresponds to the quenching factor. Values of the a_2 parameter obtained in this paper are different from those in other publications, for example in [48], what means that this parameter can be different for different detector geometry and readout system. Of course, values of the a_0 and a_1 parameters depend on the setting of the electronics in individual experiments.

Calibration quality can be judged from comparison of experimental two-dimensional spectra - the signal from the first detector of the telescope (Si detector) versus signal from the CsI detector for all detected particles - with the lines representing dependence of these two signals predicted by the formula.

In Fig. 5.6 such a two-dimensional spectrum is presented to show the quality of achieved calibration of the detectors. The signal ΔE_1 from the silicon detector is a linear function of the particle energy (as it was discussed in the previous section) whereas the signal from the scintillator detector L depends on the energy of the particle via expression (5.2). Black lines correspond to predicted energy loss with adjusted values of the parameters whereas the density of points in the figure (represented also by different colors) indicates the occupation of the L-ΔE_1 plane by values of the experimental signals for various detected particles. The formula:

$$L = a_0 + a_1 \left\{ E - \varepsilon(A, Z)\, a_2 A Z^2 \ln \left| \frac{E + a_2 A Z^2}{a_2 A Z^2} \right| \right\}, \tag{5.2}$$

differs from the previous one by the correction factor $\varepsilon(A, Z)$, which takes into account the fact that the quenching factors are not identical for different detected particles. The a_0, and a_1 parameters were fixed at values specific for individual detectors whereas the parameter $a_2 = 75$ MeV was the same for all detectors and particles. The correction factor $\varepsilon(A, Z)$ had the following values for different particles:

$\varepsilon_p = 2.1$ for protons,

$\varepsilon_{d,t} = 2.0$ for deuterons and tritons,

$\varepsilon_{\mathrm{He}} = 1.8$ for He isotopes.

The need to introduce the correction factor $\varepsilon(A, Z)$ to properly reproduce the experimental two-dimensional spectra from Si - CsI(Tl) telescopes was also reported by Letourneau, which used the same telescopes in a previous experiment [88]. As can be seen, very good agreement of the experimental and predicted spectra was achieved.

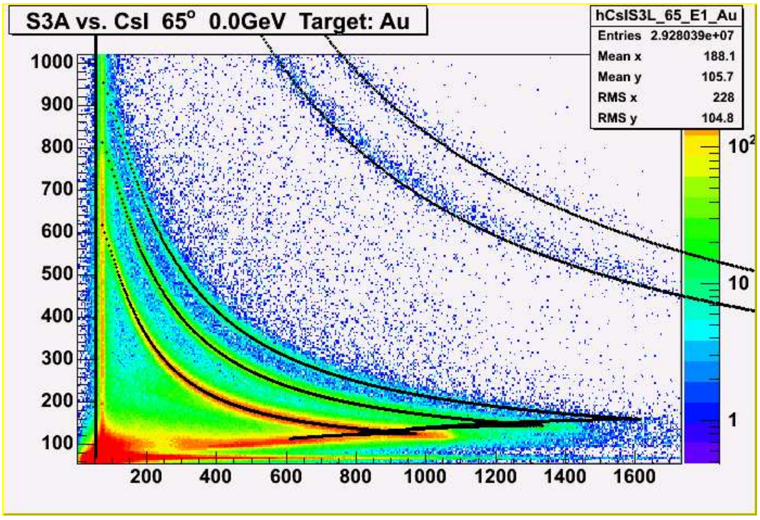

Figure 5.6: The illustration of the calibration quality for the telescope consisted of the pair of 1mm thick silicon detector and 7cm thick CsI(Tl) detector. The black lines depict the energy losses evaluated with assumed calibration and the colored points represent experimental data. The legend of colors corresponded to number of counts in the bin is shown on the right hand side of the figure.

The application of the thick scintillator detector as the last detector of the telescope was dictated by request to detect and identify the ejectiles in possibly broad energy range. The specific construction of the scintillator detector together with the fact that signals from scintillator have very different time characteristics in comparison to silicon detectors enables to well distinguish the particles of the highest energy stopped in the detector from those which punched through the detector (for details see text below). This is not easy for the silicon detectors because the signals from the preceding and the following detectors of the telescope - corresponding to both kinds of particles - are positioned very closely in the two dimensional ΔE-E plot and there is no possibility to use the time characteristics of the signals to distinguish them. Such property of the scintillator detectors - besides possibility to use thick scintillators - is appealing for using them in the detector telescopes.

The scintillator detectors used in the telescopes of the present experiment are built of inorganic scintillating crystal - cesium iodide activated by thallium (CsI(Tl))- and of the silicon photodiode placed behind the detector. The scintillator is characterized by two decay time constants ≈0.5 μs, and ≈ 7 μs [141], which are orders of magnitude longer than time constants typical for silicon detectors. The main goal of the silicon photodiode is to give the appropriate fast signal as an answer to the light emitted from the crystal. However, if the particle punches through the scintillator and hits the photodiode, an additional impuls appears - induced by this particle in the photodiode. Since the average decay time of the scintillator is much longer than the time characteristic for the photodiode, this additional signal appears earlier than (or simultaneously with) the impuls which is induced by the light from the scintillator.

Using the fast signal from the thin silicon detector of the telescope as the time reference signal, it is possible to clearly distinguish the photodiode signal, which was caused only by the light from the scintillator, from signals which were caused by the particles passing through the scintillator and hitting the photodiode.

5.3 Electronics setup and data acquisition in PISA experiment

The goal of PISA experiment was to simultaneously measure $\frac{d\sigma}{d\Omega dE}$ for different reaction products, with the yield varying by more than four orders of magnitude - from the most abundant protons to particles as rare as ^{9}Li or ^{10}Be. The time of such measurements must be quite long because it is determined by the condition to obtain satisfactory statistics for the least abundant ejectiles. Furthermore, not all from the detected, least abundant particles can be stored because other particles, detected together with them, compete in occupation of the data acquisition system causing a large dead time. Hence the time of measurement must be even longer than that which is estimated from the production cross section for the least abundant particles. A separate measurement of the cross sections for individual types of the ejectiles might be performed to avoid elongation of the measurement time by the above effect of competition of different products in access to the data acquisition system. This solution is, however, not acceptable with regard to very long total beam time necessary for such an experiment. Moreover, the conditions of the experiment (as e.g., the target thickness or the beam quality) could be changed during such a long measurement and thus the obtained results would be biased by different systematic errors for different ejectiles. Another solution of this problem was realized in the PISA experiment: The signals from the most abundant particles were on-line identified and prescaled, i.e., only one per k signals corresponding to these particles was allowed to be sent to data acquisition system whereas each signal from the less abundant particles was accepted for this purpose. This procedure reduces k-times the statistics for most abundant events, thus brings near the relative statistics for all ejectiles and simultaneously assures the same experimental conditions for the measurement of the cross sections for all particles.

It was necessary to find the measured quantity which could serve for easy selecting the events corresponding to the largest yields of the ejectiles. It is known from the literature (see section 7.3) that the yield of the reaction products may be approximated by the power low $\sim A_F^{-\tau}$, where A_F denotes mass number of the product and τ is the power exponent with typical value of $\sim 2-4$. This means that the most abundant are the LCPs - the hydrogen and helium isotopes. These lightest particles have also the smallest charge number and therefore they evoke the smallest energy loss, hence the smallest signal in the detectors. Thus the number of particles which give the smallest signal in the detectors should be prescaled.

As it was discussed in the sections 5.2.1 and 5.2.2 the identification of particles in the telescope built of semiconductor detectors (or semiconductor plus scintillating detector) is done by means of two-dimensional coincidence spectra - signal from the preceding detector versus signal from the following detector. On Fig. 5.7 such a two-dimensional plot is shown as an example, for the first pair (left panel) and for the second pair of silicon detectors of the telescope (right panel). The horizontal lines denoted by **L1** and **H1** in the left panel present lower and upper limit, respectively, of the signals attributed to the LCPs which were selected to be prescaled before storing the data by the acquisition system. The horizontal lines **L2** and **H2** in the right panel represent these limits for the second pair of detectors. The dashed, vertical line denoted by **L2** in the left panel corresponds to the horizontal line **L2** in the right panel.

The **L1** and **L2** limits were set on such a low level, which assures rejection of the electronic noise without losing significant number of signals from the particles. Furthermore the **L1** limit was positioned highly enough to cut small signals corresponding to LCPs which punched through the second detector. This was done to avoid the overloading of the electronics by abundant signals which would be further not used in data processing. The **H1** and **H2** limits were put high enough

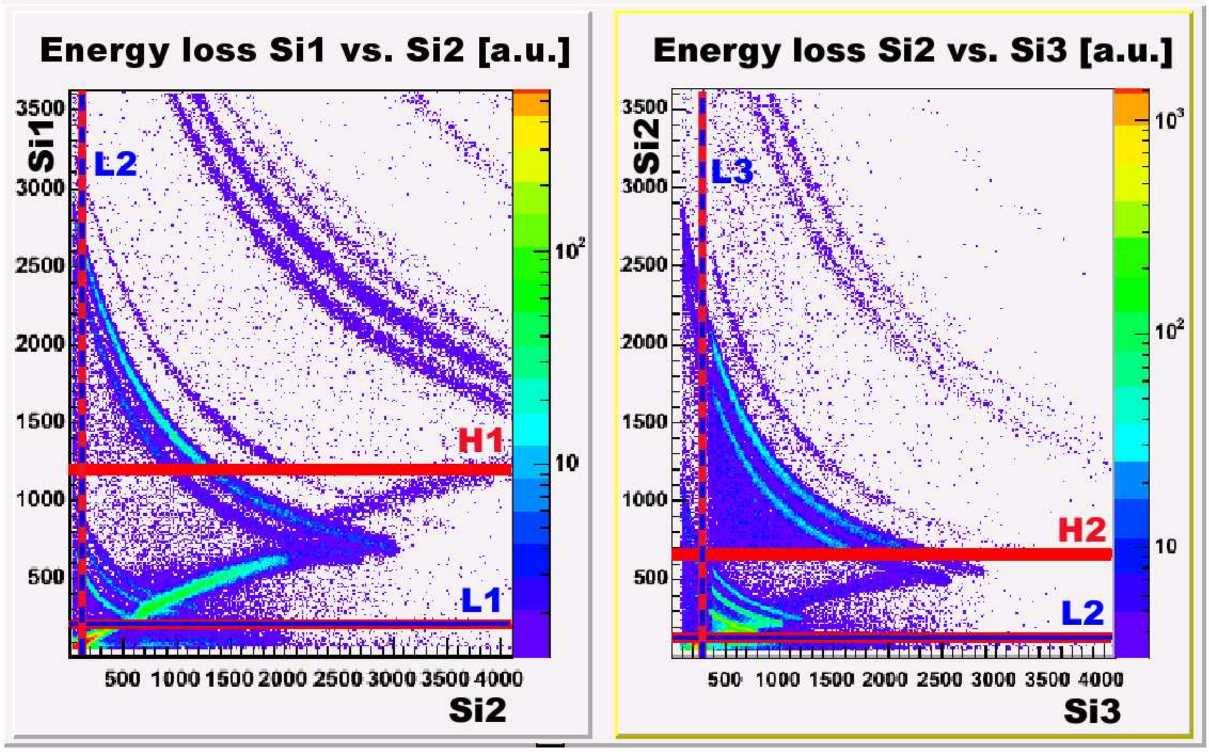

Figure 5.7: Two dimensional plot - signal from the preceding vs signal from the following silicon detector in the telescope; from the first vs the second and from the second vs the third, in the l.h.s. part and in the r.h.s. part of the figure, respectively. Lines correspond to different thresholds used for the first detector in the l.h.s. part of the figure and for the second detector in the r.h.s. part. Events with signal above the lower threshold **L** and below the higher threshold **H** were prescaled.

to include all events from the hydrogen isotopes and simultaneously as low as possible to minimize number of events corresponding to the helium isotopes. The setting of corresponding levels was realized in the experiment by splitting the signal from the detector into two branches and putting them in separate discriminators, where two individual threshold levels **L** and **H** were set.

The logical signals from the discriminators will be named in the present section according to the following rule: the name **Si1L** (**Si1H**) is attributed to such signal from the detector **Si1** which is higher than level **L** (**H**), etc. The signals which fulfill the condition **Si1H**$\wedge$**Si2L** - placed above the horizontal line **H1** and to the right from the vertical line **L2** in the left panel of the Fig. 5.7 - should not be prescaled, whereas those with the property **Si1L**$\wedge$**Si2L** - placed above the horizontal line **L1** and to the right from the vertical line **L2** on this figure - should be prescaled. Since all the signals, which fulfil the condition **Si1H**$\wedge$**Si2L**, accomplish also the condition **Si1L**$\wedge$**Si2L**, the information on both logical signals **Si1L**$\wedge$**Si2L** and **Si1H**$\wedge$**Si2L** has to be preserved and stored to further data analysis.

The dead time of the electronics effects that not all particles hitting the detectors can be registered. To determine full number of particles it is necessary to know how many particles were not recorded. Usually, the information from scalers about number of counts is sufficient to reconstruct precisely real number of particles. However, it is important to know if the stored event was trig-

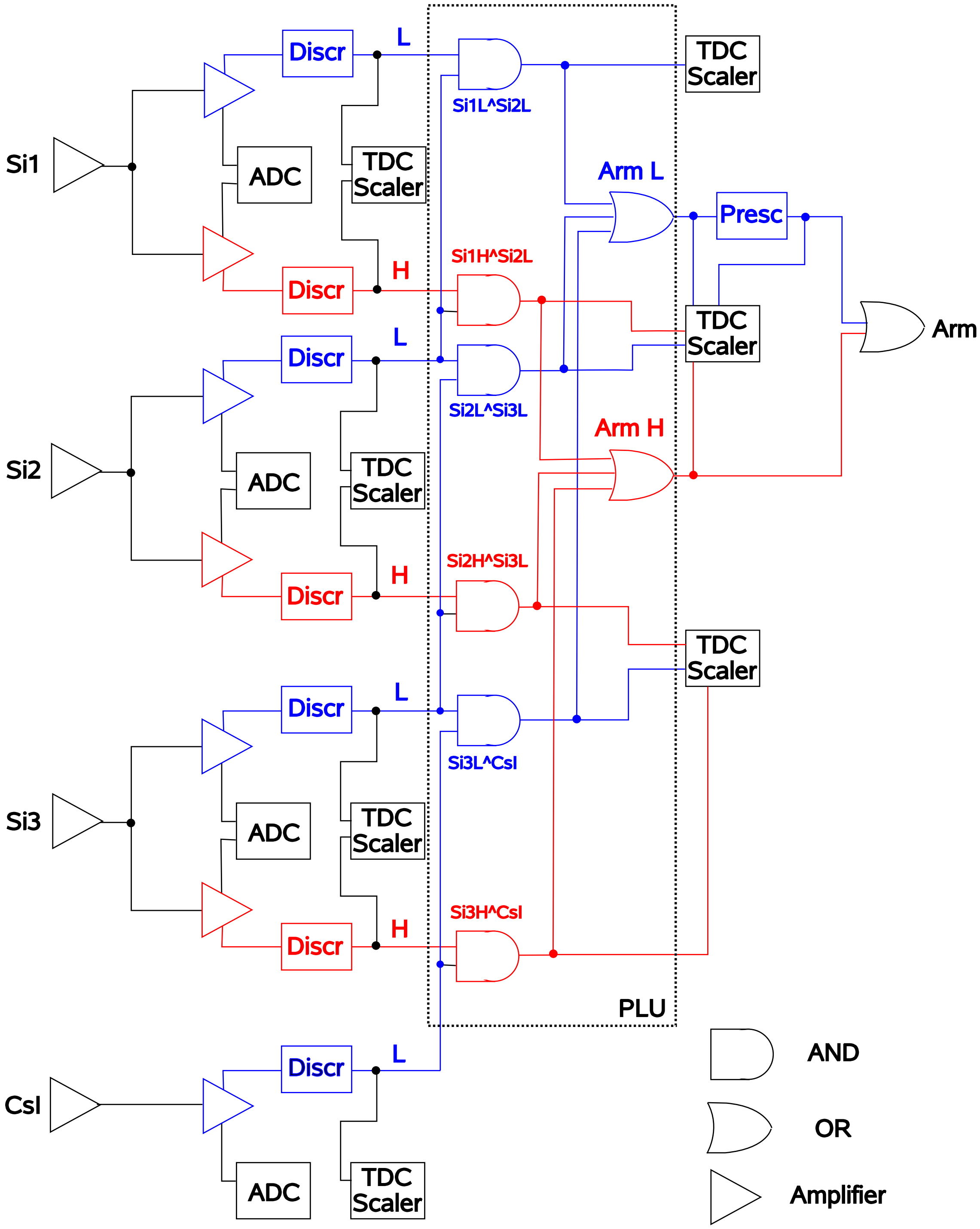

Figure 5.8: Logic circuit of electronics in one of the Pisa detection arm. With blue and red colour are marked prescaled and no prescaled branches respectively. More detailed information are in text.

gered by not prescaled branch or by prescaled one for given detector pair. To precisely define what sort of information was stored in the PISA experiment, the scheme of logic setup for one detection arm is shown in Fig. 5.8. The detector telescope placed in this detector arm is consisted of three silicon detectors; **"Si1"**, **"Si2"**, and **"Si3"** and the thick scintillator detector **"CsI"** - represented in the Fig. 5.8 by their symbols.

Let us follow the way of the signal induced by the particle in the **"Si1"** detector. The signal from the detector is amplified by the preamplifier and then it is split into two signals, which enter two separate electronics branches shown in the figure by the red and blue symbols, respectively. The splitting of the signal allows for:

(i) setting different levels of discrimination in each branch (the **"L"** and **"H"** levels),

(ii) setting two different amplifications on analog signal from each detector.

The former subject will be described here, leaving the latter for further discussion. The analog signal after preamplifier is passed to the amplifier, which provides two amplified signals - with the fast and with the slow rising time. The signal with the slow rising time, is read out by ADC (Analog Digital Converter) and that with the fast rising time is passed to discriminator. The amplitude of the signal, amplified with the slow rising time is characterized by very good linear dependence on the input signal and hence it is implemented to give information on the energy loss in the detector. The signal amplified with the fast rising time is used to get logical signal from the discriminator when the height of the signal is larger than fixed level of discrimination, and provides also very well determined information on the time, when particle hits the detector.

Logical signal from the discriminator (in each electronics branch) is split by means of the fan-in fan-out module into three signals. Two of them are passed to the TDC (Time Digital Converter) and to the scaler modules whereas the third is sent to the Programable Logic Unit (PLU). It is important to note, that the black rectangles on the Fig. 5.8 denoted by **TDC**, **scaler**, and **ADC** are used as a *single* symbol to represent *all* the corresponding modules reacting independently on each incoming signal. The information provided by these modules is written as a part of the information characterizing a given event.

The TDC information is stored for all signals recorded by the data acquisition system whereas the scalers count number of all events corresponding to detected particles even if they are not stored by the data acquisition system.

All logic gates defined in the Programable Logic Unit (PLU) are positioned on the Fig. 5.8 inside the rectangle drawn by the dotted line. Coincidences of detector signals with the lower and the higher thresholds are described as e.g., **Si1L∧Si2L**, and **Si1H∧Si2L** - using blue and red color, respectively. It should be noted that information on the presence of such coincidences is also put on the TDC modules and is written as a part of the information characterizing each stored event.

Coincidences of signals from all neighboring detectors with low (high) thresholds are connected by OR gate and are described as **Arm L** (**Arm H**), respectively. Signal from coincidences with low threshold **Arm L**, is passed on the prescaler and then split to TDC, scaler module and as an input to the OR gate, where together with signal from coincidences with high threshold **Arm H** builds logic signal **Arm**. This signal informs that the particle detected by given telescope should be recorded. Such signals from all detection arms were sent to the OR gate and used as a trigger to the data acquisition system. Time information from TDCs allows to precisely determine which pair of detectors triggered concrete event, and which of the registered events were prescaled. This information allows to properly build off-line the energy spectra for all particles.

The data acquisition system used in the PISA experiment was discussed in detail in the Ref. [30], therefore description of this system is skipped in the present thesis.

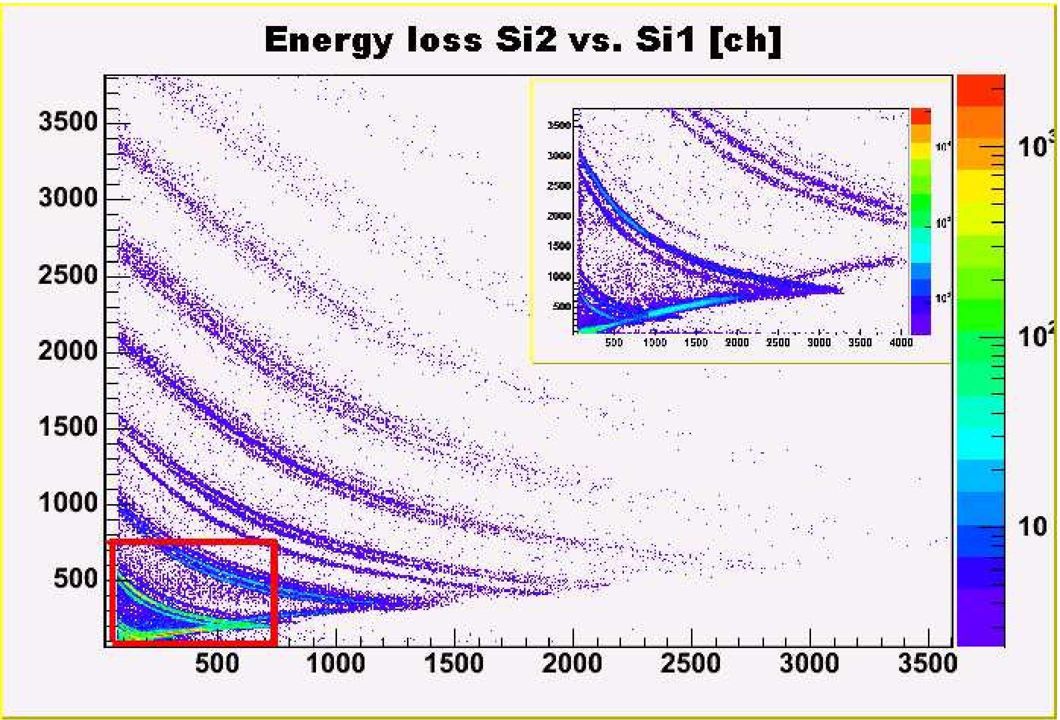

Figure 5.9: Two different amplification for silicon detector, allowing to measure ejectiles in wide range of mass and simultaneously measured individual isotopes of hydrogen with good energy resolution.

As it was stated above, a splitting of the detector signal, performed just after preamplifier, allows to use two different amplifications of the signal. It was possible to measure light particles with high energy resolution ,because large amplification allows to increase height of small signals - characteristic for LCPs - to occupy full range of signals accepted by ADC. On the other hand the need to measure as many as possible IMFs was realized by using small amplification of the signals. Then the analog signal which is the largest for such ejectiles like Nitrogen or Oxygen was small enough to be accepted inside the input range of the ADC.

On Fig. 5.9 the effect of two different amplifications for the same pair of detectors is illustrated. The main figure presents two dimensional spectrum obtained with small amplification of the signals from the detectors. The part of this figure, marked by the red rectangle in the left, bottom part of the main figure, is presented - after using of high amplification of detectors - in the right top corner of the main figure. It is evident that high amplification allows to perfectly resolve Li, He and even hydrogen isotopes, whereas in the main figure the resolution is poorer, however, the broader range of elements and isotopes of measured particles (from H to O isotopes) is visible due to the smaller amplification.

In the PISA experiment two amplifications and two thresholds had been adjusted for each detector. This adjustment, especially the setting of appropriate thresholds, could be only done during measurements, when coincidences of real signals from the detectors inside the telescope were available.

Moreover, the adjustment should be done for each pair of detectors separately. This leads to quite long procedure which has to be performed during the beam time and thus should be shortened as much as possible.

The serious problem which slows down and makes difficult the adjustment of thresholds and amplifications is the presence of abundant signals evoked by LCPs which punched through both detectors. They are not important for tuning of the pair of detectors under investigation but compete with the proper signals in access to ADCs and logical units. To avoid this problem and speed up the adjustment procedure a dedicated input-output interface was written as Tool Command Language (TCL) script which allowed to properly and user friendly set logical conditions in Programable Logic Unit. Screen shot of its graphical input-output interface is presented on Fig.5.10. The program allowed to chose logical conditions which were equivalent to switching off the detector signals which were not important for tuning of thresholds and amplifications for selected detectors. All changes in settings of Programable Logic Unit were saved in the log file to check and analyze obtained results.

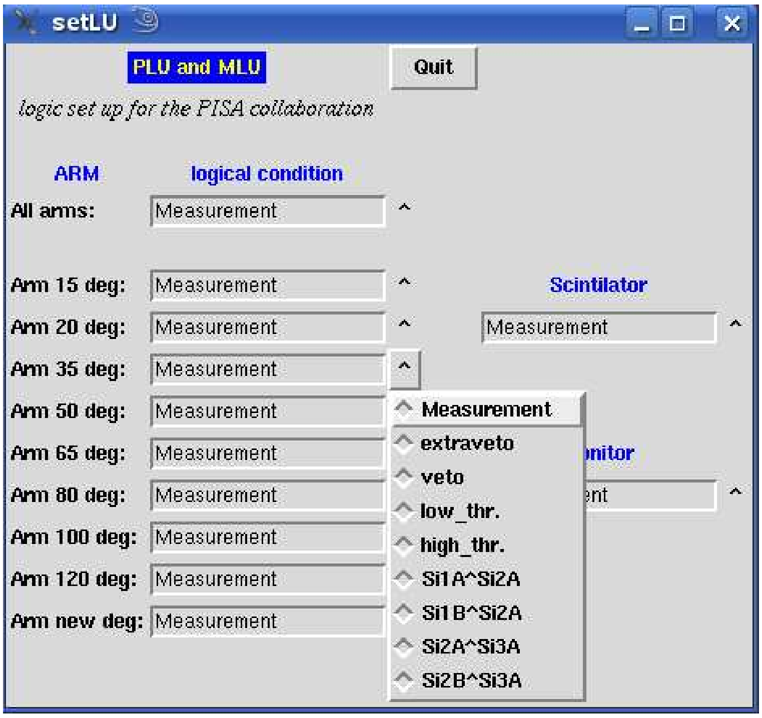

Figure 5.10: Screenshot of TCL-program written two set up logic condition in PLU for Pisa experiment and to accelerate and enhance procedure of finding amplifications and thresholds for detector signals. For further details see the text.

5.4 Absolute normalization

The straightforward method of normalization of PISA experimental data would be the comparison of presently measured double differential cross sections $\frac{d\sigma}{d\Omega dE}$ with absolutely normalized data, known from the previous experiments. In this case all unknown factors, which are difficult to be controlled during internal beam experiment, as e.g., the beam overlapping with the target, are automatically taken into account. As shown in the following paragraph, it was possible to apply such a procedure for the measurement at the lowest proton beam energy, i.e., 175 MeV, where the experimental $\frac{d\sigma}{d\Omega dE}$ results exist for reaction Ni(p,p') [50]. In case of measurements at higher energies such experimental data are not available in the literature. Thus, it was necessary to implement another method of absolute normalization of the cross sections. The following procedure has been used: The double differential cross sections $\frac{d\sigma}{d\Omega dE}$, measured in the present experiment for ^{7}Be ejectiles, were integrated over angle and energy to extract total production cross section of ^{7}Be, which was then compared with the known from the literature, absolutely normalized cross section of ^{7}Be production [32]. Details of the integration procedure and its accuracy are discussed below. It was checked for the lowest proton beam energy (175 MeV) that both methods give compatible results within 20%.

5.4.1 Normalization of data to proton spectra for 175 MeV proton beam.

In 1991 Förtsch et al. [50] measured $\frac{d\sigma}{d\Omega dE}$ for Ni(p,p') reaction using external beam of protons of 175 MeV energy. The energy spectra of protons were determined from 15° to 70° degrees in 5 degree steps, and for 80° , 90° , 100° , 120° . Thus it was possible to compare our data measured at exactly the same beam energy at several angles (15° , 20° , 65° and 100°) with those of Förtsch et al.. It was found that the shapes of all compared spectra agree very well and, moreover, the ratio of our data to those of Förtsch et al. is the same for all angles. Therefore, relying on the absolute normalization of the proton data of Förtsch et al., we were able to normalize cross sections for all products observed in our experiment.

Normalized proton data at 20° , 65° , and 100° from the present experiment are shown in Fig. 5.11 together with data of Förtsch et al. It is well visible, that the shape of spectra from both experiments agrees very well and the maximal deviation between energy spectra from both experiments is smaller than 15% for all angles.

The normalization factor α was determined by minimization of the following function Q^2 for each angle separately:

$$Q^2 \equiv \sum_i w_i \left(y_i - \alpha x_i\right)^2$$

where y_i and x_i represent double differential cross sections of Förtsch et al. and corresponding data from PISA experiment, respectively. The weights w_i were taken as squares of reciprocals of experimental errors from PISA experiment. The obtained values of the normalization factor α were then averaged over the angles to obtain the final result. The error of the final value of the normalization factor was estimated to be around 1 %.

As can be seen on Fig. 5.11 the proton cross sections used for normalization are almost constant for the full spectrum measured at 20° whereas they vary four orders of magnitude for larger angles. Such a large variation may influence value of the normalization factor α because the statistical weights are different for small and for large values of the cross sections. Therefore another normalization factor β was searched for by minimization of the following function:

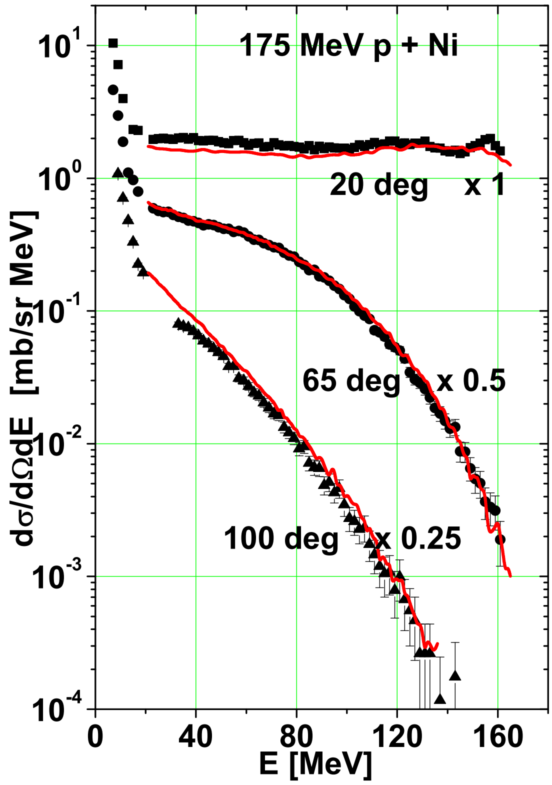

Figure 5.11: Proton energy spectra measured at 20° , 65° , and 100° in the laboratory system. Lines represent Förtsch et al. data from ref. [50], symbols depict the data from PISA experiment. The spectra were multiplied by factors written in the figure to avoid overlapping the spectra obtained at different angles.

$$P^2 \equiv \sum_i w_i \left(\frac{y_i}{x_i} - \beta \right)^2$$

where all the symbols have the same meaning as above. The error of the averaged over angles value of normalization factor β was estimated to be equal 3 %. Values of α and β normalization factors agree well inside the estimated statistical errors. The absolute value of the cross sections is of course additionally biased by the systematic error of the reference data used for normalization. Förtsch et al. estimated that the systematic error of their (p,p') data is about 10 %.

5.4.2 Normalization of data to total production cross sections of ^{7}Be ejectiles

Experimental energy spectra of ^{7}Be particles from the present experiment were fitted by a phenomenological formula of single moving source, emitting isotropically these ejectiles. The detailed formulation of this model and interpretation of the parameters are given in the Appendix A. One of the parameters, i.e., σ is equal to angle and energy integrated $\frac{d\sigma}{d\Omega dE}$. Values of the parameters were searched for by simultaneous fit of the model predictions to the spectra measured at all scattering angles investigated in the present experiment. Very good description of all ^{7}Be spectra was achieved, assuring good interpolation of the data over energy and angle. The error of extrapolation of the data in the angular integration should be also negligibly small because of smooth variation of the data with the angle.

The main error of integration can appear due to inaccuracy in extrapolation of the $\frac{d\sigma}{d\Omega dE}$ to low, not measured energies of ^{7}Be where the cross sections may achieve large values. Unfortunately the detecting system used in the present experiment, i.e., telescopes built of silicon detectors, could not register very low energy particles. This was because the identification of such particles was done due to coincidence signal from the first and the second detector. Thus, the particles which were stopped in the first detector could not be identified. This lack of knowledge on low energy data can lead to ambiguities in extraction of the model parameters producing large error of the integrated cross section σ. The main factor influencing the total cross section is the height of the Coulomb barrier between the ^{7}Be ejectile and the residual nucleus.

Independent experimental information on the low energy part of ^{7}Be spectrum and, especially, on the position of the Coulomb barrier, could be found from experiments in which the inverse kinematics has been applied, i.e., the hydrogen target was bombarded by heavy ions. In such an experiment all ejectiles have high enough energy in the laboratory system to be detected. Therefore the part of the spectrum of ^{7}Be ejectiles, which corresponds to relative motion energy smaller than the Coulomb barrier between the ejectile and the residual nucleus, can be observed without any problem. Results of the recent experiment performed by CHARMS collaboration at 1 A GeV energy of ^{56}Fe beam on hydrogen target show that the experimental energy spectra of ^{6}Li, ^{12}C (cf. Fig 12 of Ref. [109]) and ^{7}Be, ^{9}Be [108] have Maxwellian shape with position of the maximum slightly below the simple estimation of the Coulomb barrier by the formula $Z_1 Z_2/(A_1^{1/3} + A_2^{1/3})$ MeV, where Z_1,Z_2 and A_1,A_2 are the atomic and mass numbers of the ejectile and residual nucleus, respectively.

The total cross sections for ^{7}Be emission, taken from the literature parametrization [32], were compared with the parameter σ of the phenomenological model of one moving source (see Appendix A), fitted simultaneously to spectra measured at all seven scattering angles in PISA experiment. The parameter k which determines the height of the Coulomb barrier in units of the simple estimation of the barrier height given above was fixed to be close to unity. Very good description of ^{7}Be data was obtained and the ratio of the obtained σ parameter to known values of the total production cross sections of ^{7}Be allowed for extraction of the absolute normalization of the data.

The accuracy of the absolute normalization has been estimated from the spread of the parameter values in equivalent quality fits to be of the order of 20 %.

5.4.3 Comparison of both methods of normalization

It is interesting to compare results of both methods of normalization, i.e., normalization to differential cross sections of (p,p') reaction and normalization to the total ^{7}Be production cross section. It was possible to perform such a comparison due to the fact that both kinds of data exist for proton induced reactions on Ni target at 175 MeV beam energy.

The present differential cross section data of ^{7}Be production at 175 MeV proton beam energy, normalized absolutely by the factor obtained from comparison of the present (p,p') data to the literature data, were fitted by phenomenological formula of one moving source to extract total ^{7}Be production cross section, i.e., σ parameter in milibarns. The observed deviation of this value of the total production cross section of ^{7}Be from that known from the literature [32] is approximately equal to 20%. This agreement may be treated as very good, taking into consideration the fact that both methods rely on very different cross sections, i.e., the proton and ^{7}Be production cross sections differ by orders of magnitude. It should be emphasized that the systematic errors of literature data are at least of the order of 10% both for the proton data [50] as well as for ^{7}Be data [32].

Taking into account the fact, that two different methods of normalization lead to variation of the absolute cross section of about 20% it is reasonable to conjecture, that the relative error of normalization for different beam energies should be even smaller. This is very important for our purposes because the subject of the present work was to study beam energy dependence of the reaction mechanism.

Chapter 6

Experimental data

In this Chapter the experimental data of the present study are discussed and compared with differential as well as total cross sections published in the literature.

The experimental data collected for p+Ni reactions in the present PISA experiment consist of a large amount of spectra. There are spectra for 16 various ejectiles: p, d, t, ^{3}He, ^{4}He, ^{6}He, ^{6}Li, ^{7}Li, ^{8}Li, ^{7}Be, ^{9}Be, ^{10}Be, ^{10}B, ^{11}B, C, and N) taken at 7 scattering (lab) angles (15° , 20° , 35° , 50° , 65° , 80° , 100°), and at 4 proton beam energies: 0.175, 1.2, 1.9, and 2.5 GeV - together almost 450 spectra. As far as we know, this is the largest set of differential cross section data available at present in the scientific literature for p+Ni reactions in this energy range.

6.1 Comparison of present data with literature cross sections

It is important to emphasize that the *differential* cross sections of proton induced reactions on Ni target are very scarce in the literature what causes that the straightforward comparison of present data with those from the literature is difficult. The only published, to our knowledge, differential data were obtained at 0.175 GeV beam energy for proton elastic and inelastic scattering by Förtsch et al. [50], at 1.0 GeV for production of ^{3,4}He and ^{6,7}Li by Volnin et al. [140], and at 3.0 GeV for production of ^{6,7}Li, ^{7,9,10}Be, and ^{10,11}B by Raisbeck et al. [117] .

The agreement of present data and those of Förtsch et al. for 0.175 GeV *proton scattering* on Ni target is excellent for both, energy and angular distributions as it was discussed in section 5.4.1 and presented on figure 5.11. Furthermore, it turned out that the absolute cross sections of both experiments are identical within the limits of error (cf. section 5.4.1).

The comparison of present differential cross sections measured for *other light ejectiles* at 0.175 GeV with the literature results can be done only indirectly, i.e., by using data obtained from experiments performed on targets with the mass number in the neighborhood of Ni, and/or at slightly different beam energies. This is reasonable to assume that the differential cross sections do not change strongly with variation of the target mass and beam energy. Following this assumption the ^{3,4}He and ^{6,7}Li data, obtained by Machner et al. [91] in 200 MeV proton induced reactions on Co target, were compared on Fig. 6.1 with the present data. The agreement of results from both experiments is excellent taking into consideration the difference in target mass, beam energy and detection angles of the particles.

In case of higher proton beam energies studied in this work the data on differential cross sections for *proton, deuteron and triton* production on Ni target are not available in the literature.

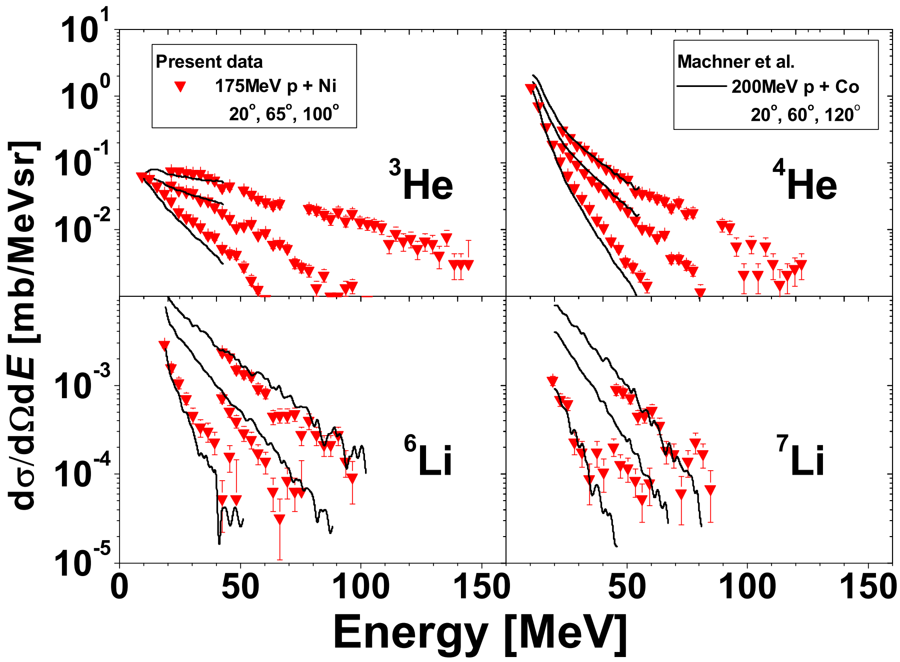

Figure 6.1: Comparison of double differential cross sections for ^{3}He, ^{4}He, ^{6}Li, and ^{7}Li particles measured at 20° , 65° , and 100° in the present study using 0.175 GeV proton beam interacting with Ni target (red triangles) and data from Machner et al. [91] determined in reaction of 0.2 GeV p+Co at angles 20° , 60° , and 120° (solid lines connecting individual points).

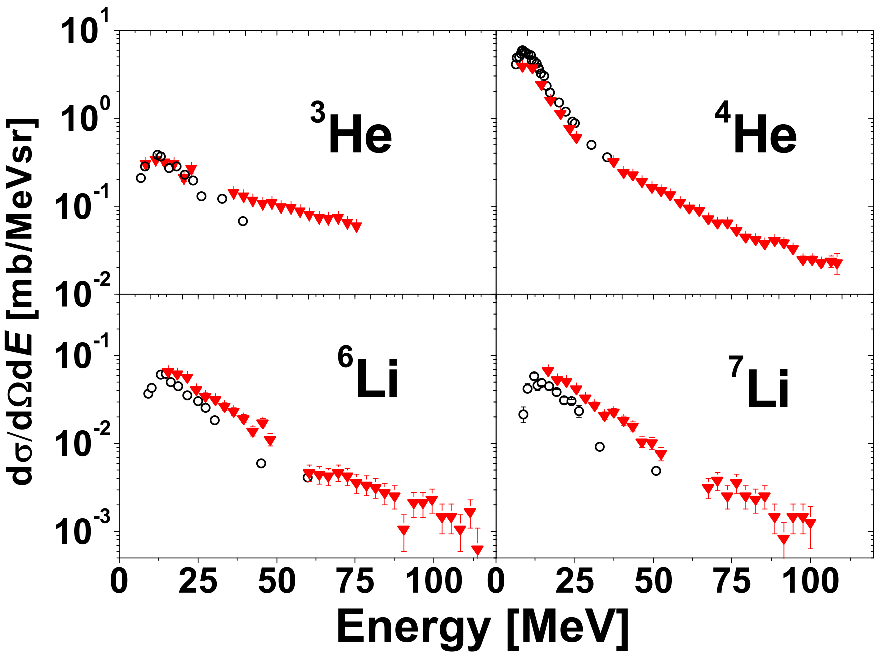

Figure 6.2: Spectra of ^{3}He, ^{4}He,^{6}Li, and ^{7}Li from p+Ni reactions measured at 50° in PISA experiment for proton beam energy 1.2 GeV (full triangles) compared with spectra from p+^{58}Ni reactions measured in Leningrad Institute of Nuclear Physics, Gatchina USSR [140] at 60° for proton beam energy 1.0 GeV (open dots). The Gatchina data were multiplied by factor 3.

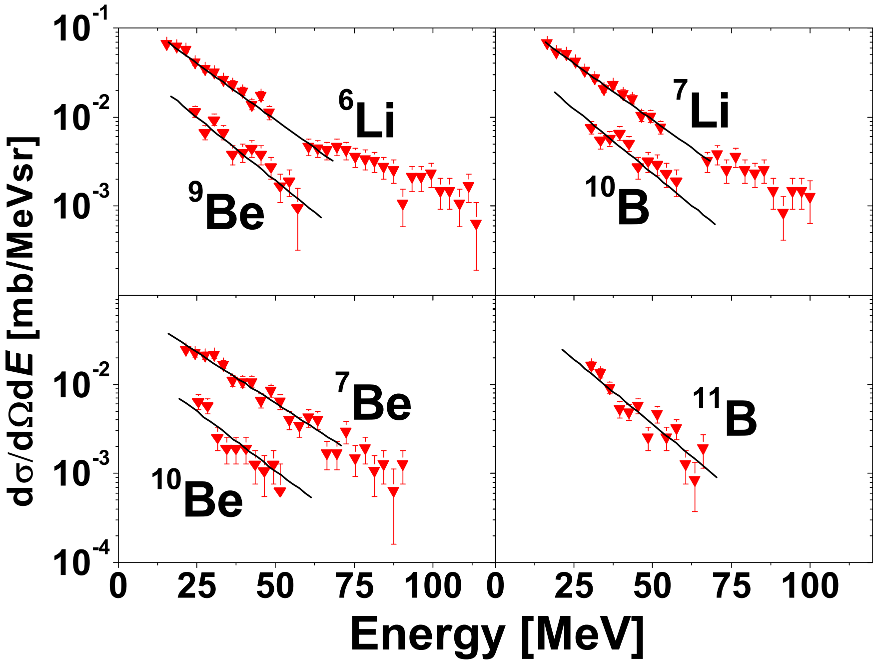

Figure 6.3: Spectra of ^{6,7}Li, ^{7,9,10}Be, and ^{10,11}B from p+Ni reactions measured at 50° in PISA experiment for proton beam energy 2.5 GeV (full triangles) compared with spectra from p+^{58}Ni reactions induced by 3.0 GeV protons, measured at 60° [117] (solid lines). Not normalized differential cross sections of Raisbeck et al. [117] were multiplied by common factor to be compared with absolutely normalized data from PISA experiment.

The production cross sections of He and IMFs were published by Volnin et al. [140] for spectra of ^{3,4}He and ^{6,7}Li from p+^{58}Ni reaction at 1.0 GeV proton beam energy as well as for spectra of ^{6,7}Li, ^{7,9,10}Be, and ^{10,11}B isotopes from p+^{nat}Ni by Raisbeck et al. [117] at 3.0 GeV. These literature spectra, measured at 60° are shown together with the present data, determined at 50° , on Figs. 6.2 and 6.3 for 1.0 and 3.0 GeV, respectively. The shape of the present spectra measured at 1.2 GeV agrees very well with shape of spectra determined at 1.0 GeV by Volnin et al. [140], however, the absolute cross sections from [140] are smaller by factor ∼3 than the present data. It can be conjectured that this is caused by wrong normalization in experiment of Volnin et al. since the present data fit well to other literature cross sections as will be discussed below (cf., e.g., Figs. 6.4 and 8.2). The shape of spectra from Raisbeck et al. [117] obtained at 3.0 GeV agrees perfectly with that of present spectra determined at 2.5 GeV as it is visible on Fig. 6.3. To make this comparison possible the not normalized spectra of Raisbeck et al. were multiplied by single factor, common for all ejectiles.

The agreement of the absolute values of the cross sections from the present experiment with literature data can be judged from comparison of total production cross sections which were more frequently measured than the differential cross sections. Such cross sections were published, e.g., by NESSI collaboration in paper of Herbach et al. [66] for 1.2 GeV proton beam energy and by Raisbeck et al. [117] for 3.0 GeV energy. The differential cross sections $\frac{d\sigma}{d\Omega dE}$ measured in the present study were integrated over energy of detected particles and over their emission angle in the way described in the next Chapter of the thesis to obtain total production cross sections.

The total production cross sections of H, He, Li, Be, and B isotopes from present experiment are depicted together with those from [66] on the upper panel of Fig. 6.4. As can be seen the agreement of data from both, completely different experiments is perfect. This is also true for agreement of present total production cross sections determined at 2.5 GeV and data of Raisbeck et al. [117] obtained at 3.0 GeV. Comparison of these data is shown on the lower panel of Fig. 6.4.

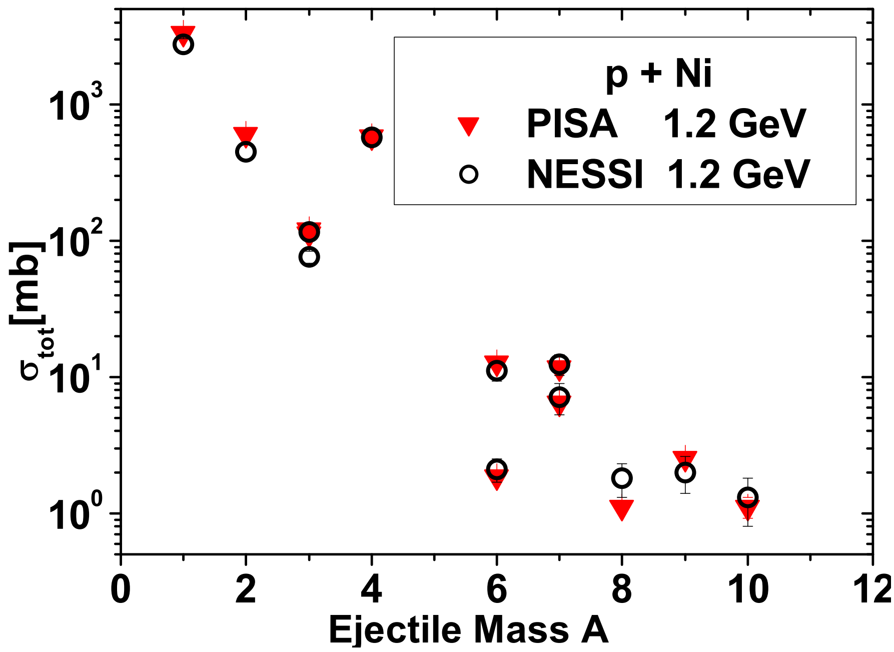

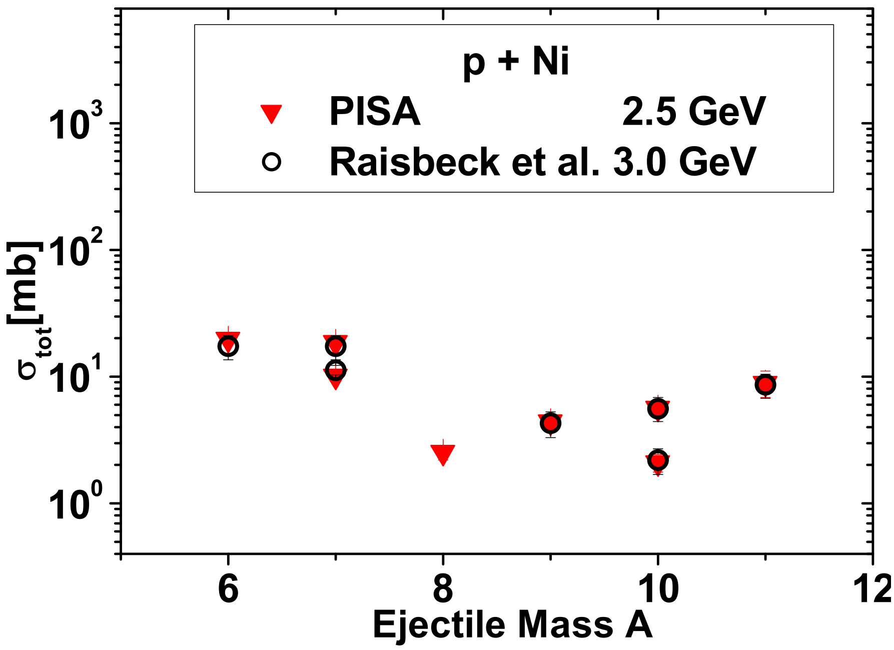

Figure 6.4: Top panel: Total production cross sections for 1.2 GeV proton induced reactions on Ni target measured by PISA collaboration (red triangles) and those obtained by NESSI collaboration (open dots) [66]. Bottom panel: Total production cross sections determined by PISA collaboration for 2.5 GeV proton induced reactions on Ni target (red triangles) and cross sections obtained by Raisbeck et al. [117] for 3.0 GeV (open dots).

6.2 Qualitative discussion of properties of the present data

To assure that the discussion of properties of the data is not overloaded with to many figures a selected subset of the data is presented below. The selection is based on the observation that:

- *The shape of the spectra is almost the same for given ejectile when measured at high energies: 1.2, 1.9, and 2.5 GeV, however, it is different for lowest energy 0.175 GeV*. Thus, presentation of the energy variation of the spectra must be done by showing the lowest beam energy data and at least one of the high energy data. Here, the data measured at 1.2 GeV and 2.5 GeV are used together with 0.175 GeV spectra.

- *The shape of the spectra varies in monotonic manner when the scattering angle increases.* Therefore, showing the spectra at three selected angles assures good illustration of the behavior of the data. Hydrogen and helium isotopes are not so strongly ionizing the matter as the intermediate mass fragments (Li, Be, and B isotopes). It was, therefore, appropriate to choose for the presentation of light charged particles the thickest telescopes to guarantee that broad energy range is present in the spectra. Of course, these telescopes assure deposition of even larger range of the energies of IMFs, however the thickest telescopes - placed at 15.6° , 20° , and 65° were positioned outside the scattering chamber, behind thin foil of stainless steel, which was used to separate high quality vacuum of the scattering chamber from the air under atmospheric pressure. The foil causes quite large energy losses for IMFs while being almost transparent for LCPs. Thus, the telescopes placed at 20° and 65° were found to be the most adequate for presentation of spectra for hydrogen and helium isotopes, whereas the spectra for heavier ejectiles are shown at 35° , 80° scattering angles where thinner silicon telescopes were present, however, without the steel foil in front of them. The third scattering angle chosen for the presentation was 100° , where thick telescope was positioned straightforward in the vacuum of the chamber, thus it assures low energy threshold and broad range of the deposited energies for all ejectiles.

To check, whether the angular and energy dependence of the differential cross sections agrees with predictions of the conventional two-step model the theoretical cross sections are presented for comparison in the same figures as the experimental data. The fast stage of the reaction has been described as the intranuclear cascade of nucleon-nucleon collisions which results in emission of fast nucleons and light charged particles created by coalescence of the nucleons. The calculations have been done by means of the INCL4.3 program of Boudard et al. [29] using default values of the parameters recommended by the authors. The slow stage of the reaction has been treated as evaporation of the particles from equilibrated residuum of the fast stage of the reaction. The calculations have been done in the frame of the statistical model by means of the GEM2 computer program of Furihata [52, 54] applying also default values of the parameters [53].

6.2.1 Light charged particles

The data and results of calculations obtained in the frame of the conventional two-step model are shown in Figs. 6.5 (for p, d, and t) and in 6.6 (for ^{3}He and ^{4}He) as symbols with the error bars and the solid lines, respectively. The lines oscillate at larger energies, because there the statistics of theoretical results obtained by means of Monte-Carlo calculations becomes low. The spectra are multiplied by factors 1, 0.1 and 0.01 for angles 20° , 65° , and 100° , respectively, to separate them well in the figures.

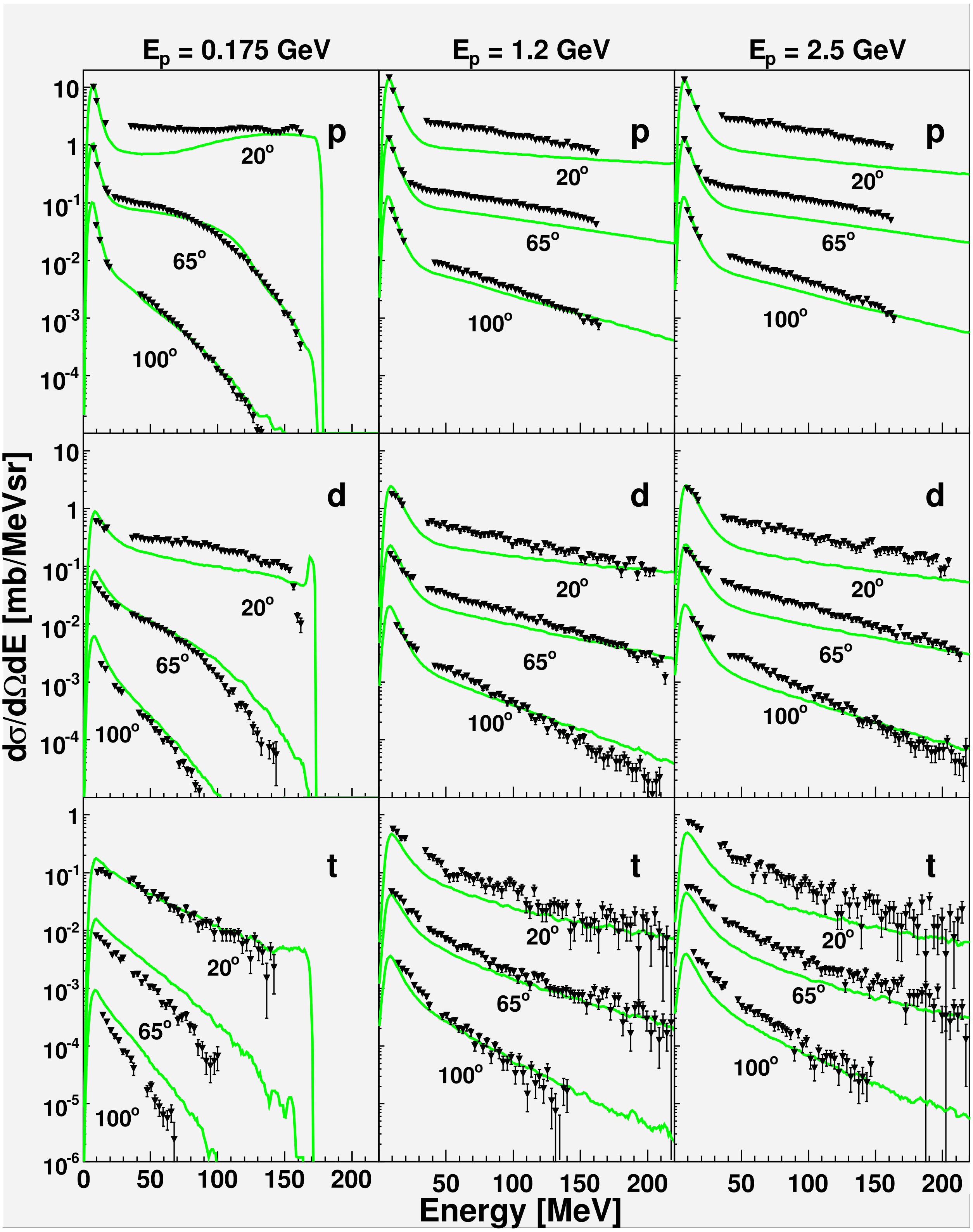

Figure 6.5: Experimental spectra (symbols) and results of two-step conventional model (lines) for protons (upper part), deuterons (central part) and tritons (lower part) for three selected angles 20° , 65° , and 100° . The left column presents the cross sections at lowest beam energy - 0.175 GeV, the central column at 1.2 GeV, and the right column the cross sections at 2.5 GeV

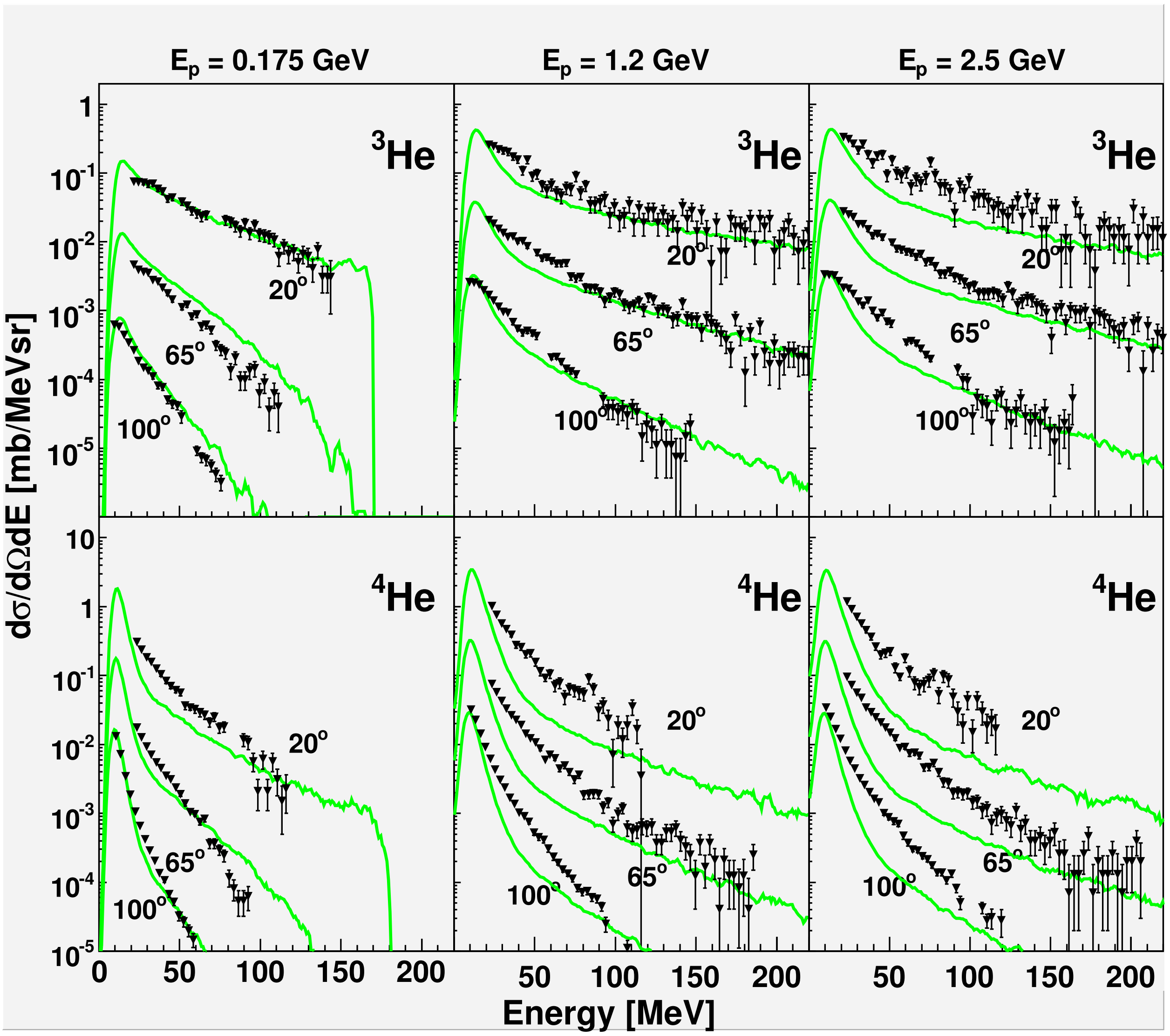

Figure 6.6: Same as in Fig. 6.5 but for ^{3}He (upper part) and for ^{4}He (lower part)

It is evident from inspection of the figures that the spectra demonstrate the presence of two different components for all LCPs, at all angles, and at all beam energies:

- Low energy part of the spectra is almost independent of the detection angle. It has a Gaussian shape with very similar position of the maximum and its height for all scattering angles. One can thus conjecture, that such an isotropic component is due to evaporation mechanism from the excited, equilibrated nucleus.
- The cross sections of tritons, ^{3}He and ^{4}He, at energies above this low energy region, decrease in approximately exponential way for all scattering angles. The slope of the exponential functions increases significantly with increasing scattering angle, thus this part of the spectra is clearly anisotropic. This anisotropic component of the spectra originates from some fast, non-equilibrium process.

In the two-step model it is assumed that fast nucleons are emitted from the nucleon-nucleon collisions during the intranuclear cascade whereas the coalescence of the nucleons with similar position and momentum is responsible for the emission of the high energy composite light charged particles [29]. It is visible on the Figs. 6.5 and 6.6 that, *the two-step model reproduces qualitative properties of the spectra of LCPs produced in broad range of proton beam energies from 0.175 GeV up to 2.5 GeV for p+Ni reactions. However, the quantitative reproduction of the data is not satisfactory and it deteriorates with increasing of the beam energy.*

All the data at 2.5 GeV beam energy are underestimated by the model calculations by factor 2 - 5 whereas at lower energies the differences are smaller. It is also evident that the angular dependence of the experimental spectra is different than that of the theoretical ones. With exception of protons at the lowest beam energy, all the experimental cross sections decrease with the angle faster than the theoretical calculations. *Such a behavior may be treated as an indication, that the two-step model does not take into account some significant non-equilibrium process which gives mainly contribution to forward scattering angles and its significance increases with the beam energy. It was shown in the recent papers of PISA collaboration [31, 33], that the contribution from fast moving sources, created in the fast break-up of the Au target by protons, has exactly the appropriate angular and energy dependence needed to reproduce this lacking non-equilibrium process.*

6.2.2 Intermediate mass fragments

If the mechanism mentioned above is appropriate for description of LCPs it should also manifests itself in the spectra of intermediate mass fragments. Thus on the Figs 6.7, 6.8, 6.9 the spectra of lithium, beryllium and boron isotopes are collected and compared with calculations of the two-step reaction model. In the model calculation the coalescence of interacting nucleons is not taken into consideration since the relative contribution of the coalescence decreases quickly with the mass of created complex particles [66] and therefore this mechanism of IMFs production is not implemented in the present version of the intranuclear cascade program (INCL4.3) [29].

The experimental and theoretical spectra shown in the figures are multiplied by factors 0.01 and 0.0001 for angles 80° and 100° , respectively, to separate them one from another as well as from the not scaled spectrum at 35° .

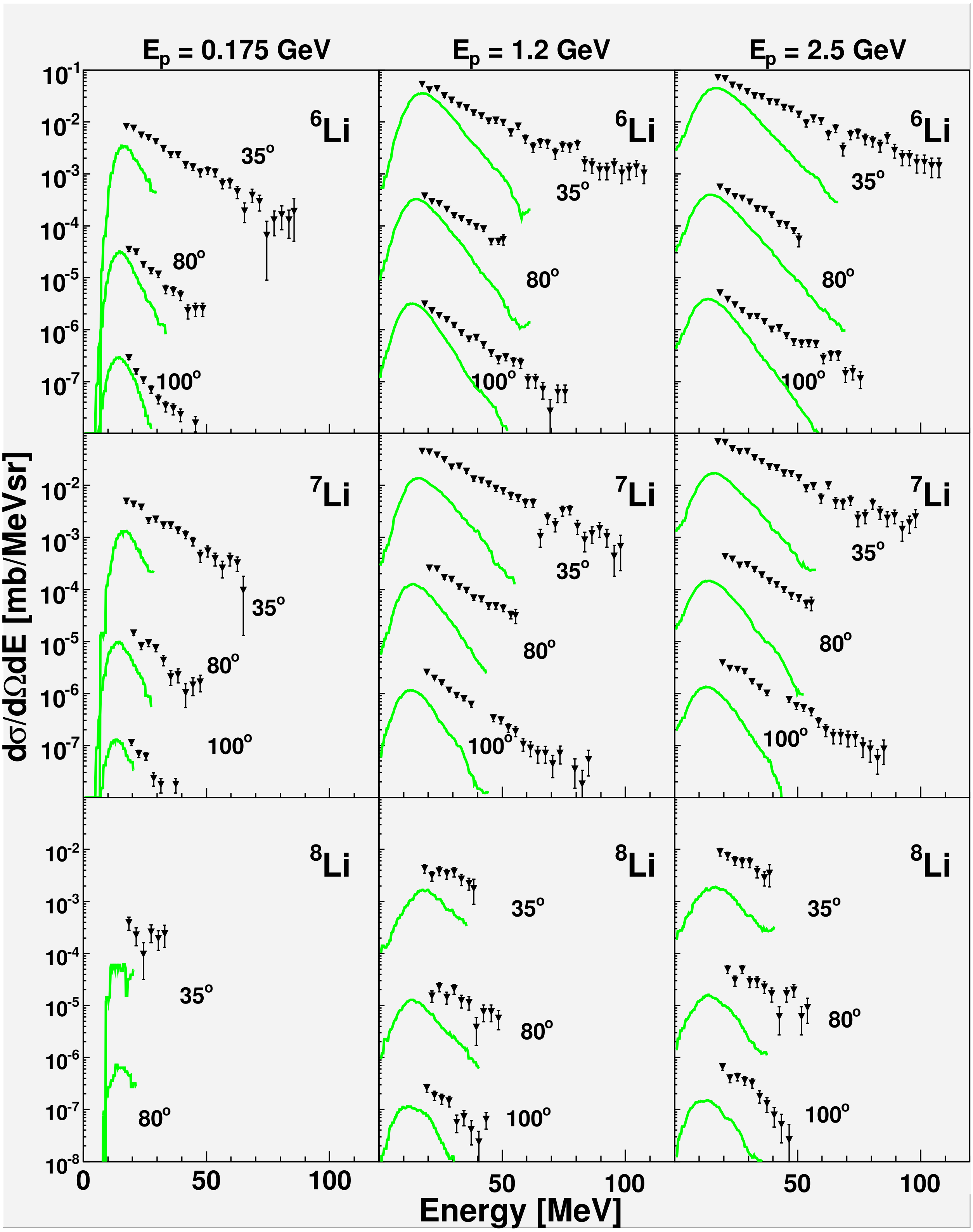

Figure 6.7: Experimental (symbols) and theoretical (lines) spectra for Li ions found at three energies: 0.175, 1.2, and 2.5 GeV. The spectra are multiplied by factors: 1.0, 0.01, and 0.001 for 35° , 80° , and 100° respectively to prevent overlapping the spectra in the figure.

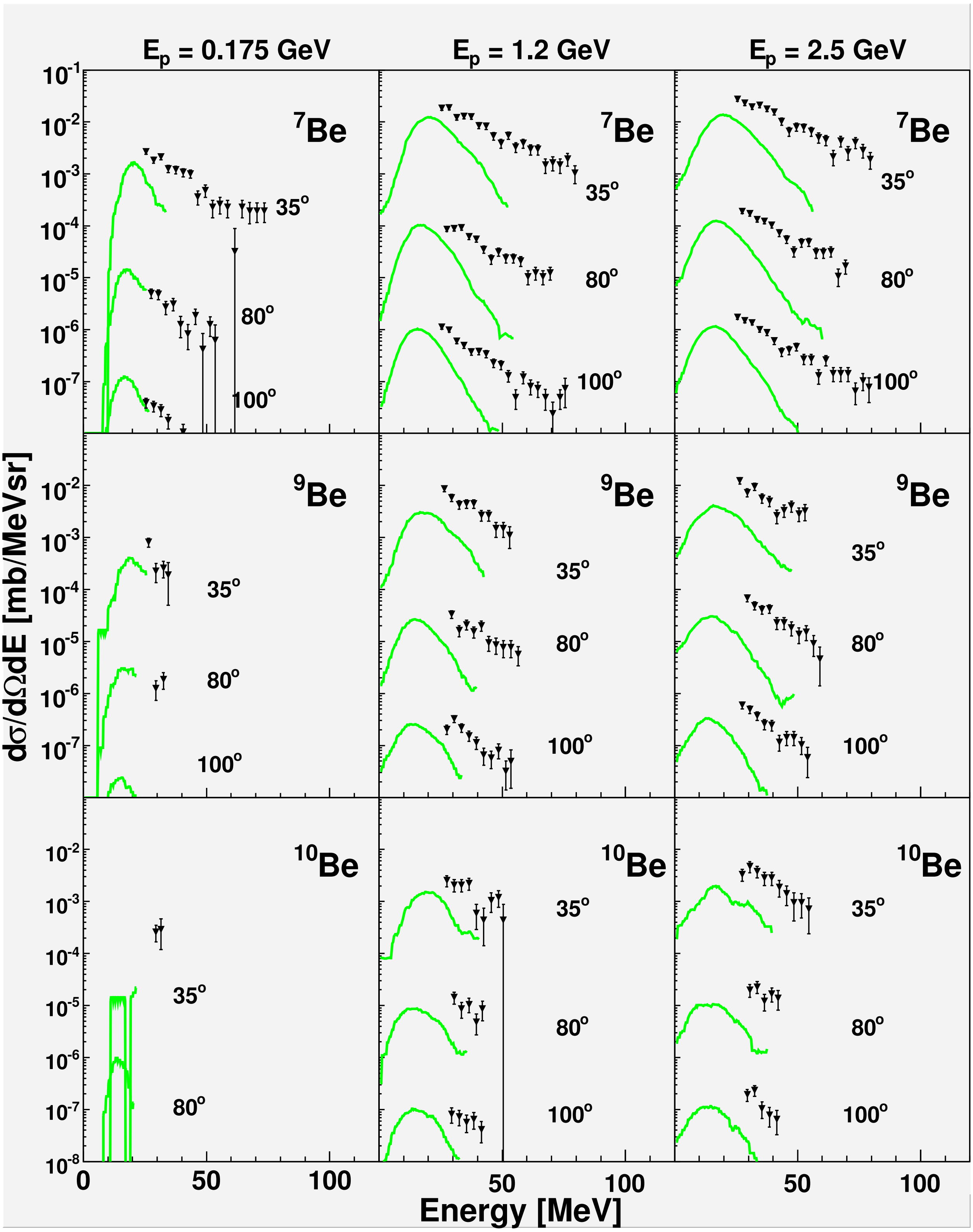

Figure 6.8: Same as Fig. 6.7 but for Be isotopes.

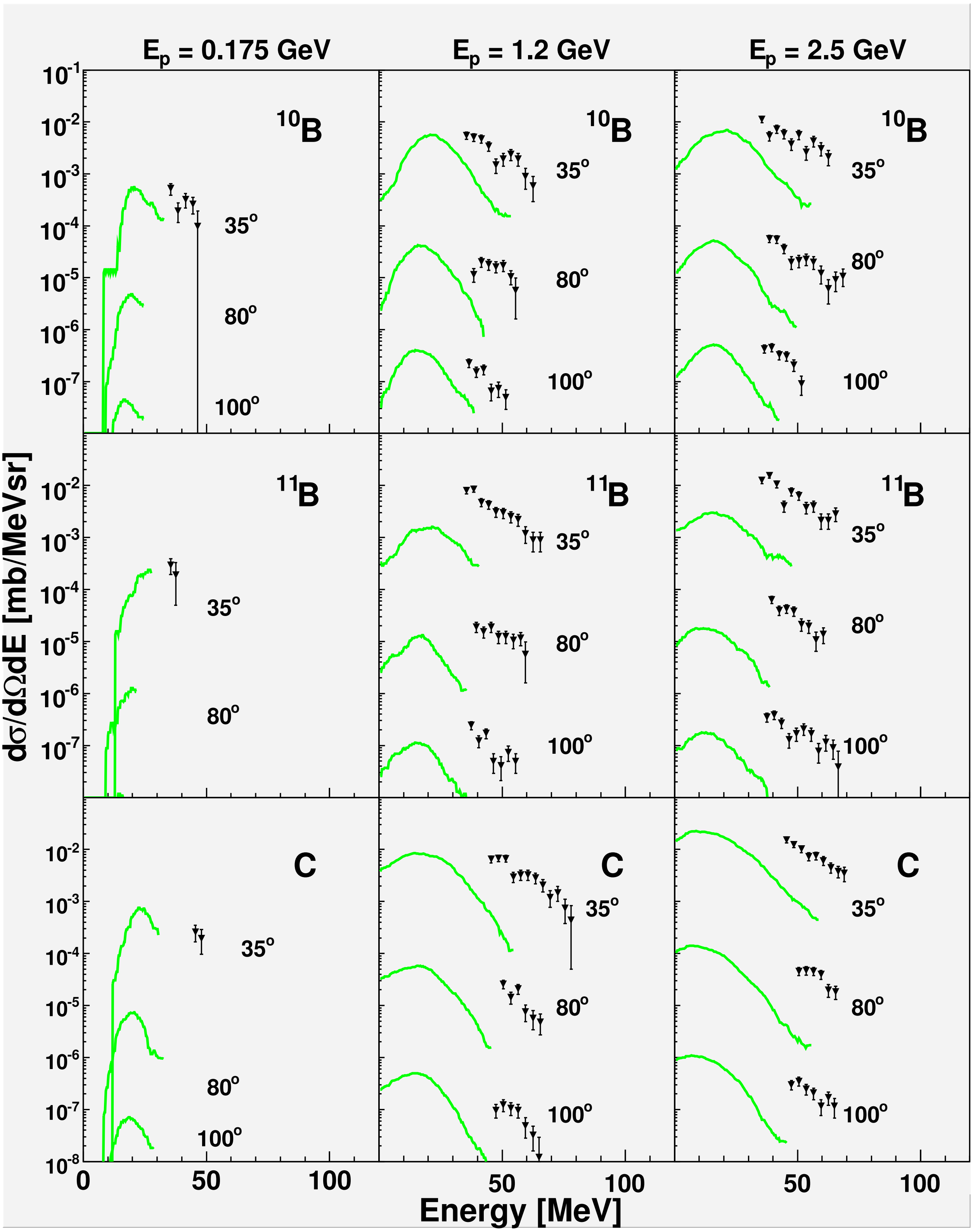

Figure 6.9: Same as Fig 6.7 but for ^{10}B, ^{11}B and C.

It is evident from inspection of the figures that the theoretical spectra of two-step model are much steeper than the experimental ones for ^{6}Li, ^{7}Li, ^{7}Be, and ^{9}Be, i.e., the theoretical cross sections underestimate the data for large energies of ejectiles even by two orders of magnitude. Furthermore, the absolute value of the evaluated cross sections is smaller than the experimental cross sections even in the maximum of the spectrum, which seem to be placed at the same energy for theoretical and experimental distributions. The spectra of other ejectiles are also not reproduced by theoretical model which predicts absolute value of the cross sections much smaller (even 1-2 orders of magnitude) than the experimental value.

These facts confirm the conclusions derived for the data of LCPs, i.e. to reproduce the experimental data there is a need to introduce a non-equilibrium mechanism of reaction apart the mechanism of intranuclear cascade followed by evaporation of composite particles. Contribution of this additional mechanism increases with beam energy and is more pronounced for forward than for backward scattering angles. Emission of particles from moving sources, which are created by break-up of the target has qualitative behavior corresponding well to the observed properties of the data therefore the quantitative analysis discussed in the next Chapter was performed taking this facts into account.

Chapter 7

Competition of the conventional two-step mechanism and the fast break-up mechanism

The qualitative analysis of the data as well as comparison of the data to the two-step model calculations discussed in the previous chapter shows that additional mechanism must be taken into consideration to reproduce the observed, experimental facts. Such a combination of the two-step model with the contribution of emission from moving sources has been, to our best knowledge, for the first time applied by PISA Collaboration for proton induced reactions on the gold target and was presented in the paper of Budzanowski et al. [33].

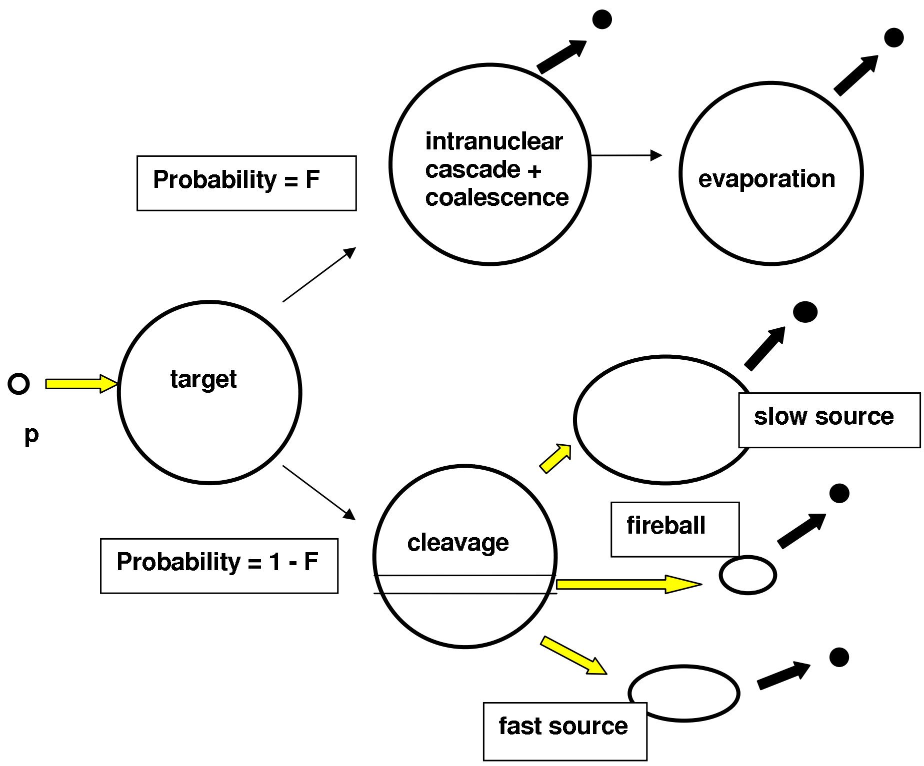

Figure 7.1: Schematic representation of the two-step model (upper part) and the fast break-up (lower part) mechanisms

Figure 7.1 presents schematically two competing mechanisms, which were taken into account in the analysis of the data. The two-step mechanism, consisting in the intranuclear cascade of collisions with inclusion of possibility to form complex LCPs due to coalescence of nucleons escaping from the nucleus, can lead to equilibration of the target residuum and to evaporation of LCPs and IMFs from the residuum. This mechanism of the reaction is shown in the upper part of the figure. Another reaction mechanism appears, when the proton impinging the nucleus drills a cylindrical hole through the nucleus removing the nucleons placed on his way as spatially correlated entity - the "fireball". The fireball emits nucleons and LCPs whereas the excited, "wounded" nucleus may emit also IMFs. Moreover, the deformation and excitation of this nucleus may be so large that it breaks-up in two parts, which may be also able to emit particles.

Allowing for competition of two reaction mechanisms, shown in Fig. 7.1, leads in consequence to the assumption that the contribution of the two-step process, evaluated e.g., by INCL and GEM computer programs with the default parameters (cf. Chapter 4), should be scaled down by some factor F to make room for another process. Factor F represents the probability that proton from the beam initiates the two-step process, whereas $(1-F)$ is the probability of the competing mechanism.

The challenge arises how to calculate absolute contributions of both mechanisms. Whereas the cross section of the two-step process may be treated as fixed by using default parameters of INCL4.3 and GEM2 computer programs, it is obvious that at present there are no possibilities to calculate without free parameters the cross sections of the moving sources model. The usual method applied in the literature is to assume:

- Maxwell-like distribution of the energy available in the decay of moving source with emission of the detected ejectile,
- isotropic angular distribution of the ejectiles in the center of mass system of the source,
- parallel to the beam direction of the source motion,

and to fit the parameters characterizing the source. There are: the temperature parameter of the source T, its speed β (in units of velocity of light), and its yield σ, i.e., angle and energy integrated cross section for emission of the observed ejectile.

Such a procedure is efficient when parameters of only one source are fitted to the data. However, the model of fast break-up allows, in general, for emission of particles from three sources. The IMFs can be emitted only from two heavier sources because of to small mass of the fireball whereas in the case of LCPs all three sources can participate. Then it may happen that the large number of fitted parameters of the model do not allow to fix their values unambiguously. This seems to be the case for present p+Ni data. The spectra of LCPs and especially those of IMFs are smooth, structureless and, what is most important, the experimental low energy cut-off does not permit to determine exactly the Coulomb barrier position.

To check robustness of the values of the parameters, another method of data analysis has been applied putting specific constraints to the model. This procedure is described in Appendix D together with comparison of total production cross sections obtained with both methods. It was found that results are not sensitive to such variation of the method of analysis.

The cross sections for LCPs, calculated in the frame of the two step model with inclusion of the surface coalescence (see the upper part of the Fig. 7.1), were scaled by the factor $F (F \leq 1)$

and added to the contribution of the fast break, evaluated as the emission from three sources; the fireball, the fast and the slow moving sources. It was found that the fireball contribution is very important for protons and deuterons whereas the contributions from the fast and the slow sources are negligible. The fireball contribution was, on the other hand, not visible in the case of ^{4}He emission but the fast as well as the slow moving sources gave significant contributions.

The IMFs were described by emission from two sources - the slow and the fast moving source. The emission from the fireball could not contribute to the IMFs production because of the small mass of the fireball. The IMFs might be, in principle, produced also by the coalescence of the nucleons in the early stage of the reaction. However, according to Herbach et al. [66], this does not present a plausible scenario and therefore was not taken into consideration.

The evaporation from the heavy residuum of the intranuclear cascade was in this version of calculations simulated by fixing the velocity of the slow source - β_1 at such a value as the average velocity $\overline{v}$ of heavy residuum created after fast stage of the two-step process. Values of this velocity used for different beam energies are listed in the Table 7.1. All other parameters were freely varied.

Table 7.1: Average values of the velocity $\overline{v}$ of residual nuclei produced in p+Ni collisions after the intranuclear cascade (in units of the speed of light), and the standard deviations of the velocity $\sigma(v)$ distribution. These values were extracted from INCL4.3 computer program calculations.

Proton Beam Energy [GeV]	$\overline{v}$ [c]	$\sigma(v)$ [c]
0.175	0.0036	0.0034
1.2	0.0051	0.0067
1.9	0.0049	0.0073
2.5	0.0047	0.0074

This method of parametrization is exactly analogous to that used in the publications of PISA collaboration dealing with proton induced reactions on the gold target [31,33]. Hence, the parameters obtained in the present study for nickel target can be compared directly with those determined for the gold target.

7.1 Light charged particles

It was assumed that the original contribution from the two-step reaction model has to be scaled down by factor F representing the probability of initiating the intranuclear cascade by the impinging proton in competition with the fast break-up, which should then appear with the probability $(1 - F)$. The factor $(1 - F)$ is not used explicitly since the absolute magnitude of the latter mechanism cannot be evaluated without free parameters. Hence values of the parameters which determine contribution of the moving sources contain implicitly also this factor.

The contribution from all three sources has been parameterized according to formulae given in the Appendix A. It was checked by fitting the theoretical curves to the experimental spectra, that the only one source is sufficient together with the contribution of the two-step model to reproduce well the data for protons, deuterons, tritons and ^{3}He particles. The contribution from two moving sources was necessary to describe well the α-particle spectra. The single source were identified with the fireball for p, d, t, and ^{3}He whereas two source needed for the α-particles were interpreted as the slow and the fast source (see Fig. 7.1. This interpretation was based on comparison with results obtained for IMFs which will be discussed below. The scaling factor F of the contribution of the two-step mechanism was treated in the fits as a free parameter. Quality of the data description is illustrated by Figs 7.2 - 7.4.

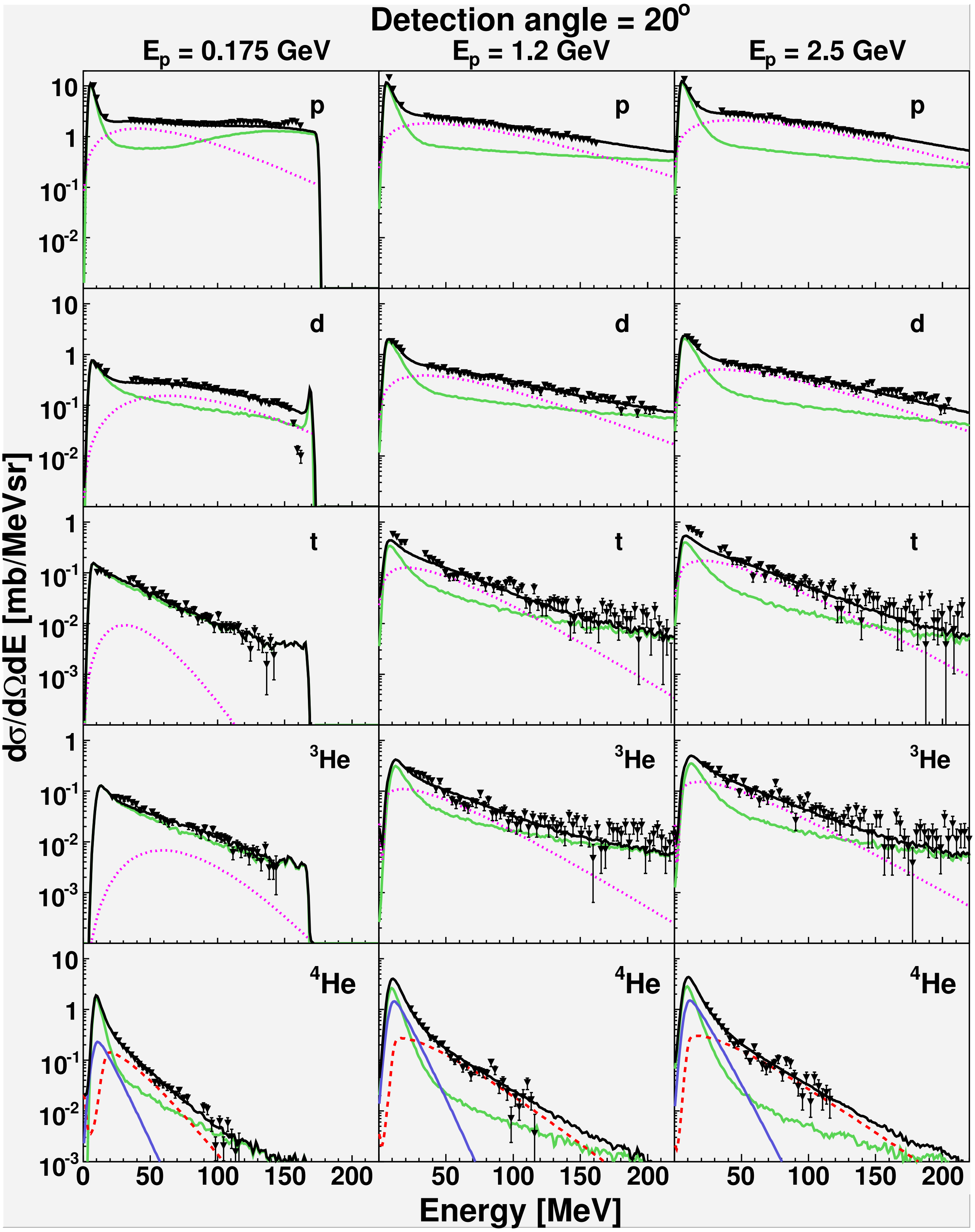

Figure 7.2: The experimental data (symbols) measured at 20° for protons, deuterons, tritons, ^{3}He and α-particles together with theoretical spectra (lines). The solid - black line shows sum of contributions from two-step model (solid - green line) and from moving sources. The dotted - magenta line represents the fireball, the dashed - red line shows contribution from the fast source and the solid - blue line contribution from the slow source.

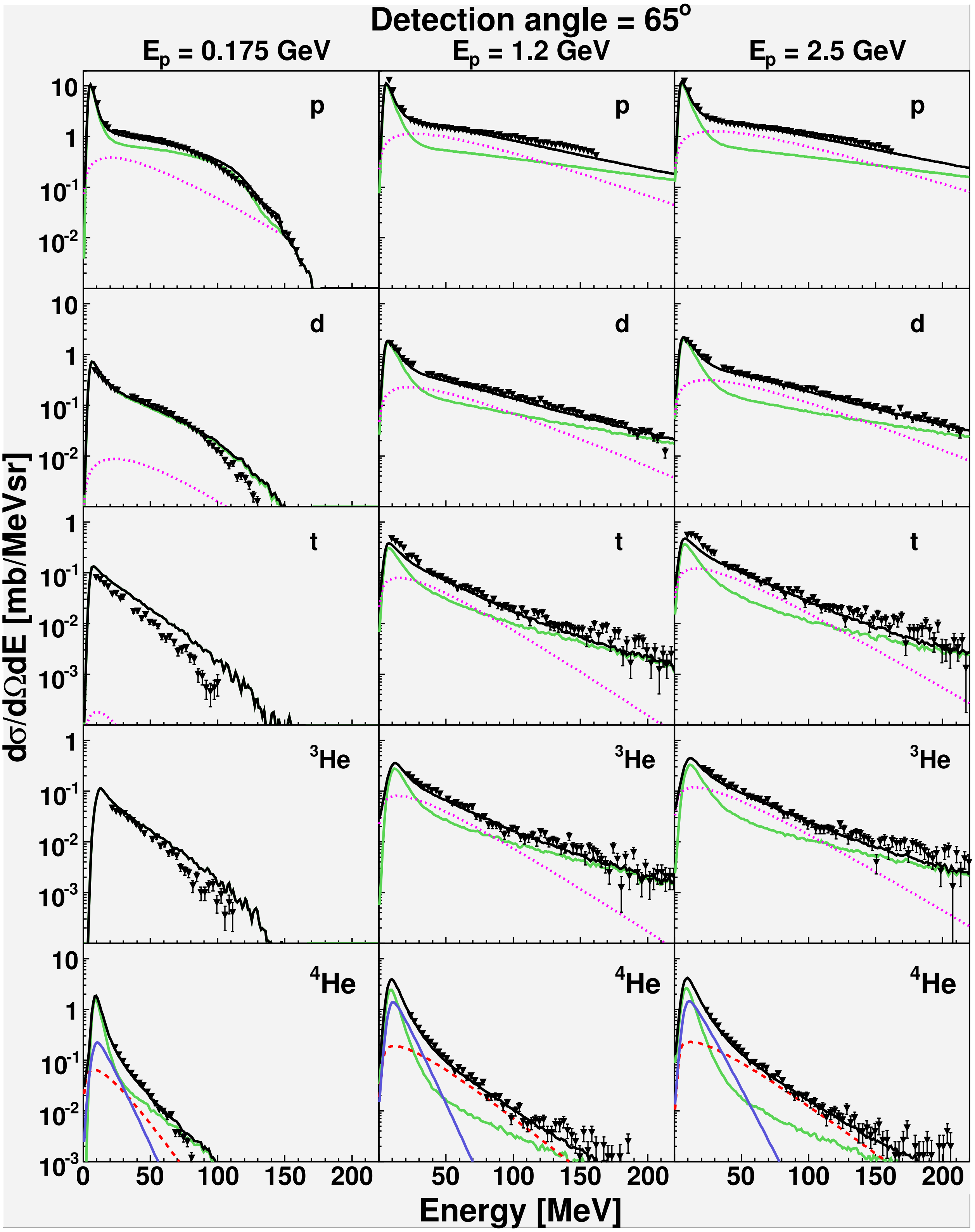

Figure 7.3: Same as Fig 7.2 but for 65°

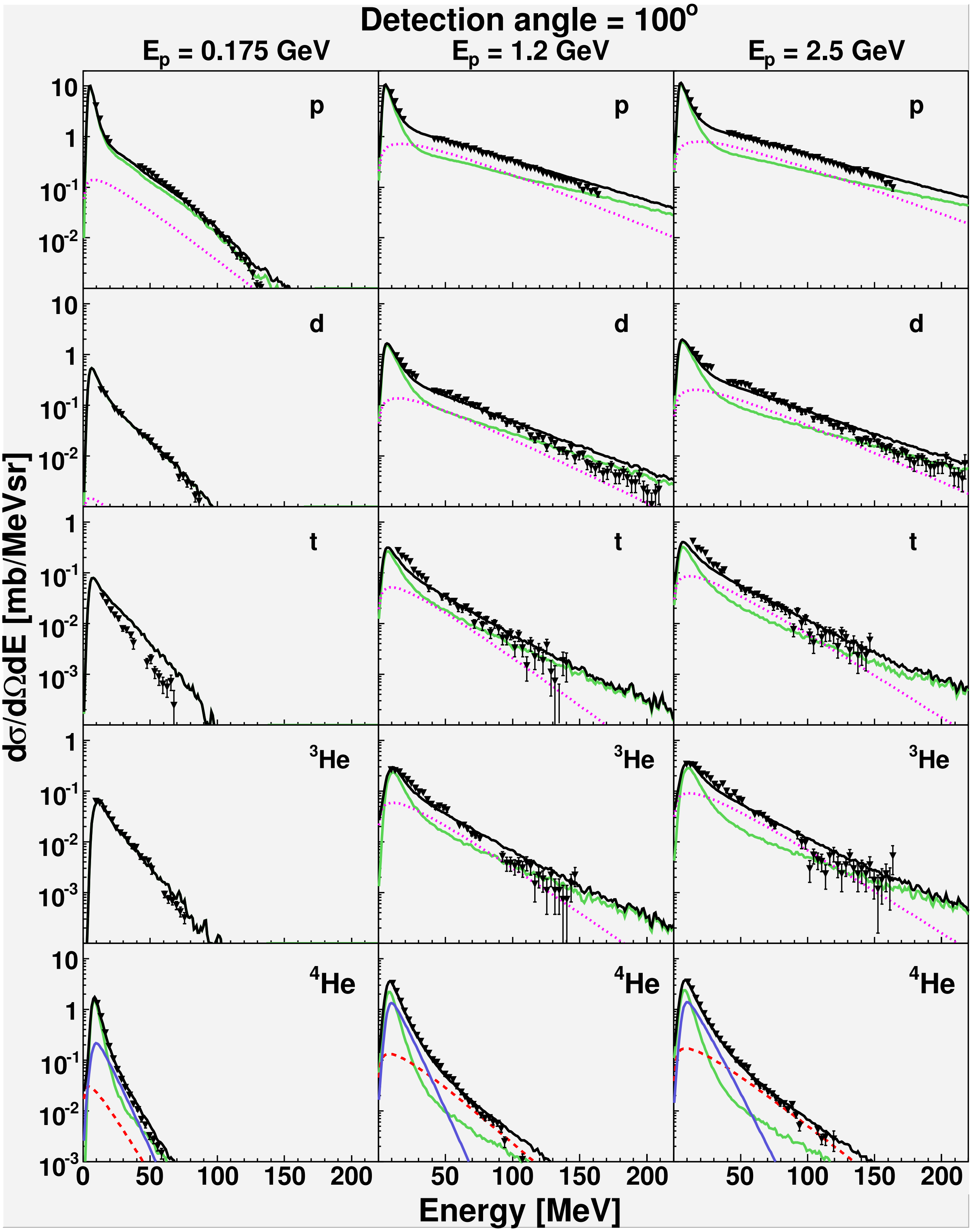

Figure 7.4: Same as Fig 7.2 but for 100°

The parameters of single moving source (fireball), i.e., k_3- reduced height of the Coulomb bar-

Table 7.2: The parameters used in the fit of one moving source (the fireball) and the contribution F of the two-step process to the experimental spectra of protons, tritons, deuterons and ^{3}He for different beam energies. The numbers in the table closed into parentheses represent values of the parameters which were fixed during the fit (see description in the text). Parameters k_3 and B/d ar fixed at values 0.07 and 4.8, respectively what was estimated from the hypothetical mass of the fireball $\sim$ 4 nucleons. For the description of ^{4}He energy spectra it was necessary to introduce the contribution from two sources: slow and fast, but the presence of the fireball was not requested. Parameters of these two new sources are presented in the table 7.3.

Beam Energy/GeV	Ejectile	Fireball β_3	T_3/MeV	σ_3/mb	F	$F * \sigma_{\rm INCL}$/mb	$F * \sigma_{\rm GEM}$/mb	χ^2
0.175	p	0.232±0.005	21.2±1.3	320±32	0.83±0.05	567	697	26.8
1.2	p	0.149±0.012	38.9±2.1	1071±61	0.70±0.03	1094	994	179
1.9	p	0.156±0.010	41.7±1.9	1222±53	0.70±0.02	1139	1005	95.1
2.5	p	0.163±0.008	43.2±1.5	1343±44	0.79±0.02	1286	1123	48.8
0.175	d	0.240±0.009	16.8±2.0	22.9±3.7	0.80±0.03	104	31	5.24
1.2	d	0.105±0.004	32.5±0.8	181±5	[0.70]	202	174	9.48
1.9	d	0.099±0.003	33.7±0.6	234±5	[0.70]	201	196	3.15
2.5	d	0.100±0.004	35.8±0.8	272±7	[0.79]	220	225	7.39
0.175	t	0.142 ± 0.027	6.1 ± 4.9	[0.5]	[0.81]	24.1	2.82	14.3
1.2	t	0.062±0.003	21.9±0.6	41.9±1.6	[0.70]	40.9	28.9	1.33
1.9	t	0.055±0.003	23.8±0.6	59.8 ±2.1	[0.70]	41.3	34.1	1.36
2.5	t	0.054±0.003	25.0±0.6	71.5 ±2.2	[0.79]	45.3	39.4	1.26
0.175	^{3}He	0.205±0.020	7.3±3.0	[0.5]	[0.81]	16.0	4.77	18.8
1.2	^{3}He	0.046±0.002	22.9±0.5	43.1±1.0	[0.70]	31.2	32.6	3.43
1.9	^{3}He	0.039±0.002	23.5±0.4	60.5 ±1.2	[0.70]	31.6	37.5	2.82
2.5	^{3}He	0.040±0.002	25.0±0.5	69.4±1.4	[0.79]	34.5	43.1	2.85
0.175	^{4}He				[0.81]	11.5	129	32.5
1.2	^{4}He	parameters of slow and fast			[0.70]	16.8	277	7.24
1.9	^{4}He	sources are presented in table 7.3			[0.70]	16.6	281	4.68
2.5	^{4}He				[0.79]	18.1	312	4.37

rier for emission of fragments, T_3- apparent temperature of the source, β_3- its velocity, and σ_3- total production cross section (integrated over angles and energy of detected particles) were searched for by fitting theoretical spectra simultaneously to experimental data measured at seven different angles: 16° , 20° , 35° , 50° , 65° , 80° , and 100° . Contribution from intranuclear cascade (for protons) and from the coalescence (for other LCPs) as well as from the evaporation was multiplied by the scaling factor F, which was found for each energy from the fit to the proton spectra (in case of the lowest energy to the proton and deuteron spectra). Its value has been then fixed for all other ejectiles at this energy. The parameter k_3, which determines the height of the Coulomb barrier between ejectile and the rest of the emitting source is given in units of simple estimate of the height of the barrier between the ejectile and the target (see Appendix A). Since the fireball should be very small ($\sim$ 4 nucleons), the Coulomb barrier between the ejectile and the rest of the fireball has to be also very small in comparison to the Coulomb barrier between the ejectile and the target nucleus. Thus, the k_3 parameter was arbitrarily fixed at the small value 0.07. The same arbitrariness was used fixing the parameter B/d) at value 4.8 given in the Table. Interpretation of this parameter may be found in the Appendix A. Its value does not influence significantly the spectra in the studied energy range of the ejectiles.

Very good description of the spectra was obtained in the fit procedure as can be seen in Figs. 7.2 - 7.4. The improvement in comparison to results of two-step model alone is impressive taking *into consideration that experimental spectra at seven different angles are described by the same set of parameters. Even for tritons and ^{3}He spectra, which for the smallest energy were overestimated by two-step model, the scaling down this contribution improved the description. Furthermore, the parameters vary smoothly with the beam energy - with exception of triton and ^{3}He data at the lowest energy, where the contribution of the fireball to these reaction channels is very small and therefore is not well established. Such smooth variation of the parameters indicates that the assumed additional mechanism can be treated as serious competitor of the two-step model.*

7.2 Intermediate mass fragments

The spectra of IMFs were parametrized by two moving sources – without taking into account the fireball because the mass of the fireball is to small. This may be deduced from the fact that even in the emission of the heaviest LCPs - the α-particles - the parameters of the phenomenologically added moving sources deviate from the parameters of the fireball found for tritons and ^{3}He. This is, of course, meant for higher energies, because at the lowest beam energy the presence of fireball contribution to these channels may be questioned.

It was shown in the Chapter 6 that the two-step model predicts the cross sections, which are much smaller than the experimental cross sections. Thus adding some non-equilibrium contribution seems to be justified. In the case when this additional contribution dominates and the method of its evaluation allows for fitting the parameters it may be reasonable to assume that a contribution representing the slow source from the fast break-up imitates simultaneously similar contribution from the evaporation of the heavy residuum created in the intranuclear cascade. Such an idea was used in description of IMFs emission from p+Au reactions studied earlier by PISA collaboration [31, 33]. Therefore, repetition of the same method of analysis for nickel target hopefully allows to observe the trend of the parameters while changing strongly (by factor larger than 3) the mass of the target.

Results of the fitting are presented in Figs. 7.5 - 7.8 for four scattering angles: 35° , 50° , 80° , and 100° . The spectra for representative isotopes of Li, Be, and B as well as for three beam energies (0.175, 1.2, and 2.5 GeV) are presented as panels placed in different rows and columns of the same figure, respectively. The triangles and vertical bars stand for the experimental data and their errors, black - solid line represents sum of contributions from two moving sources, the blue - solid line depicts the spectra from slow moving source (and imitating also contribution from evaporation of particles from heavy residuum of the intranuclear cascade), and the red - dashed line shows contribution from the fast moving source. As can be seen, it was possible to achieve perfect description of the data at all scattering angles, at all beam energies and for all investigated ejectiles.

The parameters of two moving sources for IMFs are listed in the Table 7.3. There is also added information on the slow and fast source used to fit spectra of α-particles presented earlier in Figs. 7.2 - 7.4.

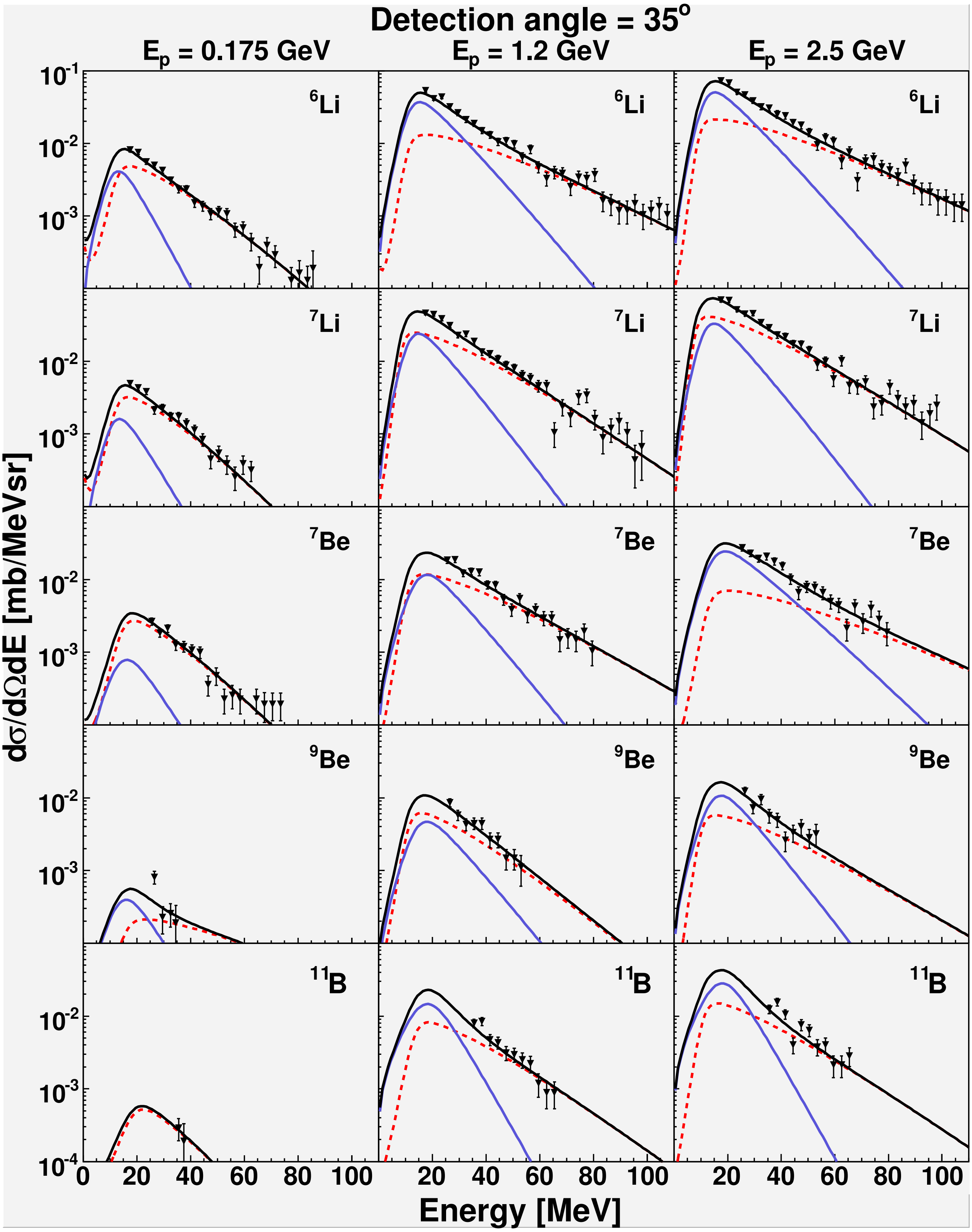

Figure 7.5: Results of fitting parameters of two moving sources to experimental data measured at 35° . For the explanation of different graphs, lines see text above.

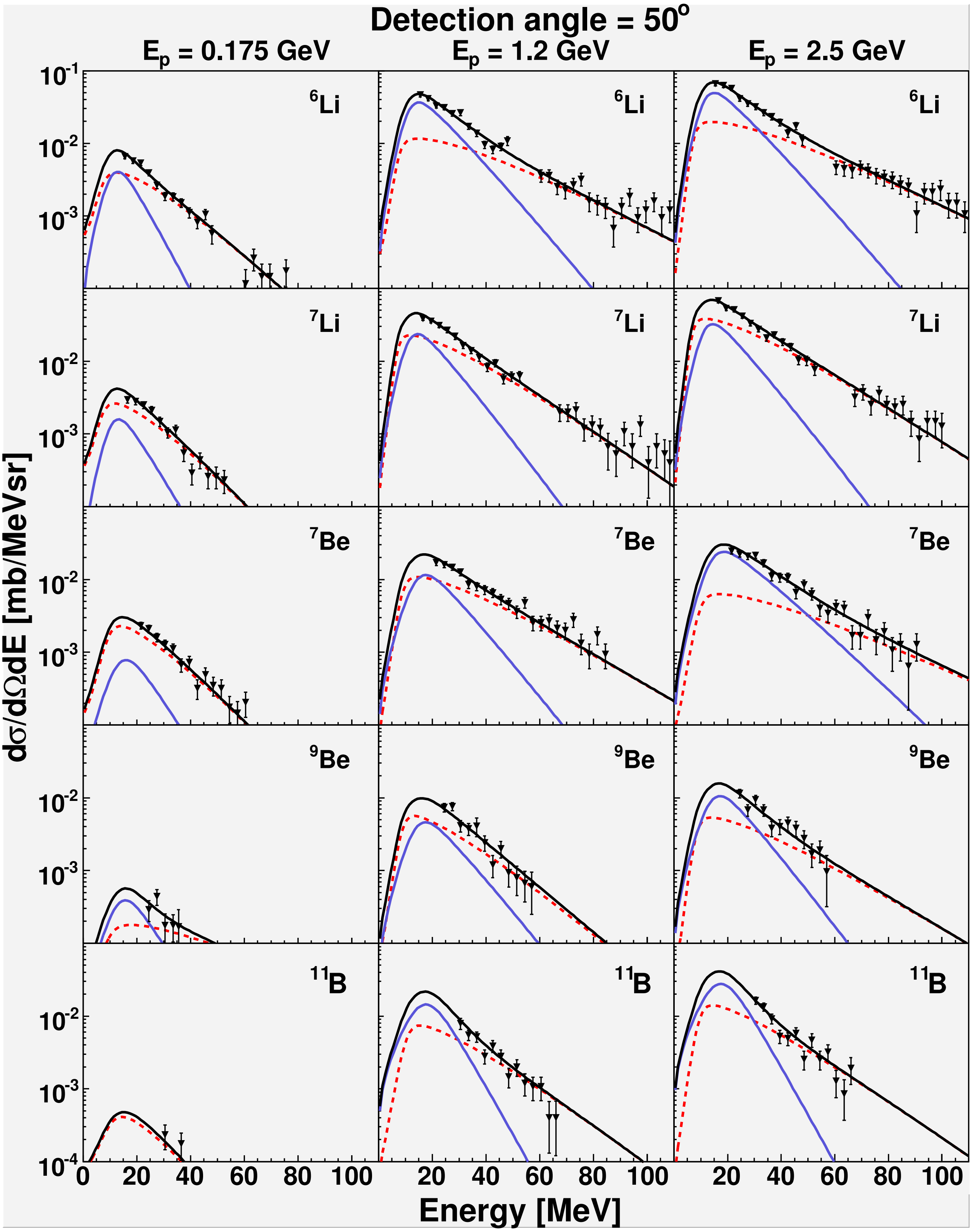

Figure 7.6: Same as Fig.7.5 but at 50°

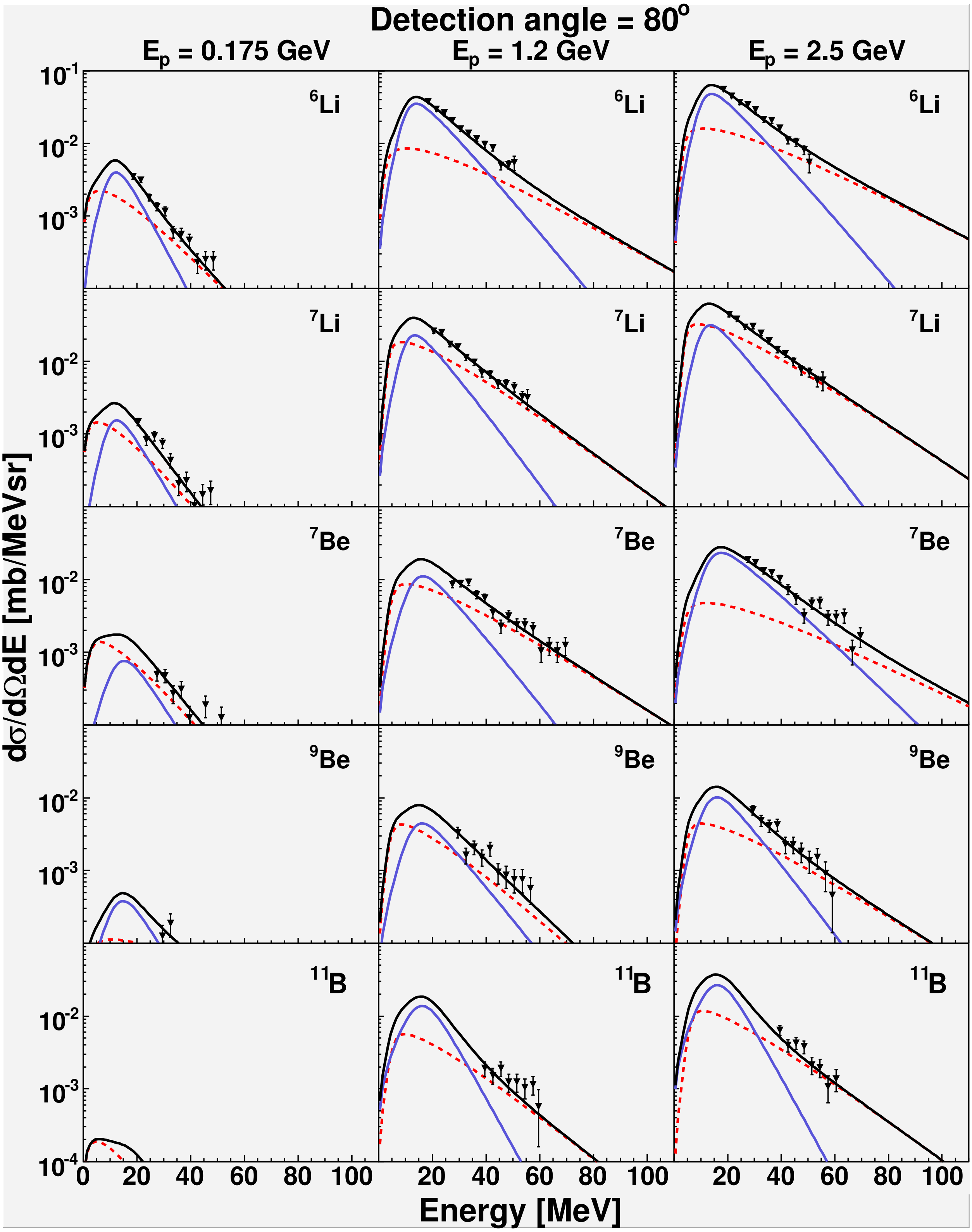

Figure 7.7: Same as Fig.7.5 but at 80°

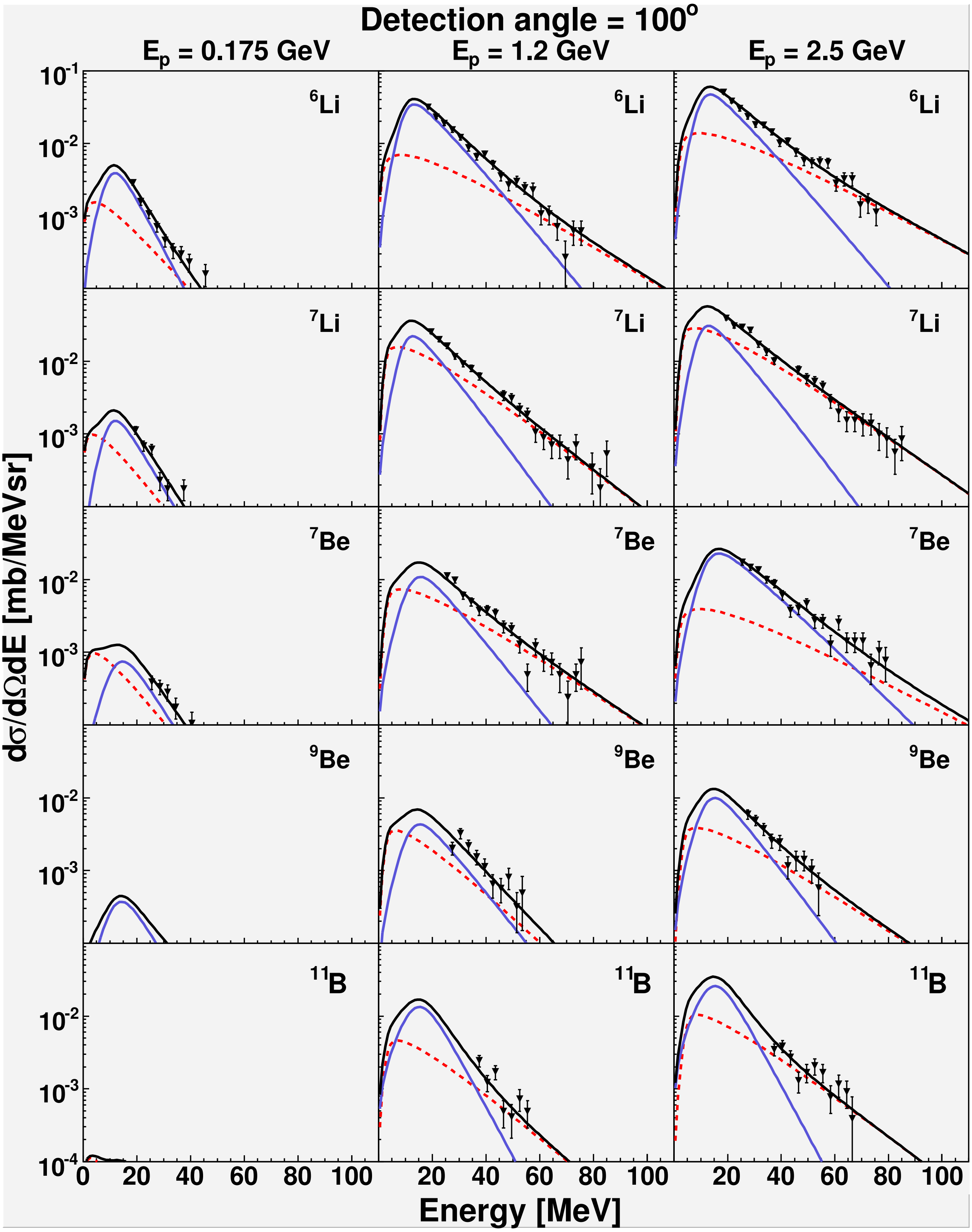

Figure 7.8: Same as Fig.7.5 but at 100°

Table 7.3: The parameters of two moving sources used in the fit of the spectra of IMFs. The velocity of the slow source β_1 was fixed at value of heavy residuum of the intranuclear cascade (see Table 7.1). The B/d parameter was fixed to be equal 4.8 and values of $k_1 = 0.75$ and $k_2 = 0.3$ were used (see Appendix A). The parameters of the slow and fast sources used for description of the α-particle spectra are listed in the first four rows of the table . The factor F used for scaling of the contribution of the two-step process to these spectra is also shown in the Table.

Beam		Slow source		Fast source				
Energy/GeV	Ejectile	T_1/MeV	σ_1/mb	β_2	T_2/MeV	σ_2/mb	F	χ^2
0.175	^{4}He	7.0±0.3	39.3±3.2	0.060±0.006	9.7±0.4	16.8±2.7	[0.81]	32.5
1.2	^{4}He	7.0±0.2	244±6	0.040±0.003	18.1±0.5	76±6	[0.70]	7.24
1.9	^{4}He	7.3±0.2	269±6	0.036±0.002	19.4±0.5	94±6	[0.70]	4.68
2.5	^{4}He	7.9±0.2	283±8	0.035±0.002	20.1±0.5	101±7	[0.79]	4.37
0.175	^{6}Li	5.7±0.4	0.70±0.06	0.045±0.002	10.0±0.2	0.71±0.05	—	1.38
1.2	^{6}Li	9.1±0.4	8.3±0.4	0.035±0.003	18.6±0.5	4.1±0.5	—	1.53
1.9	^{6}Li	10.4±0.4	11.5±0.6	0.037±0.003	19.8±0.5	4.5±0.6	—	1.39
2.5	^{6}Li	9.4±0.5	11.6±0.8	0.026±0.003	20.5±0.6	8.0±0.9	—	1.26
0.175	^{7}Li	6.3±0.8	0.29±0.05	0.041±0.003	8.7±0.4	0.41±0.04	—	1.40
1.2	^{7}Li	8.1±0.7	4.9±0.7	0.022±0.002	14.7±0.4	6.6±0.9	—	1.26
1.9	^{7}Li	9.6±0.7	8.0±1.0	0.025±0.003	15.9±0.5	7.0±1.2	—	1.25
2.5	^{7}Li	9.6±1.0	5.2±1.3	0.018±0.002	16.0±0.5	12.3±1.8	—	1.35
1.2	^{8}Li	[8.0]	[0.2]	0.022±0.002	13.9±0.8	0.91±0.07	—	1.44
1.9	^{8}Li	9.4±3.8	0.6±0.5	0.023±0.008	15.8±1.7	1.1±0.6	—	1.01
2.5	^{8}Li	8.0±1.8	1.25±0.38	0.025±0.007	17.7±2.4	1.26±0.49	—	0.99
0.175	^{7}Be	6.8±1.8	0.164±0.065	0.040±0.004	9.0±0.6	0.37±0.06	—	1.16
1.2	^{7}Be	8.7±1.3	2.75±0.47	0.025±0.003	16.8±0.7	3.6±0.7	—	1.35
1.9	^{7}Be	9.5±0.9	4.91±0.53	0.025±0.003	19.2±0.9	3.9±0.8	—	1.09
2.5	^{7}Be	11.3±0.7	6.86±0.56	0.032±0.006	21.4±1.3	2.6±0.7	—	1.04
0.175	^{9}Be	[6.5]	0.12±0.06	0.08 ±0.02	[9.0]	0.02±0.01	—	1.40
1.2	^{9}Be	[8.6]	1.09±0.20	[0.023]	12.1±0.8	1.27±0.18	—	1.06
1.9	^{9}Be	8.1±1.6	2.03±0.49	0.024±0.007	14.2±1.2	1.57±0.70	—	0.78
2.5	^{9}Be	8.3±2.0	2.42±0.66	0.019±0.007	16.9±2.4	1.81±1.04	—	0.94
1.2	^{10}Be	6.1±1.9	0.95±0.33	0.030±0.016	27.8±9.0	0.39±0.17	—	0.69
1.9	^{10}Be	7.9±1.7	0.93±0.33	[0.023]	17.6±3.1	0.71±0.15	—	0.95
2.5	^{10}Be	6.1±1.9	1.72±0.56	0.024±0.011	23.0±4.6	0.77±0.34	—	0.64
0.175	^{10}B	[6.5]	0.10±0.09	[0.04]	7.1±3.8	0.07±0.04	—	0.98
1.2	^{10}B	[6.0]	1.6±1.2	0.018±0.004	15.5±3.1	1.7±0.6	—	1.71
1.9	^{10}B	[6.0]	3.3±1.2	[0.023]	16.4±1.5	2.4±0.4	—	1.75
2.5	^{10}B	[6.0]	3.2±1.4	[0.023]	17.7±1.8	2.7±0.4	—	1.84
0.175	^{11}B	[6.5]	0.02±0.14	[0.04]	7.0±7.3	0.06±0.04	—	1.10
1.2	^{11}B	[6.0]	3.1±0.9	[0.023]	13.4±1.2	1.8±0.3	—	1.30
1.9	^{11}B	[6.0]	5.2±1.2	[0.023]	17.8±2.2	2.3±0.3	—	1.45
2.5	^{11}B	[6.0]	5.9±3.6	0.016±0.004	14.8±3.2	4.1±1.8	—	1.72

7.3 Energy dependence of model parameters

It is important and instructive to check qualitative properties of the obtained parameters. For example, the linear decreasing of the apparent temperature of the source with the mass of ejectile may be attributed to the recoil of the source, due to emission of the detected ejectile in quasi two-body break-up of the source [150]. This can give information on the mass of the source. Furthermore, the simple picture of the fast break-up should lead to some interrelations between values of the velocity of the source and its temperature. This will be discussed below.

Ejectile mass dependence of the velocity of the moving sources and the apparent temperature of the sources found in the present analysis are shown in Fig. 7.9. As can be seen, values of both parameters vary smoothly with the mass of ejectile and they are concentrated into three groups, similar for each proton beam energy. Each group represents one moving source: the fireball parameters are shown as magenta triangles connected by the dotted line (for LCPs lighter than 4), the fast and slow sources are represented by the red triangles connected by the dashed line, and the blue squares merged by solid line, respectively (for heavier ejectiles). Variation of the parameters inside each group may be well approximated by linear functions with the parameters depicted in the figures.

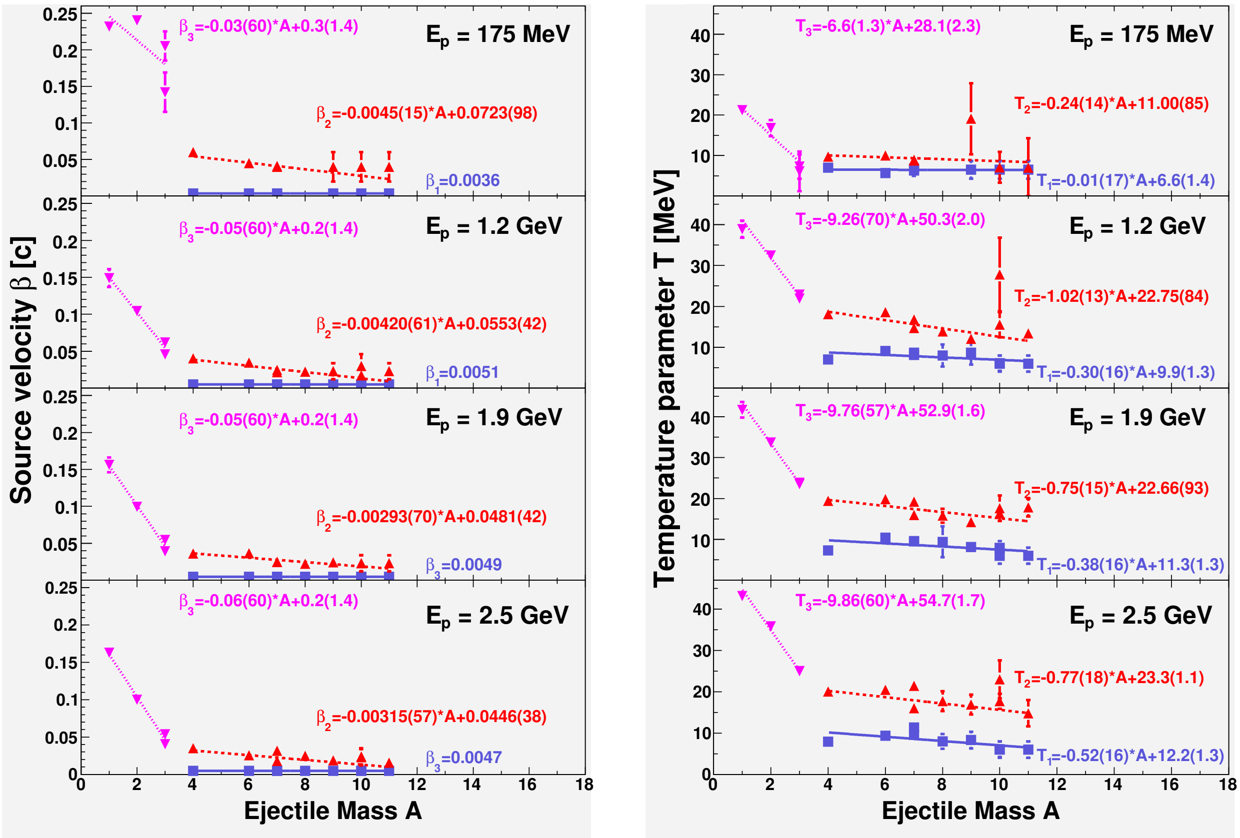

Figure 7.9: Parameters of the fit. Left part of the figure; velocity of the source - β and the right part; apparent temperature parameter - T presented as function of the ejectile mass. Symbols and lines are described in the text.

It is very unlikely that such a very regular and smooth behavior is accidental. Indeed, the momentum conservation during the two body break-up of the source emitting the ejectile with a mass A, comparable to mass A_S of the source, leads to the linear dependence of the apparent temperature on the ejectile mass [150]; $T = \tau(1 - A/A_S)$. Here τ is corrected for the recoil temperature of the source, and the slope parameter of the straight line - $(- \tau/A_S)$ contains information on the source mass A_S. Hence, the heavy source, which does not recoil significantly, should have the apparent temperature independent of the mass of the ejectile, whereas the light source, which recoils strongly, should be characterized by decreasing dependence of the apparent temperature on the mass of the ejectile.

It was found long time ago, that in the high energy proton induced reactions, see e.g. Refs. [46, 67, 92, 101] the power low: $Yield(A_f) \sim A_f^{-\tau}$ is successful in describing the fragment mass

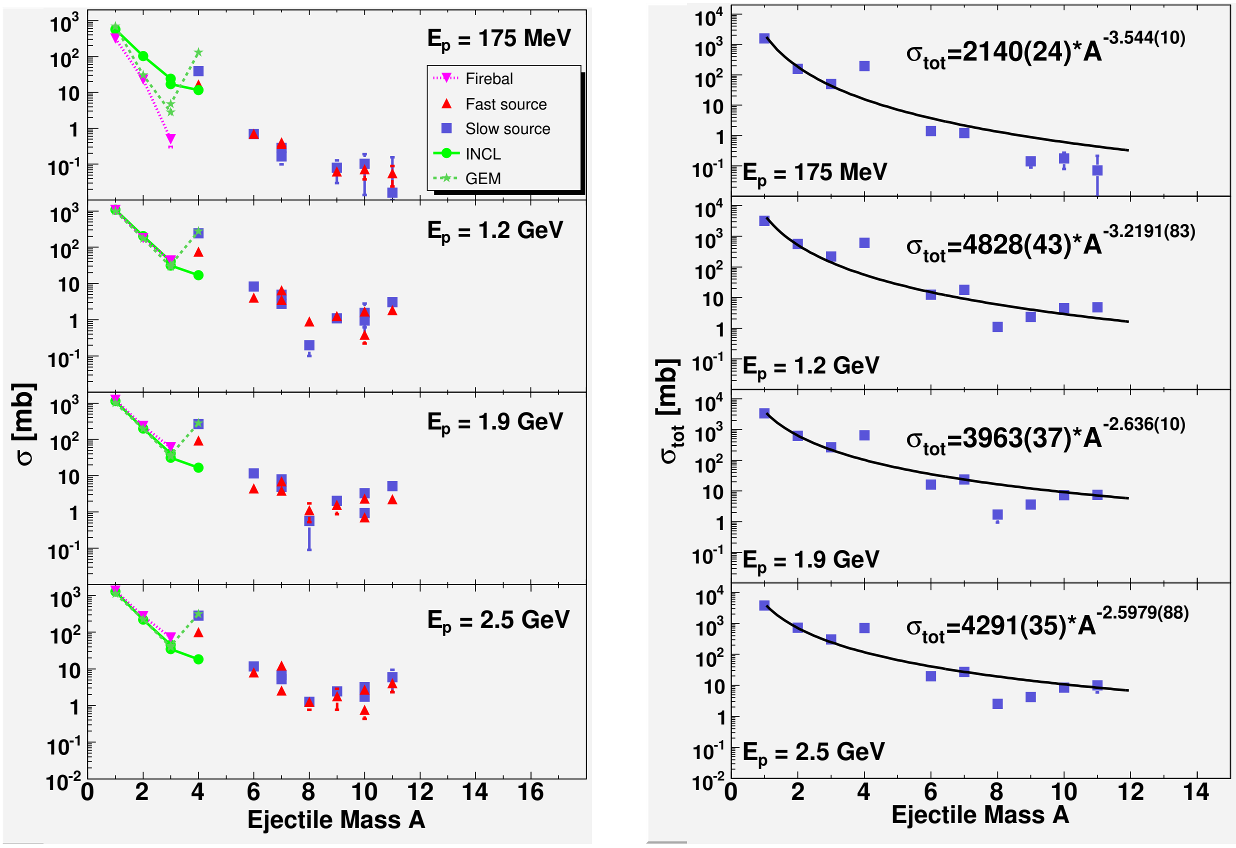

Figure 7.10: Total cross section versus mass of the ejectile for various mechanisms evaluated in analogous way as those for the p + Au reactions [31, 33]. L.h.s. of the figure presents cross sections found for individual mechanisms and for each available isobar, whereas the r.h.s. of the figure shows total cross sections - summed over various possible mechanisms and over different isobars for given mass number of the fragment.

yields over three orders of magnitude. This fact was interpreted, by analogy with the droplet model of Fisher [47], as possible indication of the phase transitions in high energy proton induced reactions. However, it was shown using the Quantum Molecular Dynamics model [3], that the power law form of the inclusive mass yield may be treated as accidental. According to authors of this paper "*it does not reflect a phase transition – which would require a mass yield independent of the impact parameter – but it is merely a parametrization of the sum of different forms of mass yields at different impact parameter*s."

Even if interpretation of the power low character of the fragment yields is ambiguous, there is no doubt in validity of such dependence, both experimentally and theoretically. Therefore, the total cross sections found in the present thesis were presented in Fig. 7.10 as function of mass of the ejectiles. In the l.h.s. part of the figure the cross sections evaluated according to different reaction mechanisms are collected, whereas in the r.h.s. part of the figure the sum of all contributions and all isobars is shown. It can be seen, that total cross sections for individual mechanisms as well as their sum follow the general trend of the power low dependence on the mass of detected particles.

The following properties of the contributions of individual mechanisms may be observed in the l.h.s. part of the Fig. 7.10:

- The fireball contribution (triangles connected with the solid line of the magenta color) increases faster with the energy than contributions of other mechanisms, being the smallest among all contributions at 0.175 GeV beam anergy but becoming the largest one at 2.5 GeV. This mechanism, seems to be not participating to the reactions with production of particles heavier than tritons and ^{3}He. Small dimensions of the fireball (mass $\leq$ 4 nucleons) may be the reason of such behavior.

- The coalescence contribution (full dots connected with the solid line of the green color) decreases very quickly with the mass of ejectile. Therefore, this contribution becomes very small for ^{4}He (with exception of the lowest energy) and is neglected for IMFs.

- The evaporation cross sections for p, d, t and ^{3} He (dark green stars connected by dashed line) have almost the same values as cross sections due to coalescence at 3 higher energies. The situation is quite different at 0.175 GeV where the coalescence provides significantly larger cross sections. The evaporation cross section of alpha particles is order of magnitude larger then the coalescence cross sections for all studied energies.

- The contributions from the slow source (blue squares) and from the fast source (red triangles) are of comparable magnitude for all beam energies. They dominate for all IMFs and are comparable in magnitude to evaporation component for alpha particle cross sections. Contributions of emission from slow and fast source are negligibly small for particles lighter than ^{4}He.

The total - summed over all mechanisms and isobars - cross sections are shown on the r.h.s. part of the Fig. 7.10. Inspection of this figure indicates that the cross sections follow the typical power low dependence $\sigma(A) = CA^{-\tau}$. It is suggested in the literature [123], that the possible transition from the nuclear liquid to gaseous phase appears at the critical energy E_c, at which the power exponent τ reaches its minimal value lying between 2 and 3. Furthermore, the energy dependence of the power low exponent is expected to be more steep for energies below the critical energy E_c than above it, as this can be seen, e.g., on Fig. 5 of the Ref. [92].

Comparison of absolute values of the power exponent τ can be misleading because the parameters "C" and "τ" are correlated and therefore they rather strongly depend on the range of masses for which the fit is done. However, the relative values of power exponent, obtained from the fit performed for the same range of masses of the ejectiles, can be compared unambiguously. In the present study the data have been taken for different beam energies at the same experimental conditions. Thus it may conjectured that using the same range of masses for extraction of τ assures proper relative values of the power exponent τ. These values obtained from the dependence shown in r.h.s. part of Fig. 7.10 are equal to 3.54(1), 3.22(8), 2.64(1), and 2.60(1) for the the beam energies equal to 0.175, 1.2, 1.9, and 2.5 GeV, respectively. Variation of the τ with the beam energy seems to indicate that the present range of beam energies is placed below the (possible) critical value of the energy. Therefore, it may be concluded that there is no evidence for the nuclear liquid-gas transition in the studied beam energy range, even assuming for granted the adequacy of the of picture of the liquid-gas transition as the mechanism of proton induced reactions on the nickel target.

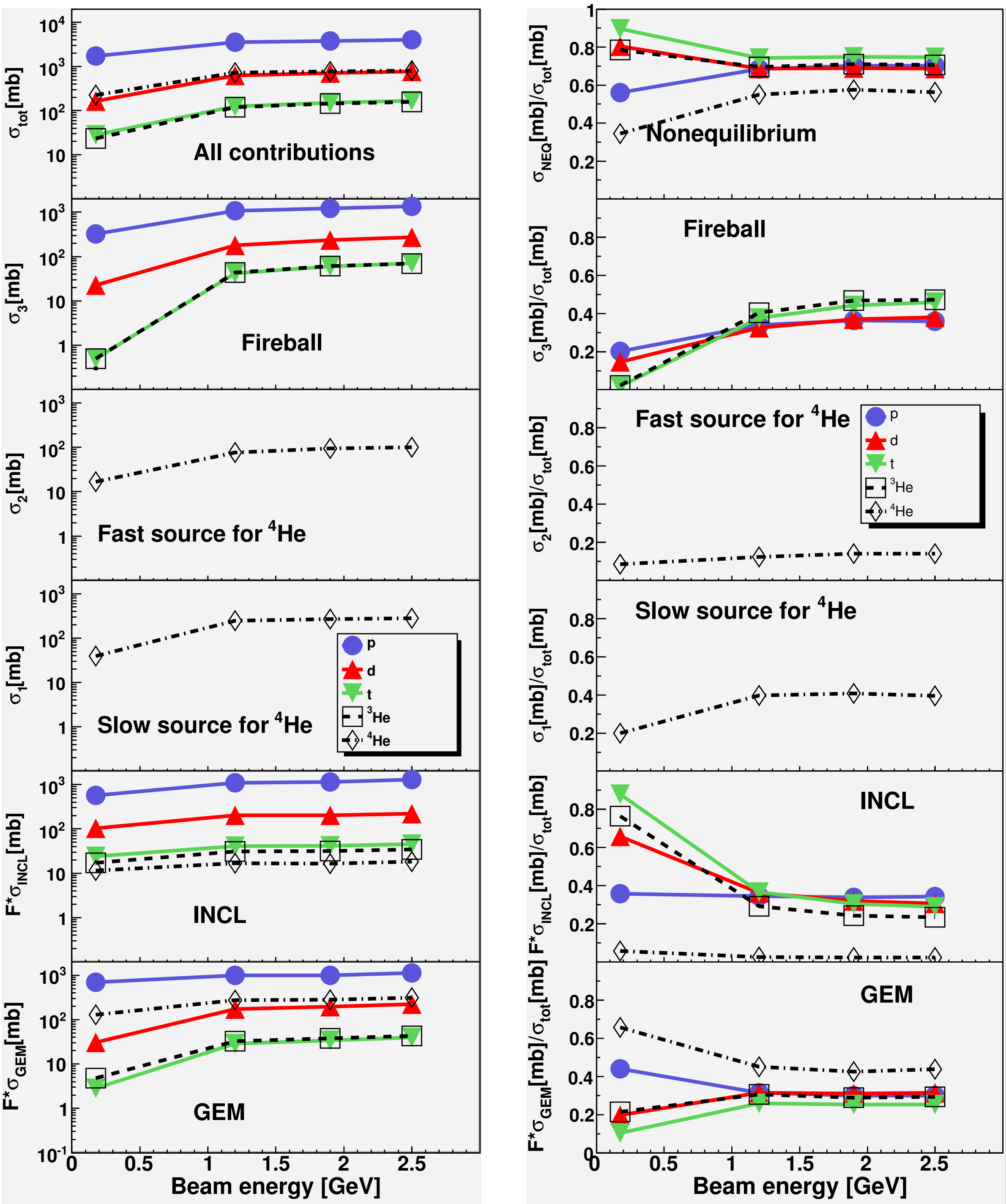

Figure 7.11: Energy dependence of the absolute (l.h.s. of the figure) and the relative (r.h.s. of the figure) contributions of different reaction mechanisms to the total production cross sections of LCPs. For detailed description see text.

The energy dependence of the absolute cross sections for all mechanisms under investigation is presented on individual pads in the left hand side (l.h.s.) part of the Fig. 7.11 whereas in the r.h.s.

part of the figure the energy dependence of the relative contributions is shown. The contributions of individual mechanisms are depicted in the following order - from the bottom to the top of the figure: evaporation - calculated by means of the GEM2 computer program (scaled by factor F), intranuclear cascade with coalescence of nucleons - calculated with INCL4.3 computer program (also scaled by factor F), emission from the slow source, emission from the fast source, and from the fireball, respectively. The total cross section, i.e., the sum of all contributions is presented at the top of the l.h.s. part of the figure, whereas the ratio of the sum of all contributions (with exception of the evaporation) to the total cross section is shown in the top of the r.h.s. part of the figure. To facilitate the comparison, the scale of the cross section values (l.h.s. part of the figure) has the same range for all pads, with exception of that for the total cross sections, where this scale has range multiplied by factor 10. The same linear scale is also applied for all pads in the r.h.s. part of the figure. Symbols corresponding to different ejectiles are explained in the figure's legend. The lines connecting the symbols are only used to guide the eye.

A monotonic increase of the absolute value of the cross sections can be observed in the studied energy range 0.175 - 2.5 GeV, for all ejectiles and for all mechanisms of the reaction. This increase is very significant for low energies (between 0.175 GeV and 1.2 GeV) whereas it almost saturates at higher energies, being however visible in the full studied energy range. The largest increase is present for the fireball cross sections. This, in turn, is reflected in the energy dependence of the relative contributions of various mechanisms of the reaction shown in the r.h.s. part of the figure. For example, it is evident, that for complex light charged particles the relative contribution of the first stage of the reaction (intranuclear cascade accompanied by coalescence) decreases quickly with the beam energy. The relative contribution of this pre-equilibrium stage of the reaction is, however, almost constant for protons. The relative contribution of the evaporation decreases with energy for protons and α-particles but it increases for other light charged particles. Rather oposit energy dependence is observed for the relative contribution of the non-equilibrium processes to the reaction mechanism, i.e., it increases between 0.175 GeV and 1.2 GeV for protons and α-particles but it decreases in this energy range for other LCPs. For higher energies it almost saturate for all LCPs. The non-equilibrium mechanism dominates exhausting 60 - 80 % of the total cross section at lowest energy and approximately 70 % at all higher energies, only α-particles regularly contribute 20 % less then protons.

Similar general trend of emission from the slow and from the fast source with varying beam energy can be observed for all IMFs, as it is presented on the l.h.s. part of Fig. 7.12. For the lowest beam energy, cross section is an order of magnitude smaller than that obtained for the three higher energies. The relative increase of the cross sections with the energy is the same - in the limits of errors - for all IMFs, what is illustrated by the r.h.s. part of Fig 7.12. Ratios of the total cross sections found at 0.175 GeV, 1.2 GeV, and at 1.9 GeV to the cross sections found at 2.5 GeV are shown in this figure as red squares, blue up triangles, and black down triangles, respectively.

Following properties of the energy dependence of production cross sections for the IMFs may be concluded from the Fig. 7.12:

- The contributions of the slow and the fast moving sources to the production cross sections have comparable values,

- The ratios of the cross sections obtained at 1.2 GeV and 1.9 GeV to those determined at 2.5 GeV are the same - in the limits of errors - for all IMFs. This seems to be not the case for

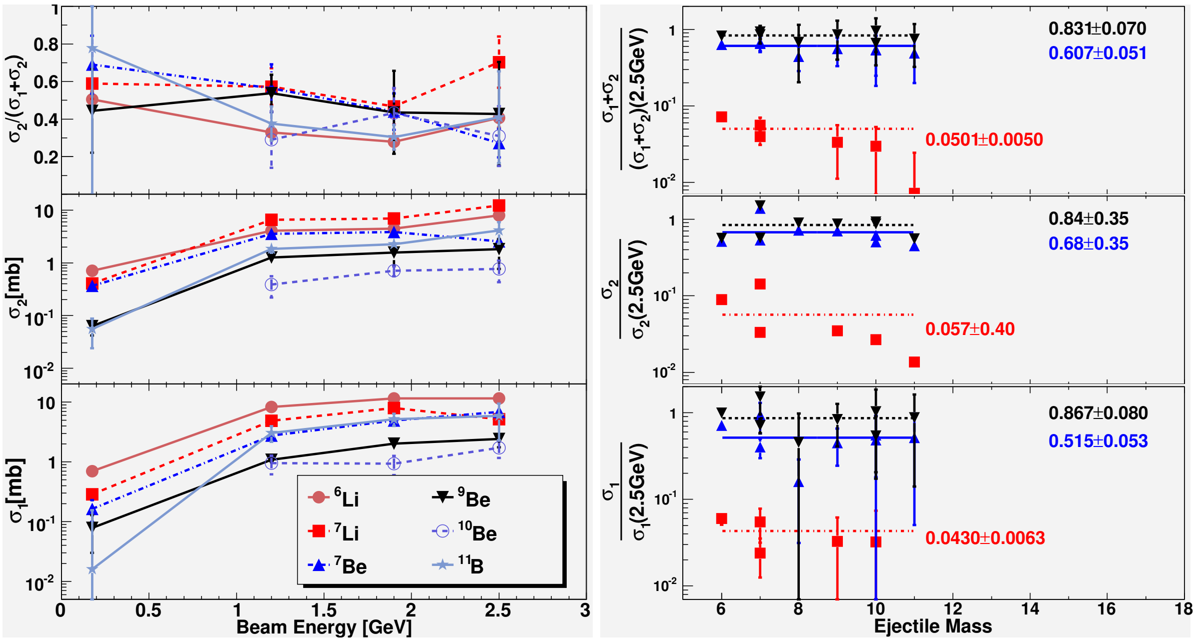

Figure 7.12: Symbols σ_1 and σ_2 correspond to slow and fast moving sources, respectively. On the l.h.s. part of the figure, the energy dependence of the absolute contribution from slow and fast moving source is presented on the lower and the middle pad, respectively. The relative contribution of the fast moving source is depicted on the top pad. Different symbols and lines connecting them represent different IMFs as it is shown on the legend. The ratio of production cross section at beam energy 0.175 GeV (red full squares), 1.2 GeV(blue triangle up) and 1.9 GeV(black triangle down) to those found at 2.5 GeV is presented as a function of mass of emitted IMFs in the r.h.s. part of the figure. The lines represent average values. The ratios of contribution from the slow moving source, the fast source, and from the sum of the both sources to corresponding quantities determined at 2.5 GeV are depicted on the bottom, medium, and the top pads, respectively.

the lowest beam energy 0.175 GeV. This reflects the fact that the exponent τ of the power low relation of the product yield $yield(A)$ and product mass A: $yield(A) \sim A^{-\tau}$ is the largest (3.54) at the smallest beam energy, differing rather strongly from that at 2.5 GeV beam energy (2.6).

7.4 Conclusions concerning the reaction mechanism

Let us consider the physical consequences of the assumed break-up mechanism presented schematically in Fig. 7.1. They can be treated as a crude cross check of validity of this mechanism for the reactions under investigation. It may be expected that the momentum and excitation energy of the fast and the slow sources should be the same, because they are due to the friction of the fast fireball with both these pieces of the target along the same path. This causes identical momentum transfer, forward directed, to these parts of target which appear as two moving sources: $A_{S1} \cdot \beta_1 = A_{S2} \cdot \beta_2$. Hence it may be expected, if the model is valid, that velocities of the sources should be proportional to reciprocals of the masses of the sources.

$$\frac{\beta_1}{\beta_2} = \frac{A_{S2}}{A_{S1}}.$$

The lighter source should be the faster. This is indeed the case what can be checked by comparing the temperature and velocity dependencies of both sources on the ejectile mass, which are shown in r.h.s. part of the Fig. 7.9 and l.h.s. part of the Fig.7.9, respectively.

Furthermore, using a simple estimation of the relation between excitation energy E^* and the temperature τ, valid in the Fermi gas model ; $E^* = a\tau^2$, where $a \approx A/const$ one gets the following relationship:

$$\frac{\tau_1^2}{\tau_2^2} \approx \frac{A_{S2}}{A_{S1}}.$$

The lighter source should have the higher temperature, i.e., the more steep straight line in the temperature dependence on the ejectile mass should be placed above the less steep line.

These two expectations arising from the break-up picture are very well fulfilled as it can be seen in Fig. 7.9 for all beam energies. Moreover, validity of both above formulae means, that the following relationship between temperatures and velocities of the sources should be fulfilled: $\beta_1/\beta_2 \approx \tau_1^2/\tau_2^2$ or equivalently

$$\frac{\beta_1\,\tau_2^2}{\beta_2\,\tau_1^2} \approx 1.$$

Taking values of the recoil corrected temperature of the slow source τ_1 and the fast source τ_2 from parameterizations presented in the r.h.s. part of the Fig. 7.9, and values of velocities β_1 and β_2 evaluated from the parameterizations shown in the l.h.s. part of the same figure for the average mass of IMFs ($A = 7$), the following values of the above function have been obtained: 0.25 $\pm$ 0.19, 1.0 $\pm$ 0.5, 0.7 $\pm$ 0.3, and 0.8 $\pm$ 0.4 for the proton beam energies 0.175, 1.2, 1.9 and 2.5 GeV, respectively.

Having in mind the simplifications introduced in the assumptions, these values agree at high beam energies very well with unity as predicted by the model. It is, however, evident that the calculated value for the lowest beam energy deviates significantly from unity. This might indicate that the break-up of the target at the lowest beam energy is not necessarily caused by fireball emission.

Further inspection of Figs. 7.9 provides additional arguments in favor of the hypothesis of different reaction mechanism at low and high energies and allows to propose the explanation of this fact:

- Velocity of the fireball is approximately two times larger at low beam energy than at high energies. Furthermore, it is so large that the momentum of the fireball evaluated with assumption, that its average mass is $\sim$ 2.5 mass units, exhausts total available momentum. In contrast, the momentum of fireball evaluated at high energies is several times smaller than the beam momentum and practically does not change with the beam energy.

  This indicates, that the impinging proton does not contribute to the fireball at high beam energies but it must be a part of the fireball at low energy.

- The temperature parameter of the fireball at low energy is smaller by factor ~ 2 than at high energies. This means that the energy of internal motion inside the fireball is much smaller at low beam energy than at high energies. Moreover, this internal energy almost does not change for beam energies between 1.2 and 2.5 GeV. This indicates that the internal motion of nucleons in the fireball created at high energies resembles the relative motion of these nucleons in the target nucleus. Thus they represent property of the nucleus, independent of the beam energy. However, the internal motion of nucleons in the fireball created at low beam energy depends on this energy because the proton from the beam, slowed down in the collision, belongs to the fireball.

  Thus, the observed behavior of the temperature parameter of fireball is in agreement with hypothesis that the fireball at low energy contains the proton from the beam as its constituent part, whereas the fireball at high energies is built of nucleons of the target only.

- For lowest beam energy, i.e. 0.175 GeV, the dependence of the temperature parameter on the ejectile mass is very weak for the fast source, what may indicate that its mass is large. The large errors of the temperature parameter do not allow to estimate exactly its mass. However, the momentum conservation, based on the velocity parameter of the source, limits this value to approx. 20 mass units. Assuming that this estimation is correct, the interesting conclusion appears:

  The emission of fireball cannot be accompanied by break up of the rest of the nucleus at such low beam energy.

  This fact together with observation, that two moving sources (different than fireball) are necessary for description of IMFs cross sections, suggests that:

  At the lowest beam energy the nucleus breaks-up without emission of fireball, i.e., break-up appears when the proton of the beam is captured by nucleus with dissipation of its full energy.

In summary, the following picture of the reaction mechanism emerges from present analysis of the experimental data:

For all beam energies studied in this work, a strong competition of two mechanisms is visible.

First of these mechanisms corresponds to conventional two step model; In the fast stage of the reaction the intranuclear cascade of nucleon-nucleon collisions appears, enriched by possibility of coalescence of nucleons into complex particles. In the second stage the evaporation of nucleons and complex particles from equilibrated residuum of the target takes place.

The second mechanism consists in a collective interaction of the impinging proton with nucleons placed on its straight way through the nucleus. This interaction may lead to emission of this group of nucleons as a single, highly excited entity - the fireball. It was concluded that such emission at high beam energies induces always a break up of the remnant nucleus into two parts which are sources for emission of particles. At lowest beam energy emission of fireball exhausts practically total available momentum, therefore the excitation energy of the remnant nucleus is too small to cause its break-up, however, this nucleus can be a source for particle emission. It can also happen at the lowest beam energy, that the impinging proton can be captured due to collective interaction with the part of the target nucleus causing local high excitation of the nucleus leading to its break-up. The fragments of the nucleus from its break-up are also sources for emission of particles.

Chapter 8

Confirmation of the postulated mechanism by literature data

It was shown in previous two Chapters that the shape of energy and angular distributions of $\frac{d\sigma}{d\Omega dE}$ vary for all ejectiles in the same, very regular manner with increasing of the beam energy. Therefore only spectra for protons, deuterons and tritons taken at 100° are shown below - on Fig 8.1 - as a typical example. Since the spectra measured in the present experiment at 0.175 GeV differ significantly from those obtained at 1.2, 1.9, and 2.5 GeV, the literature data determined at energies between 0.175 GeV and 1.2 GeV are also presented in the figure to allow for observation of the energy variation of the differential cross sections.

It is known from p+Au experiments [31, 33] that the production cross sections vary very smoothly within the beam energy range from 1.2 GeV to 2.5 GeV. This is also the case for the data of the present experiment for p+Ni system. Shapes of the spectra are almost the same for 1.2, 1.9, and 2.5 GeV as it is visible on Fig. 8.1, and the absolute cross sections increase only moderately with energy – changing no more than by factor two between the lowest and highest energy.

The spectra determined at 0.175 GeV beam energy are much steeper than those at higher energies, nevertheless their shapes fit well to the general energy trend as can be seen in Fig. 8.1. This energy trend is also preserved for 105° proton spectra measured at 0.09 GeV by Wu et al. [153] and for 90° proton spectra determined by Roy et al. [124] at 0.5 GeV protons on Ni target. The deuteron and triton spectra of experiment by Wu et al. [153] follow the same energy trend as the proton spectra. It is interesting to note that the cross sections of neutron induced reactions measured by Franz et al. [51] at 90° for almost the same energy (0.542 GeV) as experiment of Roy et al. have quite similar values. Thus, for further comparison the 90° spectra of Franz et al. [51] for Cu(n,p), Cu(n,d), and Cu(n,t) reactions are also presented in Fig. 8.1. The shape and magnitude of these spectra fit well to the data of the present experiment.

The slope of the low energy parts of energy spectra appear to be almost independent of the beam energy. In contrast, the high energy tails of the spectra spread to higher energies and increase monotonically with the beam energy. The presence of such two different components of the spectra leads to the conclusion that two different mechanisms contribute to the reactions. It was shown in Chapter 7 that quantitative analysis of the double differential cross sections allows to disentangle contributions of both reaction mechanisms and to get information on their energy dependence. The particles with energy lower than 20 - 30 MeV are predominantly evaporated from equilibrated residua of the fast stage of the reaction. For emission of particles with higher energies another reaction mechanism has been proposed. It consists in competition of two mechanisms: the coalescence of nucleons into light charged particles and the fast break-up of target nucleus which leads to appearing of two or three moving sources of emitted particles.

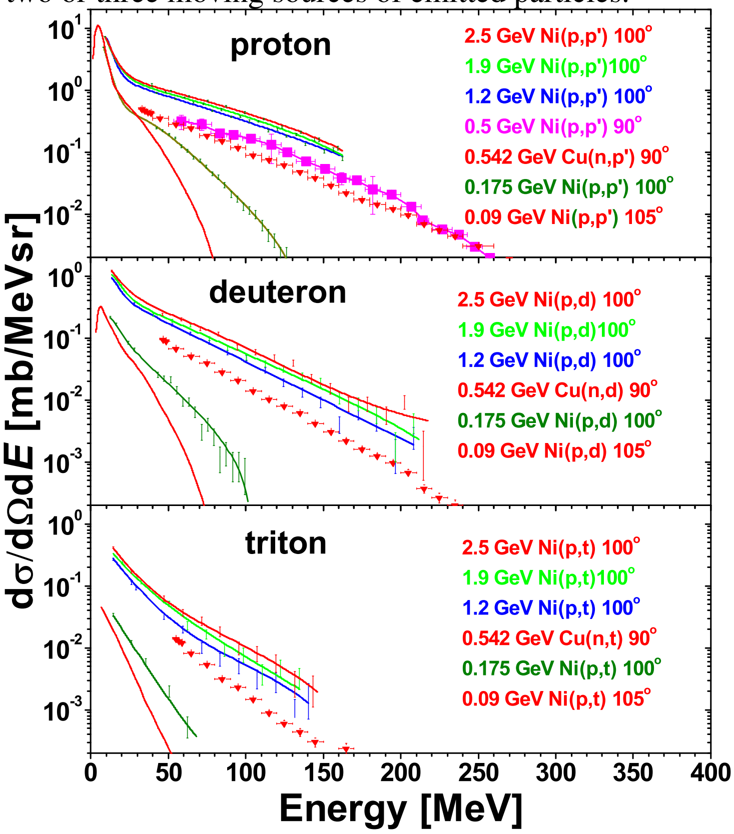

Figure 8.1: Variation of energy spectra of protons, deuterons and tritons emitted under 100° in lab system with increasing beam energy in the range from 0.09 GeV [153] to 2.5 GeV (present experiment). Energy spectra of nucleon induced reactions, listed on the figure, on targets with mass close to Ni are used for the presentation. The data from present study, measured at 0.175, 1.2, 1.9, and 2.5 GeV are depicted as solid lines accompanied by error bars representing statistical errors. Data from 500 MeV and 542 MeV nucleon induced reactions, published by Roy et al. [124] and Franz et al. [51], respectively, are presented as full symbols whereas data of Wu et al. [153] are marked by solid lines without error bars.

This model explains also in the natural manner the fact that ratio of low energy component of the spectra to the high energy one is different for different particles. For example, the inspection of data shows that the isotropic contribution is most significant in case of ^{4}He which can be easily evaporated from compound nucleus, whereas it is almost negligible for ^{3}He, which is not so strongly bound as ^{4}He and thus its evaporation as stable particle is less probable. On the other hand, the coalescence as well as contribution from moving sources is comparable for these both ejectiles. This results in different relative contributions of isotropic - low energy, and anisotropic - high energy emissions and thus leads to different shapes of ^{3}He and ^{4}He spectra observed experimentally.

While the model of fast break-up with smoothly varying parameters is able to reproduce energy dependence of differential cross sections of LCPs and IMFs, it is not clear whether such a reaction

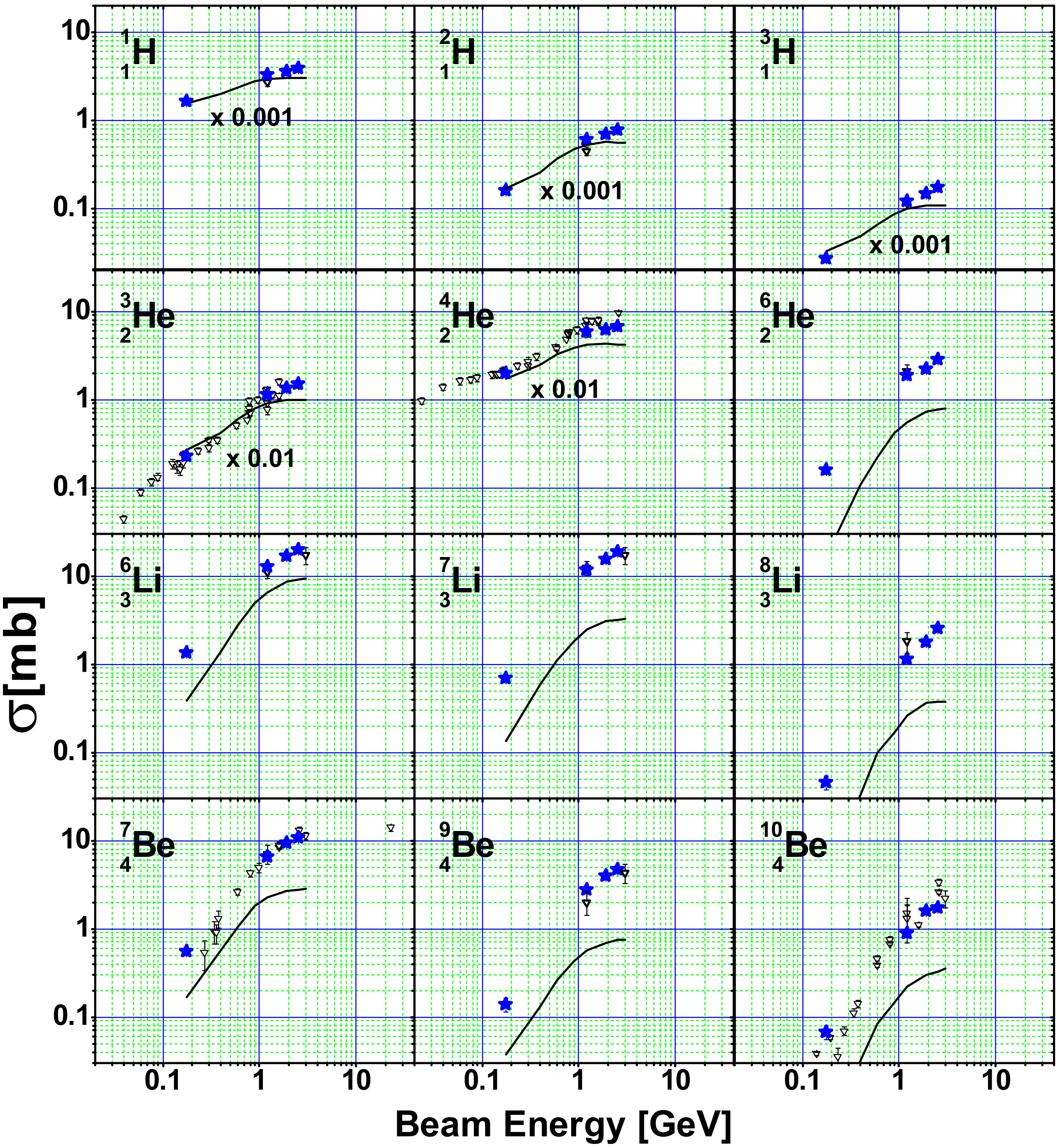

Figure 8.2: Excitation function of LCPs and IMFs produced in proton induced reaction on Ni target. Blue stars show the data from present thesis, open triangles are data from literature described in text, solid line corresponds to two step model prediction. Cross sections for LCPs were scaled by factors depicted in the figure.

mechanism is compatible with energy dependence of production cross sections for heavier ejectiles, which were not measured in the present experiment. Since the *differential* cross sections for such products are not available in the literature, the following discussion is based on the energy dependence of *total* production cross sections and its comparison to predictions of two step model

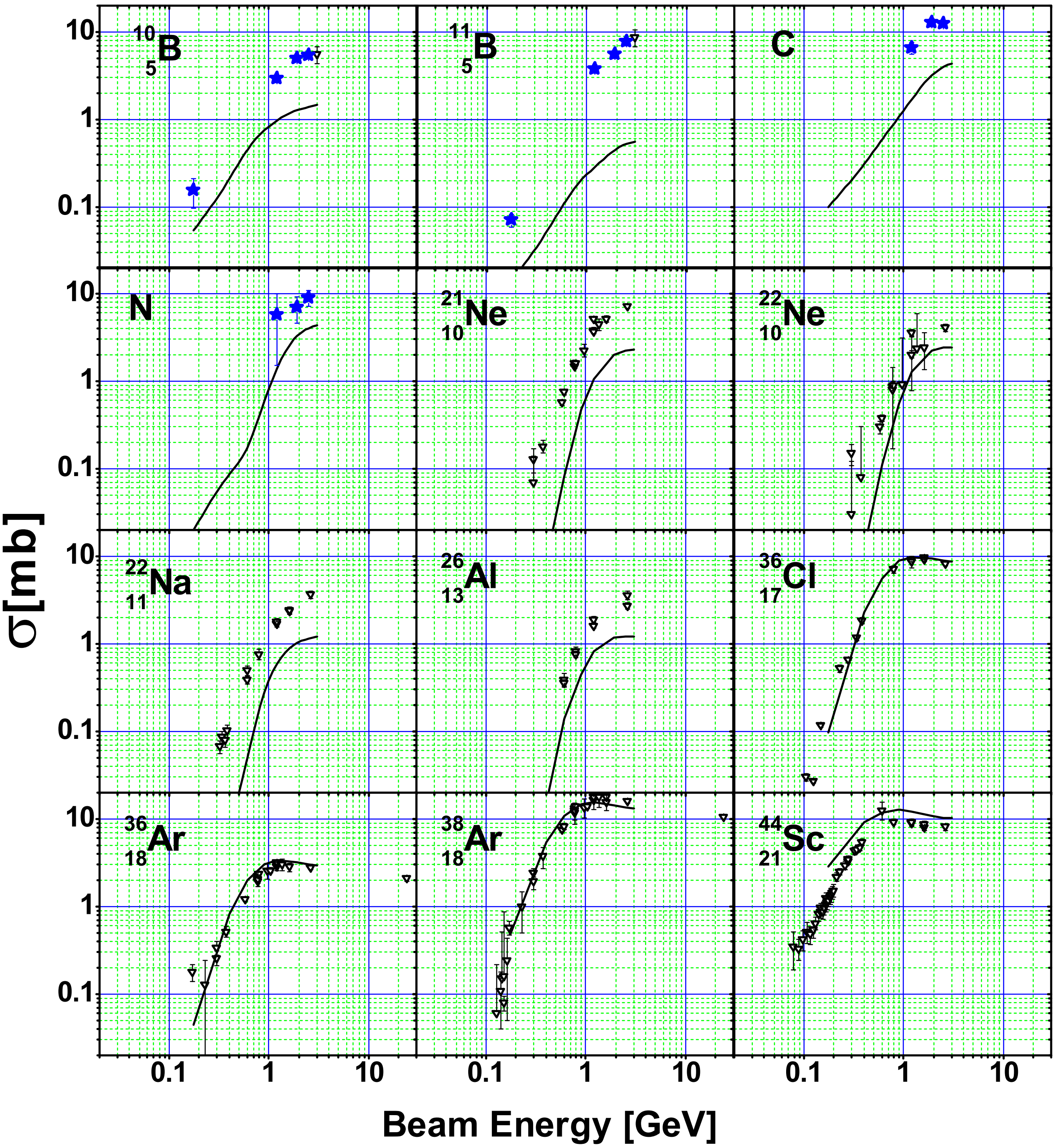

Figure 8.3: Same as Fig. 8.2, but for heavier products up to ^{44}Sc.

of the reaction without contribution of the fast break-up mechanism. This should allow to validate conclusions derived from the present study of $\frac{d\sigma}{d\Omega dE}$ for production of LCPs and IMFs which postulate necessity to introduce an additional reaction mechanism competing with that of two step model.

Whereas the angular and energy distributions gave clear indication of presence of two different reaction mechanisms, values of the total production cross sections, do not provide any distinction

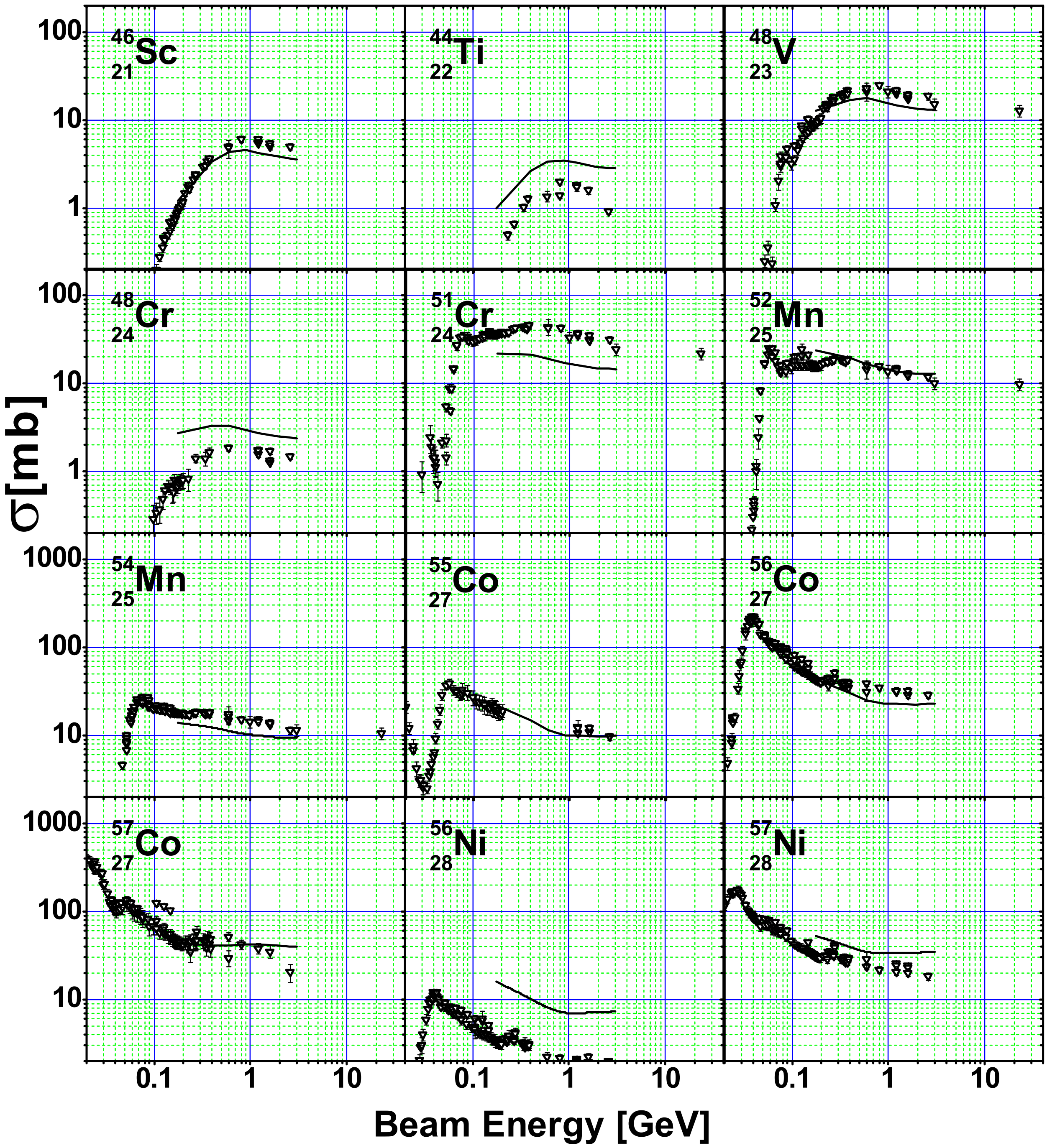

Figure 8.4: Same as Fig. 8.3, but for the heaviest products

between equilibrium and preequilibrium contributions to the reaction.

There is, however, a chance that the theoretical analysis performed in the frame of the two step model gives cross sections so much smaller from the experimental data that the preequilibrium component becomes evident also for the total cross sections. It is indeed the case as can be seen on Figs. 8.2, 8.3, where experimental cross sections for production of LCPs and IMFs obtained in the present thesis (blue stars), and those from the literature (open triangles) are compared with predictions of the two step model (lines).

It should be pointed out that the experimental total cross sections were measured mainly for specific products which could be analyzed by radiochemical methods. Most of the data were taken from papers of R. Michel et al. [98, 99, 126]. Data for noble gases are from Ammon et al. [4], and few single points were adapted from [60, 117, 122]. The experimental cross sections from the present thesis fit very well to the literature data. The theoretical cross sections were evaluated by means of INCL4.3 program of A. Boudard et al. [29] supplied by nuclear evaporation code GEM2 of S. Furihata [52–54].

The experimental and theoretical cross sections increase in full studied energy range i.e. from 0.175 GeV to 3.0 GeV, thus it may be stated that the two step model predicts properly the general energy trend of the data. However, the absolute cross sections derived from the model differ significantly from the experimental ones. This is most evident for IMFs where the experimental data are larger by factor ~ 5 than the theoretical cross sections in the whole available beam energy range. The data for LCPs agree reasonably well with theoretical cross sections at low energies but are clearly larger at energies above 1.0 GeV.

Such energy dependence fits very well with the presence of the fireball and break-up contributions derived from analysis of differential cross sections.

Indeed, inspection of Fig. 7.11 indicates that relative contributions of these processes for LCPs quickly increase from negligible values at 0.175 GeV to significant values at 1.2 GeV and almost level at higher energies. On the other hand the relative contribution of these processes to production of IMFs is quite large and approximately constant in full energy range from 0.175 GeV to 2.5 GeV (cf. Fig. 7.12). Thus, the energy dependence of contribution of nonequilibrium mechanism induced by fast break-up resembles exactly the energy dependence of the difference between experimental data and predictions of two step model present on Fig. 8.2. This is also true for heavier IMFs (^{10}B - ^{26}Al) shown in Fig. 8.3.

It is important to note, that *described above systematic underestimation of total cross sections by two step model is not present for products heavier than ^{26}Al.* This can be seen in Figs. 8.3 and 8.4. The energy trend predicted by two step model follows exactly the trend of the data for all heavy products. The absolute value of the cross sections is reproduced perfectly for some isotopes as, e.g., ^{36}Cl, ^{36,38}Ar, ^{52}Mn, and ^{55,57}Co but for other isotopes the agreement is poorer. It should be, however, pointed out that deviations of both sign, positive and negative, between the model cross sections and the data are present. It means, that no systematic trend of deviations appears for products heavier than ^{26}Al.

The following procedure has been applied to present in compact form the comparison of data and model predictions for all products, i.e. products studied in the literature as well as those from the present investigation. The experimental and two step model total production cross sections were averaged over energy range from 1.1 GeV to 3.0 GeV. This energy range was chosen because there systematic departure of the theory from experiment is present for all ejectiles with mass number $A < 30$. Relative (to the model cross sections) and absolute differences between experimental and model cross sections were calculated and depicted on Fig. 8.5. Results of the present thesis are shown as blue stars when the analogous data were not available in the literature and as red squares when the averaging over present data and literature cross sections could be done. The results based only on the literature data are depicted as open triangles.

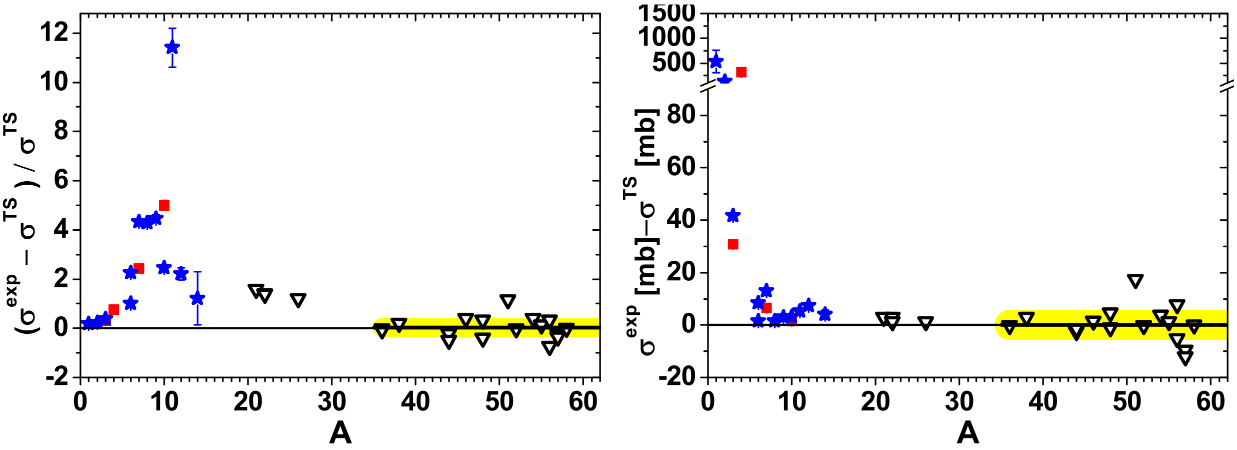

Figure 8.5: Relative to the two step model predictions (left figure) and absolute (right figure) deviations between the experimental total cross sections and results of calculations in the frame of the two step model versus mass of the product. Symbols are described in the text. The experimental errors are presented as vertical bars in the case when they are larger than dimension of symbols.

The systematic positive difference is clearly visible in both representations for light products (A < 30). On the other hand, departures of the two step model predictions from the data for heavy products are randomly scattered around zero value. The height of yellow horizontal bars represents one standard deviation characterizing the scatter of results for this group of the products. Presence of random character deviations is likely due to the fact that the theoretical model is properly reproducing average trend of the data, however is not able to take exactly into account properties of individual reaction products, as e.g., details of level densities, which can influence significantly the evaporative stage of the reaction.

The described above properties of deviations of the data from predictions of two step model suggest that additional mechanism is present for light but absent for heavy products. This additional mechanism may be identified as the break-up process which was introduced for analysis of the differential cross sections in previous chapters. It explains in natural way why the cross sections of target like products are well reproduced by two step model itself whereas cross sections for light products are influenced by this mechanism. *Break-up of the target nucleus involves emission of ejectiles from prefragments which are smaller than target nucleus, thus the target-like products cannot appear due to this mechanism in contrast to light ejectiles.*

The same hypothesis allows to explain why the relative deviations, shown in the left part of Fig. 8.5 are quite large for products of mass number 6 - 30 and rather small for LCPs. Rearrangement of the target nucleus due to break-up is wider-reaching than that caused by intranuclear cascade, therefore excitation energy of break-up prefragments should be in most cases higher than excitation energy of heavy residuum of the intranuclear cascade. It is clear that emission of IMFs requires larger energy than emission of nucleons and other LCPs. Thus it is reasonable to conjecture that break-up will result in larger ratio of IMFs to LCPs emissions than ratio predicted by two step model.

One might, however, argue that small relative deviations between two step model cross sections and experimental data for LCPs indicate that no break-up mechanism is present. Inspection of *absolute* deviations of the data from model cross sections presented in the r.h.s. part of Fig. 8.5 allows to reject this argument by the following reasoning. It is clear that the absolute deviations are much larger than the experimental errors. Furthermore, the deviations are of the same order of magnitude for protons, deuterons and alpha particles (250 - 600 mb) as the total absorption cross section of protons impinging onto Ni target ($\sim$ 720 mb). This means, that the deviations are equivalent to emission of at least one among these LCPs for each event of proton - target collisions. Such big effect cannot be assumed as negligible, thus the contribution of break-up is significant.

It was found in the present analysis of differential cross sections that the best fit of the data for LCPs was achieved when the two step model cross sections were multiplied by factor $F \sim 0.7$. It was justified by requirements to make a room for contribution from break-up mechanism which in original studies of authors of INCL and GEM programs was completely omitted, and its virtual presence was effectively simulated by appropriate adjusting of two step model parameters. The necessity of scaling two step model cross sections for LCPs production by factor $F \sim 0.7$ seems to be in apparent contradiction to the fact that the cross sections for target-like products of the reaction are well reproduced by two step model without involving any scaling factor as it was discussed above.

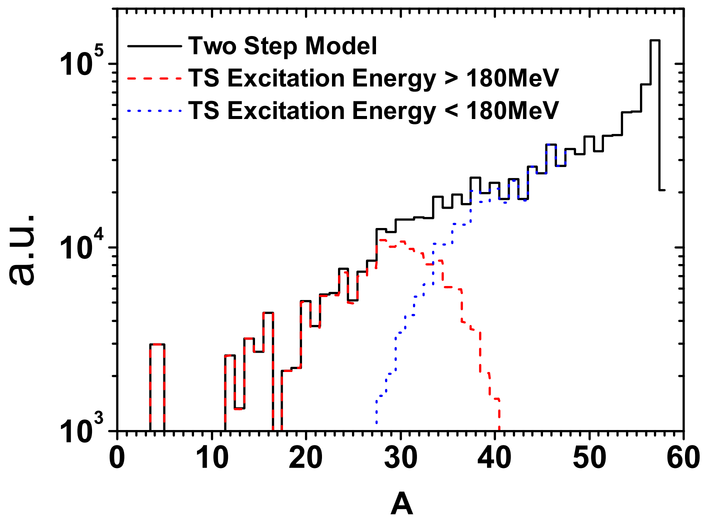

Figure 8.6: Mass yield of the heaviest product of intranuclear cascade followed by evaporation from the target residuum. The solid line histogram presents results of two step model calculations performed by means of INCL+GEM programs without imposing any conditions. The dashed and dotted line histograms correspond to target residua excited to energies larger than and smaller than 180 MeV, respectively.

The mentioned contradictions may be reconciled by following reasoning: The target-like products, which differ from initial target nucleus by lack of several nucleons, can appear only in soft collisions, i.e., collisions involving small energy transfers. The light ejectiles may be, however, produced in soft as well as in violent collisions. Thus it may be conjectured, that the competition of the break-up mechanism, which introduces large rearrangement of the target nucleus and therefore needs large energy transfer, should mainly influence emission of light reaction products. This is illustrated on Fig. 8.6 where mass yield of the heaviest product of intranuclear cascade followed by evaporation from the target residuum is shown for three different situations appearing in 2.5 GeV proton induced reaction on Ni target: (a) without imposing any conditions on the excitation energy of the target residuum before evaporation (solid line histogram), (b) the excitation energy of target residuum larger than 180 MeV (red - dashed histogram), and (c) the excitation energy of target residuum smaller than 180 MeV (blue - dotted histogram). It is evident that *all* products heavier than $A \sim 40$ are produced only in soft collisions, i.e. those in which the target residuum is excited to energies smaller than 180 MeV. On the other hand, the reactions which lead to the heaviest product lighter than $A \sim 27$ correspond to violent collisions in which target residuum is excited to energies higher than 180 MeV.

It should be noted that light ejectiles may appear with or without heavy partners and therefore Fig. 8.6 does not present influence of gating on the excitation energy on yield of *all* light products. Such an effect is depicted on Fig. 8.7 where the ratio is shown of production cross sections evaluated with the cut on the 180 MeV of the excitation energy of the target residuum and cross sections obtained without putting this gate.

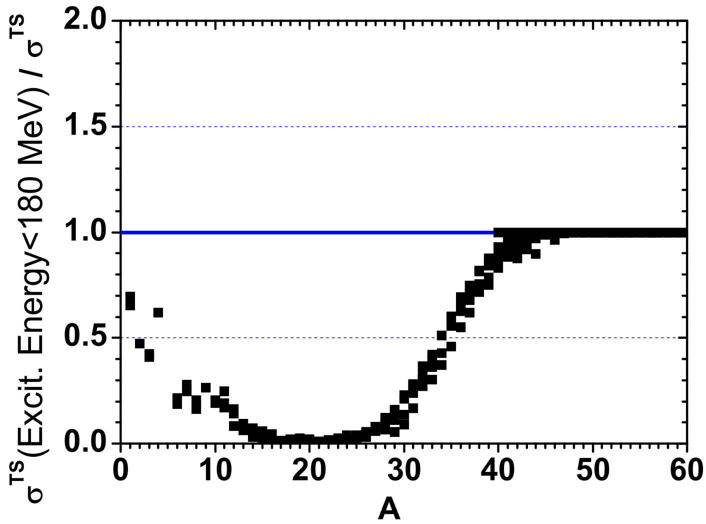

Figure 8.7: Ratio of production cross sections evaluated in the frame of two step model with restriction on excitation energy of target residuum to be lower than 180 MeV to cross sections evaluated without any restriction.

The ratio presented on Fig. 8.7 is equal to unity for masses larger than $A > 40$, what means that these products appear only due to soft proton - target collisions. It is reasonable to conjecture that such collisions may be well described by two step model. However, for lighter products the ratio becomes much smaller than unity, what indicates that the excitation energy of the target residuum is generally larger than 180 MeV in this case. It means that lighter ejectiles appears due to violent collisions, which can also lead to break-up of the nucleus instead of intranuclear cascade. Reduction of the two step model cross section by gating out the violent collisions justifies the phenomenologically introduced reduction factor F used in the analysis of differential cross sections of LCPs discussed above.

The question appears, whether removing of violent collisions from two step mechanism results only in magnitude of differential cross sections, i.e. whether the shape of energy spectra and angular distributions remains unchanged. The answer to this question may be found from inspection of Fig. 8.8.

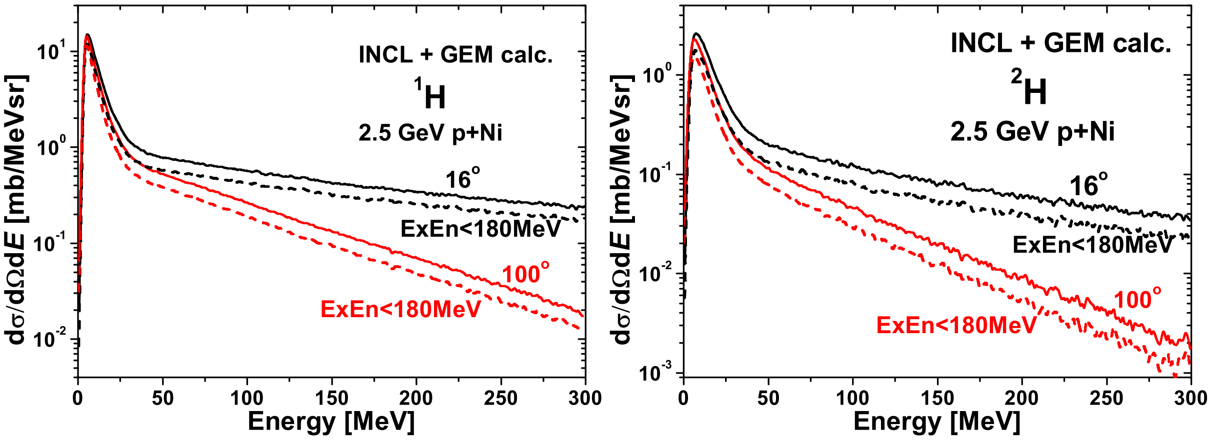

Figure 8.8: Double differential cross sections of protons (l.h.s.) and deuterons (r.h.s.) without (solid line) and with (dashed line) putting gate on excitation energy for two chosen detection angle. Prediction of two step model for proton induced reaction on Ni target at 2.5 GeV.

It is evident that the spectra shown on Fig. 8.8 have the same shape for calculations in which the excitation energy gate was imposed and for calculations without any restrictions on the excitation energy of target residuum. This shows that the scaling of the two step model cross sections in the phenomenological analysis described in Chapter 7 is equivalent to attributing violent collisions to break-up mechanism instead of describing them by intranuclear cascade.

Chapter 9

Summary and conclusions

In the present study double differential cross sections $\frac{d\sigma}{d\Omega dE}$ were measured for light charged particles (LCPs) and for intermediate mass fragments (IMFs) produced in proton induced reactions on Ni target. In the experiment the following beam energies were used: 0.175, 1.2, 1.9, and 2.5 GeV. Double differential cross sections were determined for: ^{1,2,3}H, ^{3,4,6}He, ^{6,7,8,9}Li, ^{7,9,10}Be, ^{9,10,11}B, C and N, detected at seven scattering angles: 16°, 20°, 35°, 50°, 65°, 80°, and 100° in the laboratory system. The differential cross sections were measured in ejectile energy range broad enough to permit for determination of energy integrated cross sections with accuracy better in most cases than 10 %. Together with the knowledge of angular distributions this allowed to estimate total production cross sections for ejectiles listed above.

The obtained differential cross sections form, to our knowledge, the most extensive set of data existing in literature for reactions induced by protons on Ni targets in the studied beam energy range. Due to this, they could be used to put severe constraints to models of the reaction mechanism.

Energy spectra of all light charged particles and intermediate mass fragments studied in the present work indicate a presence of two different components. The low energy part of the spectra is isotropic whereas the high energy part varies monotonically with scattering angle. Such character of energy spectra is very similar to that observed in previous study of proton induced reactions on Au target at proton beam energies 1.2, 1.9, and 2.5 GeV, published by Bubak et al. [31] and Budzanowski et al. [33]. It was, therefore, assumed that the reaction mechanism proposed in these papers for Au target is also valid for Ni target. This reaction mechanism consists in *competition* of two processes:

(i) the intranuclear cascade of nucleon-nucleon collisions with inclusion of coalescence of nucleons into LCPs, followed by evaporation of ejectiles from equilibrated target residuum, and

(ii) fast break-up of target nucleus followed by emission of ejectiles from moving, excited prefragments of the target nucleus.

The cross sections for the first of these processes were calculated using the INCL4.3 [28] computer program for description of the fast stage of the reaction and GEM2.0 computer program [52,53] for evaporation of particles from the remnant of the intranuclear cascade. The calculations were performed with default values of the model parameters recommended by the authors of the programs.

The cross sections of the emission from the moving sources – excited fragments of the target nucleus – were evaluated assuming isotropic emission in the center of mass of the sources moving along the direction of the proton beam, and assuming Maxwell distribution for the energy spectra. The velocity of sources, their temperature, height of the Coulomb barrier for emission of detected particles, and the total cross section for the emission were treated as free parameters.

The analysis of differential cross sections $\frac{d\sigma}{d\Omega dE}$ performed according to the above procedure lead to very good description of all the data. Moreover, the obtained values of free parameters, characterizing the moving sources of ejectiles vary smoothly from ejectile to ejectile and are similar for three higher beam energies (1.2, 1.9, and 2.5 GeV) indicating that *the main properties of the reaction mechanism do not change in this energy range*. The total cross sections of all model processes increase smoothly in the range of energies between 1.2 GeV and 2.5 GeV. Relative contributions of competing mechanisms remain approximately constant and of comparable magnitude.

The description of low energy data was equally good as that for higher energies, however, values of obtained parameters indicate that *the mechanism of the reaction competing with the intranuclear cascade is different at 0.175 GeV than that at high beam energies*.

This is illustrated by Figs. 9.1 and 9.2 below. The high energy proton impinging on to nucleus is able to knock-out the nucleons lying on its straight way through the nucleus. These nucleons are depicted in the left part of Fig. 9.1 as that part of the nucleus, which is separated from the rest of the nucleus by dashed lines. This group of nucleons flies away in forward direction as one entity - "the fireball", whereas the highly excited remnant nucleus breaks-up forming two excited prefragments. These prefragments as well as the fireball serve as moving sources emitting the particles. The momentum of the fireball and the momenta of two remaining moving sources, found from the fits to experimental spectra at high beam energies, are significantly smaller than the beam momentum. This means, that the proton from the beam does not "belong" to the fireball. The situation after collision is shown in the right part of the Fig. 9.1.

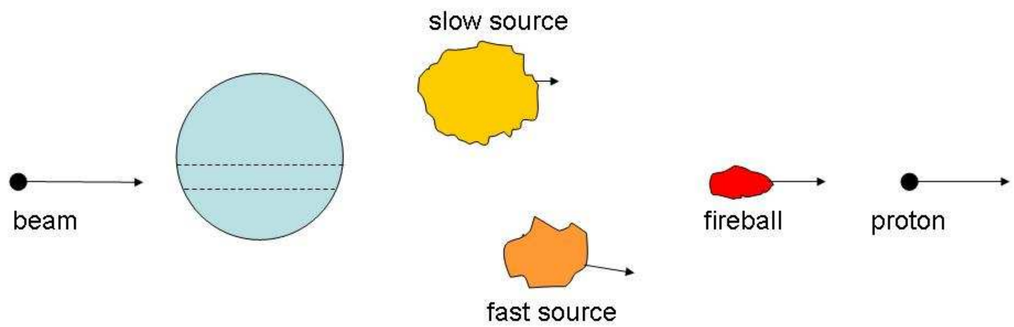

Figure 9.1: Fireball emission at high beam energies (1.2, 1.9, and 2.5 GeV).

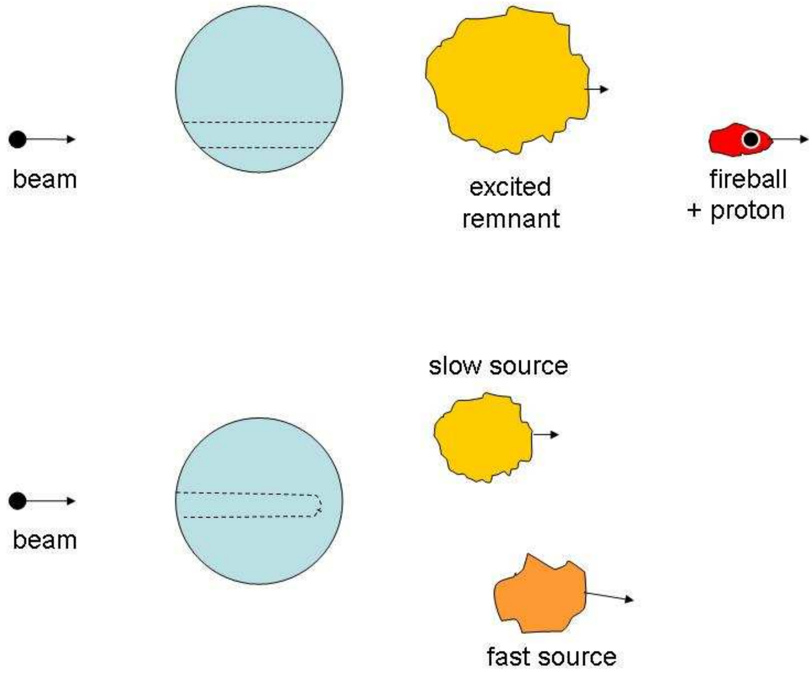

Figure 9.2: Upper part of the figure shows the fireball emission at 0.175 GeV beam energy. The excited remnant has to low excitation energy to breaks-up but may evaporate particles. In the lower part of the figure the capture of the proton beam – without emission of fireball – is followed by break-up of the nucleus into two excited parts emitting particles.

At low beam energy – 0.175 GeV, the velocity of the fireball is larger (*sic!*) than at higher energies, where this velocity seems to be almost energy independent. Moreover, the momentum of the fireball at low beam energy is close to the beam momentum what suggests, due to the momentum conservation, that *the fireball contains the proton from the beam as its constituent part*. It also means that most of the kinetic energy of the beam is transferred into kinetic energy of the fireball and thus the remnant nucleus cannot be very highly excited. This is in agreement with observation, that the remnant nucleus does not break-up into two excited sources of ejectiles, nevertheless, it is excited enough to appear as single source evaporating particles. The above statement means, that *emission of the fireball cannot be followed by break-up of the target nucleus at low beam energy*. Such a situation is shown in upper part of Fig. 9.2. It can be conjectured, that at 0.175 GeV *the break-up into two excited prefragments emitting particles proceeds only, when the bombarding proton is captured by the target nucleus with deposition of its full momentum and energy* as it is presented in the lower part of the Fig. 9.2.

It turned out that the fireball created at low beam energy emits only protons and/or deuterons whereas the fireball created at higher energies contributes also to triton and He spectra. The explanation of this fact may be based on the following, simple reasoning: At low beam energy the fireball is mainly created in peripheral, soft collisions, because hard, central collisions would lead to full dissipation of its momentum and energy what would result in the capture of the bombarding proton by the nucleus without appearing of the fireball. At high energies, on the contrary, the fireball may be created both in peripheral and central collisions because the energy and momentum of impinging proton cannot be so easily dissipated. This means, that at low beam energy the bombarding proton, which initiates the creation of the fireball, meets effectively on his way a smaller number of nucleons than at high beam energy. This is caused by two effects; a shorter path of the proton through the nucleus and a smaller density of nucleons in the nucleus for peripheral than for central collisions. From this reason the fireball at low beam energy should be smaller than that at high energies even if the presence of the proton from the beam in the fireball at low beam energy compensates this effect to a large extent.

Conclusions concerning the reaction mechanism were in the present work obtained from analysis of the cross sections for ejectiles lighter than Nitrogen. It was, therefore, important to check whether the presence of the postulated reaction mechanism leads to an agreement with the behavior of cross sections for heavier products, which were not measured in the present experiment. The data available in the literature were used for this purpose. It turned out that these data, which consist only of the total production cross sections, provide convincing support to the postulated reaction mechanism. It was found, that the cross sections for ejectiles heavier than ^{26}Al are well reproduced by intranuclear cascade mechanism followed by evaporation from an equilibrated target remnant, whereas the experimental cross sections for all lighter ejectiles require an additional contribution from another mechanism. *This is in accordance with the hypothesis of competition of the fast break-up of the target nucleus with two step mechanism because the latter results in the production of all ejectiles whereas the break-up may contribute only to production of light ejectiles, lighter than fragments of the target nucleus emitted during break-up.*

The model analysis of reaction events, which proceed via intranuclear cascade followed by evaporation of particles and contribute to production of heavy, target-like residual nuclei lead to interesting inference, that *competition between fast break-up and two step mechanism is limited to violent collisions only, i.e., those which correspond to large energy transfer.*

In summary, it can be stated that the reaction mechanism postulated in [31, 33] for p+Au nuclear system is consistent with all available data for p+Ni at beam energies 1.2, 1.9, and 2.5 GeV, however, at beam energy 0.175 GeV a modification of this mechanism must be taken into consideration. Since Ni and Au targets differ significantly in mass, in dimensions as well as in neutron to proton number ratio, such *similarity of observed effects for both targets leads to the hypothesis, that the described mechanism is typical for all target nuclei. It is very interesting to proof this hypothesis experimentally.*

The break-up contribution was parameterized in the present work by simple phenomenological formula with several free parameters which varied smoothly with beam energy. They were also not very different for Au and Ni targets. This may indicate that the investigation of proton induced reactions on other nuclei could allow for some kind of general parametrization of this reaction mechanism. A more ambitious project might consist in the microscopic description of the break-up process on the equal footing as the intranuclear cascade process. Each of these tasks requires the data for proton induced reactions on several targets, lighter and heavier than Ni, more abundant than those available at present in the literature.

Appendix A

Phenomenological parametrization

In this appendix the assumptions and details of formulation of the one moving source model are presented. In the case of assumed larger number of moving sources the contributions from individual sources are added incoherently. The original formulation of the model may be found in the paper of Westfall et al. [150] and the further implemented modifications are discussed by Bubak et al. [31].

There are three basic assumptions of the moving source model:

- The source is moving along the beam direction with velocity β.
- The ejectiles are emitted isotropically in the source frame.
- The kinetic energy E^* available in the two-body break-up of the source is characterized by a Maxwellian distribution with temperature parameter τ.

$$\frac{d^2\sigma}{dE^* d\Omega^*} = \frac{\sigma}{2(\pi\tau)^{3/2}} \sqrt{E^*} \exp\left[-\frac{E^*}{\tau}\right] . \tag{A.1}$$

The normalization of the above distribution is done in such a way that the parameter σ is the total cross section integrated over energies and angles of the ejectile emission.

Since both, the source and the emitted ejectile, have finite masses (A_S and A_F, respectively) the conservation laws of the momentum and energy can be fulfilled simultaneously only when the recoil of the source is taken into account. Then the energy of the ejectile observed in the frame of the source - E' - will be related to the full kinetic energy E^* by the equation:

$$E^* = \nu E', \text{ where } \nu \equiv \frac{\mathrm{A_S}}{\mathrm{A_S} - \mathrm{A_F}} . \tag{A.2}$$

Inserting the above expression for E^* into equation (A.1) allows to rewrite the latter as the formula for distribution of kinetic energy E' of the emitted fragment in the rest frame of the source, where instead τ - the temperature of the source - an **apparent** temperature $T \equiv \tau/\nu$ is introduced:

$$\frac{d^2\sigma}{dE' d\Omega'} = \frac{\sigma}{2(\pi T)^{3/2}} \sqrt{E'} \exp\left[-\frac{E'}{T}\right] . \tag{A.3}$$

Treating the apparent temperature as a free parameter in fitting the double differential cross sections $\frac{d^2\sigma}{dE'd\Omega'}$ for individual ejectiles allows to obtain information on the mass of emitting source A_S and the recoil corrected temperature τ of the source from parameters of the linear dependence of apparent temperature T on the ejectile mass A_F:

$$T \equiv \frac{\tau}{\nu} = \tau - \left(\frac{\tau}{A_S}\right) A_F. \tag{A.4}$$

The presence of the Coulomb barrier, preventing the charged ejectiles to leave the source, was neglected in deriving of the (A.3) expression. Hence it is appropriate only for neutral reaction products. For charged particles the low energy part of the kinetic energy distribution has to be modified by taking into consideration the finite transmission probability through the barrier. In the present thesis this effect was introduced by multiplying formula (A.3) by energy dependent probability $P(E)$ to overcome the Coulomb barrier and modifying normalization of the energy distribution to leave unchanged interpretation of the parameter σ (i.e. the total production cross section of observed ejectiles). The following functional form of $P(E)$ has been assumed:

$$P = \frac{1}{1+\exp\left[-\left(\frac{E-kB}{d}\right)\right]}, \tag{A.5}$$

where k and d determine the height of the Coulomb barier and the diffuseness of the transmission function $P(E)$, respectively.

The k is the height of the Coulomb barrier in the units of B - the height of the Coulomb barrier of two touching, spherical nuclei with the mass and atomic numbers (A_F, Z_F) (for the ejectile), and $(A_S - A_F, Z_S - Z_F)$ (residuum of the source after emission of the ejectile):

$$B = \frac{Z_F(Z_S - Z_F)e^2}{1.44[A_F^{1/3} + (A_S - A_F)^{1/3}]} \;. \tag{A.6}$$

Since the mass and atomic numbers of the source are not known during the fitting procedure, they were fixed at the largest possible values: A_S=58, and Z_S=28 - corresponding to the most abundant isotope of the target nucleus. Thus, the k parameter is expected to be smaller than one and can be easily compared for different considered ejectiles.

The d parameter characterizes the diffuseness of the transmission probability function $P(E)$ which increases from value of 0.1 to 0.9 in the energy range equal $[kB - 2.2d,\ kB + 2.2d] \equiv 4.4d$ around energy kB. Thus it seems to be more intuitive to present values of B/d instead d as result of the fit. It was found that results of the analysis do not depend strongly on this parameter and therefore it was usually fixed at some reasonable value: $B/d = 4 - 10$.

It was necessary to introduce additional factor $1/I(kB, d, T)$ to assure proper normalization of the energy distribution , i.e. to preserve previous interpretation of the σ parameter as the total production cross section after multiplication the formula (A.3) by transmission probability factor $P(E)$:

$$\frac{d^2\sigma}{dE'd\Omega'} = \frac{\sigma}{4\pi T^{3/2} I(kB,d,T)} \frac{\sqrt{E'}\exp\left(-\frac{E'}{T}\right)}{1+\exp\left(\frac{kB-E'}{d}\right)}, \tag{A.7}$$

$$\text{where} \quad I(B,d,T) = \int_0^\infty \frac{dx\sqrt{x}\exp(-x)}{1+\exp\left(\frac{kB-Tx}{d}\right)} \tag{A.8}$$

The evaluation of the integral $I(B, d, T)$ was done numerically by the Gauss-Laguerre method.

The transformation of the above formula is necessary from the rest frame of the emitting source to the laboratory system, while fitting its predictions to the experimental cross sections. The transformation can be performed by the following formula:

$$\frac{d^2\sigma}{dEd\Omega} = \frac{p}{p'} \frac{d^2\sigma}{dE'd\Omega'} \approx \sqrt{\frac{E}{E'}} \frac{d^2\sigma}{dE'd\Omega'}. \tag{A.9}$$

The first equality is exact, and the second approximation is precise in nonrelativistic limit, which is well fulfilled in case of most of the detected ejectiles.

The kinetic energy E of the ejectile measured at the angle θ in the laboratory frame was evaluated from kinetic energy E' determined in the frame of the moving source by the following nonrelativistic relation:

$$E' = E + \frac{m\beta^2}{2} - \sqrt{2mE}\beta \cos\theta_{LAB}, \tag{A.10}$$

where β is the velocity of the source in the laboratory system, and m is the mass of the emitted ejectile.

Appendix B

Data analysis

B.1 Detector calibration

One of crucial point for receiving proper double differential cross sections is precise detector calibration. Admittedly PISA experiment is not interested in measure monoenergetic peak of some resonance, but in achieve smooth energetic spectrum. However each error in energetic calibration will affect not only on shape of spectra, but also on absolute value of $\frac{d\sigma}{d\Omega dE}$. The best way to achieve proper detectors calibration is to measure well known few monoenergetic line spread as wide as possible in energetic range of detection. Unfortunately in most case of PISA detector it is not possible what is caused by the fact that experimental setup is positioned on internal station of COSY synchrotron. There was no possibility to instal intensive α-source. Additionaly α particle emitted from the source could reach only the first detector. For all detectors, calibration were done using program estimating energy loss in detectors material.

B.1.1 Program used for detector calibration

It is necessary to obtain a proper detector's energy calibration. It is possible using well known parametrisation of $\frac{dE}{dx}$ for different isotopes passing through the detectors. Such a parametri sation was made by J.F.Ziegler at al. [155] , and it's available via Internet in form of PC program SRIM [156]. This program is "user friendly" and include a lot of information, such a particle mass, target density, and it counts also compound correction for such a molecule as butane and many different. Program SRIM 2003 ver.26 was used to generate $\frac{dE}{dx}$ table for all interesting isotopes, passing through Silicon, CsI. Also, in the program are included air and stainless steal to take into accout layers beetween detectors, or beetwen detector and target. As author, mentioned parametrisation for one compound material, is well known, because it's directly compared with experiment, and precision is better than data consistency of different experiments. One can see on picture B.1 than inconsistency in experimental data is quite large but SRIM parametrisation fits these data as well as possible.

It was written dedicated program using the generated $\frac{dE}{dx}$ tables to create a lot of useful information, for PISA experiment. The program interpolate $\frac{dE}{dx}$ table using split function, so it can obtain interesting quantity for wish energy. In Figure B.2 one can see that all points from SRIM tables are laying on line obtain by interpolation function from the program.

The most important abilities of the program it is counting energy loss in telescope detectors

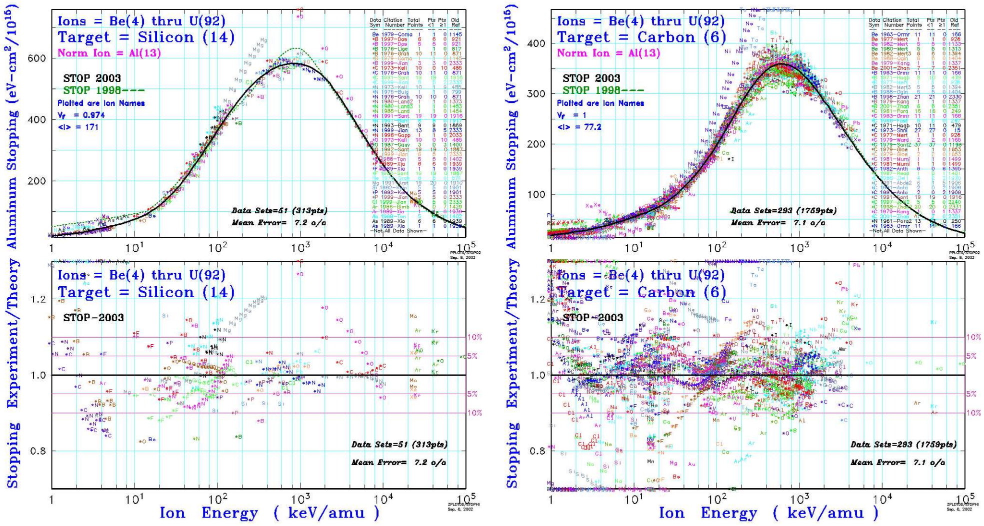

Figure B.1: Comparison of experimental data and parametrisation result of SRIM-2003 for Silicon and Carbon target respectively.

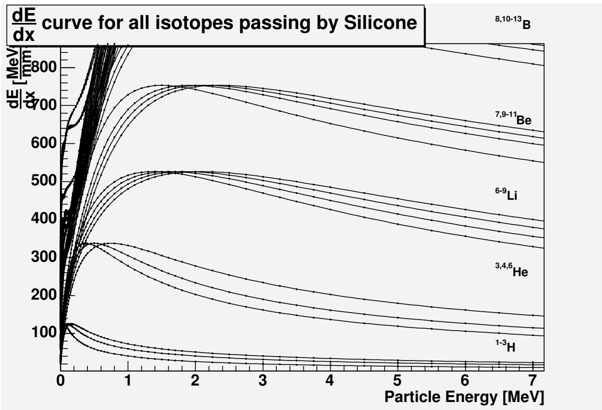

Figure B.2: $\frac{dE}{dx}$ vs. particle energy for different isotopes stopping in Silicon, points are plotted directly from $\frac{dE}{dx}$ generated by SRIM program, lines symbolise interpolation by spline function made by the program.

when particle has enough energy to reach the end of one of the telescope detector. Meantime it can provide energy loss for lower energy particle, so in dE-E diagram it generate “bananas” curve for all isotopes. This curves can be used for detector calibration. In picture B.3 one can see example of such “bananas” curves provided by the program for two silicon detectors of thickness 50 μm (dE detector) and 400 μm (E detector)

This program is able to count energy loss for many different layers with various thickness. The only limitation is existance of adequate $\frac{dE}{dx}$ tables, but there is easy way to implement new material.

The program can also provide Bragg curves, which theoreticaly can be used not only to energetic calibration of PISA’s detector, but also to calculate, thicknes of active and daed layer of Silicon detector.

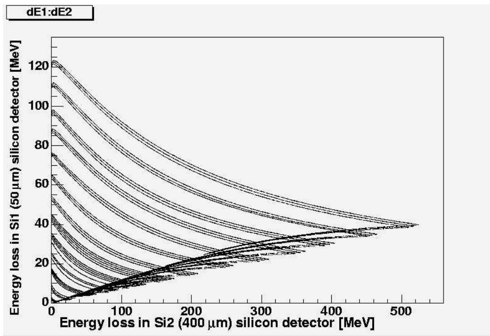

Figure B.3: "Bananas" curves obtained for dE-E detectors. as dE detector is used 50 $/mu$m and as E 400 $/mu$m silicon detector.

B.1.2 Thickness of silicon detector

As was mentioned in section B.1.1, calibration method using energy loss calculation, needs well defined detector thickness. In case of silicon detectors used for PISA experiment, only few detectors has no documentation (Quality Assurance Data Sheet provide by producer) and "nominal" thickness were asumed to be the proper one, hovewer producer point out that generally that nominal thickness can vary in 10% from the real thickness. All available information concerning silicon detectors are colected in table B.1.

B.1.3 Silicon detector calibration

Unfortunately for such procedure well knowledge of thickness is necessary. It was assumed that uncertainty of thickness of last detector (5000 μm) is relatively small, less then 1%. Then I had only to change thickness of second detector and observe changes of shape of banana curves. I take three peripheral possibility, "nominal" (400μm) thickness and minus/plus 40μm (360/440μm). I have fitted "by eyes" computed values as well as possible to experimental results. In case of second pair of detectors I have focused on high energy part, because low energy part is extremely sensitive on some death layers between detectors, which lower curve for low energy particle.

On picture B.4 one can compare quality of calibration for different thickness of second detector. They are slightly different but it seems that for "nominal" thickness results are the best. For each case calibration of first detector is changing only of 4%. So it is maximal uncertainty in first detector calibration, of course if we will know thickness of second detector this uncertainty will be much lower.

B.1.4 Calibration of Si-CsI telescope

As described in 5.2, telescope positioned in 15.6°, 65°, 20°, were mounted in air, and were separated of target by 50μm stainless steal foil. Between detectors were of course air so in calibration, this was taking into account. As it's well known impulse obtain from silicon detector is proportional to energy loss of detected particle. For calibration of silicon detector it is enough to find two parameters (linear calibration). When experimental data were plotted on (ΔE-E) graph where on ordinate are marked impulses (proportional to energy loss) from previous detector, and on abscissa

Table B.1: Information concerning Silicon detectors achieved from producer information. (Intertechnique was change to Eurisys Mesures and now is Canberra Eurisys). Thickness of entrance and exit window are stated in equivalent stopping power for Silicon measured with 5.486 MeV natural alpha particles.

Place of detector installation	producer and type of detector	"Active thickness" (Li-compensated) "depletion depth" (totally depleted)	maximum thickness variation	thickness and material of entrance window	thickness and material of exit window
35° Si1	Ortec - Planar Totally Depleted	47.8 μm	$\pm1.0\mu$m	Au - Si equ. of 0.08μm	Al - Si equ. of 0.225μm
50° Si1	Ortec - Planar Totally Depleted	40.5 μm	$\pm1.0\mu$m	Au - Si equ. of 0.08μm	Al - Si equ. of 0.225μm
80° Si1	Ortec - Planar Totally Depleted	56.3 μm	$\pm1.0\mu$m	Au - Si equ. of 0.08μm	Al - Si equ. of 0.225μm
100° Si1	Ortec - Planar Totally Depleted	51.7 μm	$\pm1.0\mu$m	Au - Si equ. of 0.08μm	Al - Si equ. of 0.225μm
35° Si2	Ortec - Totally Depleted	426 μm	n/a	Au - Si equ. of 0.08μm	Al - Si equ. of 0.225μm
50° Si2	Ortec - Totally Depleted	398 μm	n/a	Au - Si equ. of 0.08μm	Al - Si equ. of 0.225μm
80° Si2	Ortec - Totally Depleted	420 μm	n/a	Au - Si equ. of 0.08μm	Al - Si equ. of 0.225μm
100° Si2	Ortec - Totally Depleted	401 μm	n/a	Au - Si equ. of 0.08μm	Al - Si equ. of 0.225μm
100° Si3	Ortec - Totally Depleted	950–1050 μm	n/a	Au - Si equ. of 0.08μm	Al - Si equ. of 0.225μm
100° Si4	Ortec - Totally Depleted	2012 μm	n/a	Au - Si equ. of 0.08μm	Al - Si equ. of 0.225μm
35° Si3	Intertechnique Li-compensated	$\approx6000\mu$m$\pm$n/a	n/a	Au - Si equ. of 0.2μm	not transmitted
50° Si3	Intertechnique Li-compensated	$\approx6000\mu$m$\pm$n/a	n/a	Au - Si equ. of 0.2μm	not transmitted
80° Si3	Intertechnique Li-compensated	$\approx5000\mu$m$\pm$n/a	n/a	Au - Si equ. of 0.2μm	not transmitted

from following detector, it is possible to identify isotopes. Using such (ΔE-E) graph and knowing detectors thickness one can calibrate both detectors. In first approximation there are taking into account only point of "punch through". Next by successive iteration changing slightly parameters "by hand" all energy loss points obtain from program should appear exactly in the maximal intensity of experimental banana shape.

On picture B.5 is shown quality of performed calibration.

B.1.5 Range of energies for detected products

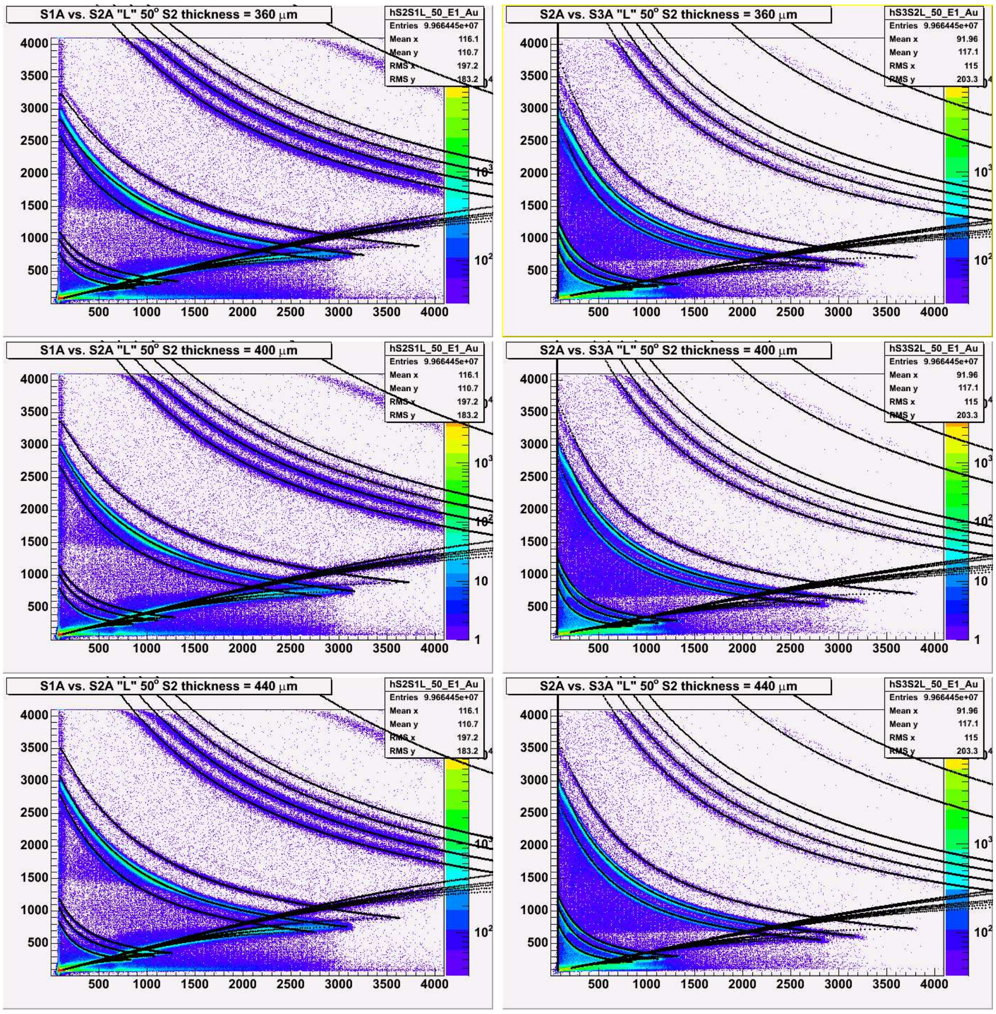

Figure B.4: Results of calibration, for first (left side) and second (right side) pair of detectors in telescope installed at 50° . Thickness of Si2 taking into account in calculation is 360 μm, 400 μm, and 440 μm for respectively top, middle, and bottom pictures. Dots (line) correspond to energy loss obtain from program, color shapes to experimental data when each color correspond to different counts in bin (according to legend on left side)

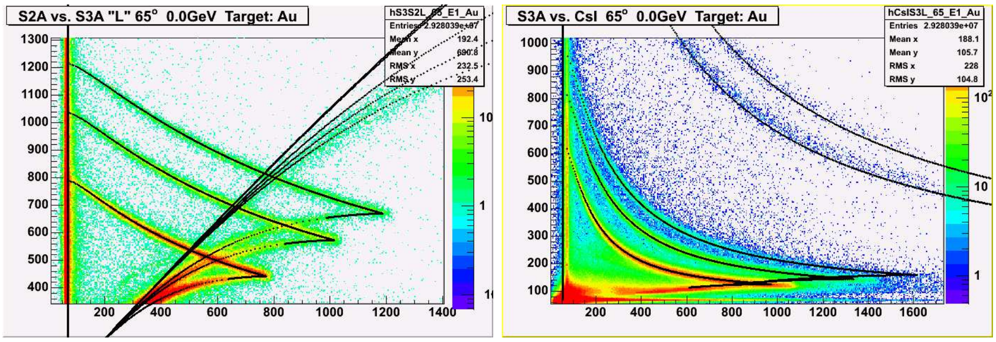

Figure B.5: Example of calibration quality for pair of 1 mm Silicon detector (left histogram), and for 1mm Silicon vs 7cm CsI (right histogram), black dots (line) correspond to energy loss obtain from program, color shapes to experimental data when each color correspond to different counts in bin (according to legend on left side)

Table B.2: Range of energies (in MeV) of isotopically identified reaction products detected at various scattering angles

Ejectile	Angle [degrees]						
	15.6	20	35	50	65	80	100
p	7.5 – 163.5	7.5 – 163.5	3.5 – 21.5	3.5 – 21.5	7.5 – 163.5	3.5 – 6.5	9.5 – 162.5
d	9.5 – 207.5	9.5 – 204.5	4.5 – 34.5	4.5 – 34.5	8.5 – 212.5	4.5 – 10.5	13.5 – 217.5
t	10.5 – 240.5	11.5 – 242.5	4.5 – 34.5	4.5 – 28.5	9.5 – 249.5	4.5 – 10.5	14.5 – 162.5
^{3}He	21.5 – 296.5	21.5 – 296.5	8.5 – 95.5	8.5 – 86.5	21.5 – 292.0	12.5 – 21.5	9.5 – 161.5
^{4}He	23.5 – 277.5	23.5 – 253.0	9.5 – 120.5	8.5 – 113.5	23.5 – 185.5	13.5 – 25.5	10.5 – 122.5
^{6}He	26.5 – 83.5	26.5 – 74.5	10.5 – 122.5	10.5 – 106.5	26.5 – 77.5	15.5 – 24.5	11.5 – 53.5
^{6}Li	42.5 – 145.5	42.5 – 147.5	17.5 – 178.0	15.5 – 178.0	43.5 – 143.5	18.5 – 48.5	18.5 – 105.5
^{7}Li	45.5 – 155.5	45.5 – 156.5	17.5 – 159.5	16.5 – 136.5	46.5 – 152.5	20.5 – 56.5	19.5 – 117.5
^{8}Li	47.5 – 113.5	47.5 – 110.5	18.5 – 115.5	17.5 – 98.5	46.5 – 112.5	21.5 – 51.5	19.5 – 85.5
^{9}Li	49.5 – 85.5	50.5 – 118.5	20.5 – 82.5	17.5 – 53.5	49.5 – 85.5	22.5 – 52.5	20.5 – 65.5
^{7}Be	61.5 – 136.5	62.5 – 146.5	24.5 – 123.5	24.5 – 138.5	61.5 – 136.5	27.5 – 69.5	27.5 – 90.5
^{9}Be	68.5 – 116.5	68.5 – 119.5	25.5 – 94.5	25.5 – 94.5	68.5 – 107.5	29.5 – 80.5	27.5 – 84.5
^{10}Be	71.5 – 116.5	71.5 – 128.5	26.5 – 101.5	23.5 – 98.5	71.5 – 122.5	30.5 – 87.5	29.5 – 80.5
^{10}B	90.5 – 123.5	92.5 – 122.5	35.5 – 92.5	30.5 – 99.5	90.5 – 111.5	38.5 – 86.5	36.5 – 90.5
^{11}B	94.5 – 136.5	94.5 – 130.5	35.5 – 116.5	31.5 – 100.5	96.5 – 114.5	39.5 – 105.5	37.5 – 91.5
^{12}B			36.5 – 96.5	35.5 –83.5		41.5 – 83.5	39.5 – 78.5

Appendix C

Sensitivity of INCL calculations to modification of free parameter values

C.1 Crosscheck of INCL results compiled on different shells

It is well known that complex computer programs can provide different results when the calculations are performed using different computers, especially if the difference concerns the operating system or compiler. This may be crucial for Monte Carlo programs which can use different, computer- or compiler-dependent generators of random numbers. Therefore, it was checked, whether cross-sections obtained from current compilation of the INCL program, which was used to calculate the intranuclear cascade results presented in this thesis, are in agreement with calculations, published by authors of the program in Ref. [29]. Results presented in the mentioned paper were obtained using INCL4.3 program combined with ABLA or GEM evaporation programs, respectively. For both evaporation programs, satisfactory agreement of isotopic energy spectra, evaluated in the present thesis and those from Ref. [29], was achieved. Some discrepancy was only caused by statistical fluctuations - inherent property of Monte Carlo calculations.

On the picture C.1 examples of such a comparison are presented. The agreement of proton spectrum evaluated in the present work with that taken from Ref. [29] means that both program, i.e. INCL and statistical evaporation program give identical results when using different computer systems. To see distinctly possible differences resulting from the INCL calculations alone, the ABLA evaporation program was used in these test calculations for evaluation of ^{3}He spectrum. This spectrum has no evaporation contribution because the ABLA code evaluates only evaporation of protons, neutrons and ^{4}He particles.

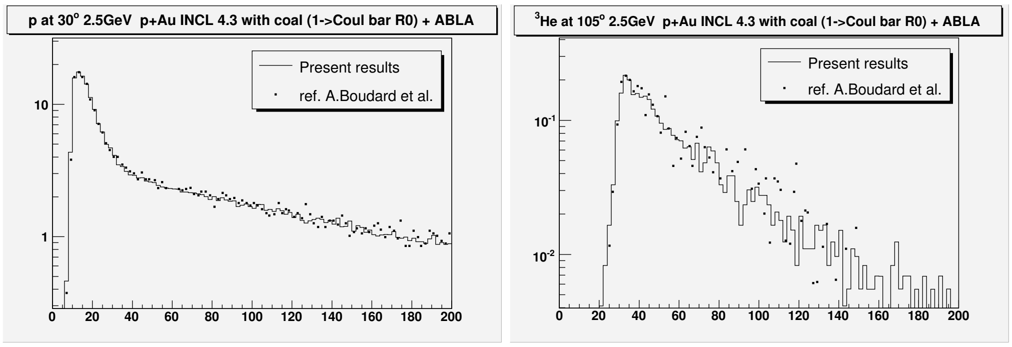

Figure C.1: Comparison of INCL results obtained while using different computers. Dots represent results of calculations published in ref. [29] and histograms represent those obtained by the same INCL program running on the computer used to prepare this PhD thesis. Parameters in both cases are the same. Differences between results are not larger then statistical deviations characterizing the Monte Carlo sampling.

C.2 Stopping time of cascade propagation for Ni target

One from two free parameters of INCL code is stopping time of cascade propagation. Authors of program suggest that for all targets and energies should be used default value of parameter. In section 4.1 and in paper [28] are listed criteria when cascade should be stopped and example of 1GeV p+Pb target are investigate. In picture C.2 excitation energy of nucleus after Intranuclear cascade are presented in function of cascade stopping time.

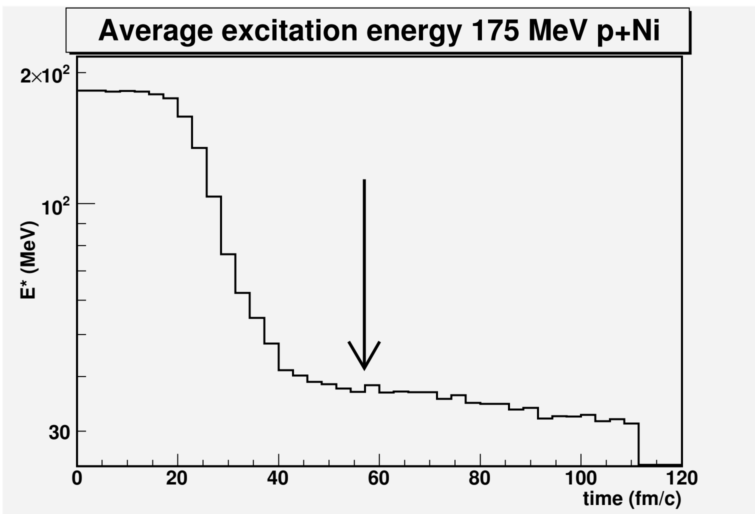

Figure C.2: Time variation of the excitation energy. The results correspond to collision of 175 MeV protons with Ni nuclei with an average impact parameter. The arrow indicate chosen stopping time.

C.3 Influence of coalescence model parameters on energy spectra shapes.

It was explained in the chapter 4.2 that the coalescence model implemented by Alain Boudard et al. [29] into the INCL program has two free parameters: h_0 and D. Their meaning is described in the above chapter. Authors of the program suggest to use the following default values of the parameters: $h_0 = 387$ MeV $(= p_F \times 1.4\text{fm})$ and $D = 1.75\text{fm}$. In the present appendix results of calculations performed with other values of these parameters are presented to show sensitivity of differential cross sections to variation of the parameters. In these calculations all other parameters of INCL model and GEM model are fixed.

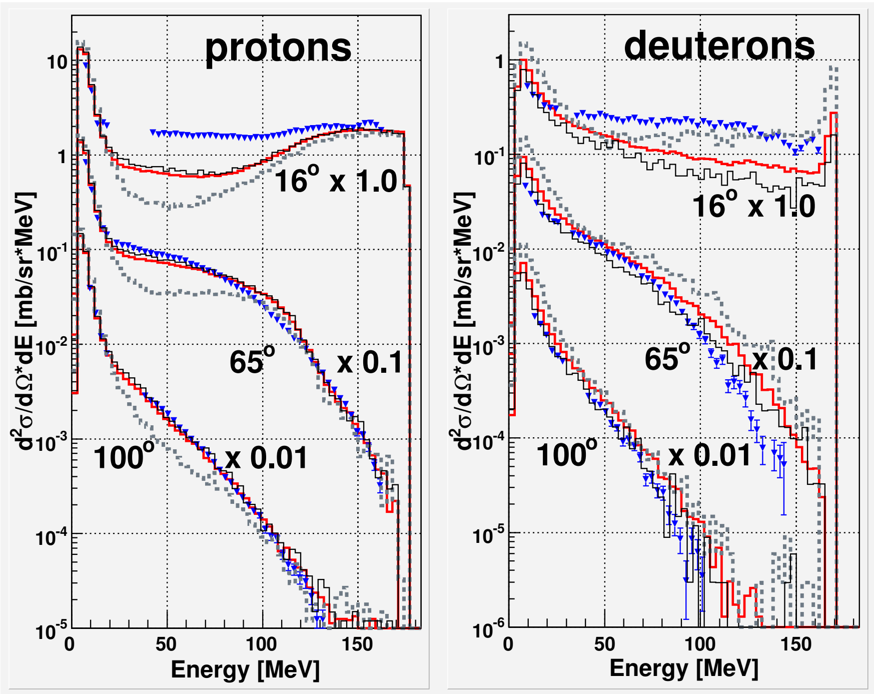

Figure C.3: Energy spectra for protons (left frame) and deuterons (right frame) at 16° , 65° , and 100° from 175 MeV protons induced reaction on ^{nat}Ni. Blue points correspond to experimental data obtained from PISA experiment. Lines correspond to different parameter h_0 of coalescence model (see text): solid red thick line – $h_0 = p_F \times 1.4$ fm (default value), dashed red thick line – $h_0 = p_F \times 2.0$ fm, thin line – $h_0 = p_F \times 1.2$ fm. To ease the reading of the figure, the successive spectra have been multiplied by decreasing powers of 10.

Due to coalescence of nucleons escaping from the nucleus during cascade of nucleon-nucleon collisions there are created composite particles. It is, therefore, obvious that the spectra of composite particles evaluated without and with coalescence can be quite different. On the other hand, the protons which take part in creating of these composite particles cannot be observed in the proton channel, thus the proton spectra must be also modified by inclusion of coalescence.

Probability that some nucleon finds companions to create composite particle increases with parameter h_0 because this parameter determines volume of this part of the phase space, which contributes to the coalescence:

$$r_{i,[i-1]} \cdot p_{i,[i-1]} \leq h_0.$$

It is, therefore, natural to expect that increasing of h_0 parameter should increase number of emitted composite particles and decrease number of emitted protons. However, besides modification of the magnitude of the cross sections also modification of the shape of angular and energy dependence of the differential cross sections can be anticipated, both for protons and composite particles.

Results of the calculations performed with two values of h_0, i.e. $h_0 = p_F \times 1.2$ fm, and $h_0 = p_F \times 2.0$ fm are compared with spectra evaluated with the default value of $h_0 \equiv p_F \times 1.4$ fm in Figs. C.3 and C.4.

much more complicated and differences of energy spectra shapes are not so predictable. Similarly, smaller parameter h_0 change quantitatively energy spectra in opposite way. For protons spectra, most discrepancy are in energy range between 20 and 80 MeV, especially in forward angles. Difference between spectra with default parameter and with $h_0 = p_F \times 1.2$ fm, are much smaller than with $h_0 = p_F \times 2.0$ fm what is cause with much smaller difference beetween both values of parameters h_0. Values of parameter were set up to present significant difference for heavier particles. In case of deuterium, increasing of volume of momentum phase space, increase number of emitted composit particle, especially in low energy range (up to 30 MeV) and over 60 MeV. For forward angles such change of parameter improve accordance with experimental data for higher energy part of spectra but in the same moment it deteriorate accordance for low energy part and for all backword and sidewards angles. For heavier particles (see figure C.4) difference of energy

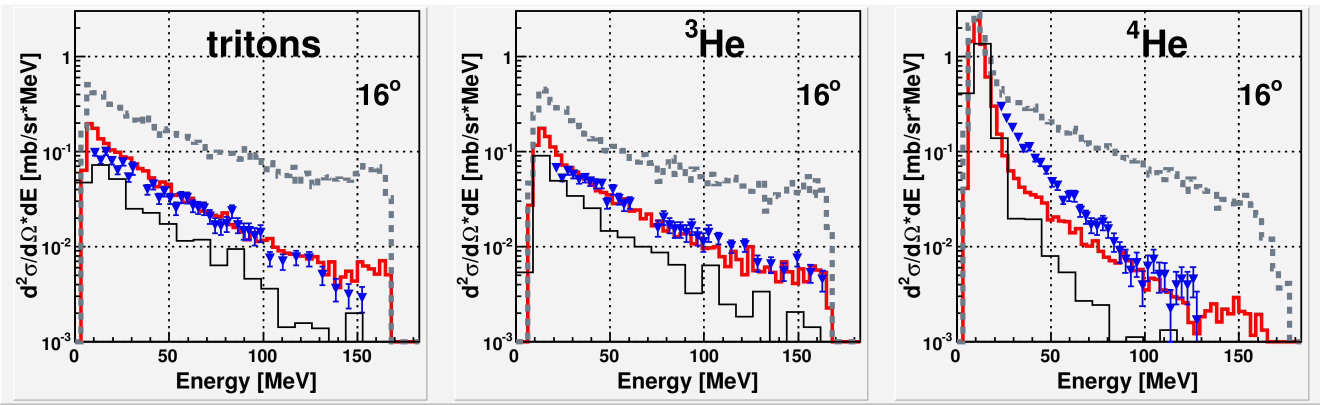

Figure C.4: Energy spectra for tritons (left frame), ^{3}He (middle frame) ^{4}He (right frame) at 16 ° . Meaning of symbols same as in Figure C.3.

spectra are even more significant. Shape is only slightly change preferring more energetic particle when h_0 is bigger. For all angles energy spectra are systematically multiplied so playing with that parameter can not improve angular distribution of calculated particle. It seams that generally on average parameters proposed by author are most convenient.

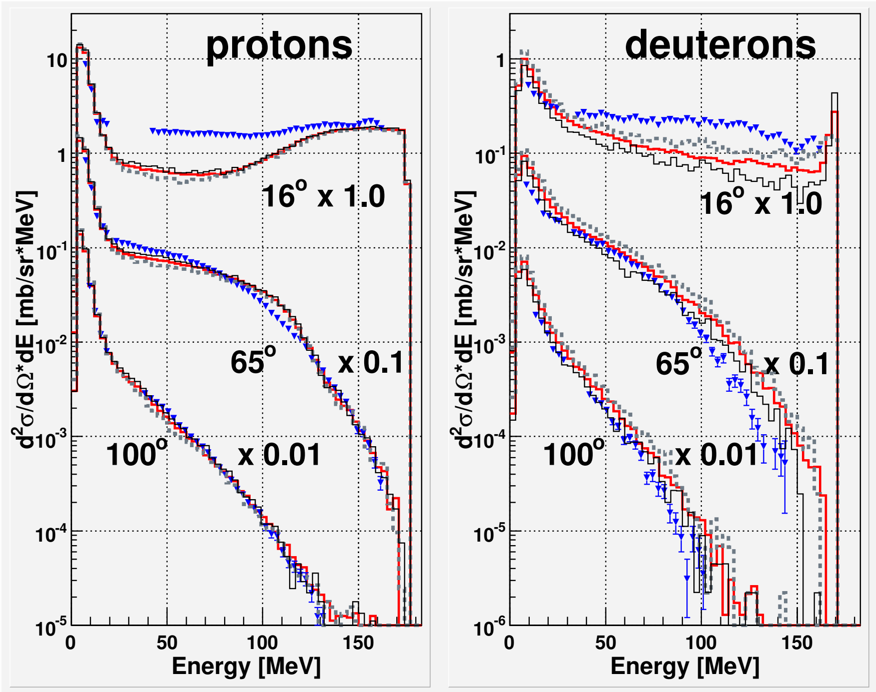

Figure C.5: Energy spectra for protons (left frame) and deuterons (right frame) at 16° , 65° , and 100° from 175 MeV protons induced reaction on ^{nat}Ni. Blue points correspond to experimental data obtained from PISA experiment. Lines correspond to different parameter D of coalescence model (see text): solid red thick line – D = 2.25fm (default value), dashed red thick line – $h_0 = p_F \times 2.0$ fm, thin line – $h_0 = p_F \times 1.2$ fm. To ease the reading of the figure, the successive spectra have been multiplied by decreasing powers of 10.Energy spectra for tritons (left frame), ^{3}He (middle frame) ^{4}He (right frame) at 16 ° . Meaning of symbols same as in Figure C.3.

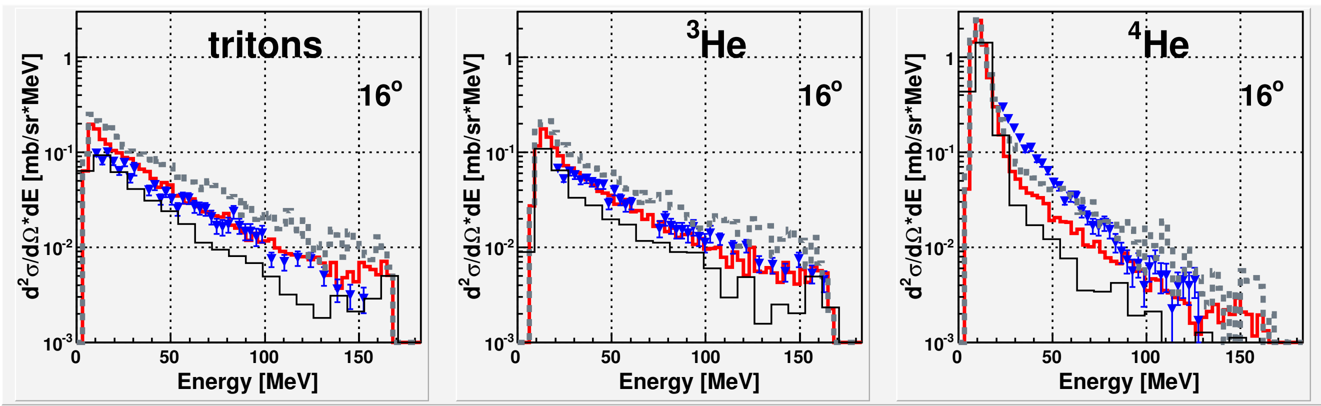

Figure C.6: Energy spectra for tritons (left frame), ^{3}He (middle frame) ^{4}He (right frame) at 16 ° . Meaning of symbols same as in Figure C.5.

Appendix D

Imitation of the slow moving source by evaporation from heavy residuum of the fast stage of the reaction

The energy spectra of IMFs measured in present experiment have the low energy threshold placed so high that the maxima of the spectra are not visible. Therefore, the fit of Maxwell distributions may involve ambiguity of parameter k - defining height of the Coulomb barrier felt by ejectiles, and σ - which correspond to total production cross section. It is desirable to avoid such an ambiguity because values of production cross sections are very important for all applications. To check accuracy of cross section determination the second, alternative version of the data analysis, described in the present Appendix, was performed. It is based on the same general scheme of the reaction mechanism which was proposed previously, i.e., it is assumed that the reaction can proceed via two competing mechanisms: the conventional two-step mechanism (with the probability F) or via the fast break-up of the target nucleus (with probability $1 - F$) - see Fig. 7.1 . However, to decrease the number of free parameters of the model, another method of estimation of the contribution from the fast break-up mechanism is realized. It is assumed that the properties of the heaviest product of the fast break-up, i.e., properties of the slow moving source, are very similar to properties of the heavy residuum of the intranuclear cascade. Due to this assumption the emission of particles from heavy residuum evaluated by means of the GEM2 computer program can describe simultaneously two contributions: true evaporation from the heavy residuum of intranuclear cascade, and evaporation from heavy (slow) moving source created due to the fast break-up of the target. Of course, this procedure relies on the fact that the default values of the parameters of INCL4.3 computer program, used for description of the intranuclear cascade with inclusion of coalescence of nucleons, as well as parameters of the GEM2 computer program, which calculates statistical evaporation of particles, were adjusted by the authors to obtain reasonable agreement of theoretical cross sections with the experimental data. As it was obvious from Chapter 6, where the comparison of preset experimental cross sections with predictions of the two-step model was discussed, it is necessary to introduce besides the two step model cross sections also a non-equilibrium contribution. Here, the emission from the fast moving source and from the fireball is used for reproduction of this contribution. Cross sections corresponding to these non-equilibrium reactions were described by phenomenological parametrization performed along the lines presented in Appendix A.

As it was mentioned in Chapter 6, the experimental conditions did not allow to measure the low energy part of the spectra - below the energy corresponding to the height of the Coulomb barrier between the emitted particles and the residual nuclei. From this reason it was not possible to extract values of the parameters responsible for shape and position of Coulomb barrier by straightforward fit of the data. The following procedure has been proposed to avoid possible ambiguities of the parameters: The parameter k_2 which determines the height of the Coulomb barrier for the fast source was fixed at value 0.3 (i.e., it was assumed that the charge of the fast source is approximately 3 times smaller than the charge of the target Ni nucleus $Z \sim 8-9$). Similarly, the k_3 parameter, which defines the Coulomb barrier for the particles emitted by the fireball was fixed at value 0.07, i.e., it was assumed that the charge of the fireball is $Z \sim 2$). It was found that modifications of these parameters in quite large range of values did not influence significantly the shape of the spectra in the measured ejectile energy range. The same was true for the parameter responsible for the diffuseness of the transmission through the Coulomb barrier B/d (see Appendix A). Therefore this parameter was kept at the fixed value; B/d=10 for all particles and beam energies. Three other parameters of both moving sources, i.e., β-velocity of the source, T-its apparent temperature parameter, and σ- the total production cross section, were varied to obtain the best fit of the experimental data by phenomenological formulae. The search for the best values of the parameters has been done fitting simultaneously the spectra measured at all seven scattering angles, i.e., 16° , 20° , 35° , 50° , 65° , 80° , and 100° .

D.1 Light charged particles

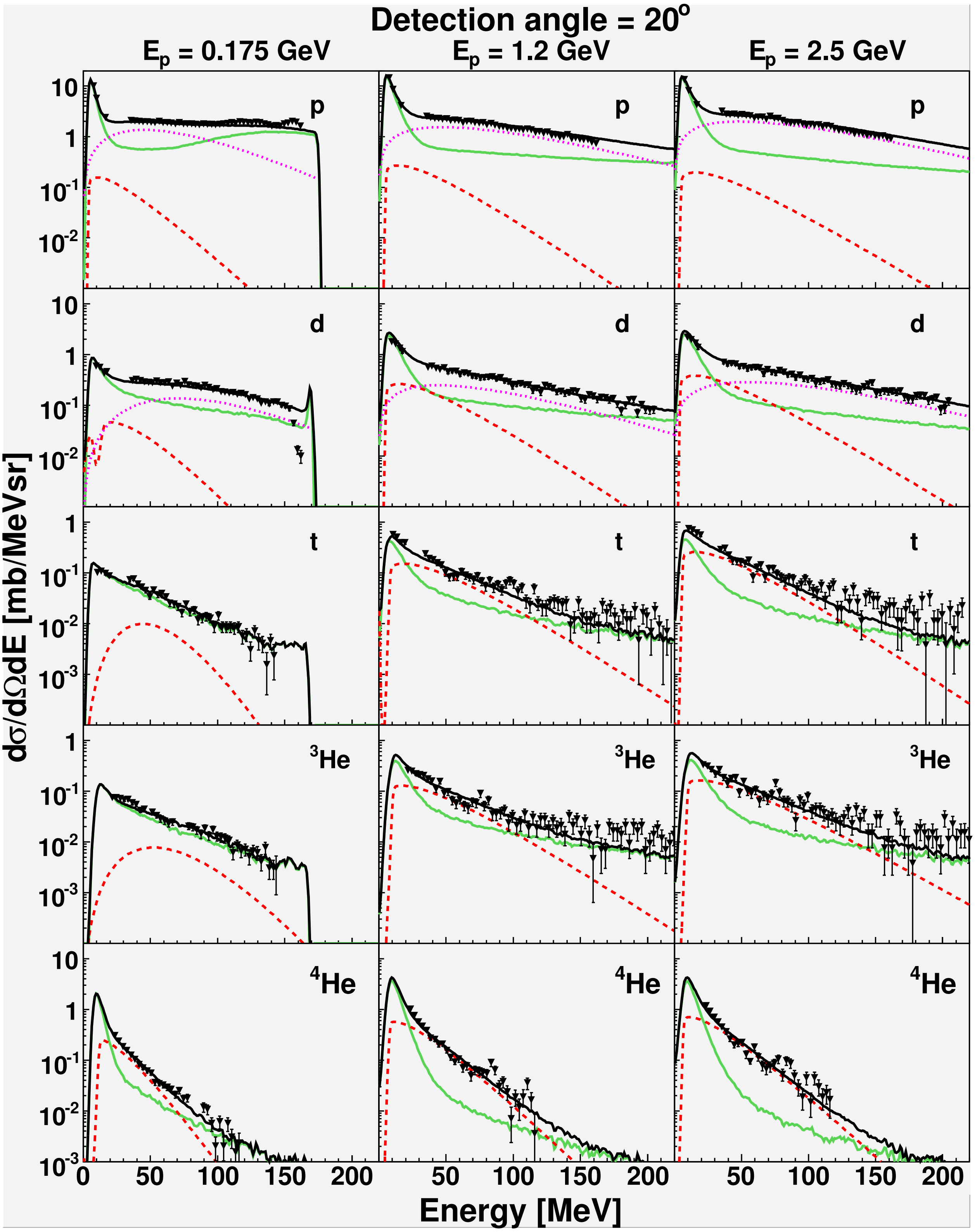

Figure D.1: The experimental data (symbols) measured at 20° for protons, deuterons, tritons, ^{3}He and α-particles together with theoretical spectra (lines). The solid - black line shows sum of contributions from two-step model (solid - green line) and from moving sources. The dotted - magenta line represents the fireball, and the dashed - red line shows contribution from the fast source.

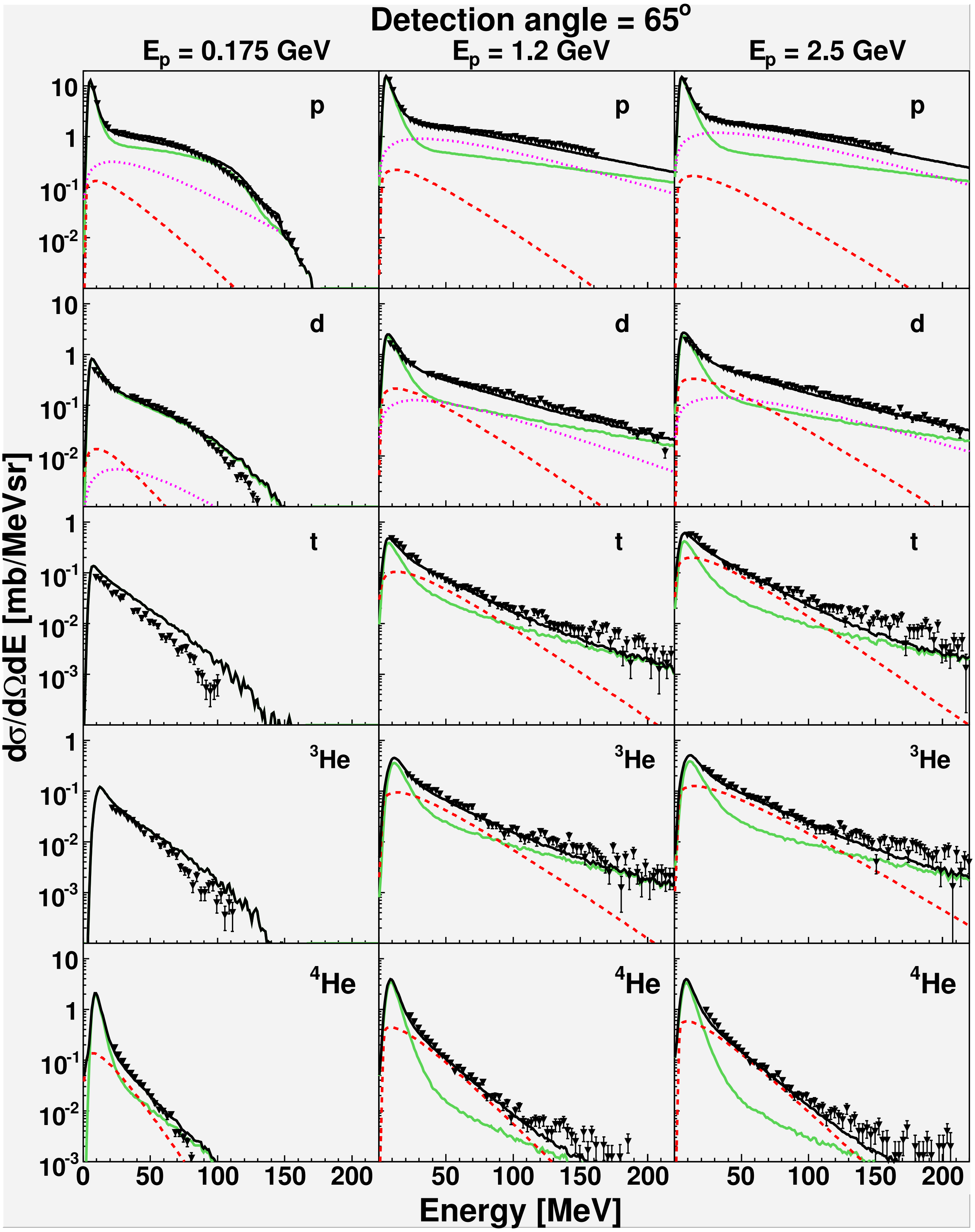

Figure D.2: Same as Fig.D.1 but for 65°

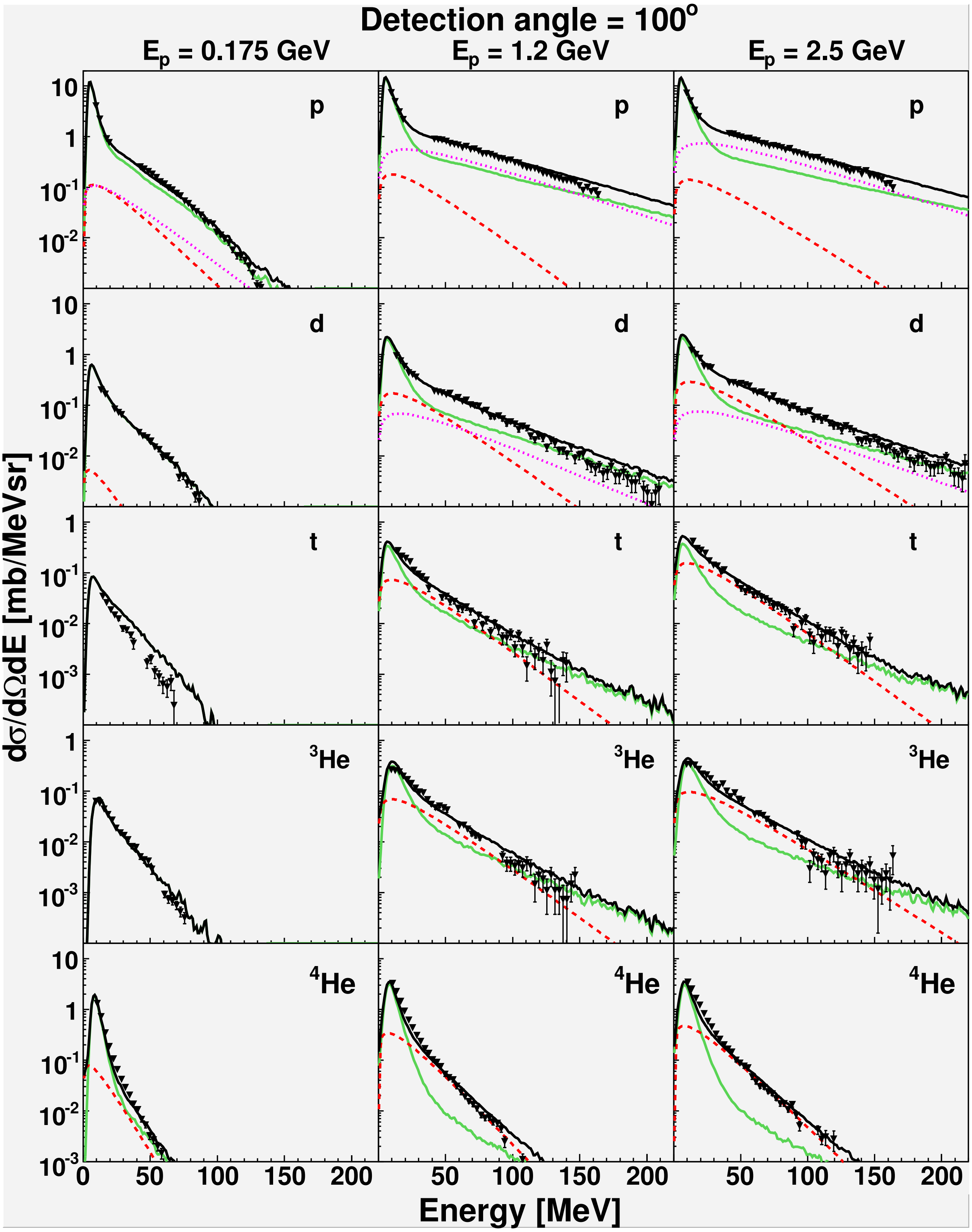

Figure D.3: Same as Fig.D.1 but for 100°

The scaling factor for the INCL4.3 calculations delivering the cross sections for the fast protons from intranuclear cascade or fast LCPs from the coalescence of nucleons during the intranuclear cascade, was determined by fitting the deuteron data for each energy. This value was then fixed for all other LCPs for given energy. Values of the parameters are listed in Table D.1, below.

The quality of the data reproduction by the present method of analysis is equally good as that obtained in the previous version of the analysis. This is well illustrated by Figs. D.1 - D.3 for three beam energies; 0.175, 1.2, and 2.5 GeV. The data and calculations for the beam energy 1.9 GeV are not shown in the figures because the quality of data reproduction for this beam energy was very similar as that for lower (1.2 GeV) and higher (2.5 GeV) beam energies.

It may be also judged from comparison of the χ^2 values listed in the tables D.1 and 7.2 that slightly better agreement was achieved in the present analysis (with exception of ^{3}He ejectiles) than that in the first version of the analysis.

It was found, that for protons and deuterons the fireball contribution is unavoidable for good description of the data, whereas for other LCPs (as well as for protons and deuterons) the presence of the fast moving source improves the fit significantly - especially at forward scattering angles and/or at higher beam energies.

Table D.1: Parameters of moving sources for LCPs: k- corresponds to reduced height of the Coulomb barrier for emission of fragments (see Appendix A for explanation), T- apparent temperature of the source β- its velocity, and σ- total production cross section (integrated over emission angle and energy of detected particles). Index "2" and "3" labels parameters of the fast moving source and the fireball, respectively. Calculations of INCL4.3 which include coalescence of nucleons were multiplied by scaling factor F whereas scaling factor for evaporation part is set to 1 (see the text for the explanation).

Beam Energy GeV	Ejectile	Fast source			Fireball			F	$F * \sigma_{\mathrm{INCL}}$ mb	σ_{GEM} mb	χ^2
		β_2	T_2/MeV	σ_2/mb	β_3	T_3/MeV	σ_3/mb				
0.175	p	0.038	16.1	[50]	0.250	22.0	309	[0.79]	546	850	25.9
1.2	p	0.051	21.0	109	0.174	45.8	1025	[0.63]	979	1412	12.4
1.9	p	0.034	22.9	54	0.172	46.2	1207	[0.64]	1043	1438	7.1
2.5	p	0.046	24.0	96	0.174	47.7	1340	[0.65]	1064	1429	5.1
0.175	d	0.11	10.8	[5.0]	0.258	16.9	20.5	0.79	102	38.6	4.73
1.2	d	0.038±0.023	21.7±4.2	109±37	0.135±0.022	37.0±3.4	121±44	0.63	180	248	3.08
1.9	d	0.036±0.016	23.1±3.0	157±27	0.151±0.019	42.8±3.3	132±33	0.64	184	281	2.52
2.5	d	0.026±0.013	24.1±2.5	192±26	0.151±0.017	44.2±2.7	169±32	0.65	182	286	1.81
0.175	t	0.178±0.031	5.2±3.9	[0.5]	—	—	—	[0.79]	23.5	3.5	43.7
1.2	t	0.051±0.003	21.3±0.5	52.5 ±1.4	—	—	—	[0.63]	36.6	41.0	3.29
1.9	t	0.043±0.003	21.7±0.5	75.5 ±1.7	—	—	—	[0.64]	37.8	48.8	2.81
2.5	t	0.037±0.003	21.5±0.4	101.0 ±2.2	—	—	—	[0.65]	37.5	50.1	3.10
0.175	^{3}He	0.191 ±0.011	7.5±1.3	[0.5]	—	—	—	[0.79]	16.6	5.9	5.10
1.2	^{3}He	0.044±0.002	21.6±0.4	44.5 ±1.0	—	—	—	[0.63]	27.9	46.4	1.63
1.9	^{3}He	0.039±0.002	23.1±0.5	58.6 ±1.3	—	—	—	[0.64]	28.9	53.7	1.84
2.5	^{3}He	0.041±0.002	24.8±0.5	70.2 ±1.5	—	—	—	[0.65]	28.6	54.9	1.92
0.175	^{4}He	0.046±0.002	9.53±0.19	30.6 ± 1.8	—	—	—	[0.79]	11.3	159	6.32
1.2	^{4}He	0.027±0.001	15.0±0.2	144 ±4	—	—	—	[0.63]	15.1	393	5.43
1.9	^{4}He	0.025±0.001	16.0±0.2	168 ±4	—	—	—	[0.64]	15.2	401	3.87
2.5	^{4}He	0.022±0.001	16.1±0.2	203 ±6	—	—	—	[0.65]	15.0	398	3.92

D.2 Intermediate mass fragments

It was found in the analysis of LCPs data that the fireball contribution is significant only for proton and deuteron spectra. Hence, it is reasonable to conjecture that the fireball is small, i.e., it is built of 2 - 3 nucleons. From this reason the fireball cannot give any contribution to the production of IMFs. The assumption, that the slow, heavy prefragment of the fast break-up behaves in similar way as the heavy residuum from the intranuclear cascade, allows to use evaporation cross sections evaluated by GEM2 program to reproduce without free parameters the contribution from the slow moving source. It should be emphasized that the only undetermined in this version of analysis are the parameters of the fast moving source.

The fits of the parameters of one moving source have been done simultaneously for spectra at seven scattering angles: 16°, 20°, 35°, 50°, 65°, 80°, and 100°. The quality of the data description is presented on Figs. D.4-D.7 for the same set of isotopes and angles as in case of the version I, i.e., ^{6}Li, ^{7}Li, ^{7}Be, ^{9}Be, and ^{11}B, for 35°, 50°, 80°, and 100°. Black, solid line represent sum of contribution from GEM program calculation (green, solid line) and from fitted fast moving source (red, dashed line). The excellent reproduction of the experimental data has been achieved.

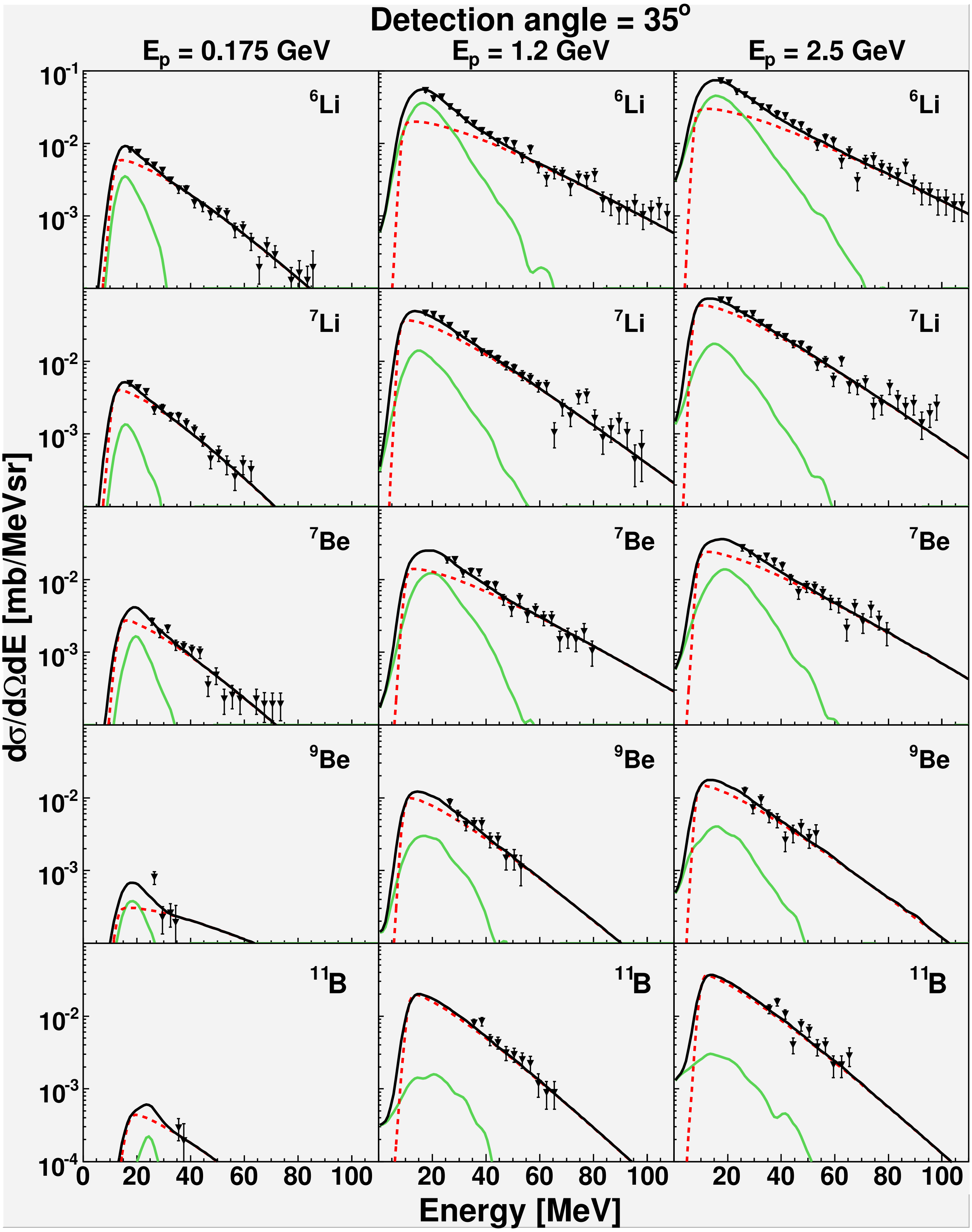

Figure D.4: Experimental (symbols) and theoretical (lines) spectra of IMFs from p+Ni collisions measured at 35° for three proton beam energies: 0.175 GeV (l.h.s. part of the figure), 1.2 GeV (central part of the figure) and 2.5 GeV (r.h.s. of the figure). Green, solid line represents calculations made by means of INCL4.3. program coupled with statistical evaporation code GEM2. The red, dotted line shows the fitted contribution of the fast moving source and the black, solid line depicts sum of both contributions.

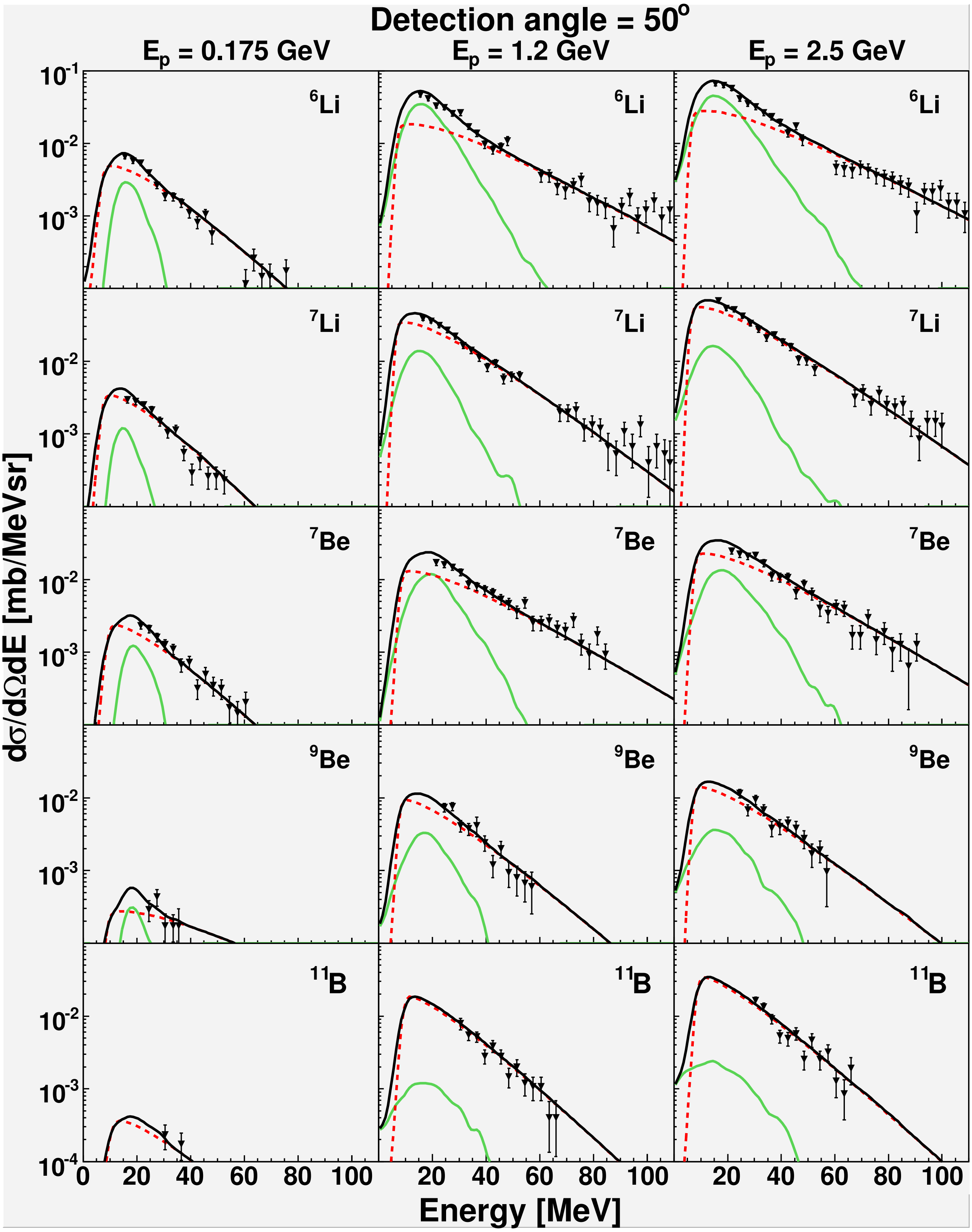

Figure D.5: Same as Fig.D.4 but at 50°

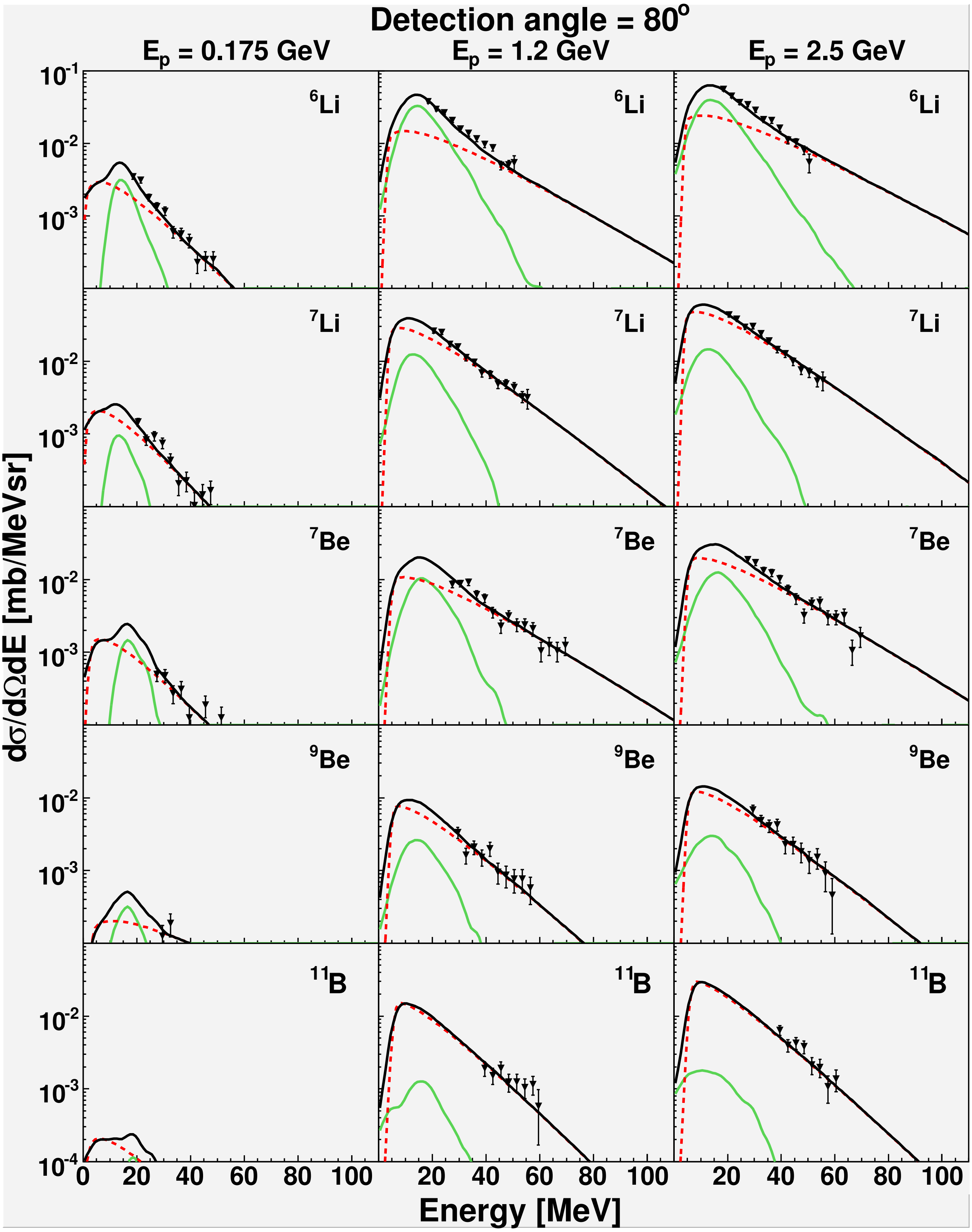

Figure D.6: Same as Fig.D.4 but at 80°

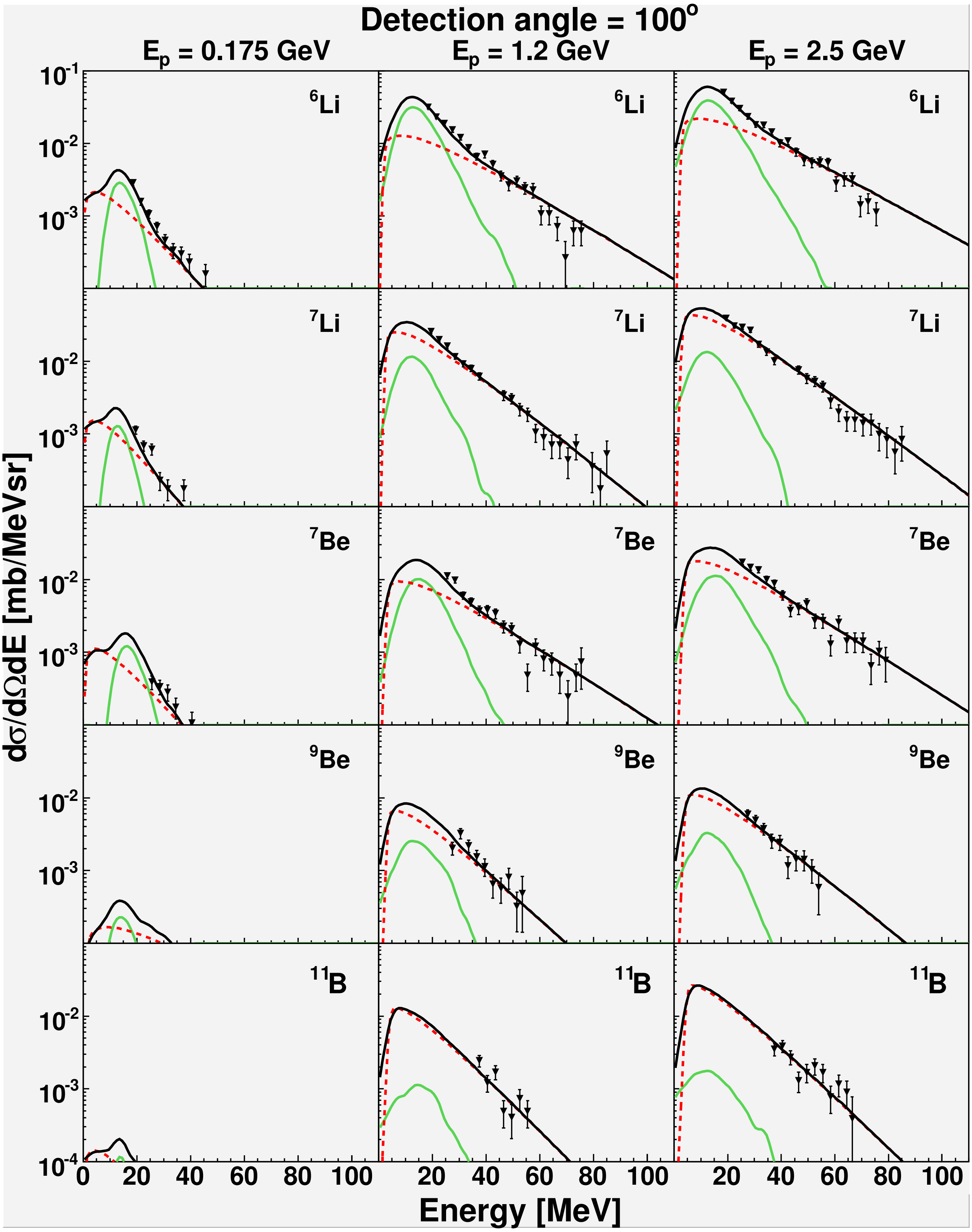

Figure D.7: Same as Fig.D.4 but at 100°

Values of the parameters are listed in the Table D.2 for four proton beam energies: 0.175, 1.2,

Table D.2: Parameters of single moving source for IMFs: T_2- apparent temperature of the source β_2- its velocity, and σ_2- total production cross section (integrated over angles and energy of detected particles). Parameters k and B/d (see the text for the explanation) are fixed on values respectively 0.3 and 10. Index "2" for all parameters indicates that emission from this source is second contribution to energy spectra, the first one comes from GEM calculation.

Beam Energy/GeV	Ejectile	Fast source β_2	T_2/MeV	σ_2/mb	σ_{GEM}	χ^2
0.175	^{6}He	0.035±0.004	8.41±0.74	0.14 ±0.02	0.017	3.65
1.2	^{6}He	0.024±0.003	13.3±1.0	1.31 ±0.09	0.56	2.40
1.9	^{6}He	0.030±0.004	15.5±1.4	1.48 ±0.12	0.73	2.56
2.5	^{6}He	0.025±0.003	14.6±1.0	2.08 ±0.13	0.77	1.97
0.175	^{6}Li	0.040±0.001	10.3±0.2	0.91 ±0.03	0.39	1.65
1.2	^{6}Li	0.024±0.001	17.9±0.4	6.40 ±0.19	6.5	1.99
1.9	^{6}Li	0.021±0.001	18.9±0.4	8.66 ±0.26	8.6	2.06
2.5	^{6}Li	0.018±0.001	19.6±0.4	11.2 ±0.3	9.1	1.40
0.175	^{7}Li	0.034±0.002	9.4± 0.3	0.56±0.03	0.14	1.77
1.2	^{7}Li	0.017±0.001	13.8±0.2	9.42 ±0.21	2.46	1.38
1.9	^{7}Li	0.017±0.001	14.4±0.2	13.0 ±0.3	3.05	1.55
2.5	^{7}Li	0.015±0.001	14.9±0.2	16.7 ±0.4	3.16	1.45
0.175	^{8}Li	[0.034]	[10]	0.039	0.006	2.03
1.2	^{8}Li	0.021±0.003	15.1±1.0	0.86 ±0.07	0.26	1.54
1.9	^{8}Li	0.018±0.002	15.7±0.8	1.42 ±0.08	0.36	0.95
2.5	^{8}Li	0.017±0.002	14.4±0.6	2.18 ±0.11	0.37	1.08
0.175	^{7}Be	0.035±0.002	10.1±0.4	0.384±0.022	0.167	1.19
1.2	^{7}Be	0.020±0.002	17.0±0.4	4.37 ±0.17	2.24	1.57
1.9	^{7}Be	0.018±0.002	17.3±0.4	6.57 ±0.22	2.71	1.30
2.5	^{7}Be	0.015±0.002	17.1±0.4	7.97 ±0.28	2.80	1.34
0.175	^{9}Be	0.028±0.011	19.9 ±5.9	0.102±0.024	0.037	1.08
1.2	^{9}Be	0.016±0.002	12.1±0.6	2.16 ±0.14	0.57	1.04
1.9	^{9}Be	0.016±0.002	12.6±0.5	3.24 ±0.18	0.70	0.86
2.5	^{9}Be	0.012±0.002	13.6±0.6	3.91 ±0.22	0.74	0.82
0.175	^{10}Be	[0.034]	[10]	0.061	0.006	0.26
1.2	^{10}Be	0.018±0.004	19.3±2.2	0.67 ±0.06	0.22	0.90
1.9	^{10}Be	0.016±0.003	15.2±1.4	1.30 ±0.13	0.30	1.02
2.5	^{10}Be	0.016±0.003	16.6±1.5	1.39 ±0.12	0.33	0.82
0.175	^{10}B	0.036±0.010	7.5 ±3.3	0.100±0.057	0.055	0.86
1.2	^{10}B	0.015±0.003	15.2±1.7	1.94 ±0.26	0.97	1.72
1.9	^{10}B	0.011±0.002	15.8±0.9	3.67 ±0.29	1.29	1.06
2.5	^{10}B	0.011±0.002	17.0±1.1	4.00 ±0.36	1.40	1.28
0.175	^{11}B	[0.034]	[10]	0.057	0.014	0.56
1.2	^{11}B	0.016±0.002	11.0±0.7	3.48 ±0.41	0.29	1.17
1.9	^{11}B	0.013±0.002	12.3±0.8	5.08 ±0.48	0.45	1.28
2.5	^{11}B	0.012±0.002	11.7±0.8	7.23 ±0.82	0.53	1.74
1.2	C	0.017±0.002	11.7±0.8	4.9 ±1.0	1.70	1.43
1.9	C	0.012±0.002	12.0±0.7	9.7 ±1.4	3.22	0.96
2.5	C	0.016±0.002	14.9±1.1	8.5 ±1.0	3.96	0.99
1.2	N	0.024±0.008	7.7±2.5	4.4 ±4.3	1.38	1.22
1.9	N	0.004±0.005	14.6±4.8	3.6 ±2.3	3.26	0.91
2.5	N	0.010±0.003	13.2±1.9	4.9 ±1.8	4.06	0.25

1.9, and 2.5 GeV and their behavior is discussed in the next section.

D.3 Discussion of results

The present method of data analysis and the previous one are based on the same physical picture of reaction mechanism. Thus, the same qualitative behavior of the parameters can be expected. Since the slow moving source from the fast break-up is simulated by part of statistical evaporation from heavy residuum of the intranuclear cascade, its parameters were not varied in the fits. Hence their values are not explicitly known and cannot be compared with the parameters of the fireball - for protons and deuterons, and/or parameters of fast moving source - for all particles. It is, however, possible to check behavior of the parameters of these two latter sources.

Velocity and apparent temperature of moving sources are presented on Fig. D.8 as functions of the ejectile's mass. The fireball parameters are depicted as magenta down triangles connected by dotted line, the parameters of the fast moving source are marked by red up triangles connected by dashed line. Both lines represent the least square fits of linear functions to the dependence of velocity (temperature) on the ejectile mass.

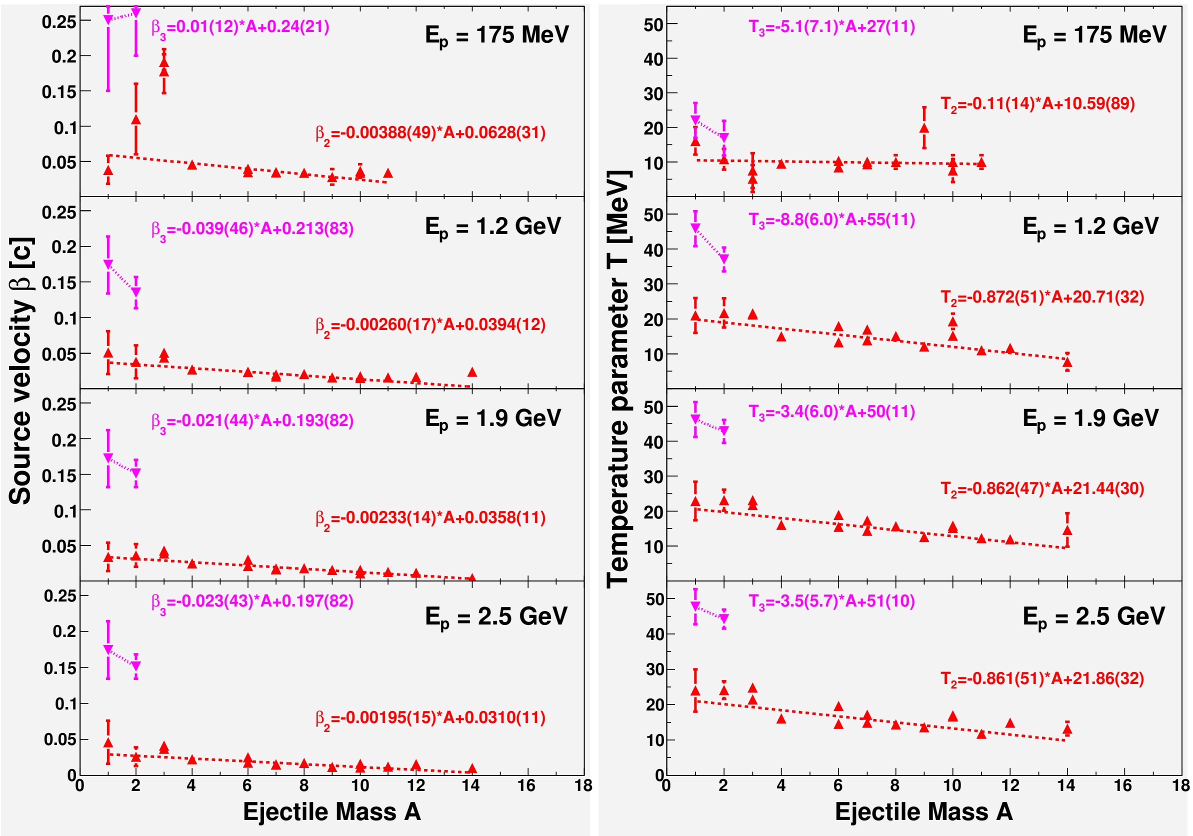

Figure D.8: Left part of the figure; velocity of the fast source - β_2, and the right part; apparent temperature parameter - T_2 presented as the function of an ejectile mass. Symbols and lines are described in the text.

The apparent temperature of the source decreases linearly with the mass of the ejectile. This can be interpreted as result of the recoil of the source, which should be pronounced because the mass of the ejectiles is comparable to the mass of the emitting source. It is possible to estimate mass of the source A_S and its temperature τ from the parameters of the linear function describing the variation of the apparent temperature T with the mass of the ejectile A; $T = -(\tau/A_s)A + \tau$ (see Appendix A).

The estimated mass of the fast moving source A_s is equal to 23.8(1.5), 24.9(1.4), and 25.4(1.6) for 1.2 GeV, 1.9 GeV, and 2.5 GeV beam energy, respectively. For the lowest beam energy - 0.175 GeV, the slope of the mass dependence of the apparent temperature is so small and its error so large that it is not possible to estimate the mass of the fast source. Values of A_s seem to increase slowly with the proton beam energy, however, it is also possible to claim that they are constant, in the limits of errors, and equal to their mean value of $\overline{A_s}$=24.7(0.9).

Decreasing of the source velocity with the mass of the ejectile can be explained by the fact that the source emitting heavy ejectiles must be in average heavier than the source emitting light ejectiles. This is because the light ejectile may originate from light and heavy sources whereas the heavy ejectile cannot be emitted by a light source.

The total, i.e., angle and energy of ejectile integrated, cross sections representing different reaction mechanisms are shown in the l.h.s. part of Fig. D.9. It can be stated that the relative contribution of various mechanisms does not change at high energies but it varies at the lowest (0.175 GeV) beam energy.

For LCPs the contribution from the fast stage of the two-step process, i.e., emission of fast protons or fast LCPs from intranuclear cascade, dominates at the lowest beam energy. The contribution from the fast moving source is very small at this energy but it becomes quite large - comparable with evaporation contribution and with contribution originating from intranuclear cascade - at high beam energies.

For IMFs the situation is different. The contribution from the fast moving source is larger than evaporation of IMFs for all beam energies. The dominance of this mechanism seems to increase slightly with the beam energy.

The summed over various mechanisms and over various isobars total cross sections are shown in the r.h.s. part of the Fig. D.9. It is evident that the cross sections fulfill well the power low dependence on the mass of the ejectiles. The power exponent decreases monotonically with the beam energy. Its values; 4.561(7), 3.888(8), 3.874(8), and 3.726(9) for beam energies 0.175, 1.2, 1.9, and 2.5 GeV behave in analogous way as for the version I analysis, i.e., do not indicate the evidence of the nuclear liquid - gas phase transition.

The beam energy dependence of the absolute and relative contributions of individual reaction mechanisms is shown in the l.h.s. and r.h.s. parts of the Fig. D.10, respectively. The contributions of individual mechanisms are presented in the following order - from the bottom to the top of the figure: evaporation - calculated by means of the GEM2 computer program, intranuclear cascade with coalescence of nucleons - calculated with INCL4.3 computer program (scaled by factor F), emission from the fast source, and from the fireball, respectively. The sum of all contributions is presented at the top of the l.h.s. part of the figure, whereas the ratio of the sum of all contributions (with exception of the evaporation) to the total cross section is shown in the top of the r.h.s. part of the figure.

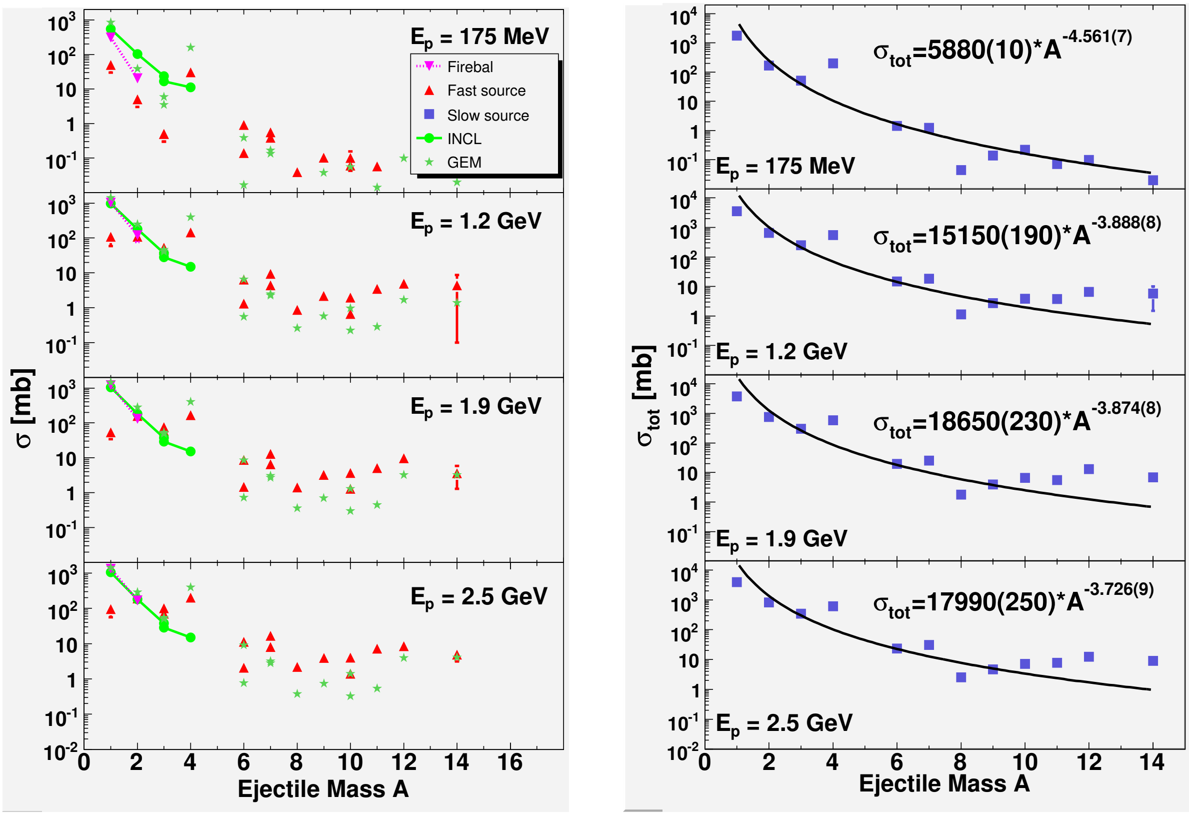

Figure D.9: Total cross section versus mass of the ejectile for various mechanisms evaluated with imitation of the slow moving source by evaporation from heavy residuum of the fast stage of the reaction. Contributions from fireball, fast moving source, coalescence, and evaporation are depicted as magenta triangles connected with the solid line, red triangles, green dots connected with the solid line, and dark green stars, respectively. L.h.s. part of the figure presents cross sections found for individual mechanisms and for each available isobar, whereas the r.h.s. part of the figure shows total cross sections - summed over various possible mechanisms and over different isobars for a given mass number of the fragment. (The present figure is analogous to Fig.7.10 for the first method of data analysis.)

The absolute value of the total cross sections for production of LCPs increases monotonically for all mechanisms in the studied beam energy range. The only exception is the cross section for protons emitted from the fast moving source, but its relative contribution to the total cross section is negligible. In general, the increasing of the cross sections is faster for low beam energies (0.175 GeV - 1.2 GeV) than for higher energies. The largest increase is present for the fast moving source, and the smallest for coalescence cross sections which are almost constant (in the absolute scale) in the full studied energy range.

The relative contribution of non-equilibrium processes, i.e., those which cannot be simulated by evaporation from heavy residuum of the target nucleus, is quite large; 0.5 - 0.9 depending on the type of ejectiles and the beam energy. Only for alpha particles this mechanism gives small contribution (increasing from 0.2 at beam energy 0.175 GeV to $\sim$ 0.4 at 2.5 GeV). The relative contribution of non-equilibrium reactions increases with the beam energy for protons and alpha particles in the full energy range, whereas such an increase is visible for other LCPs only starting from the beam energy 1.2 GeV (it even drops from 175 MeV to 1.2 GeV).

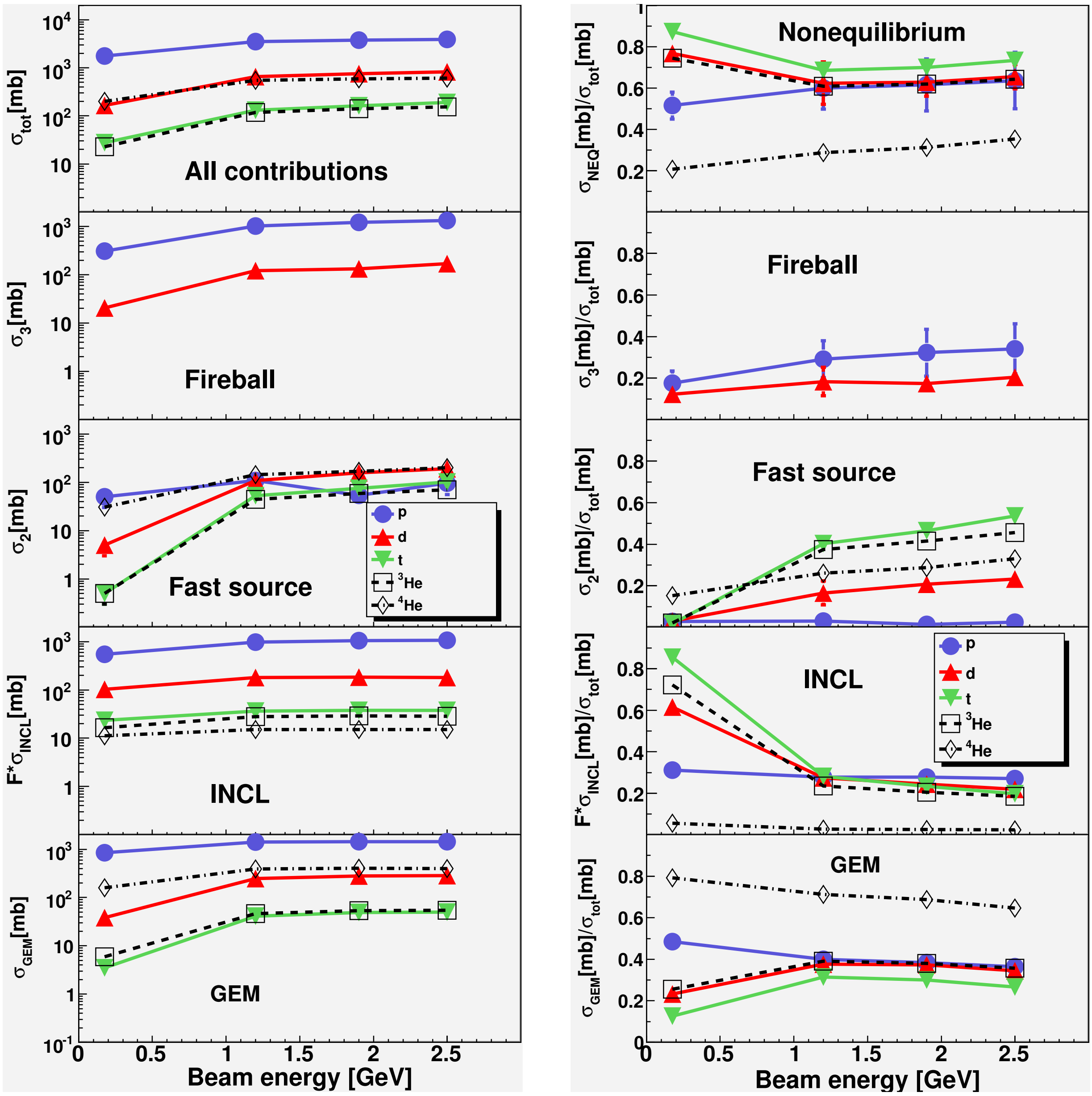

Figure D.10: Energy dependence of the absolute (l.h.s. of the figure) and the relative (r.h.s. of the figure) contributions of different reaction mechanisms to the total production cross sections of LCPs. For detailed description see text. The cross sections denoted by GEM (the lowest part of the figure) were evaluated by the GEM2 computer program and are interpreted as sum of the evaporation cross sections from heavy residuum of the intranuclear cascade and contribution from the slow moving source. (This figure is analogous to Fig.7.11 for the first method of data analysis)

Energy dependence of IMFs has the same general trend as that described for LCPs. On the l.h.s. part of the Fig.D.11 the energy dependence of the absolute cross sections for evaporation (from heavy target residuum and from the slow source) is presented (bottom panel) as well as the energy dependence of the absolute contribution of the emission from fast moving source (central panel), and its relative contribution to the total cross section (upper panel). The absolute cross section are increasing with beam energy. In the case of the lowest energies (from 0.175 GeV to 1.2 GeV) it is very fast increase - even one order of magnitude.

The contribution from non-equilibrium mechanism (emission from the fast moving source) to the total cross sections is slightly decreasing for the lowest energies for all ejectiles except ^{7}Li and ^{11}B, and then it increases with the beam energy. The non-equilibrium contribution dominates for all IMFs and for all beam energies.

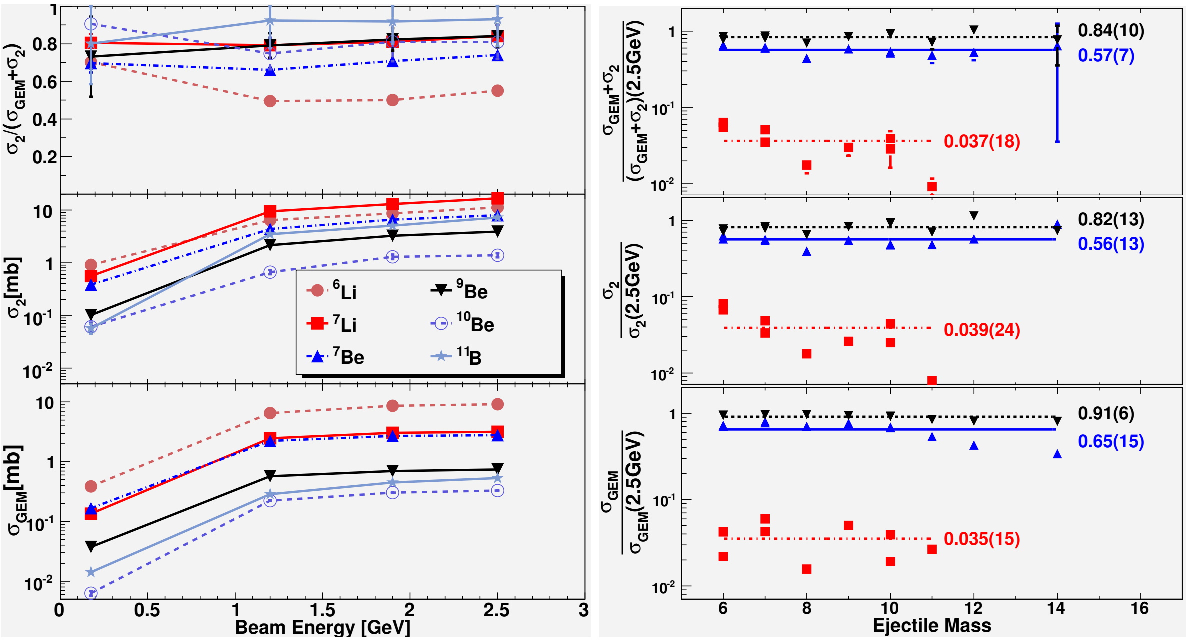

Figure D.11: σ_{GEM} and σ_2 correspond to total cross section of GEM calculation and to emission from the fast moving source, respectively. On the l.h.s. part of the figure, the energy dependence of the absolute contribution from slow and fast moving source is presented on the lower and the middle pad, respectively. The relative contribution of the fast moving source is depicted on the top pad. Different lines connecting symbols represent different IMFs as it is shown on the legend. The ratio of production cross section at beam energy 0.175 GeV (red full squares), 1.2 GeV(blue triangle up) and 1.9 GeV(black triangle down) to those found at 2.5 GeV is presented as a function of mass of emitted IMFs in the r.h.s. part of the figure. The lines represent average values. The ratios of contribution from the slow moving source, the fast source, and from the sum of the both sources to corresponding quantities determined at 2.5 GeV are depicted on the bottom, medium, and the top pads, respectively.(Figure analogous to Fig.7.12 for second method of data analysis)

The relative increase of cross section with beam energy is the same for all ejectiles from 1.2 to 2.5 GeV, and from 1.9 GeV to 2.5 GeV, what is illustrated on the r.h.s part of the Fig.D.11. There the ratios of the total cross sections estimated for 0.175 GeV, 1.2 GeV, and 1.9 GeV to the cross section determined for 2.5 GeV beam energy are presented as red squares, blue up triangles and black down triangles, respectively. The ratio of cross sections measured at lowest energy to data obtained at 2.5 GeV is evidently smaller for heavy IMFs than for light IMFs. This means that the production cross sections of heavy IMFs increase faster at low beam energies than those for lighter products. Such an effect is not visible at higher energies as it was mentioned above.

D.4 Comparison of both versions of evaluation of the fast break-up contribution

It is concluded that both methods of realization of the fast break-up contribution to the cross sections are equivalent in description of the differential and total inclusive cross sections.
This is because:

- The quality of the spectra description is perfect for both methods as can be judged from the χ^2 values, listed in the Tables 7.2, 7.3 and D.1, D.2 for the LCPs and IMFs in the first and the second version of analysis, respectively. The χ^2 values are in most cases very close to unity. Equally good description of the shape of the energy spectra and their angular dependence is also illustrated by the Figs. 7.2 - 7.4, 7.5 - 7.8 for the LCPs and IMFs in the first version of analysis and and by the Figs. D.1 - D.3, D.4 - D.7 for the LCPs and IMFs in the second version of analysis, respectively.

- The total cross sections obtained by summing all mechanisms contributions in the first and in the second method have the same values in the limits of errors. This can be checked by inspection of Table D.3 and Fig. D.12.

Thus, from the point of view of application of the cross sections of proton induced reactions for other purposes, e.g., estimation of cross sections of heavy-ions induced reactions or application for astrophysical, medical, and technological purposes, both methods of evaluation of the contribution of non-equilibrium processes are equally good. It seems that the more practical (i.e., less sensitive to ambiguity of fitted parameters), is the second method.

The question remains whether both methods give equivalent interpretation of the reaction mechanism. The main assumption, i.e., competition of the fast break-up of the target nucleus with the conventional mechanism of the intranuclear cascade followed by evaporation of particle, remains the same in both versions of analysis. Therefore, they differ only in interpretation of the relative contributions of individual mechanisms. It is, however, quite difficult to conclude on the basis of the present data whether the contribution to triton and ^{3}He spectra due to the moving source should be attributed to the fireball (as it is in the first version of analysis) or to the fast source accompanying the fireball (as it is done in the second version). Since all these contributions vary with the beam energy in very analogous way there is no clear argument for the first or the second interpretation. The smooth extrapolation of the parameters of the fast source from IMFs to LCPs, visible in Fig. D.8 (at least for higher energies) seems to be rather in favor of the second interpretation. Lack of such smooth extrapolation for the lowest beam energy may indicate that the fast break-up mechanism is not as important for this energy as for the higher energies.

The difficulty of interpretation appears mainly for LCPs, because for IMFs both methods of analysis assume, that the evaporation from heavy remnant of the intranuclear cascade and the

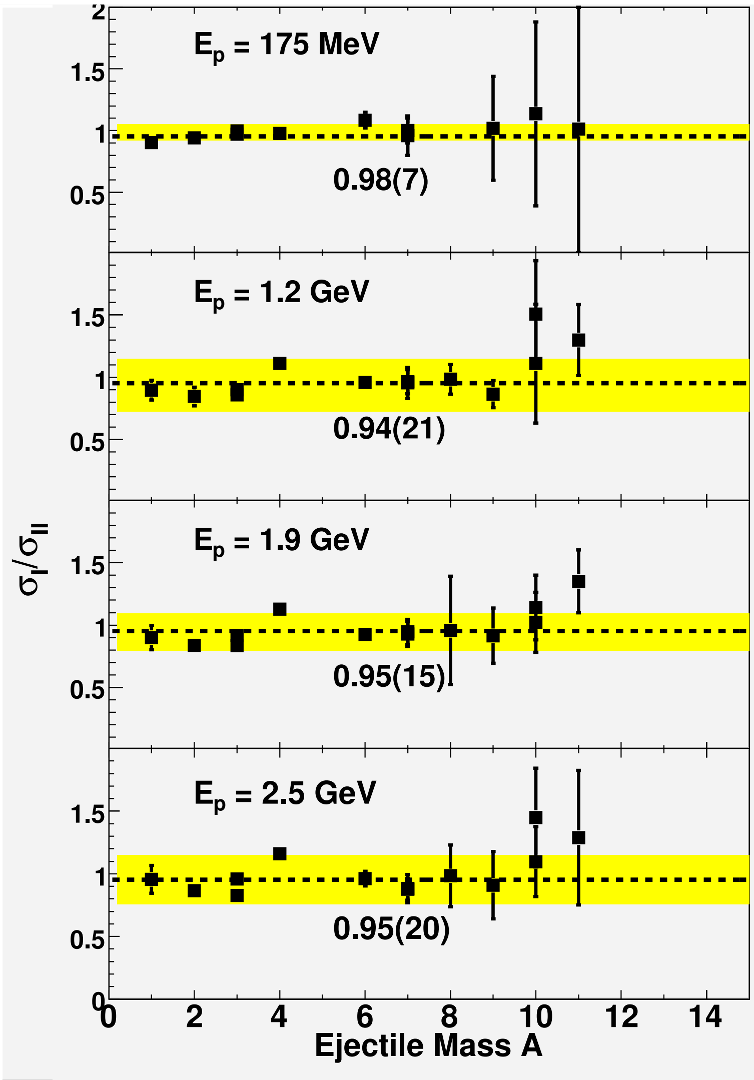

Figure D.12: Ratios of the total (i.e., summed over all reaction mechanisms) cross sections obtained in both versions of the data analysis for different beam energies; 0.175, 1.2, 1.9, and 2.5 GeV - from the top to the bottom of the figure, respectively. Dashed, horizontal lines represent the average values of the ratios and the dashed (yellow) horizontal bars depict the standard deviation of the ratios characterizing the spread of ratios values. The average values and standard deviations of the ratios are also depicted as numbers in the figure.

emission from the slow source created due to the fast break-up have similar properties and, therefore, they are indistinguishable. In the first method of analysis the sum of contributions from these two sources is described by phenomenological formula of the slow, isotropically emitted source with the parameters fitted to the data and in the second method this sum is simulated by the evaporation described by the GEM2 model with default values of the parameters. It seems, that the more practical is using of the second method since there are no free parameters for the slow source while the quality of the data description is equally good. On the other hand, such a procedure relies strongly on the fixed, default values of parameters of the INCL4.3 and GEM2 programs. Then the contribution of the fitted, fast moving source is also determined to large extent by these model assumptions. In the first method of the analysis the contribution of the slow source plus evaporation from heavy remnant of the intranuclear cascade is fitted on the equal footing as the contribution of the fast source.

The energy dependence of the contributions of the fast and slow sources is presented in the Fig. D.13 since the main goal of the present thesis is studying of the energy dependence of the reaction mechanism. The reduced cross sections are depicted in the figure to assure the same scale for the energy dependence of both reaction mechanisms, namely, the averaged over IMFs ratios of the cross sections at given energy to the cross sections at 2.5 GeV beam energy are shown. The open symbols represent results of the first version of the analysis described in section **??** and the full symbols show results of the second version of the analysis discussed in the section D. The following properties of the energy dependence of the reduced cross sections can be seen:

- Cross sections obtained by both methods are the same within errors thus the conclusions should not depend on the method of data analysis.
- They increase faster in the low energy range than at high energies.
- The contribution from the slow source starts to level at energies higher than ~ 2 GeV but the fast source contribution and hence total cross section still increases in this energy range.

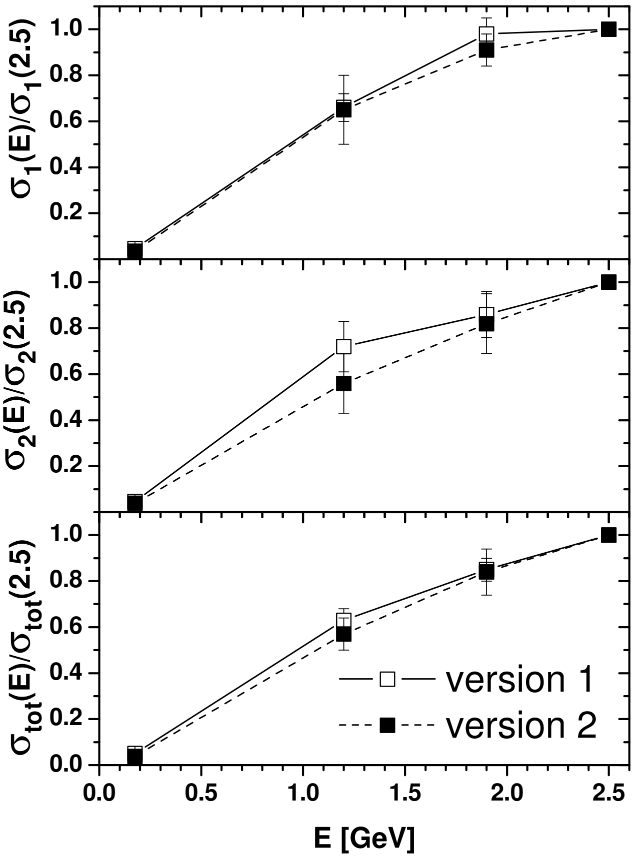

Figure D.13: Energy dependence of the averaged over IMFs ratios of the cross sections obtained at given energy to the cross sections determined at 2.5 GeV in both versions of the data analysis. In the upper panel the ratios for the slow source, in the middle for the fast source, and in the bottom panel the ratios of the total cross sections are presented.

Table D.3: Total cross sections (summed over all reaction mechanisms) for both versions of the analysis

Beam Energy/GeV	Ejectile	I Version σ_I/mb	II Version σ_{II}/mb	Ratio σ_I/σ_{II}	Average $0.5 * (\sigma_I + \sigma_{II})$/mb
0.175	p	1584 ± 32	1760 ± 100	0.902 ± 0.056	1670 ± 53
1.2	p	3160 ± 61	3530 ± 300	0.896 ± 0.080	3340 ± 160
1.9	p	3366 ± 53	3740 ± 400	0.900 ± 0.098	3550 ± 200
2.5	p	3752 ± 44	3930 ± 450	0.955 ± 0.110	3840 ± 230
0.175	d	156 ± 4	166 ± 6	0.941 ± 0.038	161.3 ± 3.3
1.2	d	556 ± 5	658 ± 58	0.846 ± 0.075	607 ± 29
1.9	d	631 ± 5	754 ± 43	0.837 ± 0.048	693 ± 21
2.5	d	716 ± 7	828 ± 42	0.864 ± 0.044	772 ± 21
0.175	t	27.46 ± 0.21	27.53 ± 0.21	0.998 ± 0.010	27.50 ± 0.14
1.2	t	111.7 ± 1.6	130.1 ± 1.4	0.858 ± 0.015	120.9 ± 1.1
1.9	t	135.2 ± 2.1	162.1 ± 1.7	0.834 ± 0.016	148.6 ± 1.4
2.5	t	156.2 ± 2.2	188.6 ± 2.2	0.828 ± 0.015	172.4 ± 1.6
0.175	^{3}He	22.27 ± 0.21	22.97 ± 0.21	0.970 ± 0.012	22.62 ± 0.14
1.2	^{3}He	106.9 ± 1.0	118.7 ± 1.0	0.900 ± 0.011	112.8 ± 0.7
1.9	^{3}He	129.6 ± 1.2	141.2 ± 1.3	0.918 ± 0.012	135.4 ± 0.9
2.5	^{3}He	147.1 ± 1.4	153.6 ± 1.5	0.957 ± 0.013	150.3 ± 1.0
0.175	^{4}He	196.6 ± 4.2	201.1 ± 1.8	0.978 ± 0.023	198.9 ± 2.3
1.2	^{4}He	613.4 ± 8.1	551.7 ± 4.2	1.111 ± 0.017	582.6 ± 4.6
1.9	^{4}He	659.8 ± 8.2	584.4 ± 4.2	1.129 ± 0.016	622.1 ± 4.6
2.5	^{4}He	714.3 ± 10.1	615.3 ± 5.4	1.161 ± 0.019	664.8 ± 5.7
0.175	^{6}He	—	0.157 ± 0.016	—	—
1.2	^{6}He	—	1.87 ± 0.09	—	—
1.9	^{6}He	—	2.21 ± 0.12	—	—
2.5	^{6}He	—	2.85 ± 0.13	—	—
0.175	^{6}Li	1.41 ± 0.077	1.30 ± 0.03	1.085 ± 0.065	1.351 ± 0.041
1.2	^{6}Li	12.38 ± 0.63	12.91 ± 0.19	0.959 ± 0.050	12.65 ± 0.33
1.9	^{6}Li	16.02 ± 0.86	17.28 ± 0.26	0.927 ± 0.051	16.65 ± 0.45
2.5	^{6}Li	19.56 ± 1.16	20.35 ± 0.26	0.961 ± 0.058	19.96 ± 0.59
0.175	^{7}Li	0.693 ± 0.065	0.693 ± 0.026	1.00 ± 0.10	0.693 ± 0.035
1.2	^{7}Li	11.5 ± 1.2	11.88 ± 0.21	0.96 ± 0.10	11.67 ± 0.58
1.9	^{7}Li	14.9 ± 1.6	16.09 ± 0.29	0.93 ± 0.10	15.51 ± 0.81
2.5	^{7}Li	17.5 ± 2.3	19.84 ± 0.34	0.88 ± 0.11	18.67 ± 1.12
0.175	^{8}Li	—	0.045 ± 0.008	—	—
1.2	^{8}Li	1.11 ± 0.12	1.127 ± 0.065	0.98 ± 0.12	1.117 ± 0.067
1.9	^{8}Li	1.7 ± 0.8	1.78 ± 0.08	0.96 ± 0.43	1.74 ± 0.39
2.5	^{8}Li	2.5 ± 0.7	2.55 ± 0.11	0.98 ± 0.25	2.53 ± 0.32
0.175	^{7}Be	0.529 ± 0.086	0.551 ± 0.022	0.96 ± 0.16	0.540 ± 0.044
1.2	^{7}Be	6.31 ± 0.81	6.61 ± 0.17	0.95 ± 0.12	6.46 ± 0.41
1.9	^{7}Be	8.77 ± 0.92	9.28 ± 0.22	0.94 ± 0.10	9.03 ± 0.47
2.5	^{7}Be	9.43 ± 0.88	10.77 ± 0.28	0.88 ± 0.085	10.10 ± 0.46
0.175	^{9}Be	0.142 ± 0.053	0.139 ± 0.024	1.02 ± 0.42	0.141 ± 0.029
1.2	^{9}Be	2.36 ± 0.27	2.73 ± 0.14	0.86 ± 0.11	2.55 ± 0.15
1.9	^{9}Be	3.60 ± 0.86	3.94 ± 0.18	0.91 ± 0.22	3.77 ± 0.44
2.5	^{9}Be	4.23 ± 1.23	4.65 ± 0.22	0.91 ± 0.27	4.44 ± 0.63
0.175	^{10}Be	—	0.067 ± 0.012	—	—
1.2	^{10}Be	1.34 ± 0.37	0.89 ± 0.06	1.51 ± 0.43	1.11 ± 0.19
1.9	^{10}Be	1.64 ± 0.37	1.60 ± 0.13	1.02 ± 0.24	1.62 ± 0.19
2.5	^{10}Be	2.49 ± 0.66	1.72 ± 0.12	1.45 ± 0.40	2.10 ± 0.33
0.175	^{10}B	0.176 ± 0.096	0.155 ± 0.057	1.1 ± 0.75	0.165 ± 0.056
1.2	^{10}B	3.2 ± 1.4	2.91 ± 0.26	1.11 ± 0.48	3.07 ± 0.69
1.9	^{10}B	5.7 ± 1.3	4.96 ± 0.29	1.14 ± 0.26	5.31 ± 0.64
2.5	^{10}B	5.9 ± 1.5	5.40 ± 0.36	1.10 ± 0.28	5.67 ± 0.75
0.175	^{11}B	0.07 ± 0.15	0.071 ± 0.012	1.0 ± 2.0	0.072 ± 0.072
1.2	^{11}B	4.9 ± 1.0	3.77 ± 0.41	1.30 ± 0.29	4.33 ± 0.51
1.9	^{11}B	7.5 ± 1.3	5.53 ± 0.48	1.35 ± 0.25	6.50 ± 0.66
2.5	^{11}B	10.0 ± 4.0	7.76 ± 0.82	1.29 ± 0.54	8.9 ± 2.1
1.2	C	—	6.59 ± 0.93	—	—
1.9	C	—	12.9 ± 1.4	—	—
2.5	C	—	12.5 ± 0.9	—	—
1.2	N	—	5.8 ± 4.3	—	—
1.9	N	—	6.9 ± 2.3	—	—
2.5	N	—	9.0 ± 1.8	—	—

Appendix E

Electronic version of experimental data

All the experimental data obtained from PISA experiment in proton induced reaction on nickel target are stored on electronic media placed as insertion on the back cover. Data for each ejectiles and beam energy are grouped in separate ASCII files, with description in header. Each file consists of data groups corresponding with detection angle, precede by line of comment with number of data rows for actual detection angle. Data are presented in three columns, the first corresponds to the ejectile energy in unity of [MeV] and the two following correspond to the double differential cross section $\frac{d\sigma}{d\Omega dE}$ $\left[\frac{\mathrm{mb}}{\mathrm{MeVsr}}\right]$ and its statistical error.

Additionally electronic version of the present thesis are include in PostScript (.ps) and Portable Document Format (.pdf) formats.

Acknowledgments

I wish to cordially thank Prof dr hab. Bogusław Kamys for multiannual introducing me to the secrets of nuclear physics, for long and fruitful discussions concerning all aspects of experiment and physics hidden behind the experimental data, for great patience and persistent stimulation to more efficient activity. In particular I would like to thank for detailed corrections of this work.

I would like to thank Prof. dr hab. Lucjan Jarczyk for constant willingness to constructive discussion concerning details of physical phenomena, for showing the other side of the coin, and for teaching me how to answer difficult questions.

I am grateful to dr hab. Frank Goldenbaum for great aid in all possible situations appearing during my stay in Jülich, for interesting discussions, friendly atmosphere and companionship during evenings in Institute.

I am indebted to Prof. dr hab. Andrzej Magiera, dr hab. Stanisław Kistryn, dr Krzysztof Pysz and dr Paweł Kulessa who have introduced me to world of experimental apparatus and signal analysis.

I am thankful to all my Colleagues from PISA collaboration, and from the room 03A, for nice atmosphere of work.

And at last but certainly not least I wish to thank my beloved wife Gabriela and our son Filip for enormous patience and support in all difficult moments, and for hearth and home.

Bibliography

[1] J. Aichelin and J. Hüfner, *Fragmentation reactions on nuclei: Condensation of vapour or shattering of glass?*, Physics Letters **B 136** (1984), 15–18.

[2] J. Aichelin, J. Hüfner, and R. Ibarra, *Cold breakup of spectator residues in nucleus-nucleus collisions at high energy*, Physical Review **C 30** (1984), 107–118.

[3] J. Aichelin, G. Peilert, A. Bohnet, A. Rosenhauer, H. Stocker, and W. Greiner, *Quantum molecular dynamics approach to heavy ion collisions: Description of the model, comparison with fragmentation data, and the mechanism of fragment formation*, Physical Review **C 37** (1988), 2451.

[4] K. Ammon, I. Leya, B. Lavielle, E. Gilabert, J.-C. David, U. Herpers, and R. Michel, *Cross sections for the production of helium, neon and argon isotopes by proton-induced reactions on iron and nickel*, Nuclear Instruments and Methods **B 266** (2008), 2–12.

[5] M.N. Andronenko, L.N. Andronenko, and W. Neubert, *Isotope ratios and isoscaling of spallation products in p(1 GeV) + A reactions*, The European Physical Journal **A 31** (2007), 125–134.

[6] M.N. Andronenko, L.N. Andronenko1, W. Neubert, and D.M. Seliverstov, *Peculiarities of isotopic temperatures obtained from p + A collisions at 1GeV*, The European Physical Journal **A 8** (2000), 9–13.

[7] T. Asano, Y. Asano, Y. Iguchi, H. Kudo, S. Mori, M. Noguchi, Y. Takada, H. Hirabayashi, H. Ikeda, K. Katoh, K. Kondo, M. Takasaki, T. Tominaka, and A. Yamamoto, *Target dependence of charge distributions in spallation reactions of medium-mass nuclei with 12 GeV protons*, Physical Review **C 28** (1983), 1718–1724.

[8] Y. Asano, S. Mori, M. Sakano, K. Katoh, K. Kondo, and M. Noguchi, *Nuclear reactions of Ti, Fe, Co, Ni, Cu, and Zn by 500-MeV protons*, Journal of The Physical Society of Japan **60** (1991), 107–113.

[9] F. Atchison, *Spallation and fission in heavy metal nuclei under medium energy proton bombardement*, Proc. Meeting on targets for neutron beam spallation source (G.S. Bauer, ed.), Jül-Conf-34, Kernforschungsanlage Jülich GmbH, 1980, pp. 17–46.

[10] ______, *A treatment of fission for HETC*, Intermediate Energy Nuclear Data: Models and Codes, Proc. of a Specialists' Meeting, Issy-Les-Moulineaux, France, 30 May-1 June, OECD/NEA, 1994, pp. 199–218.

[11] S.P. Avdeyev, V.A. Karnaukhov, L.A. Petrov, V.K. Rodionov, P.A. Rukoyatkin, V.D. Toneev, H. Oeschler, O.V. Bochkarev, L.V. Chulkov, E.A. Kuzmin, A. Budzanowski, W. Karcz, M. Janicki, E. Norbeck, A.S. Botvina, and K.K. Gudima, *Comparative study of multifragmentation of gold nuclei induced by relativistic protons, ^{4}He, and ^{12}C*, Nuclear Physics **A 709** (2002), 392–414.

[12] R. Barna, V. Bollini, A. Bubak, A. Budzanowski, D. De Pasquale, D. Filges, S.V. Förtsch, F. Goldenbaum, A. Heczko, H. Hodde, A. Italiano, L. Jarczyk, B. Kamys, J. Kisiel, M. Kistryn, St. Kistryn, St. Kliczewski, A. Kowalczyk, P. Kulessa, H. Machner, A. Magiera, J. Majewski, W. Migdal, H. Ohm, N. Paul, B. Piskor-Ignatowicz, K. Pysz, Z. Rudy, H. Schaal, R. Siudak, E. Stephan, G.F. Steyn, R. Sworst, T. Thovhogi, M. Wojciechowski, and W. Zipper, *PISA – an experiment for fragment spectroscopy at the internal beam of COSY: application of an axial ionization chamber*, Nuclear Instruments and Methods in Physics Research **A 519** (2004), 610–622.

[13] S. A. Bass, M. Belkacem, M. Bleicher, M. Brandstetter, L. Bravina, C. Ernst, L. Gerland, M. Hofmann, S. Hofmann, J. Konopka, G. Mao, L. Neise, S. Soff, C. Spieles, H. Weber, L. A. Winckelmann, H. Stocker, W. Greiner, Ch. Hartnack, J. Aichelin, and N. Amelin, *Microscopic models for ultrarelativistic heavy ion collisions*, Progress in Particle and Nuclear Physics **41** (1998), 255–369.

[14] K. Beg and N. T. Porile, *Energy dependence of the recoil properties of products from the interaction of ^{238}U with 0.45-11.5-GeV protons*, Phys. Rev. **C 3** (1971), 1631–1645.

[15] J. Benecke, T. T. Chou, C. N. Yang, and E. Yen, *Hypothesis of limiting fragmentation in high-energy collisions*, Phys. Rev. **188** (1969), 2159–2169.

[16] G. Berlad, A. Dar, and G. Eilam, *Multiparticle production in particle-nucleus collisions at high energies*, Phys. Rev. **D 13** (1976), 161–165.

[17] Hugo W. Bertini, *Nonelastic interactions of nucleons and π mesons with complex nuclei at energies below 3 GeV*, Phys. Rev. C **6** (1972), 631–659.

[18] F.E. Bertrand and R.W. Peelle, *Complete hydrogen and helium particle spectra from 30- to 60-MeV proton bombardment of nuclei with A = 12 to 209 and comparison with the intranuclear cascade model*, Physical Review **C8** (1973), 1045–1064.

[19] G. F. Bertsch, H. Kruse, and S. Das Gupta, *Boltzmann equation for heavy ion collisions*, Phys. Rev. **C 29** (1984), 673–675.

[20] R.H. Bieri and W. Rutsch, Compte Rendu de la Reunion de la Society Suisse de Physique, vol. 32, 1962, p. 553.

[21] J. B. Birks, *The theory and practice of scintillation counting*, p. 465, Pergamon, 1964.

[22] S. Biswas and N.T. Porile, *Formation of isobaric nuclides with A=131 in the interaction of ^{238}U with 0.8-11.5 GeV protons*, Physical Review **C 20** (1979), 1467–1478.

[23] D. H. Boal and R. M. Woloshyn, *Direct knockout model for nuclear fragmentation*, Phys. Rev. **C 20** (1979), 1878–1883.

[24] S. Bohrmann, J. Hüfner, and M.C. Nemes, *Cleavage: a high-energy proton can split a nucleus into pieces*, Physics Letters **B 120** (1983), 59–62.

[25] J.P. Bondorf, A.S. Botvina, A.S. Iljinov, I.N. Mishustin, and K. Sneppen, *Statistical multifragmentation of nuclei*, Physics Reports **257** (1995), 133–221.

[26] A. S. Botvina and I. N. Mishustin, *Statistical description of multifragmentation: from nuclear reactions to supernova explosions*, Nuclear Methods for Non-Nuclear Applications (Ch. Stoyanov, ed.), Heron Press Ltd, Sofia, 2007, pp. 303–319.

[27] A.S. Botvina, A.S. Iljinov, and I.N. Mishustin, *Multifragment break-up of nuclei by intermediate-energy protons*, Nuclear Physics **A 507** (1990), 649–674.

[28] A. Boudard, J. Cugnon, S. Leray, and C. Volant, *Intranuclear cascade model for a comprehensive description of spallation reaction data*, Physical Review **C 66** (2002), no. 044615, 1–28.

[29] ———, *A new model for production of fast light clusters in spallation reactions*, Nuclear Physics **A 740** (2004), 195–210.

[30] A. Bubak, *Emission of intermediate mass fragments in the p(1.9GeV)+^{nat}Ni reaction*, Ph.D. thesis, Katowice University, 2004, ISSN 0944-2952.

[31] A. Bubak, A. Budzanowski, D. Filges, F. Goldenbaum, A. Heczko, H. Hodde, L. Jarczyk, B. Kamys, M. Kistryn, St. Kistryn, St. Kliczewski, A. Kowalczyk, E. Kozik, P. Kulessa, H. Machner, A. Magiera, W. Migdał, N. Paul, B. Piskor-Ignatowicz, M. Puchała, K. Pysz, Z. Rudy, R. Siudak, M. Wojciechowski, and P. Wüstner, *Non-equilibrium emission of complex fragments from p + Au collisions at 2.5 GeV proton beam energy*, Physical Review C **76** (2007), 014618.

[32] A. Bubak, B. Kamys, M. Kistryn, and B. Piskor-Ignatowicz, *Parameterization of the total cross-section for (p,^{7}Be) reaction*, Nuclear Instruments and Methods **B 226** (2004), 507–516.

[33] A. Budzanowski, M. Fidelus, D. Filges, F. Goldenbaum, H. Hodde, L. Jarczyk, B. Kamys, M. Kistryn, St. Kistryn, St. Kliczewski, A. Kowalczyk, E. Kozik, P. Kulessa, H. Machner, A. Magiera, B. Piskor-Ignatowicz, K. Pysz, Z. Rudy, R. Siudak, and M. Wojciechowski, *Competition of coalescence and "fireball" processes in nonequilibrium emission of light charged particles from p+Au collisions*, Physical Review **C 78** (2008), 024603.

[34] A. Bujak, J. E. Finn, L. J. Gutay, A. S. Hirsch, R. W. Minich, G. Paderewski, N. T. Porile, R. P. Scharenberg, B. C. Stringfellow, and F. Turkot, *Mass yield distribution for the interaction of silver with 300 GeV protons*, Phys. Rev. C **32** (1985), 620–622.

[35] S. T. Butler and C. A. Pearson, *Deuterons from high-energy proton bombardment of matter*, Phys. Rev. Lett. **7** (1961), 69–71.

[36] R.J. Charity, M.A. McMahan, G.J. Wozniak, R.J. McDonald, L.G. Moretto, D.G. Sarantites, L.G. Sobotka, G. Guarino, A. Pantaleo, L. Fiore, A. Gobbi, and K.D. Hildenbrand, *Systematics of complex fragment emission in niobium-induced reactions*, Nuclear Physics **A 483** (1988), 371–405.

[37] C.-X. Chen, S. Albergo, Z. Caccia, S. Costa, H.J. Crawford, M. Cronqvist, J. Engelage, P. Ferrando, R. Fonte, L. Greiner, T.G. Guzik, A. Insolia, F.C. Jones, C.N. Knott, P.J. Lindstrom, J.W. Mitchell, R. Potenza, J. Romanski, G.V. Russo, A. Soutoul, O. Testard, C.E. Tull, C. Tuvé, C.J. Waddington, W.R. Webber, J.P. Wefel, and X. Zhang, *Interactions in hydrogen of relativistic neon to nickel projectiles:Total charge-changing cross sections*, Physical Review **C 49** (1994), 3200–3210.

[38] S. Chiba, M.B. Chadwick, K. Niita, Ts. Maruyama, Tm. Maruyama, and A. Iwamoto, *Nucleon-induced preequilibrium reactions in terms of the quantum molecular dynamics*, Physical Review **C 53** (1996), 1824–1832.

[39] J. Cugnon, C. Volant, and S. Vuillier, *Improved intranuclear cascade model for nucleon-nucleus interactions*, Nuclear Physics **A 620** (1997), 475–509.

[40] J. B. Cumming, R. J. Cross, J. Hudis, and A. M. Poskanzer, *Study of a fragmentation reaction by thin-target recoil techniques; Production of ^{24}Na from bismuth by 2.9-GeV protons*, Phys. Rev. **134** (1964), B167–B174.

[41] M.W. Curtin, H. Toki, and D.K. Scott, *Liquid-gas phase instabilities in nuclear systems*, Physics Letters **B 123** (1983), 289–292.

[42] B. Dittrich, U. Herpers, H.J. Hofmann, W. Wölfli, R. Bodemann, M. Lüpke, R. Michel, P. Dragovitsch, and D. Filges, *AMS measurements of thin-target cross sections for the production of ^{10}Be and ^{26}Al by high-energy protons*, Nuclear Instruments and Methods in Physics Research **B 52** (1990), 588–594.

[43] I. Dostrovsky, Z. Fraenkel, and G. Friedlander, *Monte Carlo calculations of nuclear evaporation processes. III. Applications to low-energy reactions*, Phys. Rev. **116** (1959), no. 3, 683–702.

[44] G. English, Y.W. Yu, and N.T. Porile, *Nuclear reactions of silver with 300 GeV protons*, Physical Review C **10** (1974), 2281.

[45] M. Fidelus, *private comunication*, LCP and IMF energy spectra and quantities of remnant nucleus.

[46] J.E. Finn, S. Agarwal, A. Bujak, J. Chuang, L.J. Gutay, A.S. Hirsch, R.W. Minich, N.T. Porile, R.P. Scharenberg, and B.C. Stringfellow, *Nuclear fragment mass yields from high-energy proton-nucleus interactions*, Physical Review Letters **49** (1982), 1321–1325.

[47] M.E. Fisher, *Theory of equilibrium critical phenomena*, Reports on Progress in Physics **30** (1967), 615.

[48] A.S. Fomichev, I. David, S.M. Lukyanov, Yu.E. Penionzhkevich, N.K. Skobelev, O.B. Tarasova, A. Matthiesb, H.-G. Ortleppb, W. Wagner, M. Lewitowicz, M.G. Saint-Laurent, J.M. Corre, Z. Dlouhy, I. Pecina, and C. Borceae, *The response of a large CsI (Tl) detector to light particles and heavy ions in the intermediate energy range*, Nuclear Instruments and Methods in Physics Research **A344** (1994), 378–383.

[49] D. R. Fortney and N. T. Porile, *Angular distributions of Sc fragments from the interaction of ^{238}U with 0.8-400 GeV protons*, Phys. Rev. **C 21** (1980), 2511–2518.

[50] S.V. Förtsch, A.A. Cowley, J.J. Lawrie, D.M. Whittal, J.V. Pilcher, and F.D. Smit, *Continuum protons from ^{58}Ni(p,p') at incident energies between 100 and 200 MeV*, Physical Review **C43** (1991), 691–700.

[51] J. Franz, P. Koncz, E. Rössle, C. Sauerwein, H. Schmitt, K. Schmoll, J. Erö, Z. Fodor, J. Kecskémeti, Zs. Kovács, and Z. Seres, *Neutron-induced production of protons, deuterons and tritons on copper and bismuth*, Nuclear Physics **A 510** (1990), 774–802.

[52] S. Furihata, *Statistical analysis of light fragment production from medium energy proton-induced reactions*, Nuclear Instruments and Methods in Physics Research B **171** (2000), 251.

[53] S. Furihata and T. Nakamura, *Calculation of nuclide productions from proton induced reactions on heavy targets with INC/GEM*, J. Nucl. Sci. Technol. **Suppl. 2** (2002), 758–761.

[54] S. Furihata, K. Niita, S. Meigo, Y. Ikeda, and F. Maekawa, *The GEM code — A simulation program for the evaporation and the fission process of an excited nucleus*, Report JAERI-Data/Code, 2001-015, Japan Atomic Energy Research Institute, JAERI, 2001.

[55] J.-J. Gaimard and K.-H. Schmidt, *A reexamination of the abrasion-ablation model for the description of the nuclear fragmentation reaction*, Nuclear Physics **A 531** (1991), 709–745.

[56] J. Geiss, W. Cassing, and C. Greiner, *Strangeness production in the HSD transport approach from SIS to SPS energies*, Nuclear Physics **A 644** (1998), 107–138.

[57] K. Goebel, H. Schultes, and J. Zähringer, *Production cross sections of tritium and rare gases in various target elements*, Tech. Report CERN-64-12, C.E.R.N., 1964.

[58] J. Gosset, H. H. Gutbrod, W. G. Meyer, A. M. Poskanzer, A. Sandoval, R. Stock, and G. D. Westfall, *Central collisions of relativistic heavy ions*, Phys. Rev. **C 16** (1977), 629–657.

[59] K. Gottfried, *Space-time structure of hadronic collisions and nuclear multiple production*, Phys. Rev. Lett. **32** (1974), 957–961.

[60] S.L. Green, W.V. Green, F.H. Hegedus, M. Victoria, W.F. Sommer, and B.M. Oliver, *Production of helium by medium energy (600 and 800 MeV) proton*, Journal of Nuclear Materials **155** (1988), 1350–1353.

[61] D.H.E. Gross, *Statistical decay of very hot nuclei-the production of large clusters*, Rep. Prog. Phys. **53** (1990), 605–658.

[62] S. Das Gupta, *^{12}C on ^{12}C at 800 MeV/nucleon: One fireball or two?*, Phys. Rev. Lett. **41** (1978), 1450–1453.

[63] S. Das Gupta, S. Mekjian, and M. Tsang, *Advances in nuclear physics*, j.w. negele and e.w. vogt ed., Advances in Physics of Particles and Nuclei, vol. 26, ch. Liquid-Gas Phase Transition in Nuclear Multifragmentation, pp. 89–166, Springer US, 2002.

[64] H. H. Gutbrod, A. Sandoval, P. J. Johansen, A. M. Poskanzer, J. Gosset, W. G. Meyer, G. D. Westfall, and R. Stock, *Final-state interactions in the production of hydrogen and helium isotopes by relativistic heavy ions on uranium*, Phys. Rev. Lett. **37** (1976), 667–670.

[65] W. Hauser and H. Feshbach, *The inelastic scattering of neutrons*, Phys. Rev. **87** (1952), 366–373.

[66] C.-M. Herbach, D. Hilscher, U. Jahnke, V.G. Tishchenko, J. Galin, A. Letourneau, A. Péghaire, D. Filges, F. Goldenbaum, L. Pienkowski, W.U. Schröder, and J. Tőke, *Charged-particle evaporation and pre-equilibrium emission in 1.2 GeV proton-induced spallation reactions*, Nuclear Physics **A 765** (2006), 426–463.

[67] A.S. Hirsch, A. Bujak, J.E. Finn, L.J. Gutay, R.W. Minich, N.T. Porile, R.P. Scharenberg, B.C. Stringfellow, and F. Turkot, *Experimental results from high energy proton-nucleus interactions, critical phenomena and the thermal liquid drop model of fragment production*, Physical Review **C 29** (1984), 508.

[68] P.E. Hodgson and E. Běták, *Cluster emission, transfer and capture in nuclear reactions*, Physics Reports **374** (2003), 1–89.

[69] D. Horn, G.C. Ball, A. Galindo-Uribarri, E. Hagberg, R.B. Walker, R. Laforest, and J. Pouliot, *The mass dependence of CsI(Tl) scintillation response to heavy ions*, Nuclear Instruments and Methods in Physics Research **A 320** (1992), 273–276.

[70] W.-c. Hsi, K. Kwiatkowski, G. Wang, D. S. Bracken, E. Cornell, D. S. Ginger, V. E. Viola, N. R. Yoder, R. G. Korteling, F. Gimeno-Nogures, E. Ramakrishnan, D. Rowland, S. J. Yennello, M. J. Huang, W. G. Lynch, M. B. Tsang, H. Xi, Y. Y. Chu, S. Gushue, L. P. Remsberg, K. B. Morley, and H. Breuer, *Formation of hot nuclei with GeV p and π^- beams*, Phys. Rev. Lett. **79** (1997), 817–820.

[71] J. Hüfner, *Heavy fragments produced in proton-nucleus and nucleus-nucleus collisions at relativistic energies*, Physics Reports **125** (1985), 129–185.

[72] J. Hüfner and H. M. Sommermann, *Enhanced backward emission of heavy fragments in high-energy proton-nucleus collisions*, Phys. Rev. **C 27** (1983), 2090–2095.

[73] K. Ikeda, Kyoto Conference, 1988, p. 247.

[74] B. V. Jacak, D. Fox, and G. D. Westfall, *Coalescence of complex fragments*, Phys. Rev. **C 31** (1985), 704–706.

[75] A.R. Junghans, M. de Jong, H.-G. Clerc, A.V. Ignatyuk, G.A. Kudyaev, and K.-H. Schmidt, *Projectile-fragment yields as a probe for the collective enhancement in the nuclear level density*, Nuclear Physics **A 629** (1998), 635–655.

[76] C. Kalbach, *Preequilibrium reactions with complex particle channels*, Physical Review **C 71** (2005), 034606.

[77] A.M. Kalend, B.D. Anderson, A.R. Baldwin, R. Madey, J.W. Watson, C.C. Chang, H.D. Holmgren, R.W. Koontz, J.R. Wu, and H. Machner, *Energy and angular distributions of neutrons from 90 MeV proton and 140 MeV alpha-particle bombardment of nuclei*, Physical Review **C 28** (1983), 105–119.

[78] V.A. Karnaukhov, H. Oeschler, S.P. Avdeyev, E.V. Duginova, V.K. Rodionov, A. Budzanowski, W. Karcz, O.V. Bochkarev, E.A. Kuzmin, L.V. Chulkov, E. Norbeck, and A.S. Botvina, *Critical temperature for the nuclear liquid-gas phase transition*, Physical Review **C 67** (2003), 011601(R).

[79] S. B. Kaufman and E. P. Steinberg, *Cross-section measurements of nuclides formed by the reaction of 0.20-6.0 GeV protons with* ^{197}*Au*, Phys. Rev. C **22** (1980), 167–178.

[80] M. Kleine Berkenbusch, W. Bauer, K. Dillman, S. Pratt, L. Beaulieu, K. Kwiatkowski, T. Lefort, W.-c. Hsi, V. E. Viola, S. J. Yennello, R. G. Korteling, and H. Breuer, *Event-by-event analysis of proton-induced nuclear multifragmentation: Determination of the phase transition universality class in a system with extreme finite-size constraints*, Phys. Rev. Lett. **88** (2002), 022701.

[81] C.N. Knott, S. Albergo, Z. Caccia, C.-X. Chen, S. Costa, H.J. Crawford, M. Cronqvist, J. Engelage, P. Ferrando, R. Fonte, L. Greiner, T.G. Guzik, A. Insolia, F.C. Jones, P.J. Lindstrom, J.W. Mitchell, R. Potenza, J. Romanski, G.V. Russo, A. Soutoul, O. Testard, C.E. Tull, C. Tuvé, C.J. Waddington, W.R. Webber, and J.P. Wefel, *Interactions of relativistic neon to nickel projectiles in hydrogen, elemental production cross sections*, Physical Review **C 53** (1996), 347–357.

[82] A.A. Kotov, L.N. Andronenko, M.N. Andronenko, Y.I. Gusev, K.V. Lukashin, W. Neubert, D.M. Seliverstov, I.I. Strakovsky, and L.A. Vaishnene, *Intermediate mass fragment production on Au, Ag, Ni and Al targets induced by 1 GeV protons*, Nuclear Physics **A 583** (1995), 575–580.

[83] A. Kowalczyk, *private comunication*, LCPs energy spectra.

[84] H. Kruse, B. V. Jacak, J. J. Molitoris, G. D. Westfall, and H. Stöcker, *Vlasov-Uehling-Uhlenbeck theory of medium energy heavy ion reactions: Role of mean field dynamics and two body collisions*, Phys. Rev. C **31** (1985), 1770–1774.

[85] H. Kruse, B. V. Jacak, and H. Stöcker, *Microscopic theory of pion production and sidewards flow in heavy-ion collisions*, Phys. Rev. Lett. **54** (1985), 289–292.

[86] M.S. Lafleur, N.T. Porile, and L. Yaffe, *Formation of* ^{7}*Be in nuclear reactions induced by 85-MeV protons*, Canadian Journal of Chemistry **44** (1966), 2749–2767.

[87] W. R. Leo, *Techniques for nuclear and particle physics experiments*, Springer-Verlag Berlin Heidelberg, 1987.

[88] A. Letourneau, *Etudes de la réaction de spallation p+Au à 2.5 GeV et de la production neutronique en cible épaisses (Pb, W et Hg) par des protons de 0.4 à 2.5 GeV*, Ph.D. thesis, L'Universite de Caen, 2000, GANIL T 00 06.

[89] A. Letourneau, A. Böhm, J. Galin, B. Lott, A. Péghaire, M. Enke, C.-M. Herbach, D. Hilscher, U. Jahnke, V. Tishchenko, D. Filges, F. Goldenbaum, R.D. Neef, K. Nünighoff, N. Paul, G. Sterzenbach, L. Pienkowski, J. Töke, and U. Schröder, *Composite-particle emission in the reaction p + Au at 2.5 GeV*, Nuclear Physics **A 712** (2002), 133–166.

[90] W. G. Lynch, *Nuclear fragmentation in proton- and heavy-ion-induced reactions*, Annual Reviews Nucl. Part. Sci. **37** (1987), 493–535.

[91] H. Machner, D. G. Aschman, K. Baruth-Ram, J. Carter, A. A. Cowley, F. Goldenbaum, B. M. Nangu, J. V. Pilcher, E. Sideras-Haddad, J. P. F. Sellschop, F. D. Smit, B. Spoelstra, and D. Steyn, *Isotopic production cross sections in proton-nucleus collisions at 200 MeV*, Physical Review **C 73** (2006), 044606.

[92] M. Mahi, Y.H. Chung A.T. Bujak, D.D. Carmony, G.L. Paderewski L.J. Gutay, A.S. Hirsch, N.T. Porile, T.C. Sangster, R.P. Scharenberg, and B.C. Stringfellow, *Energy dependence of proton-induced xenon fragmentation and the approach to liquid-gas criticality in nuclear matter*, Physical Review Letters **60** (1988), 1936.

[93] R. Maier, *Cooler synchrotron COSY - performance and perspectives*, Nuclear Instruments and Methods in Physics Research **A 390** (1997), 1–8.

[94] N. Metropolis, R. Bivins, M. Storm, J. M. Miller, G. Friedlander, and A. Turkevich, *Monte carlo calculations on intranuclear cascades. II. high-energy studies and pion processes*, Phys. Rev. **110** (1958), 204–219.

[95] R. Michel, R. Bodemann, H. Busemann, R. Daunke, M. Gloris, H.-J. Lange, B. Klug, A. Krins, I. Leya M. Lüpke, S. Neumann, H. Reinhardt, M. Schnatz-Büttgen, U. Herpers, Th. Schiekel, F. Sudbrock, B. Holmqvist, H. Condé, P. Malmborg, M. Suter, B. Dittrich-Hannen, P.W. Kubik, H.-A. Synal, and D. Filges, *Cross sections for the production of residual nuclides by low- and medium-energy protons from the target elements C, N, O, Mg, Al, Si, Ca, Ti, V, Mn, Fe, Co, Ni, Cu, Sr, Y, Zr, Nb, Ba and Au*, Nuclear Instruments and Methods **B 129** (1997), 153–193.

[96] R. Michel and G. Brinkmann, *On the depth-dependent production of radionuclides ($44 \leq A \leq 59$) by solar protons in extraterrestrial matter*, Journal of Radioanalytical and Nuclear Chemistry **59** (1980), 467–510.

[97] R. Michel, B. Dittrich, U. Herpers, F. Peiffer, T. Schiffmann, P. Cloth, P. Dragovitsch, and D. Filges, *Proton-induced spallation at 600 MeV*, Analyst **114** (1989), 287–293.

[98] R. Michel, M. Gloris, H.-J. Lange, I. Leya M. Lüpke, U. Herpers, B. Dittrich-Hannen, R. Rösel, Th. Schiekel, D. Filges, P. Dragovitsch, M. Suter, H.-J. Hofmann, W. Wölfli, P.W. Kubik, H. Baur, and R. Wieler, *Nuclide production by proton-induced reactions on elements ($6 \leq Z \leq 29$) in the energy range from 800 to 2600 MeV*, Nuclear Instruments and Methods **B 103** (1995), 183–222.

[99] R. Michel and R. Stück, *On the production of cosmogenic nuclides in meteorites by primary galactic particles: cross sections and model calculations*, Journal of Geophysical Research Supplement **89** (1984), B673–B684.

[100] R. Michel, H. Weigel, and W. Herr, *Proton-induced reactions on nickel with energies between 12 and 45 MeV*, Zeitschrift für Physik **A 286** (1978), 393–400.

[101] R.W. Minich, S. Agarwal, A. Bujak, J. Chuang, J.E. Finn, L.J. Gutay, A.S. Hirsch, N.T. Porile, R.P. Scharenberg, and B.C. Stringfellow, *Critical phenomena in hadronic matter and experimental isotopic yields in high energy proton-nucleus collisions*, Physics Letters B **118** (1982), 458.

[102] J. J. Molitoris, J. B. Hoffer, H. Kruse, and H. Stöcker, *Microscopic calculations of collective flow probing the short-range nature of the nuclear force*, Phys. Rev. Lett. **53** (1984), 899–902.

[103] J. J. Molitoris, H. Stöcker, and B. L. Winer, *Evolution of 4π observables in the Vlasov-Uehling-Uhlenbeck theory and the transverse momentum transfer as a barometer for hadronic matter*, Phys. Rev. **C 36** (1987), 220–229.

[104] L. G. Moretto, *Statistical emission of large fragments: A general theoretical approach*, Nuclear Physics **A 247** (1975), 211–230.

[105] L.G. Moretto and G.J. Wozniak, *Multifragmentation in heavy-ion processes*, Annu. Rev. Nucl. Part. Sci. **43** (1993), 379–455.

[106] W. D. Myers, *A model for high-energy heavy-ion collisions*, Nuclear Physics **A 296** (1978), 177–188.

[107] K. Nakai, *Study of energy deposition of GeV particles in nuclei*, Nuclear Physics **A 418** (1984), 163–176.

[108] P. Napolitani, *private comunication*, velocity and energy spectra.

[109] P. Napolitani, K.-H. Schmidt, A.S. Botvina, F. Rejmund, L. Tassan-Got, and C. Villagrasa, *High-resolution velocity measurements on fully identified light nuclides produced in ^{56}Fe+hydrogen and ^{56}Fe+titanium systems*, Physical Review **C 70** (2004), 054607.

[110] K. Niita, S. Chiba, T. Maruyama, T. Maruyama, H. Takada, T. Fukahori, Y. Nakahara, and A. Iwamoto, *Analysis of the (N,xN') reactions by quantum molecular dynamics plus ststistical decay model*, Physical Review **C 52** (1995), 2620–2635.

[111] N. T. Porile, A. J. Bujak, D. D. Carmony, Y. H. Chung, L. J. Gutay, A. S. Hirsch, M. Mahi, G. L. Paderewski, T. C. Sangster, R. P. Scharenberg, and B. C. Stringfellow, *Approach to criticality in the fragmentation of xenon by 1–19 GeV protons*, Phys. Rev. **C 39** (1989), 1914–1928.

[112] N. T. Porile, G. D. Cole, and C. R. Rudy, *Nuclear reactions of silver with 25.2 GeV ^{12}C ions and 300 GeV protons*, Phys. Rev. C **19** (1979), 2288–2304.

[113] N. T. Porile, D. R. Fortney, S. Pandian, R. A. Johns, Thomas Kaiser, Karoline Wielgoz, T. S. K. Chang, Nathan Sugarman, J. A. Urbon, D. J. Henderson, S. B. Kaufman, and E. P. Steinberg, *Unusual backward enhancement in the angular distribution of products from the interaction of ^{238}U with 400-GeV protons*, Phys. Rev. Lett. **43** (1979), 918–921.

[114] R. E. Prael, *A review of physics models in the LAHET code*, Intermediate Energy Nuclear Data: Models and Codes, Proc. of a Specialists' Meeting, Issy-Les-Moulineaux, France, 30 May-1 June, OECD/NEA, 1994, pp. 145–157.

[115] R. E. Prael and D. G. Madland, *LAHET code system modifications for LAHET 2.8*, Report LA-UR-95-3605744, Los Alamos Nat. Lab, USA, 1995.

[116] Al. H. Raduta and Ad. R. Raduta, *Simulation of statistical ensembles suitable for the description of nuclear multifragmentation*, Phys. Rev. **C 55** (1997), 1344–1352.

[117] G.M. Raisbeck, P. Boerstling, R. Klapisch, and T.D. Thomas, *Li, Be, and B production in the 3-GeV proton bombardment of Ni*, Physical Review **C 12** (1975), 527–532.

[118] G.M. Raisbeck and F. Yiou, *Production cross sections for ^{7}Be and ^{22}Na in targets of Si, Mg, Fe, and Ni irradiated by 1, 2, 3, and 23 GeV protons*, Physical Review **C 12** (1975), 915–920.

[119] J. Randrup and S. E. Koonin, *The disassembly of nuclear matter*, Nuclear Physics **A 356** (1981), 223–234.

[120] G.V.S. Rayudu, *Formation cross sections of various radionuclides from Ni, Fe, Si, Mg, O and C for protons of energies between 130 and 400 MeV*, Canadian Journal of Chemistry **42** (1964), 1149–1154.

[121] ———, *Formation cross sections of various radionuclides from Ni, Fe, Si, Mg, O and C for protons of energies between 0.5 and 2.9 GeV*, J. inorg, nucl. Chem. **30** (1968), 2311–2315.

[122] S. Regnier, *Production of argon isotopes by spallation of Sc, Ti, Fe, Co, Ni, and Cu*, Physical Review **C20** (1979), 1517–1527.

[123] J. Richert and P. Wagner, *Microscopic model approaches to fragmentation of nuclei and phase transitions in nuclear matter*, Physics Reports **350** (2001), 1–92.

[124] G. Roy, L. G. Greeniaus, G. A. Moss, D. A. Hutcheon, R. Liljestrand, R. M. Woloshyn, D. H. Boal, A. W. Stetz, K. Aniol, A. Willis, N. Willis, and R. McCamis, *Inclusive scattering of protons on helium, nickel, and tantalum at 500 MeV*, Phys. Rev. **C 23** (1981), 1671–1678.

[125] G. Sauer, H. Chandra, and U. Mosel, *Thermal properties of nuclei*, Nuclear Physics **A 264** (1976), 221–243.

[126] Th. Schiekel, F. Sudbrock, U. Herpers, M. Gloris, H.-J. Lange, I. Leya, R. Michel, B. Dittrich-Hannen, H.-A. Synal, M. Suter, P.W. Kubik, M. Blann, and D. Filges, *Nuclide production by proton-induced reactions on elements ($6 \leq Z \leq 29$) in the energy range from 200 MeV to 400 MeV*, Nuclear Instruments and Methods in Physics Research **B 114** (1996), 91–119.

[127] R.E. Segel, T. Chen, L.L. Rutledge, J.V. Maher, J. Wiggins, P.P. Singh, and P.T. Debevec, *Inclusive proton reactions at 164 MeV*, Physical Review **C 26** (1982), 2424–2432.

[128] R. Serber, *Nuclear reactions at high energies*, Phys. Rev. **72** (1947), 1114–1115.

[129] S. Shibata, M. Imamura, H. Nagai, K. Kobayashi, K. Sakamoto, M. Furukawa, and I. Fujiwara, *Measurements of ^{10}Be and ^{26}Al production cross sections with 12 GeV protons by accelerator mass spectrometry*, Physical Review **C 48** (1993), 2617–2624.

[130] A. J. Sierk, *Macroscopic model of rotating nuclei*, Phys. Rev. **C 33** (1986), 2039–2053.

[131] R. Silberberg and C.H. Tsao, *Spallation processes and nuclear interaction products of cosmic rays*, Physics Reports **191** (1990), 351–408.

[132] H. Sorge, H. Stocker, and W. Greiner, *Relativistic quantum molecular dynamics approach to nuclear collisions at ultrarelativistic energies*, Nuclear Physics **A 498** (1989), 567–576.

[133] K. Sümmerer and B. Blank, *Epax*, Physical Review C **61** (2000), 034607.

[134] Meng Ta-chung, *Multiparticle production in high-energy hadron-nucleus collisions*, Phys. Rev. **D 15** (1977), 197–205.

[135] W. Trautmann, U. Milkau, U. Lynen, and J. Pochodzalla, *Systematics of the power law parameter and minimum angular momenta for fragment production*, Zeitschrift für Physik **A 344** (1993), 447–454.

[136] R.K. Tripathi, F.A. Cucinotta, and J.W. Wilson, *Accurate universal parameterization of absorption cross sections*, Nuclear Instruments and Methods **B 117** (1996), 347–349.

[137] E. A. Uehling and G. E. Uhlenbeck, *Transport phenomena in Einstein-Bose and Fermi-Dirac gases. I*, Phys. Rev. **43** (1933), 552–561.

[138] C. Villagrasa-Canton, A. Boudard, J.-E. Ducret, B. Fernandez, S. Leray, C. Volant, P. Armbruster, T. Enqvist, F. Hammache, K. Helariutta, B. Jurado, M.-V. Ricciardi, K.-H. Schmidt, K. Sümmerer, F. Vivès, O. Yordanov, L. Audouin, C.-O. Bacri, L. Ferrant, P. Napolitani, F. Rejmund, C. Stéphan, L. Tassan-Got, J. Benlliure, E. Casarejos, M. Fernandez-Ordo nez, J. Pereira, S. Czajkowski, D. Karamanis, M. Pravikoff, J.S. George, R.A. Mewaldt, N. Yanasak, M. Wiedenbeck, J.J. Connell, T. Faestermann, A. Heinz, and A. Junghans, *Spallation residues in the reaction ^{56}fe+p at 0.3A,0.5A,0.75A,1.0A, and 1.5A GeV*, Physical Review **C 75** (2007), 044603.

[139] V.E. Viola, K. Kwiatkowski, L. Beaulieu, D.S. Bracken, H. Breuer, J. Brzychczyk, R.T. de Souza, D.S. Ginger, W-C. Hsi, R.G. Korteling, T. Lefort, W.G. Lynch, K.B. Morley, R. Legrain, L. Pienkowski, E.C. Pollacco, E. Renshaw, A. Ruangma, M.B. Tsang, C. Volant, G. Wang, S.J. Yennello, and N.R. Yoder, *Light-ion-induced multifragmentation: The ISiS project*, Physics Reports **434** (2006), 1–46.

[140] E.N. Volnin, G.M. Amalsky, D.M. Seleverstov, N.N. Smirnov, A.A. Vorobyov, and Yu.P. Yakovlev, *Fragmentation of nuclei of various nucleon composition in the interaction with 1 GeV protons*, Physics Letters **B 55** (1975), 409–410.

[141] A. Wagner, W. P. Tan, K. Chalut, R. J. Charity, B. Davin, Y. Larochelle, M. D. Lennek, T. X. Liu, X. D. Liu, W. G. Lynch, A. M. Ramos, R. Shomin, L. G. Sobotka, R. T. de Souza, M. B. Tsang, G. Verde, and H. S. Xu, *Energy resolution and energy–light response of CsI(Tl)*

scintillators for charged particle detection, Nuclear Instruments and Methods in Physics Research **A456** (2001), 290–299.

[142] Y. Watanabe and D. N. Kadrev, *Quantum molecular dynamics calculation of light-ion production in neutron-induced reactions at intermediate energies*, Radiation Protection Dosimetry Advance Access (2007), 1–5.

[143] W.R. Webber, J.C. Kish, J.M. Rockstroh, Y. Cassagnou, R. Legrain, A. Soutoul, O. Testard, and C. Tull, *Production cross sections of fragments from beams of 400-650 MeV per nucleon 9Be, 11B, 12C, 14N, 15N, 16O, 20Ne, 22Ne, 56Fe, and 58Ni nuclei interacting in a liquid hydrogen target. I. charge changing and total cross sections*, The Astrophysical Journal **508** (1998), 940–948.

[144] ______, *Production cross sections of fragments from beams of 400-650 MeV per nucleon 9Be, 11B, 12C, 14N, 15N, 16O, 20Ne, 22Ne, 56Fe, and 58Ni nuclei interacting in a liquid hydrogen target. II. isotopic cross sections of fragments*, The Astrophysical Journal **508** (1998), 949–958.

[145] W.R. Webber, J.C. Kish, and D.A. Schrier, *Formula for calculating partial cross sections for nuclear reactions of nuclei with E$\geq$200 MeV/nucleon in hydrogen targets*, Physical Review **C 41** (1990), 566–571.

[146] V. Weisskopf, *Statistics and nuclear reactions*, Phys. Rev. **52** (1937), 295–303.

[147] V. F. Weisskopf and D. H. Ewing, *On the yield of nuclear reactions with heavy elements*, Phys. Rev. **57** (1940), 472–485.

[148] H. P. Wellisch and D. Axen, *Total reaction cross section calculations in proton-nucleus scattering*, Phys. Rev. C **54** (1996), 1329–1332.

[149] G. D. Westfall, J. Gosset, P. J. Johansen, A. M. Poskanzer, W. G. Meyer, H. H. Gutbrod, A. Sandoval, and R. Stock, *Nuclear fireball model for proton inclusive spectra from relativistic heavy-ion collisions*, Phys. Rev. Lett. **37** (1976), 1202–1205.

[150] G. D. Westfall, R. G. Sextro, A. M. Poskanzer, A. M. Zebelman, G. W. Butler, and E. K. Hyde, *Energy spectra of nuclear fragments produced by high energy protons*, Physical Review **C 17** (1978), 1368.

[151] J. A. Wheeler, *Fast neutron physics, part II*, ch. Channel analysis of fission, p. 2051, Interscience Publishers Inc., New York, 1963, and references therein.

[152] B. D. Wilkins, S. B. Kaufman, E. P. Steinberg, J. A. Urbon, and D. J. Henderson, *Evidence for a new reaction mechanism in the bombardment of ^{238}U with 11.5-GeV protons*, Phys. Rev. Lett. **43** (1979), 1080–1083.

[153] J.R. Wu, C.C. Chang, and H.D. Holmgren, *Charged-particle spectra : 90 MeV protons on ^{27}Al, ^{58}Ni, ^{90}Zr, and ^{209}Bi*, Physical Review **C 19** (1979), 698–713.

[154] H.S. Xu, M.B. Tsang, T.X. Liu, X.D. Liu, W.G. Lynch, W.P. Tan, A. Vander Molen, G. Verde, A. Wagner, H.F. Xi, C.K. Gelbke, L. Beaulieu, B. Davin, Y. Larochelle, T. Lefort, R.T. de Souza, R. Yanez, V.E. Viola, R.J. Charity, and L.G. Sobotka, *Isospin fractionation in nuclear multifragmentation*, Physical Review Letters **85** (2000), 716–719.

[155] J. F. Ziegler, J. P. Biersack, and M. D. Ziegler, *SRIM - the stopping and range of ions in matter*, Lulu Press Co., USA, 2008.

[156] J.F. Ziegler, *Particle interactions with matter*, World Wide Web electronic publication, 2003, http://www.srim.org/.